Understanding, controlling and manipulating the electronic properties of layered materials

I n a u g u r a l - D i s s e r t a t i o n

zur

Erlangung des Doktorgrades

der Mathematisch-Naturwissenschaftlichen Fakultät

der Universität zu Köln

vorgelegt von

M. Sc. Wouter Jolie

aus Saint-Martin D'Hères, Frankreich

Köln 2017

Erster Berichterstatter:	Prof. Dr. Carsten Busse
Zweiter Berichterstatter:	Prof. Dr. Thomas Michely
Dritter Berichterstatter:	Prof. Dr. Philip Hofmann
Vorsitz Prüfungskommission:	Prof. Dr. Achim Rosch
Tag der mündlichen Prüfung:	21.12.2017

Abstract

This thesis is devoted to the electronic properties of layered materials, with a focus on the underlying interactions. Scanning tunneling microscopy and spectroscopy are used to measure the local density of states present on the surface at low temperatures. The layered materials studied as part of this thesis are bilayer graphene, topological insulators and transition metal dichalcogenides. These materials have attracted broad interest in recent years for their exceptional electronic properties. The experimental results are compared to density functional theory calculation or model Hamiltonians conducted by cooperation partners.

A new way to probe the layer-dependent band structure, called layer polarization, of materials with broken inversion symmetry is demonstrated, namely by measuring quasiparticle interference patterns on their surface. The role of layer polarization is studied in chemically gated bilayer graphene, which is achieved by intercalating Cs between Ir(111) and bilayer graphene, thereby shifting the chemical potential above the second conduction band minimum. Intraband and interband scattering are expected to produce four rings around Γ and K, but only two pronounced and one weak ring are observed in the experiment. Our experimental results that are complemented by simulations based on the T-matrix theory, point to the localization of the standing waves within one of the two layers as the cause for the weakness of this scattering wave vector. In addition, another scattering wave vector is globally suppressed due to the parallel velocities of the states involved in the scattering process. The latter is derived analytically for an n-band model, that will be of great relevance for future quasiparticle interference studies of materials with non-trivial band structures.

In the compensated topological insulator $BiSbTeSe_2$, strong Coulomb disorder gives rise to the formation of local accumulations of charge carriers, denoted charge puddles, both in the bulk and on the surface. Bulk charge puddles are formed when the fluctuations of the Coulomb potential are as large as half of the band gap. Surface charge puddles are already formed when small fluctuations are present due to the gapless surface state, but the potential is strongly suppressed due to the additional screening channel provided by metallic surface carriers. This study uncovers the quantitative relationship between the properties of bulk puddles and surface puddles on $BiSbTeSe_2$, a material with well-investigated bulk charge puddles. At 5.5 K, we find surface potential fluctuations occurring on a length

scale $r_s = 40 - 50$ nm with amplitude $\Gamma = 8 - 14$ meV, which is much smaller than in the bulk. In this nominally undoped compound, the value of Γ is smaller than expected for pure screening by surface carriers, which may arise most likely from a cooperative effect of bulk screening and surface screening. In addition, surface charge puddles are found to be temperature-independent up to 77 K, a temperature at which bulk puddles are already strongly suppressed. Finally, quasiparticle interference maps show the Dirac nature of the surface state, which is well described by T-matrix simulations. The latter can be used to understand the role of the scattering potential. This allows to extract otherwise hidden physical parameters such as the number of charged scattering potentials and the screening length of the surface state.

Recent advances in molecular beam epitaxy of quasi-freestanding transition metal disulfide monolayers on van der Waals substrates made it possible to study the fundamental electronic properties of MoS_2 on graphene on Ir(111). Its large band gap underlines the weak coupling and small charge transfer between MoS_2 and its substrate. Scanning tunneling spectroscopy in constant current mode is used to measure the signal of several bands near to the valence band maximum and conduction band minimum of MoS_2. The influence of line defects, such as edges and mirror twin boundaries, is demonstrated. The great advantage of epitaxial MoS_2 on graphene on Ir(111) compared to other substrates is visualized via intercalation of Eu between graphene and Ir(111), showing that epitaxial MoS_2 on graphene on Ir(111) not only gives us the opportunity to measure the fundamental electronic properties of MoS_2, but also enables us to tailor those by doping graphene from the backside.

Grain boundaries in monolayer transition metal dichalcogenides are predicted to host one-dimensional metallic states embedded in an otherwise insulating layer. These states may be electronically unstable, undergoing a Peierls transition which leads to a charge density wave at low temperatures. The grain boundaries in epitaxial monolayer MoS_2 on graphene on Ir(111) are investigated in this thesis. The MoS_2 islands feature long, straight mirror twin boundaries, which are oriented along the material's dense-packed directions. Along these we measure a small band gap together with periodic beatings in the local density of states, both characteristic of charge density waves. Several types of mirror twin boundaries are identified, each of which gives rise to a unique periodicity and electronic structure. These quasi-freestanding wires offer an opportunity to study the simple yet rich physics of charge density waves, not often seen in true one-dimensional form experimentally. Specifically, we investigate their properties based on symmetry analysis, their band structure, the impact of point defects and edges, phonon excitations, temperature

dependence, phase-behavior and their response to doping. The latter is experimentally demonstrated with Eu intercalation between graphene and Ir(111), and shows a unique tunability of the periodic beating pattern.

Bulk VSe_2 features a three-dimensional charge density wave that has not been extensively studied so far. Scanning tunneling microscopy and spectroscopy are used to image the charge density wave at the surface and to probe its local density of states. The main features in the spectrum are linked to the contribution of the p-like and d-like bands of VSe_2 found in angle-resolved photoemission and tight-binding calculations. Additionally, we find a partial gap at the Fermi level that is attributed to the charge density wave phase. Assuming weak electron-phonon coupling, the energy scale of the gap found in the experiment is in good agreement with the transition temperature of VSe_2, leading to the conclusion that the Peierls model of Fermi surface nesting is applicable in this material. The role of defects is investigated, which reveals that the partial gap in the density of states and hence the charge density wave itself is extremely stable, though the periodic modulation on the surface is strongly perturbed.

Frequently used Symbols and Abbreviations

↑↑	-	Parallel
↑↓	-	Antiparallel
1D	-	One-dimensional
2D	-	Two-dimensional
3D	-	Three-dimensional
2DEG	-	Two-dimensional electron gas
ARPES	-	Angle-resolved photoelectron spectroscopy
BCS	-	Bardeen-Cooper-Schrieffer
BL	-	Bilayer
BLG	-	Bilayer graphene
BZ	-	Brillouin zone
CB	-	Conduction band
CBM	-	Conduction band minimum
CDW	-	Charge density wave
CEC	-	Constant energy contours
CPE	-	Critical point energy
CVD	-	Chemical vapor deposition
DFT	-	Density functional theory
DOS	-	Density of states
E	-	Edge
JDOS	-	Joint density of states
FS	-	Fermi surface
FT	-	Fourier transform
P	-	Point
LDA	-	Local-density approximation
LDOS	-	Local density of states
LEED	-	Low-energy electron diffraction

QPI	-	Quasiparticle interference
MBE	-	Molecular beam epitaxy
MTB	-	Mirror twin boundary
ML	-	Monolayer
MLG	-	Monolayer graphene
PLD	-	Periodic lattice distortion
PVD	-	Physical vapor deposition
QL	-	Quintuple layers
STM	-	Scanning tunneling microscopy
STS	-	Scanning tunneling spectroscopy
SOC	-	Spin-orbit coupling
TB	-	Tight-binding
TMDC	-	Transition metal dichalcogenide
TPG	-	Temperature programmed growth
TI	-	Topological insulator
TRIM	-	Time-reversal invariant momenta
TRS	-	Time-reversal symmetry
UHV	-	Ultra-high vacuum
VB	-	Valence band
VBM	-	Valence band maximum
vdW	-	Van der Waals
VHS	-	Van Hove singularity

Contents

I Introduction **1**

II Fundamentals **7**

1 Layered materials **9**

1.1 Monolayer graphene versus bilayer graphene 9

1.2 Monolayer molybdenum disulfide 15

1.3 Vanadium diselenide 19

1.4 $BiSbTeSe_2$ 20

2 Electronic interactions **23**

2.1 Charge density waves 23

2.2 Coulomb disorder 27

2.3 Quasiparticle interference 29

2.3.1 T-matrix theory 29

2.3.2 Joint density of states 31

2.3.3 Fermi Golden Rule 32

3 Experimental techniques **35**

3.1 Scanning tunneling microscopy 35

3.2 Low-energy electron diffraction 37

4 Setup and Procedures **39**

4.1 The low-temperature, ultra-high vacuum system 39

4.2 Sample preparation 40

III Experimental results **45**

5 Visualizing layer polarization in bilayer graphene with quasiparticle interference **47**

5.1 Motivation 47

5.2 Quasiparticle interference of bilayer graphene 49

5.3 T-matrix simulations 54

5.4 Discussion 57

5.5 Conclusions 58

6 Charge puddles in the bulk and on the surface of a compensated topological insulator 59

6.1 Motivation . . . 59

6.2 Observation of surface charge puddles . . . 61

6.3 Quasiparticle interference of $BiSbTeSe_2$ . . . 65

6.4 Discussion . . . 69

6.5 Conclusions . . . 74

7 Electronic properties of quasi-freestanding epitaxial molybdenum disulfide 77

7.1 Motivation . . . 77

7.2 Probing the bands of quasi-freestanding molybdenum disulfide . . . 79

7.3 Band bending near defects . . . 84

7.4 Manipulating the substrate interaction via doping . . . 88

7.5 Discussion . . . 90

7.6 Conclusions . . . 91

8 Charge density waves in mirror twin boundaries of molybdenum disulfide 93

8.1 Motivation . . . 93

8.2 Identifying charge density waves . . . 95

8.3 Density functional theory calculations of mirror twin boundaries in molybdenum disulfide . . . 99

8.4 Phonon excitations . . . 101

8.5 Phase pinning and quantum confinement . . . 104

8.6 Controlling and manipulating charge density waves . . . 108

8.7 Discussion and outlook . . . 112

8.8 Conclusions . . . 115

9 Charge density wave order in vanadium diselenide 117

9.1 Motivation . . . 117

9.2 Structural and electronic properties of vanadium diselenide . . . 119

9.3 The role of defects . . . 124

9.4 Discussion . . . 126

9.5 Conclusions . . . 128

IV Summary 129

V Appendix 135

A Varying the hopping parameters of bilayer graphene 137

B Parallel versus antiparallel velocities in QPI - n-band model 139

C Identifying mirror twin boundaries in molybdenum disulfide 145

D Deutsche Kurzzusammenfassung *(German Abstract)* 147

E Liste der Teilpublikationen *(List of Publications)* 149

F Bibliography 155

G Danksagung *(Acknowledgments)* 175

H Offizielle Erklärung 177

PART I

Introduction

Many-body interactions are behind many of the most fascinating phenomena in solid state physics: the charge and spin of electrons, as well as lattice vibrations of the periodic ion cores, are all coupled to another, leading to peculiar correlated effects such as superconductivity [1], magnetism [2], charge density wave order [3], or topological phases [4, 5]. These are partly already incorporated in current devices such as hard drives [6] and superconducting magnets, and have great potential for future applications, especially in the growing field of spintronics [7, 8].

It is known that electronic instabilities become stronger in low-dimensional, layered materials [9], leading to a drastic increase of the transition temperature under which an ordered, correlated phase emerges, as found in high-temperature superconductors [10], or charge density waves in the metallic, layered transition metal dichalcogenides (TMDCs) [11]. Conceptually, it is evident that electrons can easily avoid each other in three-dimensional systems, while they are all strongly coupled when confined to one dimension. In this thesis, layered materials such as bilayer graphene (BLG), three-dimensional topological insulators (TIs), as well as TMDCs are investigated. The possibility to cleave or grow these materials in ultra-high vacuum enables surface scientists to study the fundamental properties of a well-defined system first, while the impact of additional perturbations, such as defects or charge, may be included step by step to control, or even manipulate, their electronic properties. Especially, they all represent model systems to uncover the effects of various interactions, such as interlayer coupling, Coulomb disorder, or electron-phonon coupling, in combination with reduced dimensionality down to the physical limit of one monolayer (ML) [12, 13].

The band structure of BLG near the chemical potential consists of massive Dirac fermions [14], which are investigated in Chap. 5. They behave markedly different from the states of monolayer graphene (MLG) due to the interlayer interaction between the two Bernal-stacked sheets. For example, when exposed to a perpendicular electric field, the equivalence of the two layers in BLG is broken, which result in a band gap opening between valence and conduction band [15, 16]. This property makes BLG superior to MLG for devices such as field effect transistors [17]. In this study, the in-equivalence of the BLG layers in a perpendicular electric field is used to visualize with quasiparticle interference its layer-dependent band structure, called layer polarization.

In the case of compensated TIs, Coulomb interactions arising from random impurities in the crystal lead to strong fluctuations of the electronic states. In the bulk, these fluctuations are of the order of the band gap, leading to local charge carriers called charge puddles [18]. The need to investigate the role of charge puddles at the surface of TIs is

evident, since the control of the chemical potential is mandatory to create spin-polarized currents of electrons or holes confined to the surface of TIs [19, 20], while the bulk conductivity needs to be globally suppressed there. The role and interplay of surface and bulk charge puddles in the compensated TI $BiSbTeSe_2$ will be the topic of Chap. 6.

ML TMDCs have many superior properties compared to their bulk counterparts, such as a direct band gap [21], flexibility and transparency [22], making them suitable for future digital electronics and optoelectronics [23]. Strong electron-electron interactions due to the reduced screening are claimed to be responsible for many peculiar properties of ML TMDCs, such as their giant excitonic binding energy [24]. When TMDCs are grown on a metallic substrate, the interaction with the latter may perturb the properties of the ML, leading to a hybridized band structure [25], as well as gating due to band alignment [26]. In Chap. 7, the electronic properties of ML MoS_2 on a weakly interacting substrate, namely MLG/Ir(111), are investigated and compared to MoS_2 grown on strong and weakly interacting substrates, such as Au(111) and HOPG. In addition, we demonstrate two ways to manipulate the size and position of the MoS_2 band gap, namely with well-defined defects and doping through Eu intercalation.

As mentioned above, interactions between electrons and phonons may lead to phase transitions at low temperatures. Chap. 8 deals with the one-dimensional states observed in mirror twin boundaries (MTBs) in ML TMDCs, which have been reported to form a charge density wave [27] with a wealth of fascinating properties such as spin-charge separation [28], inelastic tunneling [27] and quantum confinement effects [29]. While these one-dimensional, metallic states were only observed in $MoSe_2$ [27–29] and $MoTe_2$ [30] MTBs so far, we present here the electronic properties of one-dimensional, metallic states embedded in MoS_2 MTBs, and show that they represent a model system to investigate the role of dimensionality, defects, and doping on the properties of electronic states.

While weak electron-phonon interaction and the resulting Fermi-surface nesting are expected to produce electron instabilities in one dimension, is remains questionable whether this remains the main driving force toward charge density wave order in higher dimensions [31]. A three-dimensional charge density wave phase that has not been extensively investigated so far is found in the layered material VSe_2. Its charge density wave gap, which is extracted at the chemical potential, is used to test the theoretical predictions of weak versus strong electron-phonon interaction.

The remainder of this thesis is organized as follows: starting with the fundamentals (Part II), the basic electronic properties of the layered materials under investigation are introduced in Chap. 1. The main electronic interactions are described in Chap. 2. The

experimental techniques, as well as the setup and sample preparations, are briefly discussed in Chap. 3 and Chap. 4. As detailed above, Chap. 5-9 discuss the experimental results (Part III), which are summarized at the end of the thesis (Part IV).

PART II

Fundamentals

CHAPTER 1

Layered materials

The tight-binding code of monolayer and bilayer graphene was programmed by J. Lux. N. Ehlen provided the tight-binding plots for MoS_2 and VSe_2.

This chapter covers the basic structural, electronic and related symmetry properties of the layered materials which are investigated in this thesis. The electronic properties of MLG and BLG are reviewed in Ref. [14, 32, 33]. A discussion on the electronic properties of MoS_2 and its relation to symmetries and valley physics can be found in Ref. [34, 35]. A detailed introduction to topological insulators with focus on both the mathematical description and the topological insulator materials found to date can be found in Ref. [36].

1.1 Monolayer graphene versus bilayer graphene

Monolayer graphene (MLG) is the two-dimensional (2D) form of graphite. Its exfoliation down to one atomic layer was the first experimental realization of a freestanding 2D crystal [12, 37], which led to a scientific boom [38] towards the surge of novel 2D materials [13]. MLG forms a honeycomb lattice in real space that is shown in Fig. 1.1 (a). The two colors visualize the two carbon atoms (A and B) in the unit cell of the hexagonal Bravais lattice. The rhomboid visualizes one unit cell in Fig. 1.1 (a).

The first Brillouin zone (BZ) of MLG is shown in Fig. 1.1 (b). It has the hexagonal symmetry of the Bravais lattice, with the high symmetry points Γ, M, K and K'. Note that K and K' are in-equivalent due to the two-atom basis.

The electronic properties of MLG can be modeled with a tight-binding (TB) Hamiltonian that considers electron hopping between the two sublattices A and B [14]. It introduces the hopping parameter γ_0 which can be understood as the overlap of neighboring

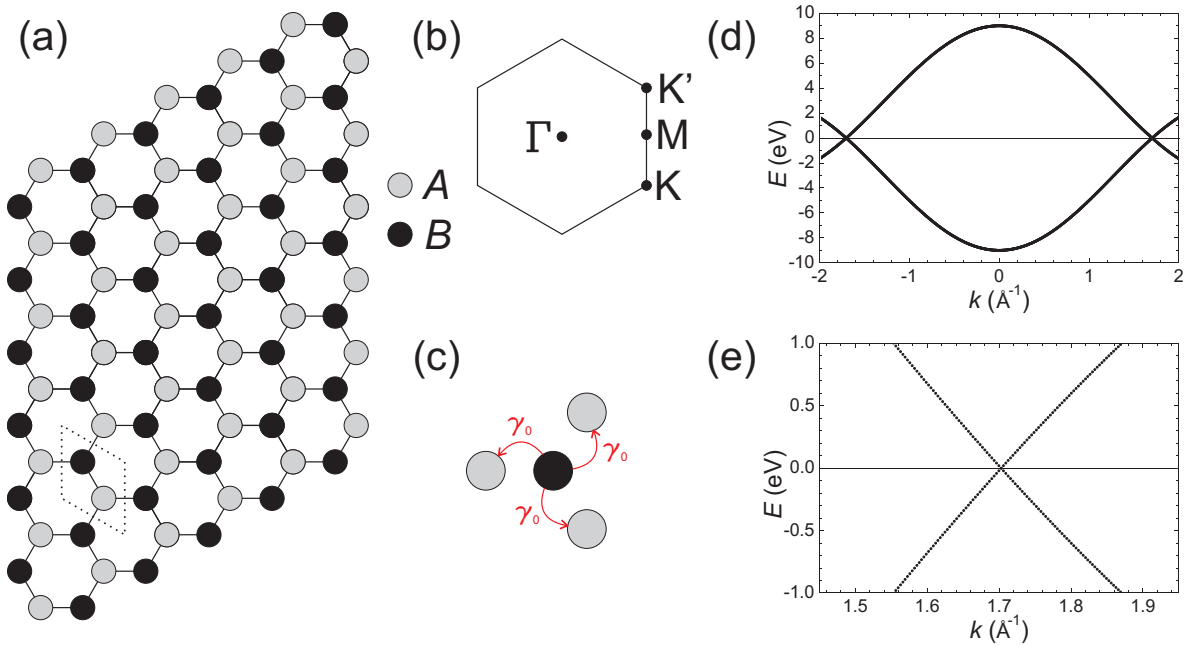


Figure 1.1: Structural and electronic properties of MLG: (a) In-plane lattice structure. The two colors visualize the two sublattices A and B (both are carbon atoms). The dotted rhomboid represents one unit cell which contains two atoms. (b) 1. BZ (hexagon) of MLG. The high symmetry points Γ, K, M and K' are indicated in the figure. (c) Visualization of the hopping parameter γ_0 between the two sublattices. (d) Band structure along MK'ΓKM using $\gamma_0 = 3$ eV. The two bands touch each other at the K and K' points near $k \approx \pm 1.7$ Å^{-1}, while Γ is at $k = 0$. The line at $E = 0$ represents the chemical potential. (e) Zoom on the band structure at energies in the vicinity of the chemical potential.

p_z orbitals. The three hopping terms connecting an electron at sublattice B to an electron at sublattice A are sketched in Fig. 1.1 (c). The resulting Hamiltonian has the following form:

$$H(\boldsymbol{k}) = \begin{pmatrix} 0 & -\gamma_0 f(\boldsymbol{k}) \\ -\gamma_0 f^*(\boldsymbol{k}) & 0 \end{pmatrix}. \tag{1.1}$$

The factor $f(\boldsymbol{k}) = \mathrm{e}^{ik_y a/\sqrt{3}} + 2\mathrm{e}^{-ik_y a/(2\sqrt{3})} \cos(k_x a/2)$ (a is the lattice constant) takes into account the location of the three nearest neighbors. The diagonal elements of the Hamiltonian are zero due to the absence of hopping within the same sublattice and the equivalence of the carbon atoms at positions A and B [14].

The band structure obtained from this Hamiltonian is shown in Fig. 1.1 (d) and (e). There are two bands that touch each other at the Dirac energy, forming a Dirac cone with linear

dispersion at the K point [32]. For freestanding MLG, the Dirac energy corresponds to the Fermi energy. The linear dispersion of the Dirac cone near K is given by [32]:

$$E(\mathbf{k}) = \pm\hbar v_{\mathrm{F}}\mathbf{k} = \pm\frac{\hbar 3\gamma_0 a}{2}\mathbf{k}, \tag{1.2}$$

and is hence directly proportional to γ_0. The Fermi velocity $v_{\mathrm{F}} \approx 10^6$ m/s is often extracted from the experiment instead of γ_0. Note that this dispersion is equivalent to that of massless Dirac fermions, which makes it possible to study the peculiar behavior of Dirac particles [12, 39, 40].

Including next-nearest hopping parameters between atoms of the same sublattice reduces the band width at M and hence enhances the asymmetry in the dispersion between KΓ and KM. This leads to stronger trigonal warping [41].

The dispersion obtained in this section only includes the p_{z} orbitals of MLG. There are additional bands arising from the sp^2 hybridization of the s, p_{x} and p_{y} orbitals of MLG. The covalent bonding leads to (occupied) bonding and (empty) anti-bonding bands that are separated by a large gap, so that they can be ignored when investigating the electronic properties at low energies, in the vicinity of the chemical potential.

There are many ways to tailor the electronic properties of MLG. Applying a magnetic field leads to quantized Landau levels with a peculiar energy separation unique to massless Dirac fermions [42]. The same quantization is observed when inducing folds in MLG such as nanobubbles [43] or wrinkles [44] that are mathematically equivalent to magnetic fields of several hundred Tesla (referred to as pseudo-magnetic fields since no field is actually applied). Confinement is another way to quantize the states of MLG [45, 46], similar to a 2D electron gas (2DEG) [47]. Terminating graphene also leads to edge states [48], while defects such as vacancies in the honeycomb lattice are proposed to be a source of magnetism [49, 50].

MLG epitaxially grown on a metal surface can exhibit a band gap at the Dirac energy due to strong hybridization of the metal bands with the bands of graphene, as for MLG on Ni(111) [51], or minigaps are formed due to the moiré induced by the lattice mismatch between graphene and the metal surface, as for MLG on Ir(111) [52]. Another important effect of the support is doping, which (mainly rigidly [53]) shifts the band structure of MLG up (p doping) or down (n doping) with respect to the chemical potential. In addition, it is possible to intercalate electron acceptors (such as alkali metals [54]) or donors (such as oxygen [45, 55]), that increase the doping range to more than 2 eV [56].

Bilayer graphene (BLG) consists of two MLG stacked on top of each other. The crystal structure of Bernal-stacked BLG (which will be referred to as BLG from now on) is shown

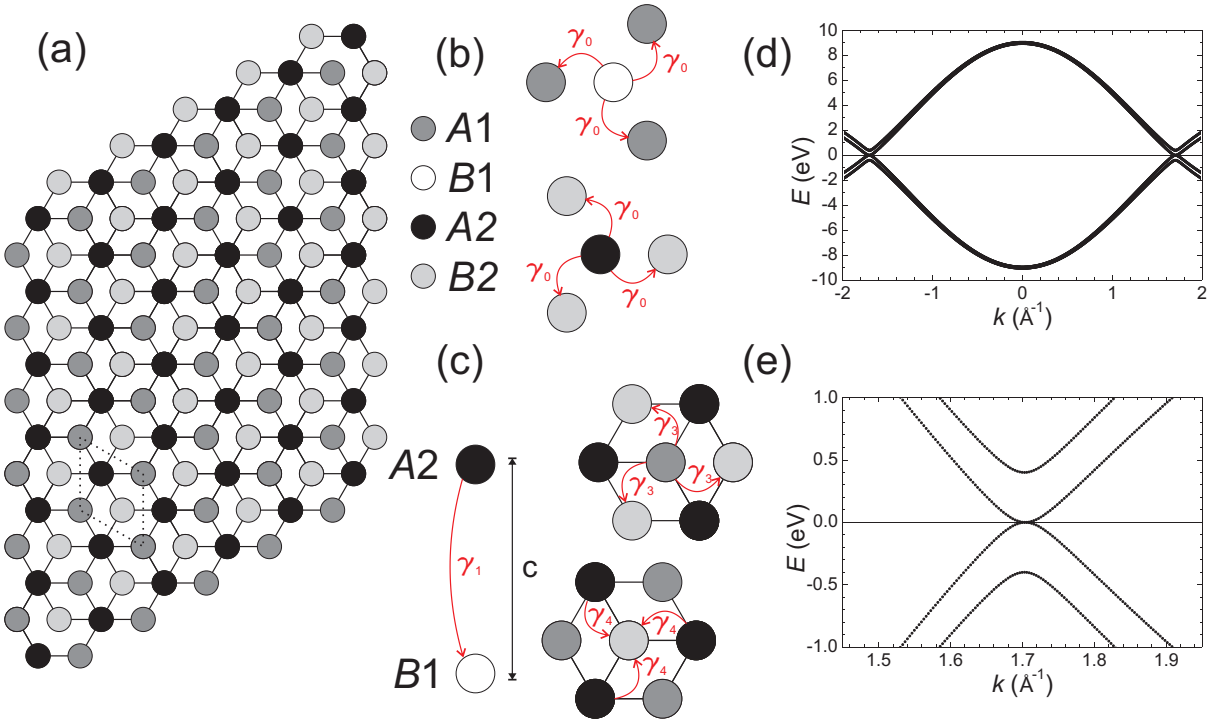


Figure 1.2: Structural and electronic properties of BLG: (a) In-plane lattice structure, with the sublattices $A1$ and $B1$ ($A2$ and $B2$) of the lower (upper) layer, respectively. The atoms $B1$ and $A2$ are directly on top of each other. The dotted rhomboid displays one unit cell which contains four C atoms. (b) Visualization of the hopping parameters in-plane (γ_0). (c) Hopping parameters (γ_1, γ_3 and γ_4) between the two layers. The parameter γ_1 is perpendicular to the layers (along the c direction) and hence higher than γ_3 and γ_4. (d) Band structure using $\gamma_0 = 3$ eV, $\gamma_1 = 0.55$ eV, $\gamma_3 = 0.1$ eV, $\gamma_4 = 0$ eV and $U = 0$ eV. The line at $E = 0$ represents the chemical potential. (e) Zoom on the band structure at energies in the vicinity of the chemical potential.

in Fig. 1.2 (a) from above. We have four atoms $A1$,$B1$,$A2$,$B2$ in the unit cell, with 1 and 2 referring to the lower and upper layer, respectively. Only three different atoms are visible since $B1$ and $A2$ are sitting directly on top of each other, while the $A1$ ($B2$) atoms are placed in the center of the honey comb rings of the lower (upper) layer.

The TB Hamiltonian for BLG in $A1$,$B1$,$A2$,$B2$-basis has the following form [14]:

$$H(\boldsymbol{k}) = \begin{pmatrix} U/2 & -\gamma_0 f(\boldsymbol{k}) & \gamma_4 f(\boldsymbol{k}) & -\gamma_3 f^*(\boldsymbol{k}) \\ -\gamma_0 f^*(\boldsymbol{k}) & U/2 & \gamma_1 & \gamma_4 f(\boldsymbol{k}) \\ \gamma_4 f^*(\boldsymbol{k}) & \gamma_1 & -U/2 & -\gamma_0 f(\boldsymbol{k}) \\ -\gamma_3 f(\boldsymbol{k}) & \gamma_4 f^*(\boldsymbol{k}) & -\gamma_0 f^*(\boldsymbol{k}) & -U/2 \end{pmatrix}. \tag{1.3}$$

The hopping parameters γ_1, γ_3 and γ_4 take into account hopping between the two layers, while γ_0 describes in-plane hopping, see Fig. 1.2 (b) and (c). The potential U describes a difference in the on-site energy of the orbitals on the two layers [14], which makes them in-equivalent and, in consequence, breaks the inversion symmetry of BLG. This symmetry breaking can be induced by an electric field perpendicular to the layers [15]. The hopping parameter between A_2 and B_1 (γ_1) is higher than the hopping parameters between A_1 and B_2 (γ_3) and between A_1 and A_2 (γ_4), since the two atoms are directly on top of each other in this case only, see Fig. 1.2 (c). Hence we have $\gamma_0 > \gamma_1 > \gamma_3 \approx \gamma_4$. Note that hopping between B_1 and B_2 is equivalent to the hopping between A_1 and A_2, leading to four matrix elements in the Hamiltonian containing γ_4. Turning off all out-of-plane hopping parameter leads to the Hamiltonian of two non-interacting MLG sheets with different on-site energies, compare to Eq. 1.1.

The band structure of BLG is shown in Fig. 1.2 (d) and (e) in the symmetric case of $U = 0$ and using $\gamma_0 = 3$ eV, $\gamma_1 = 0.55$ eV, $\gamma_3 = 0.1$ eV, $\gamma_4 = 0$ eV. Four bands are present due to the four atoms in the unit cell, two valence bands and two conduction bands. In freestanding BLG, the chemical potential lies between valence and conduction bands, as indicated in Fig. 1.2 (c) and (d) with a line at $E = 0$. Two bands touch at the K point, forming massive Dirac fermions [32], while the other two bands are separated by a gap.

Having control over the parameters of Eq. 1.3 helps to understand their influence on the band structure, see App. A. The slope of all four bands is mainly determined by γ_0, as in MLG. The gap at K between two of the four bands strongly depends on γ_1. The two bands that touch at the chemical potential hence arise from the hopping between $A1$ and $B2$, while the hybridized bands that are separated by a gap arise from the hopping between $A2$ and $B1$, that are directly on top of each other [14]. The hopping parameter γ_3 induces a small trigonal distortion near the Dirac energy [not visible in Fig. 1.2 (e)] that leads to a Lifshitz transition [14], while the hopping parameter γ_4 breaks the electron-hole symmetry [14].

Note that the (AB) stacking of the two carbon layers is crucial to obtain the band structure shown in Fig. 1.2 (d) and (e). When the two layers are AA stacked, the band structure shows two Dirac cones at K that are separated in energy by $2\gamma_1$ [33]. When the two layers are twisted, with small rotation angles up to 10°, van Hove singularities appear in the density of states (DOS) [57], in close resemblance to the minigaps induced by the moiré of epitaxial MLG. Note that at very small rotational angles, both AB and AA stacking are present, leading to the observation of coexisting massless and massive Dirac fermions in ARPES due to the large beam size [58]. However, all ARPES studies on BLG on Ir(111)

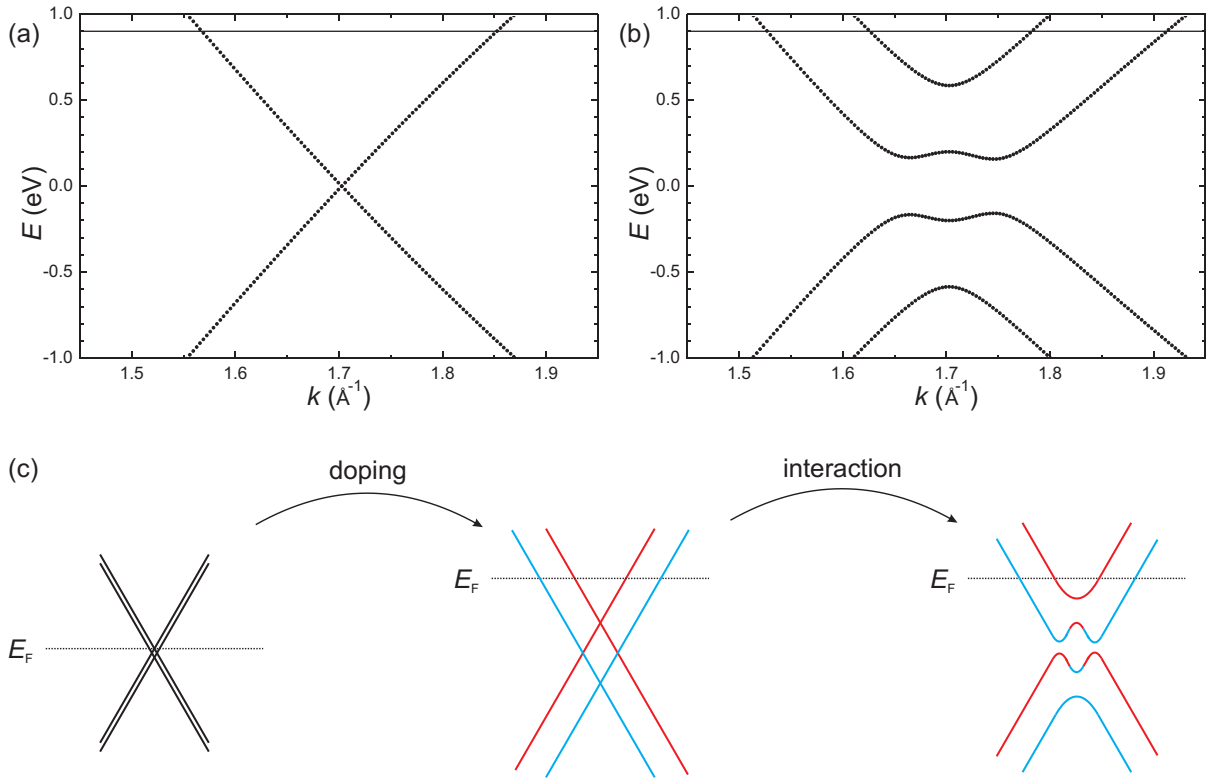


Figure 1.3: Doping MLG and BLG: (a) Doping rigidly shifts the Dirac cone away from the chemical potential in MLG. No gap opens between valence and conduction band. (b) Doping also rigidly shifts the bands on BLG, but in addition opens a gap between valence and conduction bands. The on-site energy U is responsible for the band gap, breaking the equivalence of the two layers. (c) gedankenexperiment that visualizes the physics behind the gap opening. The red (blue) band refers to the upper (lower) layers when doping from below.

(which is subject of Chap. 5) reported AB stacking when the two layers are aligned [59, 60], which can easily be verified with STM due to the appearance of a moiré pattern with a characteristic periodicity that depends on the rotation angle between the two graphene layers [61].

One important difference between freestanding and epitaxial MLG and BLG is their behavior upon doping, i.e. charge transfer between the 2D material and its substrate. The effect of doping on the band structure of both MLG and BLG is shown in Fig. 1.3. In both cases the chemical potential is set to $\mu = 0.9$ eV. As discussed above, we find that the chemical potential is not at the position of the Dirac energy in MLG, see Fig. 1.3 (a). The band structure is rigidly shifted, leaving the Dirac cone intact. Hence, it is common to define the doping level as the energy difference between chemical potential and Dirac energy. In BLG, we see that doping changes the band structure far more, see Fig. 1.3 (b).

In addition to the rigid shift of the bands we find that a band gap opens at the Dirac energy. It is caused by the on-site energy U that breaks the inversion symmetry and renders the two layers in-equivalent.

The effect of doping in BLG can be understood with a gedankenexperiment that is sketched in Fig. 1.3 (c). Imaging having two equivalent graphene layers ($U = 0$) that are not coupled ($\gamma_1 = \gamma_3 = \gamma_4 = 0$). The Hamiltonian then collapses to that of MLG, and we get two degenerate Dirac cones at low energies. Bringing an electropositive material in close proximity from below significantly dopes the lower layer (blue Dirac cone), while the chemical potential of the upper layer is only slightly shifted (red Dirac cone). The difference is given by the on-site energy U, which rigidly shifts the cones, lifting their degeneracy. This leads to two different doping levels for the non-interacting Dirac cones. By turning on interlayer interactions, we see that gaps open at the positions where bands are crossing each other, leading to the sombrero-like band gap of BLG. Note that without interlayer hopping we have two Dirac cones that are completely localized in one of the two layers. This layer polarization is also present in BLG, as sketched in Fig. 1.3 (c). While the states in our gedankenexperiment are always completely localized in one of the two layers in MLG, the degree of localization in BLG depends on the size of U and the position in the band structure. As an example, for an on-site energy of $U = 0.4$ eV, we find a layer polarization of 0.2 to 0.8 for the two conduction bands at the chemical potential.

1.2 Monolayer molybdenum disulfide

The structure of the transition metal dichalcogenide (TMDC), trigonal prismatic (2H), monolayer (ML) MoS_2 is sketched in Fig. 1.4 (a)-(b). The Mo (red) and S (yellow) atoms form a honeycomb lattice in plane, see Fig. 1.4 (a). Important symmetries of this crystal structure are the three mirror planes sketched with dashed lines. One primitive unit cell is sketched with dotted lines. In the side view along the armchair direction shown in Fig. 1.4 (b), we find that two sulfur atoms are sitting above each other in the trigonal prismatic geometry. Every Mo atom binds to 6 sulfur atoms, while one sulfur atom binds to three Mo atoms. The unit cell contains three atoms. The binding in MoS_2 is not purely covalent as in MLG, but partly ionic, since each Mo donates 4 electrons, while every S accepts 2 electrons [63]. The dashed line in Fig. 1.4 (b) defines an additional mirror plane. The reciprocal space is sketched in Fig. 1.4 (c), with the high symmetry points Γ, Γ', M, K and K'. The hexagon around Γ defines the first BZ.

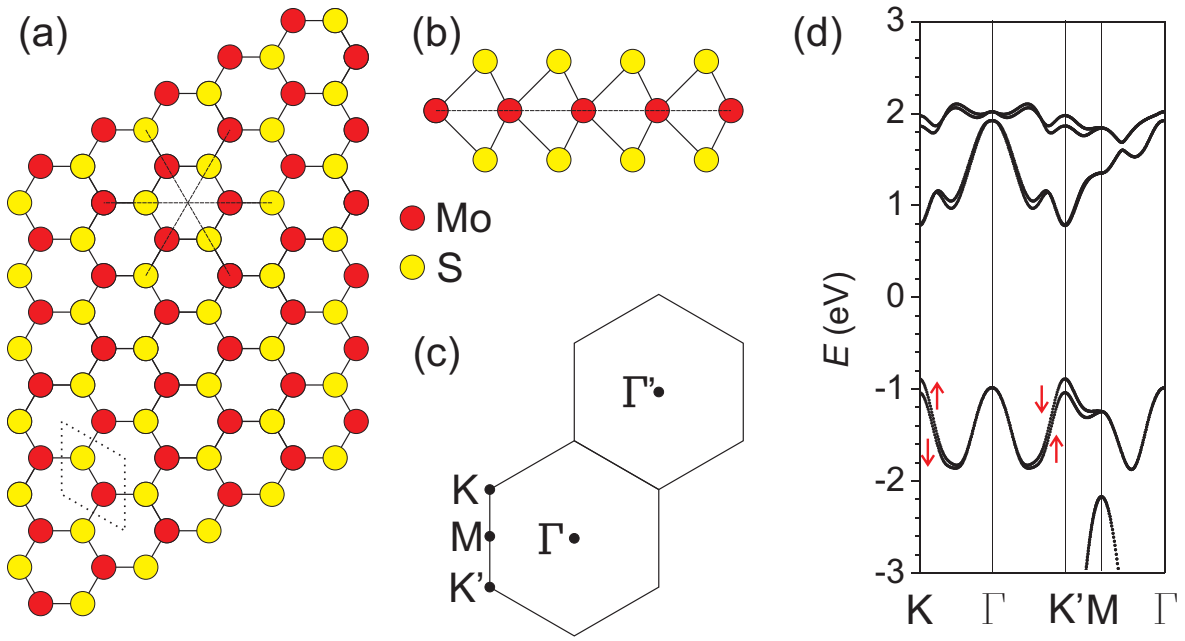


Figure 1.4: Electronic and structural properties of 2H ML MoS_2: (a) In-plane lattice structure. The dashed line visualizes the mirror planes. The dotted rhomboid is the unit cell which contains three atoms. (b) Out-of-plane crystal structure along the armchair direction. The dashed line is an additional mirror plane. (c) 1. BZ around the Γ point (hexagon). The high symmetry points at K, M and K' are marked. The length between Γ and Γ' represents one reciprocal lattice vector. (d) Band structure of ML MoS_2 along high symmetry directions using TB [62]. The valence bands have three CPEs, the conduction bands four CPEs. Some of the bands are spin-split, which is sketched with red arrows in the VB.

The band structure of ML MoS_2 close to the chemical potential is shown in Fig. 1.4 (d) along high symmetry directions [62]. It uses the TB model of Ref. [64]. A band structure calculation of MoS_2 using *GW* which shows excellent agreement to experimental absorbance [21] and photoluminescence excitation measurements [65], can be found in Ref. [66]. MoS_2 is a semiconductor, with a (theoretical) band gap of 2.8 eV using *GW* between valence band maximum (VBM) and conduction band minimum (CBM) [66]. Note that the band gap in Fig. 1.4 (d) is smaller due to the different density functional theory (DFT) calculation used for the TB fit [64]. We find three extrema, denoted critical point energies (CPEs), near the top of the valence band; one at the Γ point, the other two at K. At the bottom of the conduction band, we find 4 CPEs; one at K, two between K and Γ (near Q), and a maximum between the two.

The valence band maximum and conduction band minimum are both located at K, which makes ML MoS_2 a direct band gap semiconductor. Note that the band gap becomes

indirect when increasing the numbers of layers due to a shift of the valence band at Γ above the band at K [67], similar to the behavior of other TMDCs such as $MoSe_2$ [68].

The effect of spin-orbit coupling (SOC) is important to understand the electronic properties of 2H TMDCs in general due to the heavy transition metal atom and the broken inversion symmetry when reducing the thickness of the crystal to one ML. Zhu et al. [34] showed that SOC is responsible for the spin-splitting of some of the bands along KΓK'M, by using DFT calculations with and without SOC. Two red arrows visualize the spin-splitting at the top of the valence band of Fig. 1.4 (d). They point up or down, depending on the spin components of the states within the bands.

The link between SOC and the symmetries of MoS_2 is nicely visualized with Kramer's degeneracy: time-reversal symmetry (TRS) dictates that a state with energy E, spin $\uparrow$ and momentum $\mathbf{k}$ obeys the relation $E_\uparrow(\mathbf{k}) = E_\downarrow(-\mathbf{k})$, because changing the sign of time reverses momentum and flips the spin of a state, but does not change its energy. For crystals with inversion symmetry $[E_\uparrow(\mathbf{k}) = E_\uparrow(-\mathbf{k})]$, all states in the band structure have to be spin-degenerate, because $E_\uparrow(\mathbf{k}) = E_\downarrow(-\mathbf{k}) = E_\downarrow(\mathbf{k})$. In the case of ML MoS_2, the inversion symmetry is explicitly broken, so that spin-splitted bands are in principle allowed. However, the mirror planes sketched in Fig. 1.4 (a) and (b) lead to spin-degeneracy along the high symmetry direction ΓM and for spin components pointing in-plane, since $E_\uparrow(\mathbf{k}) = E_\downarrow(\mathbf{k})$ when spin and momentum are parallel to one mirror plane. All other states can be spin-split, with a sign change across the ΓM plane due to mirror symmetry $[E_\uparrow(\mathbf{k}) = E_\downarrow(\text{-}\mathbf{k})]$. Hence, the spin-splitting at K is reversed at K', leading to an additional degree of freedom entitled valley physics [35].

Interestingly, though bilayer (BL) MoS_2 has an inversion center, it still has spin-splitted bands [69]. This hidden spin-polarization is due to the layer-dependent band structure of BL MoS_2; The upper layer hosts the spin-up state which has the same energy as the spin-down state in the lower layer. Hence, though Kramer's degeneracy is maintained, surface sensitive method such as ARPES are able to find these hidden spin-polarized states by mainly probing the upper layer [70].

Extended line defects are known to exist in MoS_2, especially when grown epitaxially with chemical vapor deposition (CVD) or molecular beam epitaxy (MBE). These grain boundaries are potentially relevant as they are expected to enable spin- and valley polarized transport in TMDCs [71]. Different types of grain boundaries form, depending on the orientation of the two flakes that meet each other. A highly symmetrical case is found when the two grains are rotated by 60° with respect to each other. The resulting line defect is a mirror twin boundary (MTB) which is oriented along the material's

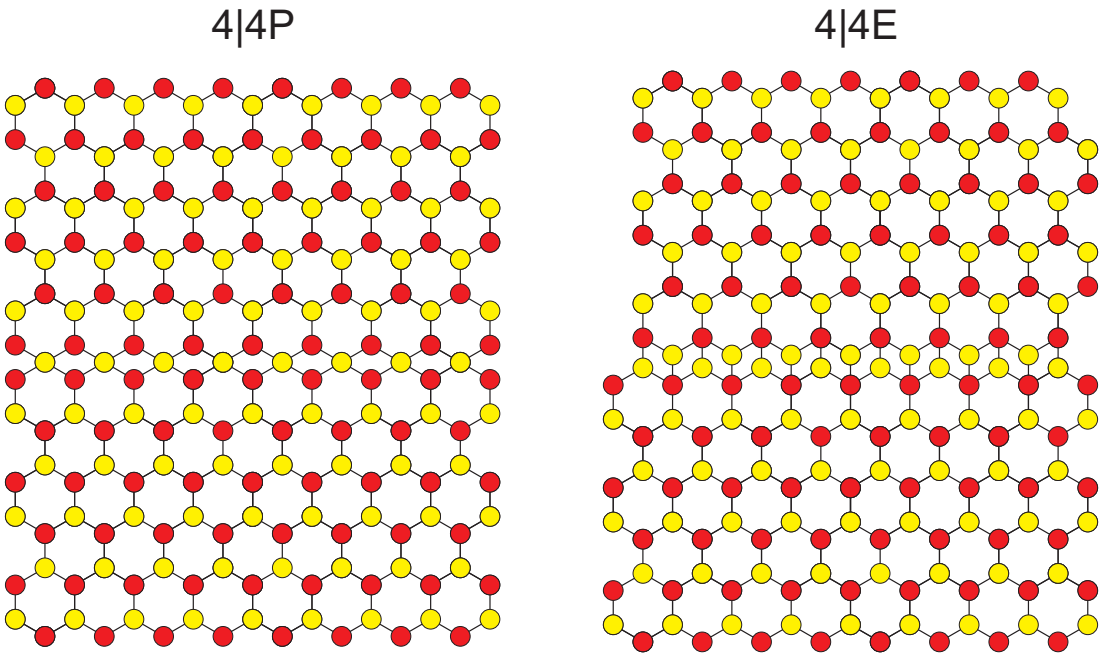


Figure 1.5: MTBs in MoS_2: The grain boundary in the 4|4P structure forms 4-membered rings that are connected by a point. In the 4|4E structure, the 4-membered rings are connected by an edge. Note that the atom positions within the MTB are not relaxed in this sketch.

dense-packed directions. Two kinds of highly symmetrical MTBs form in MoS_2 during growth [72]. Their structure is sketched in Fig. 1.5: the MTBs are defined as 4|4P and 4|4E, following the notation of Ref. [73]; The 4|4P MTB forms 4-membered rings within the grain boundary, which are connected by a single point (P). The 4|4E MTB also forms 4-membered rings within the grain boundary, which are connected by an edge (E). The relaxed 4|4P structure is flat, while the 4|4E structure shows a small height change at the boundary [72]. MTBs in TMDCs are predicted to host metallic states that are confined in one-dimension. As was shown recently for $MoSe_2$ [27, 28], these metallic states undergo a Peierls transition which leads to a commensurate charge density wave (CDW) at low temperatures.

In the 4|4P structure, the mirror plane lies exactly on the MTB. This is not the case in the 4|4E structure. However, since both 4|4P and 4|4E MTBs are inversion symmetric one can conclude that no spin-splitted bands are expected for long MTBs and when the role of the substrate is negligible. In line with this symmetry analysis, DFT calculations of the 4|4P MTB in $MoSe_2$ reported no spin-splitting when including SOC [27].

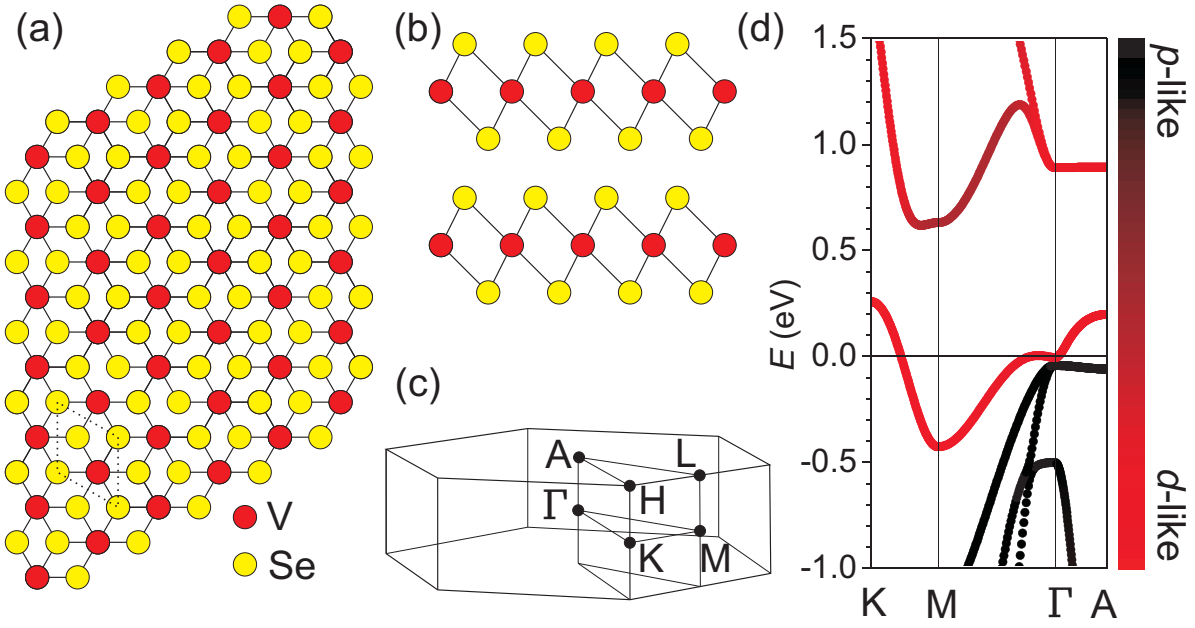


Figure 1.6: Electronic and structural properties of VSe_2: (a) In-plane lattice structure. The dotted rhomboid is the unit cell which contains three atoms. (b) Out-of-plane crystal structure along the armchair direction. Two Se-V-Se blocks are sketched, separated by a vdW gap. (c) Three-dimensional 1. BZ around the Γ point, with the high symmetry points within the ΓKM and AHL planes. (d) Sketch of the band structure of VSe_2 along certain high symmetry directions [62].

1.3 Vanadium diselenide

The structure of octahedral (1T) VSe_2 is sketched in Fig. 1.6 (a)-(b). Similar to 2H MoS_2, the unit cell consist of a transition metal (V, red) layer sandwiched between two chalcogen (Se, yellow) layers. The crystal has octahedral symmetry, forming a hexagonal structure in the top view, see Fig. 1.6 (a). Inversion symmetry is present in bulk VSe_2 and persists down to one ML, so that SOC is unable to lift the spin degeneracy in VSe_2 as long as this symmetry is not broken, as for example due to a surface termination [74, 75]. The primitive unit cell is sketched with dotted lines. The inversion symmetry is best seen in the side view along the armchair direction shown in Fig. 1.4 (b). Two layers are sketched to visualize the inversion symmetry of the BL and, in consequence, of the bulk (which is also present in 2H TMDCs) and, in addition, the inversion symmetry within each individual Se-V-Se block. The binding in bulk VSe_2 is strong within the Se-V-Se layers, while mainly van der Waals (vdW) between these layers. The unit cell contains three atoms.

The 1. BZ is sketched in Fig. 1.6 (c), with the high symmetry points Γ, M, K, A, L and H. When thinned down to one ML it is identical to the BZ of MoS_2 since both have equal Bravais lattices in plane.

The band structure of VSe_2 calculated using TB is shown in Fig. 1.6 (d) [62]. The color of the bands indicates their orbital character, from p-like to d-like. One of the bands crosses the Fermi level, hence VSe_2 is a metal. Due to the layered structure of VSe_2, the band width is largest in the Γ-M-K plane. There is, however, also a finite dispersion out-of-plane, see Fig. 1.6 (d).

Many metallic TMDCs undergo a phase transition at low temperatures, forming a CDW. In VSe_2, two CDWs are observed with the corresponding transition temperatures $T \approx 110$ K and $T \approx 80$ K as measured using electron diffraction [76], resistivity measurements [77] and Raman [78]. The high temperature CDW forms a commensurate (4×4) periodic lattice distortion (PLD) with respect to the lattice in-plane ($q_\mathrm{a} = a^*/4 = 0.54\text{Å}^{-1}$) with an (incommensurate) out-of-plane component ($q_\mathrm{c} = 0.314c^*$) [79–81], with $a^* = |\mathbf{a}^*| = |\mathbf{b}^*|$ and $c^* = |\mathbf{c}^*|$ defined as the length of reciprocal lattice vectors parallel (ab-plane) and perpendicular (c-axis) to the layers, respectively. The second CDW phase at lower temperatures stays commensurate in-plane, but has a reduced out-of-plane component ($q_\mathrm{c} = 0.307c^*$) [79, 81]. Note that a commensurate out-of-plane component ($q_\mathrm{c} = c^*/3$) has been reported in Ref. [82].

1.4 $BiSbTeSe_2$

The crystal structure of $BiSbTeSe_2$ is shown in Fig. 1.7 (a)-(b). The crystal consists of quintuple layers (QLs) with the stacking order Te/Se, Bi/Sb, Se, Bi/Sb, Te/Se. Fig. 1.7 (b) shows a side view, in which one QL is highlighted with a dashed rectangle. The (Te/Se) layers that separate two QLs are only weakly bond via vdW forces, making it the preferred cleaving plane. When substituting Bi/Sb→Bi and Te/Se→Se, the crystal structure transforms to the famous topological insulator (TI) Bi_2Se_3 [20]. The biggest advantage of $BiSbTeSe_2$ and other composition of the form $Bi_{2-x}Sb_xTe_{3-y}Se_y$ is their insulating bulk due to nearly perfect compensation [83].

Similar to Bi_2Se_3, $BiSbTeSe_2$ is a TI with a surface state that forms a spin-polarized Dirac cone at the Γ point. While the Dirac energy is close to the chemical potential in $BiSbTeSe_2$, it is possible to vary the location of the Dirac cone within the bulk band gap by changing the composition of $Bi_{2-x}Sb_xTe_{3-y}Se_y$ [84]. To understand what is actually driving these materials to become a TI, we briefly recall the basic theoretical results of TIs

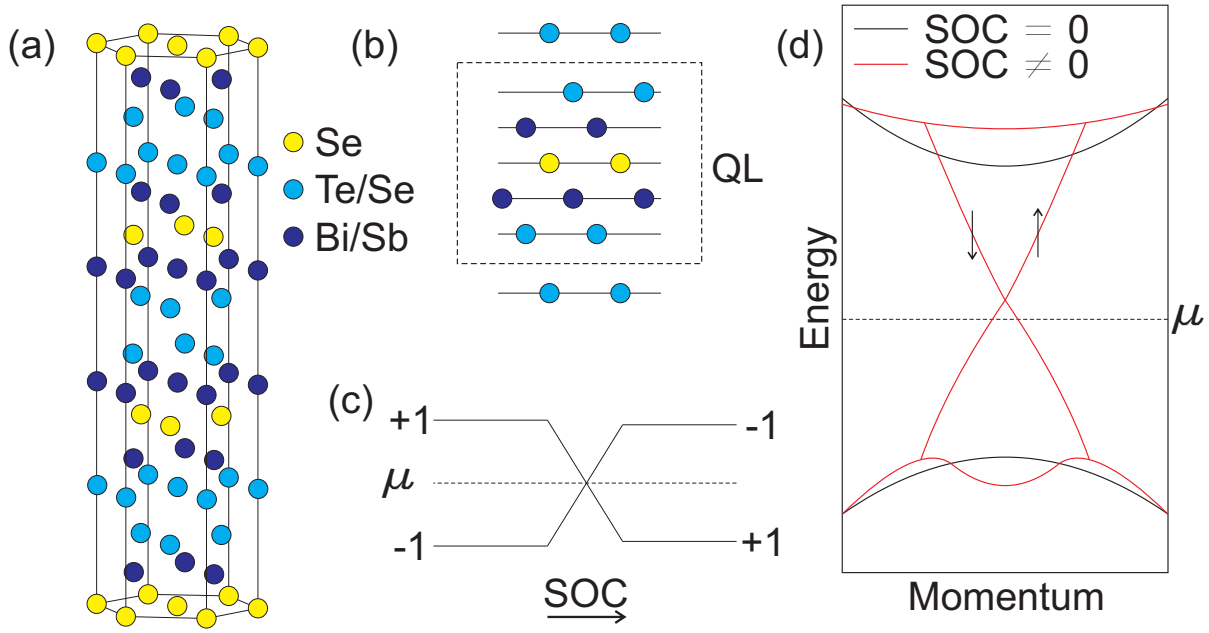


Figure 1.7: Electronic and structural properties of $BiSbTeSe_2$: (a) Unit cell of $BiSbTeSe_2$, containing layers of Se (yellow), Te/Se (cyan) and Bi/Sb (dark blue). (b) Out-of-plane crystal structure. The dashed rectangle visualizes the QL structure. The bonding between QLs is weak, while strong within the QL. (c) Visualization of the band inversion and corresponding change in the parity (± 1) due to SOC. (d) Sketch of the band structure with and without SOC.

(see Ref. [36] for a long, yet pedagogically appealing derivation and discussion), which are mainly based on fundamental symmetry arguments that are directly related to the crystal and electronic structure of the material. As already described in Sec. 1.2, when TRS is preserved, Bloch states u_{k} with spin up and momentum k are coupled to states with spin down and momentum $-k$. At time-reversal invariant momenta (TRIM), this leads to a (Kramers) degeneracy that can only be lifted when the symmetry is broken. In 3D, there exist 8 TRIM $\Lambda_{\mathrm{n1,n2,n3}}$ with all combinations $n_i = 0, |G_{\mathrm{i}}/2|$ (G_{i} is a reciprocal lattice vector). Mathematically, the two states are then coupled via a matrix of the form [36]:

$$w_{\alpha\beta}(\mathbf{k}) =< u_{\alpha,-\mathrm{k}}|\Theta|u_{\beta,\mathrm{k}} > , \tag{1.4}$$

where α and β are band indices, and Θ the TRS operator. In the simple case of a two band model, $\alpha =\uparrow$ and $\beta =\downarrow$. At TRIM, the Kramers degeneracy dictates that two Bloch states with opposite spin and momentum are equal, except for a phase factor $e^{\chi(k)}$, which in consequence enters $w_{\alpha\beta}$. With the knowledge of $w_{\alpha\beta}$, one is then able to analyze the Z_2 topological invariants ν_0 and ν_i (i = 1,2,3) for every TRIM Λ_i (without loss of generality $|G_{\mathrm{i}}| = \pi$), which are given by the following equations [19]:

$$\delta\left(\Lambda_i\right) = \frac{\mathrm{Pf}[\mathrm{w}\left(\Lambda_\mathrm{i}\right)]}{\sqrt{\det[\mathrm{w}\left(\Lambda_\mathrm{i}\right)]}} \tag{1.5}$$

$$\Rightarrow (-1)^{\nu_0} = \prod_{n_\mathrm{j}=0,\pi} \delta\left(\Lambda_{\mathrm{n}_1,\mathrm{n}_2,\mathrm{n}_3}\right), \tag{1.6}$$

$$(-1)^{\nu_i} = \prod_{n_{\mathrm{j}\neq\mathrm{i}}=0,\pi;n_\mathrm{i}=\pi} \delta\left(\Lambda_{\mathrm{n}_1,\mathrm{n}_2,\mathrm{n}_3}\right),\ (i = 1,2,3). \tag{1.7}$$

When one of the topological invariants is non-zero, the Hilbert space is *twisted* [36], and the material is topologically non-trivial in the bulk. When in contact to a topologically trivial insulator such as vacuum, the TI material will close its band gap at the interface to change its topology. This leads to topologically protected surface states at the surface of TIs. Note that ν_0 is unique to 3D systems, which is why TIs are separated into two categories: strong ($\nu_0 = 1$) and weak (at least one $\nu_i = 1$) TIs.

Another important symmetry that simplifies the search for TI materials is inversion symmetry, which is also present in $BiSbTeSe_2$ [the yellow Se atoms are inversion centers, see Fig. 1.7 (b)]. Fu and Kane [85] could show that, when inversion symmetry is present, the Z_2 topological invariants can be calculated with the parity eigenvalues (which are ± 1) of the occupied bands at TRIM. Hence, when two bands at the chemical potential with opposite parity switch positions at a TRIM, the material also changes from topological non-trivial to topological trivial or vice versa. For the isostructural compound Bi_2Se_3, Zhang et al. [20] could track down that SOC is responsible for the non-zero topological invariant $\nu_0 = 1$, since it switches the position of two p-bands with opposite parity, as visualized in Fig. 1.7 (c). The corresponding band structure with and without SOC is sketched in Fig. 1.7 (d). With SOC, one finds a band inversion at the Γ point, which in turn leads to topologically protected surface states as observed with ARPES [84]. Another consequence of SOC is that the surface state is spin polarized, so that the states near the Γ point behave like Dirac fermions with interesting properties, such as spin-momentum locking.

CHAPTER 2

Electronic interactions

This chapter introduces the reader to various interactions that lead to the peculiar properties of the materials investigated in this thesis.
Electron-phonon coupling and its connection to CDWs is described in detail in the books of Khomski [86], Gruener [87], and in the review of Rossnagel [88]. The paper of Johannes et al. [31] nicely discusses the role of the electron susceptibility to CDW formation.
Coulomb disorder and the resulting charge puddles is reviewed in Ref. [89].
The complete derivation of the T-matrix theory using scattering theory is found in the book of J.J. Sakurai [90] and in the lecture notes of A. Altland [91]. A review on JDOS and T-matrix theory with focus on graphene can be found in Ref. [92].

2.1 Charge density waves

Peierls noted in 1955 [3] that low-dimensional systems tend to be electronically unstable, undergoing a transition at low temperatures to an ordered phase which is nowadays known as charge density wave (CDW). The fingerprints of the phase are (i) a band gap (defined as CDW gap) opening in the band structure at the Fermi energy, (ii) a modulation in the LDOS with wavelength $\lambda = \pi/k_{\mathrm{F}}$, accompanied with (iii) a static lattice distortion with the same wavelength. These characteristic features are sketched in Fig. 2.1. Many materials were found to order in the CDW phase at low temperatures, especially low-dimensional, layered materials such as TMDCs [88].
A qualitative explanation of the existence of a CDW is obtained when considering Bloch wave functions of a nearly-free electron band in a weak periodic potential. When the periodicity is equal to the Bravais lattice, gaps open in the dispersion at the first BZ

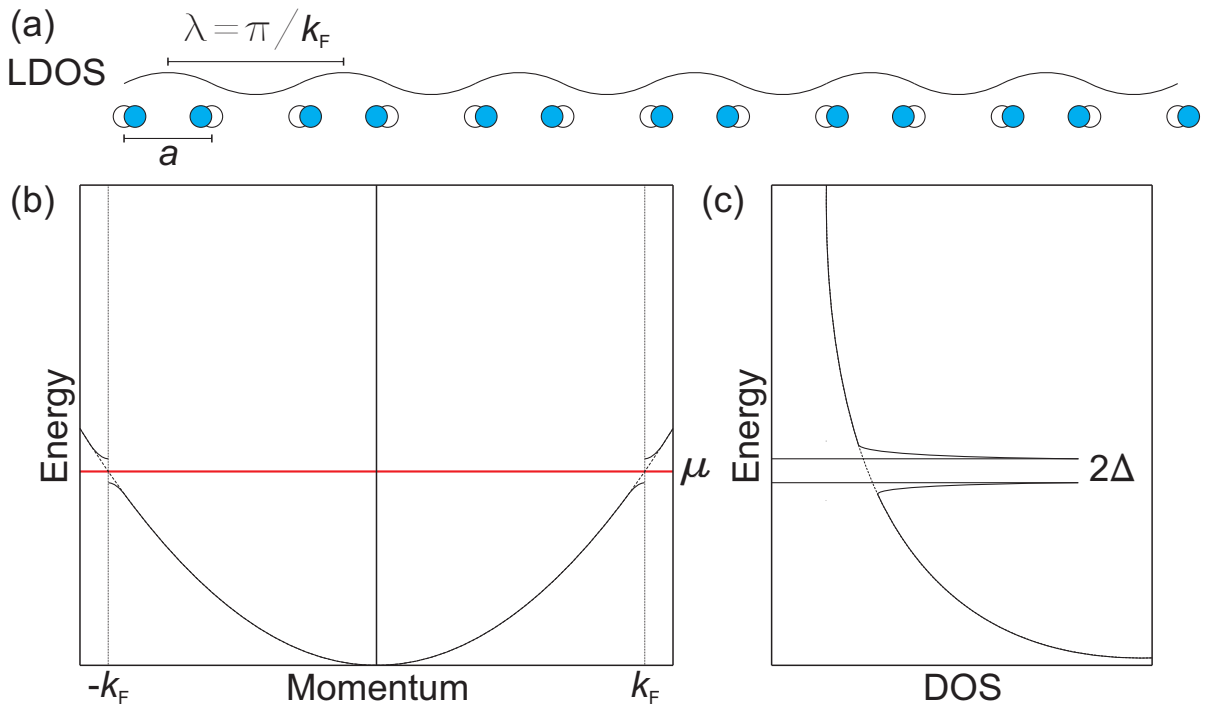


Figure 2.1: The Peierls transition of a one-dimensional chain: (a) PLD along the chain leads to a spatial modulation of the LDOS, with a periodicity of $\lambda = \pi/k_\mathrm{F}$. (b) Dispersion relation above (dashed) and below (full) the transition temperature T_C. The red line represents the chemical potential μ. (c) Corresponding DOS above (dashed) and below (full) the transition temperature T_C. The CDW gap 2Δ always opens at the Fermi energy.

boundaries, which in one dimension (1D) are located at $k = \pm\pi/a$ (a is the lattice constant). When introducing a static, periodic lattice distortion (PLD), we increase the Bravais lattice in real space, reducing the size of the BZ in reciprocal space and in consequence opening a gap at $k = \pm\pi/\lambda$, with λ being the periodicity of the PLD. This gedankenexperiment can be done for arbitrary filling (or arbitrary PLD). The CDW gap, however, is only energetically favorable at the Fermi energy, since it lowers the energy of the occupied states, while unoccupied states are energetically higher, but empty and hence do not cost energy. In conclusion, by inducing a small PLD with wavelength $\lambda = \pi/k_\mathrm{F}$, the highest occupied states are lowered in energy due to the opening of a CDW gap at the Fermi energy. There are, however, several questions that need to be answered, namely (i) when is the CDW state energetically favored and (ii) how do the electronic states interact with the lattice?

The connection between electronic states and lattice vibrations is given by the Fröhlich Hamiltonian that couples the electron and phonon systems [87]:

$$H_{\mathrm{e-ph}} = \sum_k E_{\mathrm{k}} a_{\mathrm{k}}^{\dagger} a_{\mathrm{k}} + \sum_k \hbar\omega_{\mathrm{q}} b_{\mathrm{q}}^{\dagger} b_{\mathrm{q}} + \frac{1}{\sqrt{N}} \sum_{k,q} g_{\mathrm{q}} a_{\mathrm{k+q}}^{\dagger} a_{\mathrm{k}} \left(b_{\mathrm{-q}}^{\dagger} + b_{\mathrm{q}} \right). \tag{2.1}$$

The first term is related to the electronic system, with $a_{\mathrm{k}}^{\dagger}$ (a_{k}) defined as the creation (annihilation) operators for the electronic state with wave vector k and energy E_{k}. The second term corresponds to the lattice vibrations (phonons), with $b_{\mathrm{q}}^{\dagger}$ (b_{q}) defined as the creation (annihilation) operators for the vibrational mode with wave vector q and energy $\hbar\omega_{\mathrm{q}}$. The third term couples electrons and phonons, which enables them to transfer momentum from the phononic system to the electronic system and vice versa, with the electron-phonon coupling constant g_{q} (which is assumed to be independent of k). The coupling of electrons and phonons becomes evident when recapitulating that phonons are caused by vibrating ions within the crystal.

Inducing a static displacement in this model will cost lattice strain energy $\delta E_{\mathrm{lattice}}$ associated with the PLD but gain electronic energy δE_{band} due to the CDW gap opening at the Fermi energy. The energy gain is proportional to the real part of the electronic susceptibility [87]:

$$\chi_0(q) = \frac{1}{L} \sum_k \frac{f_{\mathrm{k+q}} - f_{\mathrm{k}}}{E_{\mathrm{k}} - E_{\mathrm{k+q}}}. \tag{2.2}$$

It includes the Fermi functions $f_{\mathrm{k}} \equiv f\left(E_{\mathrm{k}}\right)$ and $f_{\mathrm{k+q}}$, the length of the atomic chain L and (in general) the electron-phonon matrix elements, which are neglected in the following. It is worth discussing some general features of $\chi_0(q)$, which gets non-zero terms when coupling an occupied state with an empty state separated by a wave vector q ($f_{\mathrm{k+q}} - f_{\mathrm{k}} \neq 0$), with the biggest contributions between states near the Fermi energy ($E_{\mathrm{k}} - E_{\mathrm{k+q}}$ small). The number of terms is drastically enhanced when the states separated by a certain q^* around the Fermi energy have a (nearly) linear dispersion with opposite slopes, since all these states contribute to $\chi_0(q^*)$, see Fig. 2.1 (b). In fact, it even leads to a divergence of $\chi_0(q)$ for $q = 2k_{\mathrm{F}}$ (in 1D at T=0). Under these conditions, all states at the chemical potential are connected by a single wave vector $q = 2k_{\mathrm{F}}$, a situation called perfect nesting. The divergence, however, is strongly suppressed when increasing both temperature and dimensionality of the system, in the latter case mainly due to the incomplete nesting with a single wave vector q. Hence $\chi_0(q)$ is responsible for the trend that only low-dimensional systems tend to form CDWs.

Turning back to the CDW formation criteria, the system will be unstable if $\delta E_{\mathrm{lattice}} + \delta E_{\mathrm{band}} < 0$ or, including the effects of Coulomb (U_{q}) and exchange (V_{q}) interactions [93], if the following general equation is fulfilled:

$$\frac{4g_{\mathrm{q}}^2}{\hbar\omega_{\mathrm{q}}} - 2U_{\mathrm{q}} + V_{\mathrm{q}} \geqslant \frac{1}{\chi_0(q)}. \tag{2.3}$$

As discussed by Rossnagel [88], this equation confirms the intuitive picture that strong electron-phonon (g_{q}) and electron-electron (V_{q}) interaction, together with weak Coulomb interaction (U_{q}), a small lattice strain energy (proportional to ω_{q}) and large electronic susceptibility [$\chi_0(q)$] tend to drive the system towards a CDW. Note that due to the divergence of $\chi_0(q)$ in 1D at $T = 0$, this system will always form a CDW at low temperatures according to this theory.

Following these arguments, it seems natural to distinguish between different types of CDWs, depending on the main contribution that lead to the phase transition. One speaks of CDWs with weak electron-phonon coupling when the phase transition is mainly due to an electronic instability, meaning strong nesting of a large part of the Fermi surface, while CDW with strong electron-phonon coupling tend to be comparable to local chemical bonds, leading to strong perturbations of the band structure. Tab. 2.1 contains a list of the main difference between the two kinds of CDWs.

	Weak coupling CDW	Strong coupling CDW
PLD/CDW amplitude	Small	Large
Energy gap	Small	Large
Coherence length	Large	Small
Electronic energy gain	Arising mostly near k_{F}	Spread over the BZ
Replica bands	Weak	Strong
CDW periodicity	Tends to be incommensurate	Tends to be commensurate
Qualitative picture	Fermi surface instability	Local chemical bonding

Table 2.1: Comparison of CDWs with weak and strong electron-phonon coupling. Adapted from Ref. [88].

Since the weak coupling CDW state is theoretically much better understood than the strong coupling CDW, the experimental classification of a CDW is often done by observing negligible or strong deviation from the theoretical results obtained in the weak electron-phonon coupling limit. In fact, many results derived for BCS superconductors are applicable to CDWs [87]. The main results relevant for STS experiments are given in the following. Their derivations can be found in Ref. [87].

The CDW gap 2Δ is connected to the transition temperature T_{C} through the following relation:

$$2\Delta = 3.52 k_{\mathrm{B}} T_{\mathrm{C}}. \tag{2.4}$$

While this equation holds for weak electron-phonon coupling, materials with strong coupling tend to have a larger CDW gap compared to their transition temperature. The same relation holds for superconductors that are described by the Bardeen-Cooper-Schrieffer (BCS) theory.
Another important result is the DOS close to the gap, which has the following energy dependence:

$$\rho(E) \propto \frac{E}{\sqrt{E^2 - \Delta^2}}. \tag{2.5}$$

Finally, integrating over the occupied states leads, in the weak coupling limit, to a periodic variation in the electronic density:

$$\rho(x) \propto \Delta \cos\left(2k_{\mathrm{F}} + \phi\right). \tag{2.6}$$

The proportionality to the CDW gap can be used to extract the CDW gap from STM images [94].

2.2 Coulomb disorder

Doping is a well established technique used to tune the electronic properties of semiconductors. Depending on the type of impurities which can be electron donors or acceptors, *n*- or *p*-doping is achieved. High purity single crystals such as Si and Ge can be grown with very precise varying concentrations of dopant that form *pn*-junctions. For less pure single crystals such as the TIs Bi_2Se_3, Bi_2Te_3 and $BiSbTeSe_2$, a global compensation of randomly distributed acceptors and donors leads to a decreased level of control on the electronic properties of the semiconductor, as will be shown below.
The physical consequences of Coulomb disorder can be understood by first recapitulating the basic results of a single *pn*-junction. A homogenous concentration of charged impurities will lead to a Coulomb potential that, within the semi-classical model and assuming a slowly varying potential [95], will rigidly shift the electronic states in energy. The energy of these states shifts up when the semiconductor is *p*-doped with electron acceptors, while it shifts down in the case of *n*-doping with donors. Changing the concentration of charged impurities abruptly from *p* to *n* leads to a junction as sketched in Fig. 2.2 (a). We find that the bands are strongly bend within the junction, forming a continuous transition

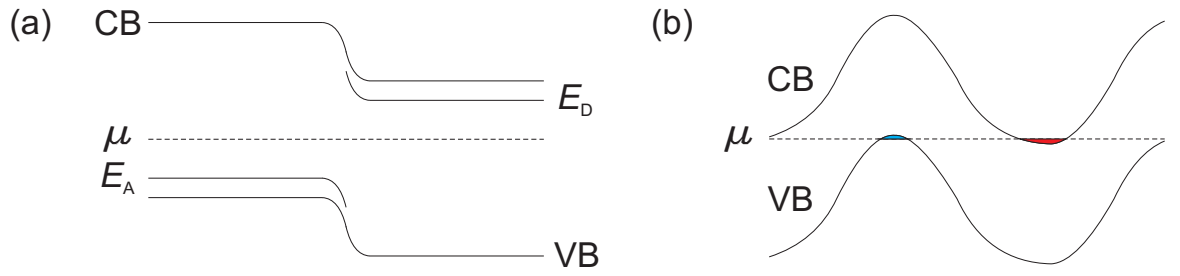


Figure 2.2: Band bending induced by charged impurities: (a) Position-dependent band structure of a *pn*-junction. The Coulomb potentials induced by the acceptor and donors lead to rigid band shift and band bending at the junction. (b) Position-dependent valence and conduction band of a semiconductor with randomly placed donors and acceptors, leading to the formation of electron (red) and hole (blue) puddles.

from *p*-type to *n*-type. The donor (E_D) and acceptor levels (E_A) are also included in the sketch, though the separation between conduction band and donor level (and similarly between valence band and acceptor level) is typically much smaller than the band gap [95] and therefore omitted in the following discussion.

With these results in mind we can now go to the more general case of a crystal with charged impurities randomly placed in a volume of size $\propto R^3$, as developed by Skinner, Chen and Shklovskii [89, 96–98]. The fluctuations of donor and acceptor densities $N_\mathrm{A} = N_\mathrm{B} = N_\mathrm{def}$ locally leads to an uncompensated charge given by the mean square of the fluctuations, $Q \propto e\sqrt{N_\mathrm{def} R^3}$, which in turn leads to a Coulomb potential of the order of $eQ/(4\pi\epsilon_0\epsilon R) \propto e^2\sqrt{N_\mathrm{def} R^3}/(4\pi\epsilon_0\epsilon R) \propto \sqrt{R}$. This potential, as already observed for the *pn*-junction, leads to a rigid shift of the valence and conduction band, which locally can be of the order of the band gap, as sketched in Fig. 2.2 (b). As soon as the band crosses the chemical potential, charge carriers are created locally, which contribute to the optical conductivity [18]. When the conduction band crosses the chemical potential the charge carriers are called electron puddles (red), while hole puddles (blue) are formed when the valence band crosses μ.

Note that the existence of the puddles hinders the fluctuations to grow further, since now charge carriers can effectively screen the charged impurities. Using the same argument, the fluctuations are expected to be suppressed when conducting electrons or holes close the gap of the semiconductor at the surface due to the additional screening channel [99, 100]. This situation is present in the case of graphene on SiO_2 or TIs with their topologically protected surface states.

2.3 Quasiparticle interference

Defects on surfaces such as vacancies, step edges or grain boundaries, perturb the local density of states (LDOS) at the surface; standing waves appear at the vicinity of the defects, which form wave trains with a dispersive wavelength. These quasiparticle interference (QPI) patterns are directly accessible with STS at low temperatures, as first observed by Crommie et al. [101] and Hasegawa et al. [102] at step edges of the Cu(111) and Au(111) surfaces, and soon after inside the famous quantum corral [47].
QPI is nowadays a powerful tool to measure the electronic properties of materials, since the Fourier transform (FT) of the standing waves is often directly related to the constant energy contours (CEC) of the band structure [103]. In addition, the intensity of the scattering wave vectors can deliver important information on the scattering mechanism, for example when spin-flip processes are involved [104, 105].
This sections is devoted to the scattering properties of electronic states on surfaces and introduces the main three theories used to model elastic electron scattering by a static potential. Many theoretical quantities (such as the T-matrix and Green's function) are defined on a general basis. Their physical meaning is discussed and linked to the local density of states, which is measured experimentally with STS.

2.3.1 T-matrix theory

QPI can be described by considering the impact of a potential scatterer on the electronic states of the system. Following Ref. [91], we start with a local potential scatterer V that enters the Hamiltonian H_0 of the (initially unperturbed) system. Focusing on elastic scattering, the Hamilton equation reads:

$$H\left|\psi\right\rangle = \left(H_0 + V\right)\left|\psi\right\rangle = E\left|\psi\right\rangle. \tag{2.7}$$

When turning off the potential scatterer ($V \to 0$), the solution $|\psi\rangle$ needs to converge to the wave function $|\phi\rangle$ that satisfy $H_0\left|\phi\right\rangle = E\left|\phi\right\rangle$, meaning it has to collapse to the wave function of the unperturbed system. A formal solution of Eq. 2.7 is:

$$\left|\psi\right\rangle = \frac{1}{E - H_0} V\left|\psi\right\rangle + \left|\phi\right\rangle. \tag{2.8}$$

This solution, however, has two drawbacks: first, it is an implicit equation, since the solution $|\psi\rangle$ appears on both sides of the equation. Second, the inverse $(E - H_0)^{-1}$ does not exist in general, specifically if E is an eigenvalue of H_0.

To guarantee the existence of $(E - H_0)^{-1}$, one may replace $E \to E^+ = E + i\delta$ with $1 \gg \delta > 0$. This infinitely small imaginary part will always remain due to the reality of the spectrum of H_0, but leaves the energy of the states practically unchanged. Note that this replacement seems crude at first, it however naturally appears when solving the Schrödinger equation in the time-dependent representation, which also reveals that the sign of δ follows from causality, meaning that the scattering potential affects the states *after* the scattering process has taken place when $\delta > 0$ [90]. The new solution is then given by

$$|\psi^+\rangle = \frac{1}{E^+ - H_0} V |\psi^+\rangle + |\phi\rangle = G_0^+(E)\, V |\psi^+\rangle + |\phi\rangle . \tag{2.9}$$

This equation is also known as Lippmann-Schwinger equation. The second equality defines the Green's function operator $G_0^+ = \frac{1}{E^+ - H_0}$.

To get an expression for $|\psi^+\rangle$, one may construct a perturbative solution by assuming that, for weak potential scattering, $|\psi^+\rangle = |\phi\rangle + \mathcal{O}(V)$. With the approximation $|\psi^+\rangle \approx |\phi\rangle$ inserted into the right-hand side of the Lippmann-Schwinger equation, one obtains the first iteration of $|\psi^+\rangle$. This iterative process leads to the solution:

$$|\psi^+\rangle = \sum_{n=0}^{\infty} \left(G_0^+(E)V\right)^n |\phi\rangle = \frac{1}{\mathbb{1} - G_0^+(E)V} |\phi\rangle . \tag{2.10}$$

Next, we define the transition operator $T(E)$ (often referred to as T-matrix), $V|\psi^+\rangle = T(E)|\phi\rangle$. Using Eq. 2.10, we can write the series representation of $T(E)$ as:

$$T(E) = V + VG_0^+(E)V + VG_0^+(E)VG_0^+(E)V + ... = V\frac{1}{\mathbb{1} - G_0^+(E)V}. \tag{2.11}$$

This equation helps to understand the physical meaning of the Green's function, which propagates the wave function in-between scattering events. The superposition of all scattering events leads to the full T-matrix. For very weak scattering potentials, the first term will dominate, and all other terms can then be neglected. This is known as the Born approximation. This approximation is often used instead of the full T-matrix calculation, especially when the scattering problem does not converged to a geometric series.

The experimentally relevant quantity is the density of states, which is given by the following equation [106]:

$$\rho(E) = -\frac{1}{\pi} \operatorname{Im} \operatorname{Tr} \left[G_0^+(E) + G_0^+(E) T(E)\, G_0^+(E)\right]. \tag{2.12}$$

The first term stems from the unperturbed system without scattering potential. The second term describes the influence of the potential, and leads to the standing waves known as QPI.

2.3.2 Joint density of states

A more phenomenological approach to electron scattering is the Joint density of states (JDOS) theory. In contrast to the T-matrix theory, it does not depend on the potential scatterer, but considers only the Hamiltonian H_0. Its eigenvalues E form the band structure of the system, and the resulting CEC are the only ingredients needed to compute the QPI pattern in k-space at the corresponding energy. The JDOS expression at the surface of a crystal has the following form:

$$J(\boldsymbol{k},E) = \int_{1.BZ} \frac{d^2\boldsymbol{q}}{S_{BZ}} \text{Im Tr}\left[G_0^+(\boldsymbol{q},E)\right] \text{ Im Tr}\left[G_0^+(\boldsymbol{q}+\boldsymbol{k},E)\right], \tag{2.13}$$

with S_{BZ} defined as the volume of the 1. BZ. Compared to the T-matrix theory, the JDOS approximation only takes into account the contribution proportional to $\text{Im}(G_0^+)\text{Im}(G_0^+)$, while it neglects completely the form of the scattering potential and is independent of the T-matrix.

Practically, the resulting QPI intensity in k-space can be obtain using the shape of the CEC. One connects a certain (incoming) state with all (outgoing) states available on the CEC. The connecting lines are the scattering wave vectors between these two states. Performing this analysis for all states of the CEC, one ends up with a QPI pattern in which the intensity of a certain scattering wave vector is proportional to its frequency of occurrence [92]. Hence, parallel segments of the CEC will always dominate the QPI pattern in the JDOS approximation.

The QPI pattern of a quadratic and circular CEC obtained with the JDOS approximation are sketched in Fig. 2.3. In the case of the quadratic CEC, one finds that scattering wave vectors connecting parallel segments of the CECs occur much more often than any other wave vector, leading to the strongest nesting for them. Hence, this will be the wave vector with the strongest intensity in the QPI pattern. All these scattering vectors collapse to one wave vector in the QPI pattern, since they all start at the origin in k-space, leading to one of the four strongest features. One of the four nesting wave vectors is sketched in Fig. 2.3 (a). This also intuitively illustrates why the QPI pattern has twice the size of the CEC. Additional features appear in the QPI pattern that are related to scattering vectors that connect near parallel segments of the CEC. However, due to the weaker nesting condition, these features will be less pronounced than the four main features.

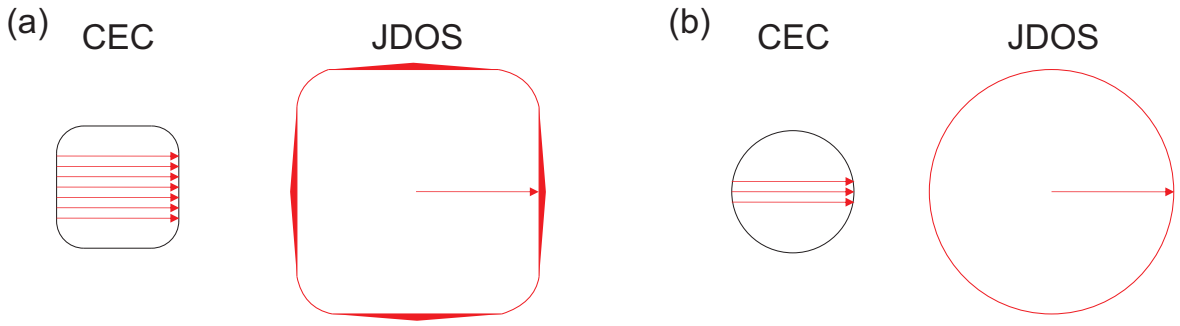


Figure 2.3: QPI pattern obtained with the JDOS approximation in k-space: (a) A quadratic CEC has four strong nesting vectors, resulting in four intense feature in the QPI pattern, that are weakened at the corners. The red arrows represent one of the nesting vectors. (b) A circular CEC favors backscattering, resulting in a circular QPI pattern twice as large as the CEC. The red arrows represent one of the backscattering nesting vectors.

Even weaker features appear in the corners of the QPI pattern that arise from the corners of the CEC.
Fig. 2.3 (b) shows the important example of a circular CEC. In the search for the strongest nesting wave vectors, we find that backscattering wave vectors connect parallel segments of the CEC, leading to the strongest intensity in the QPI pattern. These wave vectors reverse the momentum of the incoming state with respect to the center of the CEC. Every incoming state has a different backscattering wave vector, leading to a closed, circular QPI pattern with twice the radius of the CEC.
Note that many materials have (nearly) circular CECs (MLG, TIs, 2DEG), though they do not all share the same QPI pattern; While the FT of the QPI pattern of a 2DEG is indeed a ring, the pattern of TIs is a disc (with strongly suppressed intensity) that arises from the suppression of backscattering due to spin-momentum locking. This demonstrates the weakness of the JDOS approximation. Though this theory is very intuitive, one should always keep in mind that it remains phenomenological. In conclusion, JDOS may be suitable to understand basic features of experimental QPI patterns, but deeper insights are often hidden in the scattering potential or in the electronic structure of the states involved, which is only accessible when performing a T-matrix calculation.

2.3.3 Fermi Golden Rule

Another theory which is used to understand the relevance of certain QPI wave vectors is the Fermi Golden Rule, which mixes only selected incoming and outgoing states to obtain their specific scattering intensity. This technique can be used together with a JDOS

or T-matrix calculation, for example to get physical insights from the scattering rate of certain wave vectors [107]. Another advantage of this theory is the low computational effort compared to a full T-matrix calculation, since only one wave vector is computed instead of the whole k-space. Hence it can be used to compute the QPI intensity as a function of certain parameters in the Hamiltonian to reveal their role to QPI.

CHAPTER 3

Experimental techniques

This chapter summarizes the basic concepts of the experimental techniques applied in this thesis. The main physical quantities that are important to understand the results are defined. A more detailed overview on STM and STS can found in Refs. [108, 109]. LEED is discussed in Ref. [110].

3.1 Scanning tunneling microscopy

The fundamental principle of scanning tunneling microscopy (STM) and spectroscopy (STS) is to move a metallic tip in the vicinity of a surface and measure the current flowing within the junction [111, 112]. With this technique, it is possible to atomically resolve the sample surface and to probe its local density of states [113]. In this section, the theory of STM and STS is briefly reviewed, following the paper of Feenstra et al. [114].

Using the one-dimensional Wentzel-Kramers-Brillouin approximation, the current I flowing between tip and sample when applying a voltage V is composed of the sample local density of states (LDOS) ρ_{s} and tip LDOS ρ_{t}, together with the transmission probability T for an electron to tunnel through the junction:

$$I \propto \int_0^{eV} \rho_{\mathrm{s}}(E)\,\rho_{\mathrm{t}}(E-eV)\,T(E,eV,d)\mathrm{dE}. \tag{3.1}$$

The exponential transmission probability $T = \exp(-2\kappa d)$ consist of the tip-sample separation d and the inverse decay length $\kappa = \sqrt{\frac{2m\bar{\phi}}{\hbar^2} + k_{||}^2}$ with $\bar{\phi} = \left(\frac{\phi_{\mathrm{t}}+\phi_{\mathrm{s}}}{2} - E + \frac{eV}{2}\right)$ defined as the average barrier height between tip and sample, and ϕ_{s} (ϕ_{t}) being the work function

of the sample (tip). The exponential dependence of the tunneling current is the key factor to obtain atomic resolution, since the signal is dominated by the tip atom nearest to the surface.

To get a signal proportional to the LDOS of the surface, one has to take the derivative of the current, which is experimentally done with a lock-in amplifier. Using Eq. 3.1 with $\rho_\mathrm{t} = \mathrm{const}$, one gets:

$$\mathrm{d}I/\mathrm{d}V \propto e\ \rho_\mathrm{s}\left(eV\right) T\left(eV,eV\right) + e\int_0^{eV} \rho_\mathrm{s}\left(E\right) \frac{\mathrm{d}}{\mathrm{d}\left(\mathrm{eV}\right)} T\left(E,eV\right)\mathrm{dE}. \tag{3.2}$$

It is important to mention that $\mathrm{d}I/\mathrm{d}V$ is not directly proportional to the local density of states of the sample. There is an extra contribution of $T\left(eV,eV\right)$, which has an exponential dependence on the tip-sample separation and the voltage, respectively. One way to suppress this unwanted contribution is to normalize the derivative by I/V, leading to the following relation:

$$\frac{\mathrm{dI/dV}}{I/V} = \frac{\rho_\mathrm{s}\left(eV\right) + \int_0^{eV} \frac{\rho_\mathrm{s}(E)}{T(eV,eV)} \frac{\mathrm{d}}{\mathrm{d(eV)}} \left[T\left(E,eV\right)\right]\mathrm{dE}}{\frac{1}{eV}\int_0^{eV} \rho_\mathrm{s}\left(E\right) \frac{T(E,eV)}{T(eV,eV)}\mathrm{dE}}. \tag{3.3}$$

In this equation, $T\left(E,eV\right)$ and $T\left(eV,eV\right)$ appear as ratio, so that their exponential dependence on d and V tend to cancel. The resulting quantity is then a good measure of the local density of states of the surface.

Experimentally, there are two different ways to do spectroscopy with a scanning tunneling microscope: obtaining a (point-)spectrum or mapping a certain area with the tip. The first consists of driving with the tip to an area of interest and measure $\mathrm{d}I/\mathrm{d}V$ while sweeping the voltage with an open feedback loop. The resulting STS spectrum is a function of V (or energy $E = eV$) and contains the features of the local density of states at the selected area. The second way is to scan an area with a fixed bias voltage, hence obtaining an STS map at a certain energy. The latter is extensively used to probe standing wave patterns that arise when electrons scatter off defects on the surface.

The above derivations are valid in constant height mode only, when the separation between tip and sample is kept constant. STS maps obtained in constant current mode (that obviously varies d) may contain additional dispersing artifacts [115]. Even more severe changes are visible when measuring STS spectra in constant current mode, though this technique can help to measure small signals coming from states with high $k_{||}$ that are highly suppressed in constant height measurements. When using this mode, one has to

link every peak in the spectrum to a band extrema of the surface electronic structure. These extrema are denoted critical point energies (CPEs) [116].
Note that a crude statement has been used to derive this equation, namely that the local density of states of the tip is constant. This requirement is often not fulfilled, leading to possible artifacts in STS spectra. For example, measuring dI/dV on a superconducting surface with a superconducting tip leads to a superconducting gap $2\Delta_s + 2\Delta_t$ instead of $2\Delta_s$, with $2\Delta_s$ ($2\Delta_t$) defined as the gap of the surface (tip) [117]. Though the control of the LDOS of the tip is very limited, its impact on the dI/dV signal can be estimated by measuring a well investigated surface, as for example MLG/Ir(111).

3.2 Low-energy electron diffraction

Low-energy electron diffraction (LEED) is an experimental technique widely used in the surface science community to analyze periodic structures on surfaces in ultra-high vacuum (UHV). Low-energy electrons are accelerated on the surface at which they scatter, producing a diffraction pattern that is collected and amplified on a microchannel plate or a luminescent screen. LEED is very surface sensitive due to the small mean free path (on the order of 1 nm) of the incoming, low-energy electrons in solids.
This technique provides information on the symmetry, lattice spacing and quality of periodic structures present on the surface. It is often used prior to STM investigation to check the global structure and quality of the sample.

CHAPTER 4

Setup and Procedures

W. Jolie developed the growth of BLG/Cs/Ir(111), with assistance of T. Hartl. C. Murray, J. Hall and W. Jolie prepared MoS_2/MLG/Ir(111) using the recipe of Ref. [118], under the supervision of T. Michely. C. Murray and W. Jolie developed the growth of MoS_2/MLG/Eu/Ir(111). The $BiSbTeSe_2$ crystals were synthesized by Z. Wang under the supervision of Y. Ando and the corresponding section can be found in Ref. [119]. The VSe_2 crystals were synthesized by K. Nikonov under the supervision of A Grüneis.

All experimental results of this thesis were conducted in the UHV setup TSTM in Cologne (STM, STS, and LEED). The UHV system is described in detail in Ref. [108, 120, 121], so that it is only briefly introduced in this chapter, as well as the sample preparation.

4.1 The low-temperature, ultra-high vacuum system

The UHV setup TSTM consists of three chambers: a load lock for sample transfers, a main chamber used for sample preparation and first characterization with LEED, and a chamber for STM measurements. The chambers are connected to each other, so that samples can be transferred between them without having to break the vacuum, which is lower than $p < 2 \times 10^{-10}$ mbar in the main chamber and $p < 1 \times 10^{-11}$ mbar in the STM chamber. STM and STS measurements were performed at $T = 5\,\mathrm{K}$ and $T = 77\,\mathrm{K}$ using mainly a W tip (some of the STS measurements on VSe_2 were recorded with a Cr tip). For STS spectra and STS maps, the $\mathrm{d}I/\mathrm{d}V$ signal is recorded using a lock-in amplifier [$U_{\mathrm{mod}} = 4 - 10\,\mathrm{mV}$, $f = 777\,\mathrm{Hz}$] as a function of the energy $E = eV$ with open feedback loop in constant height mode and with closed feedback loop in constant current mode,

respectively. The temperature and modulation voltage lead to an energy resolution of $\Delta E = \sqrt{(3.3k_{\mathrm{B}}T)^2 + (2.5eV_{\mathrm{mod}})^2} \approx (10-25)$ meV [122]. STS maps are mainly measured in constant current mode. Only the STS maps in Chap. 8 are measured in constant height mode. When applicable, STS spectra are recorded in constant height and normalized by I/V [114]. STM images are post-processed using the SPIP and WSxM software [123].

4.2 Sample preparation

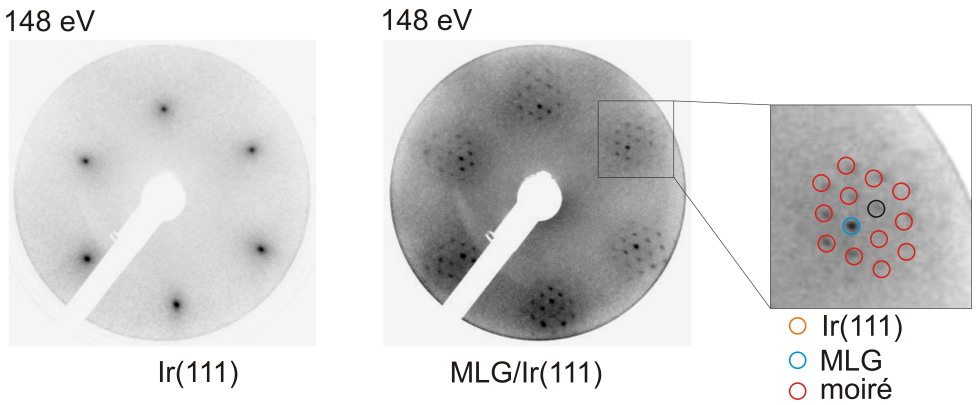


Figure 4.1: LEED images of Ir(111) and MLG/Ir(111). The energies represent the kinetic energy of the incoming electrons. The different contributions to the diffraction pattern are sketched in the enlarged view, where we find graphene (black) and Ir(111) (blue), surrounded by moiré spots (red). The small deviation from a perfect hexagon is due to the microchannel plate of the experimental setup.

Ir(111)

The Ir(111) single crystal is cleaned by cycles of Ar^+ ion bombardment followed by short annealing at $T = 1525 - 1575$ K until the corresponding LEED pattern shows six sharp spots, without any additional feature. A LEED image of Ir(111) is shown in Fig. 4.1, which shows six spots that reflect the hexagonal symmetry of the Ir(111) surface.

MLG/Ir(111)

MLG/Ir(111) is obtained by applying a temperature programmed growth (TPG) step from room temperature up to $T = 1375$ K first, followed by chemical vapor deposition (CVD) at the same elevated temperature [124]. This technique leads to a full MLG on Ir(111) [MLG/Ir(111)] of high perfection [125]. Additional wrinkles are visible on the surface due to the high temperature during CVD. The LEED of MLG/Ir(111) is shown

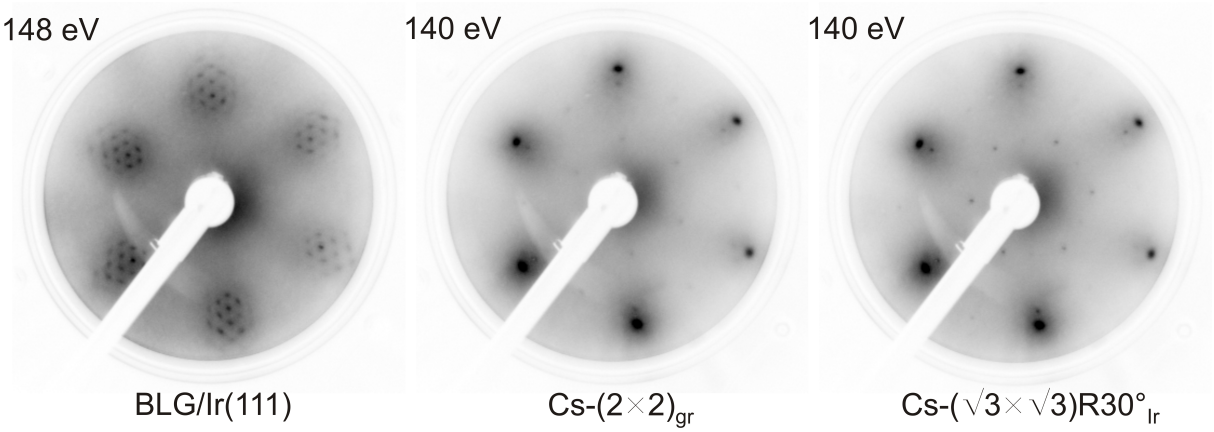


Figure 4.2: LEED images showing (from left to right) BLG/Ir(111), mainly $(2 \times 2)_{\mathrm{gr}}$ Cs under BLG/Ir(111), mainly $\left(\sqrt{3} \times \sqrt{3}\right) R30^{\circ}_{\mathrm{Ir}}$ Cs under BLG/Ir(111).

in Fig. 4.1. It consist of six pairs of spots with hexagonal symmetry. The six inner spots are attributed to the Ir(111) surface, the six outer spots to epitaxial graphene. Hence, both lattices have the same orientation, but different lattice constants. The spots of graphene and Ir(111) are surrounded by satellite spots, which are related to the moiré of MLG/Ir(111). Some of the spots are marked in Fig. 4.1. The moiré of MLG/Ir(111) also appears in STM images as a periodic pattern with a large wavelength of 2.5 nm [126].

BLG/Ir(111)

The sample synthesis of BLG on Ir(111) [BLG/Ir(111)] starts with MLG/Ir(111). An additional physical vapor deposition (PVD) step is performed, evaporating carbon from a graphite rod on MLG/Ir(111). The sample temperature is held at $T = 1225$ K during evaporation. The second graphene layer intercalates between MLG and Ir(111) [60], forming islands which mainly have the same orientation as MLG [127]. Hence, both MLG/Ir(111) and BLG/Ir(111) are present on the surface. The LEED pattern of BLG/Ir(111) is shown in Fig. 4.2. One can recognize the six outer (inner) spots of graphene (Ir) and additional satellite spots due to the moiré between both. The pattern is identical to MLG/Ir(111).

BLG/Cs/Ir(111)

BLG/Ir(111) is doped chemically by evaporating Cs atoms on the sample surface at room temperature. In the case of MLG/Ir(111), Cs forms first a $(2 \times 2)_{\mathrm{gr}}$ superstructure corresponding to 0.25 ML with respect to the graphene lattice, then a $\left(\sqrt{3} \times \sqrt{3}\right) R30^{\circ}_{\mathrm{Ir}}$ corresponding to 0.33 ML with respect to Ir(111) [54]. Both structures are observed in

LEED, see Fig. 4.2; depending on the exposure time, we find first a (2×2), then the $\left(\sqrt{3} \times \sqrt{3}\right) R30°$ structure. STM images confirm that both MLG/Ir(111) and BLG/Ir(111) are homogeneously intercalated by a compact layer of Cs.

MoS_2/MLG/Ir(111)

The growth of MoS_2 is done following the growth process of Hall et al. [118], starting with MLG/Ir(111). It consists of two steps. During the first step, the sample is kept at room temperature. Mo is evaporated from a rod with a rate of 0.125ML/min on the MLG/Ir(111) surface in a S pressure of $p_S \approx 5 \times 10^{-9}$ mbar. The latter is obtained from a pyrite (FeS_2) source that is heated to 615 K during evaporation.
During the second step, the sample is annealed for 5 minutes at $T = 1050$ K in a S pressure of $p_S \approx 5 \times 10^{-9}$ mbar. This leads to large, flat ML MoS_2 islands, which are covered with small BL on top. The LEED of MoS_2/MLG/Ir(111) is shown in Fig. 4.3. The favored epitaxial relation between $MoS_2$and MLG is evident, since the slightly elongated spots of MoS_2 have the highest intensity along the direction of the MLG spots.

MoS_2/MLG/Eu/Ir(111)

Eu is intercalated between MLG and Ir(111) before MoS_2 growth. The sample is kept at $T = 700$ K while Eu is evaporated from a Knudsen cell kept at $T = 675$ K. Eu forms first a (2×2), then a $\left(\sqrt{3} \times \sqrt{3}\right) R30°$ superstructure with respect to graphene [128]. The MoS_2 is then grown using the recipe of MoS_2/MLG/Ir(111). The superstructure of Eu is still visible in LEED after MoS_2 growth, see Fig. 4.3.

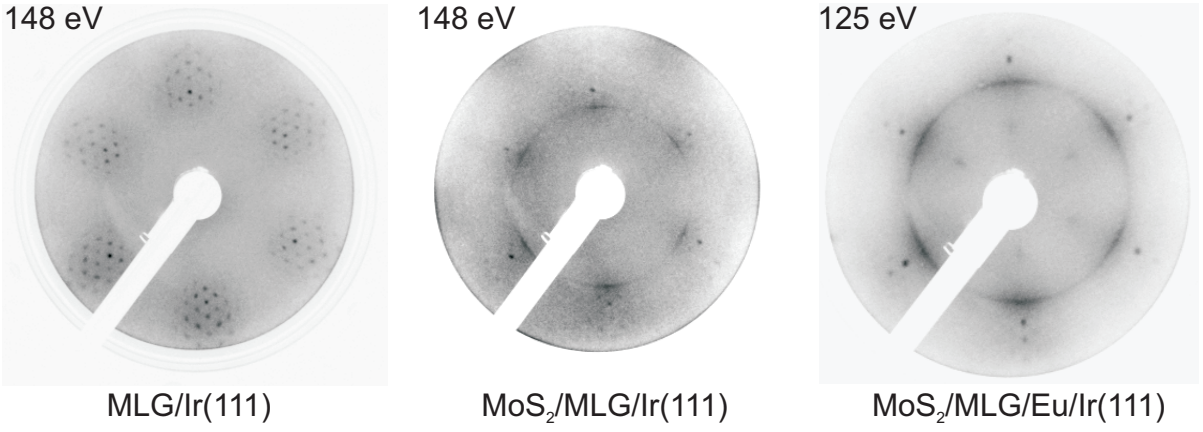


Figure 4.3: LEED images showing (from left to right) MLG/Ir(111), MoS_2/MLG/Ir(111), and MoS_2/MLG/(2×2)Eu/Ir(111).

$BiSbTeSe_2$

The single crystals of $BiSbTeSe_2$ were grown by Z. Wang from high-purity elements [Bi, Sb, and Te of 6N (99.9999%) and Se of 5N (99.999%) purities] by using a modified Bridgman method in a sealed quartz-glass tube as described in Ref. [83]. To facilitate the *in-situ* cleaving under UHV, the crystals were precut into platelets with a typical dimension of $3 \times 3\,\mathrm{mm}^2$ with the (111) plane as the wide face.
For STM measurements two different $BiSbTeSe_2$ crystals were mounted with their backside to the STM sample holder by using silver-filled epoxy glue. On their topside a metal pin was attached normal to the crystal surface using the same glue. Cleaving was performed in the STM ultrahigh vacuum preparation chamber by moving the pin against a sharp edge, causing the crystal to cleave. The cleaved sample surface was moved into the STM bath cryostat within a few minutes.

VSe_2

Elemental Se and V were inserted in a sealed quarz ampoule as starting materials, together with a transport agent. The ampoule is placed in a thermal gradient (approx $T \approx 850 - 750°\mathrm{C}$). After 3-4 days, when crystals with a decent size are formed, the ampoule is cooled to room temperature. Three batches were investigated in this thesis. The first batch had iodine as a transport agent, the second batch VCl_3. For the third batch, iodine was used and instead of elemental V and Se the crystal of the first batch was recycled.
Before STM measurements, the crystals were washed with ethanol to get rid of iodine and annealed to $T = 130°\mathrm{C}$ in vacuum to remove the Se excess. The VSe_2 crystals were then inserted and cleaved in the vacuum chamber as described above for $BiSbTeSe_2$.

PART III

Experimental results

CHAPTER 5

Visualizing layer polarization in bilayer graphene with quasiparticle interference

This chapter contains contributions from W. Jolie, J. Lux, M. Pörtner, D. Dombrowski, C. Herbig, T. Knispel, S. Simon, T. Michely, A. Rosch and C. Busse. W. Jolie proposed the experiments. W. Jolie developed the recipe to grow Cs intercalated BLG on Ir(111), BLG/Cs/Ir(111), using the recipe of Ref. [127] for the growth of BLG/Ir(111) and with the assistance of T. Hartl. M. Pörtner and W. Jolie collected the STM and STS data. W. Jolie analyzed the data. J. Lux and A. Rosch provided the band structure, JDOS and T-matrix calculations. A. Rosch developed the analytical model for an n-band material, see Appendix B. The experimental and theoretical results were mainly discussed with W. Jolie, J. Lux, C. Busse and A. Rosch. All results can be found in Ref. [129]. Similar data measured on MLG/Cs/Ir(111) is published in Ref. [130].

5.1 Motivation

Bilayer graphene (BLG), a material composed of two identical Bernal-stacked monolayer graphene (MLG) sheets, represents one of the simplest vdW materials [131, 132]. While both layers are equivalent for free-standing BLG, this equivalence is broken in the presence of an out-of-plane magnetic or electric field, leading to emergent complex states [133–136]. The band structure of BLG also strongly depends on external fields. For example, a perpendicular electric field is able to open a band gap between the first conduction and valence band [15, 16], making BLG superior to MLG for devices such as field effect tran-

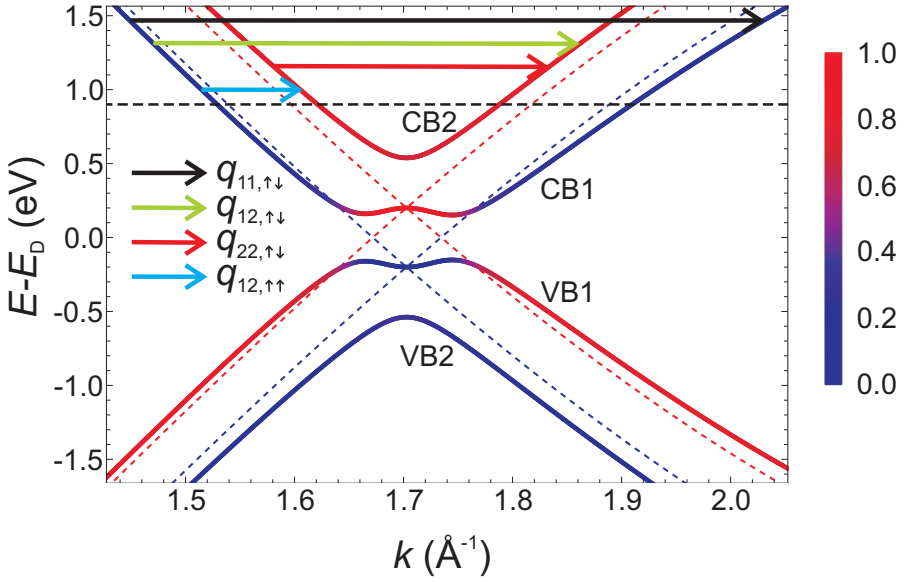


Figure 5.1: Dispersion of chemically gated BLG along ΓKM using a tight-binding approach with the hopping parameters and the interlayer potential $U = 0.4$ eV as explained in the text. The two conduction bands (CB1, CB2) and valence bands (VB1, VB2) are symmetric with respect to the Dirac energy E_D. The color code of the bands indicates the localization of the eigenstates. Red (blue) states have weight of 1 (0) in the upper layer. At the chemical potential (thick dashed line at 0.9 eV), the weights are approximately 0.8 and 0.2, respectively. The dashed Dirac cones show the dispersion of the two monolayers when they would not be coupled by interlayer hopping. The lower layer is more strongly n-doped than the upper layer. The four colored arrows represent the principal scattering vectors responsible for QPI (depicted here at different energies for clarity).

sistors. The electric field can arise from electrical gating or from a chemical environment, leading to a charge redistribution at the interface.

As a consequence of layer asymmetry, localization of eigenstates occurs in one of the two layers. This layer polarization [137, 138] can be understood using a gedankenexperiment: Turning off all out-of-plane hopping terms in free-standing BLG, one ends up with two degenerate Dirac cones. Bringing an electropositive material in close proximity from below significantly dopes the lower layer, while the chemical potential of the upper layer is only slightly shifted. Finally, turning on the interlayer hopping opens up a band gap and leads to the band structure of asymmetric BLG, see Fig. 5.1. The bands of BLG partially inherit the layer polarization of the shifted Dirac cones, which are included with dashed lines in Fig. 5.1. Near the chemical potential we find that the second conduction band (CB2) is highly localized in the upper layer, while the first conduction band (CB1) is localized in the lower layer. Layer polarization has important consequences for surface

sensitive techniques such as STM and STS or angle-resolved photoelectron spectroscopy (ARPES). For example, it explains why one of the two van Hove singularities (VHSs) of BLG is strongly suppressed in ARPES [139].

QPI in BLG is caused by elastic scattering of electronic states, either within one pocket around the K point (intravalley scattering) or between two pockets separated by a wave vector $q = \mathrm{K}$ (intervalley scattering) [140]. When two bands are present at the selected energy there are four principal scattering vectors connecting parallel segments of the constant energy contours (CEC), producing four intravalley and four intervalley scattering features, respectively. The intravalley wave vectors $q_{11,\uparrow\downarrow}$ and $q_{22,\uparrow\downarrow}$ denote intraband processes within CB1 and CB2, while $q_{12,\uparrow\uparrow}$ and $q_{12,\uparrow\downarrow}$ represent interband processes that we distinguish by the parallel ($\uparrow\uparrow$)/antiparallel ($\uparrow\downarrow$) orientation of the quasiparticle velocities $v \propto \mathrm{d}E/\mathrm{d}k$ of the two states involved. They are sketched in Fig. 5.1. Several STM studies have analyzed the band structure of BLG using QPI, however most of them were limited to the low-energy bands CB1 and VB1, where only $q_{11,\uparrow\downarrow}$ is present. Mallet et al. [141] investigated the role of pseudospin in MLG and BLG. Yankowitz et al. [142] studied the opening of the band gap upon gating by mapping QPI at different gate voltages. Simon et al. [143] observed the scattering vector $q_{22,\uparrow\downarrow}$ at energies higher than the bottom of CB2 after it had been reported in T-matrix calculations [144], while no interband scattering was found.

This chapter is devoted to QPI on Cs intercalated BLG on Ir(111). The focus lies on the energies where both CB1 and CB2 are present, where interband scattering comes into play. Our experimental results are compared to JDOS and T-matrix calculations based on a TB model.

5.2 Quasiparticle interference of bilayer graphene

This section is devoted to the QPI pattern observed on Cs intercalated MLG and BLG on Ir(111). The preparation of the sample can be found in Sec. 4.2. Our surface consists of BLG islands surrounded by MLG. Both MLG and BLG are intercalated with Cs. When the amount of Cs is gradually increased, it forms first a $(2 \times 2)_{\mathrm{gr}}$ superstructure corresponding to 0.25 ML with respect to the graphene lattice, then a $\left(\sqrt{3} \times \sqrt{3}\right)\mathrm{R30}^{\circ}_{\mathrm{Ir}}$ corresponding to 0.33 ML with respect to Ir(111). We first focus on the $(2 \times 2)_{\mathrm{gr}}$ superstructure and show below that our results are reproduced on the $\left(\sqrt{3} \times \sqrt{3}\right)\mathrm{R30}^{\circ}_{\mathrm{Ir}}$ superstructure.

For MLG, the Cs structure underneath is well visible, see Fig. 5.2 (a). Mapping QPI [Fig. 5.2 (b)] shows one long and one short wavelength oscillation. In the corresponding

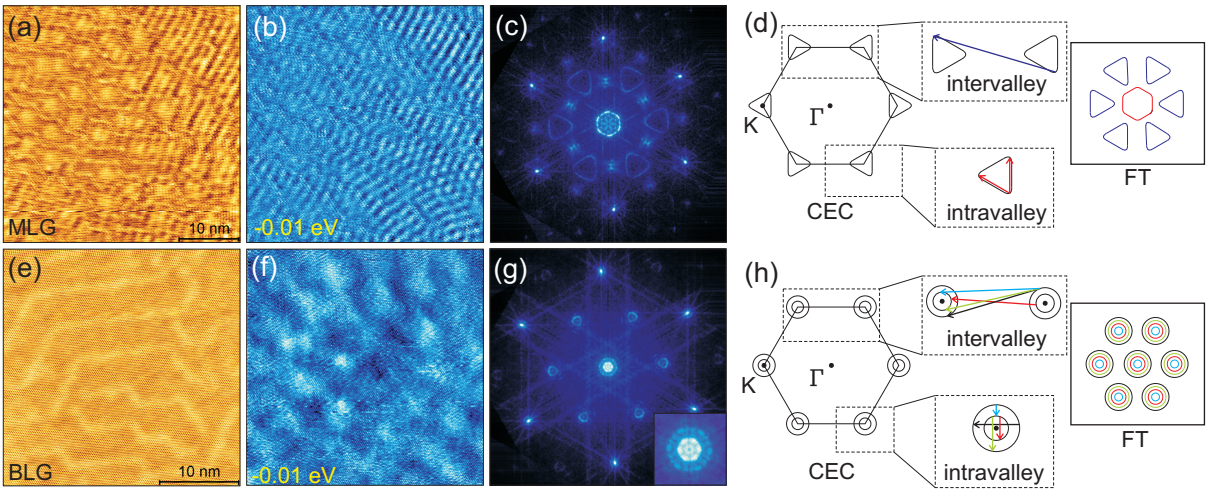


Figure 5.2: QPI in strongly doped MLG and BLG: (a) STM image of Cs intercalated MLG/Ir(111) (I = 0.1 nA, U = 0.01 V, image size 40 × 40 nm^2). (b) Corresponding STS map recorded at $E = -0.01$ eV. (c) FT image revealing electronic features at Γ (hexagonal) and K (triangular), together with structural features at Γ' from graphene and between Γ and Γ' resulting from the (2 × 2) structure of Cs. (d) Sketch of the scattering processes causing the standing wave pattern in MLG. The expected FT has one feature at Γ and K, respectively. (e) STM image of Cs intercalated BLG/Ir(111) (I = 0.1 nA, $U = -0.09$ V, image size 30 × 30 nm^2). The anti-phase boundaries of the underlying Cs superstructure are visible. (f) STS map of BLG recorded at $E = -0.01$ eV. (g) FT image, revealing features at Γ (two rings) and K (two rings). The inset shows a zoom of the feature around Γ. (h) Sketch of the principal scattering processes. The resulting FT has 4 features at Γ and K, respectively.

FT [Fig. 5.2 (c)], the six outer, bright spots belong to the reciprocal lattice of graphene located at Γ′. The features at K arise from the short waves (intervalley scattering), while the feature at Γ arises from the long waves (intravalley scattering). Note that intravalley scattering is enhanced far away from the Dirac point due to trigonal warping of the CEC [130]. Weak scattering features are found at the higher order K and Γ points. The sketch in Fig. 5.2 (d) illustrates the two most pronounced vectors for a CEC near to the Fermi energy using the JDOS formalism. Intravalley scattering is most effective between the corners of the pockets (apex scattering), leading to enhanced intensity at the corners of the hexagonal feature [130]. The resulting FT is in good agreement with the experimental observation.

For the case of BLG [Fig. 5.2 (e)], no periodicity is found besides the honeycomb lattice, though Cs is present as indicated by the observation of anti-phase boundaries. These boundaries appear when the Cs density is slightly smaller than 0.25 ML, resulting in

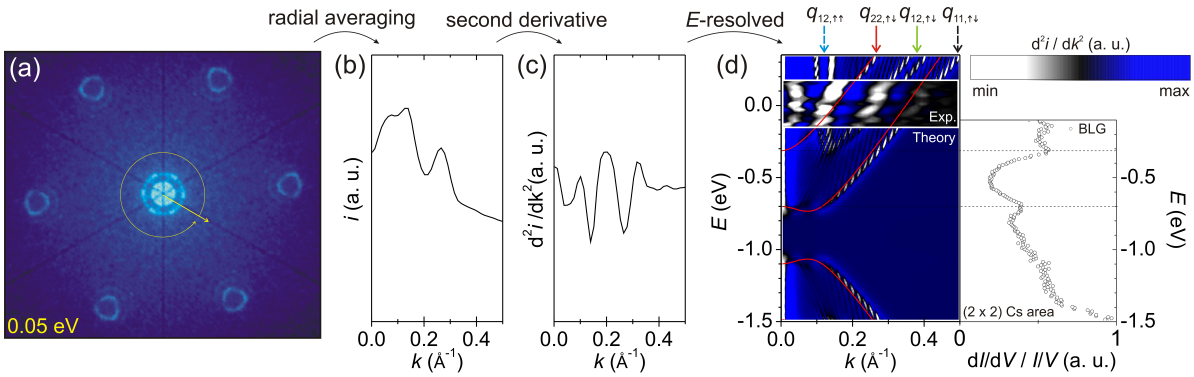


Figure 5.3: QPI analysis: (a) FT of an STS image. (b) Averaged isotropic line scan around the Γ point of the FT. (c) Second derivative of the line scan, $\mathrm{d}^2i/\mathrm{d}k^2$. (d) Energy resolved $\mathrm{d}^2i/\mathrm{d}k^2$ on a (2×2) Cs under BLG/Ir(111) area, superimposed with the band structure of BLG in the KΓ direction (red) in the form $E(2k)$ and the second derivative of the JDOS intensity in the background. The four arrows mark the positions of the expected scattering wave vectors. The apparent splitting of $q_{12,\uparrow\uparrow}$ and $q_{12,\uparrow\downarrow}$ is due to warping effects. Features of the band structure that are visible in STS spectra (right panel) are highlighted with dashed lines.

domains which are separated by one atomic row. Though it is possible to distinguish BLG from MLG in STM images, it is easier to compare their QPI patterns, see Fig. 5.2 (b) and (f). The FT in Fig. 5.2 (g) again display the reciprocal lattice of graphene. Further it reveals two pronounced rings located at the Γ point and two (weaker) rings at the K point. In some of the QPI pattern we also find a faint outer ring that is barely visible in Fig. 5.2 (g). The rings are directly related to the CEC of BLG as sketched in Fig. 5.2 (h), where we neglected trigonal warping for the sake of clarity. However, taking into account all nesting vectors connecting parallel segments of the CEC (in accordance with the JDOS formalism) lets one expect four rings around Γ and K, respectively. In the following, we will identify the missing scattering vectors.

To analyze QPI in BLG in greater detail, we radially average the FT in Fig. 5.3 (a) around Γ, see Fig. 5.3 (b). Three peaks are visible, which appear as dips with similar sizes when computing the second derivative of the line scan, see Fig. 5.3 (c). By applying this analysis to QPI maps measured at energies ranging from $E = -0.13$ eV to $E = 0.17$ eV, one can observe one non-dispersive feature near $k = 0$, two bright dispersive branches and one weak dispersive feature at higher k values, see Fig. 5.3 (d).

We compare our experimental finding to theory using the JDOS approach based on a tight-binding model of gated BLG. The simulations were performed by J. Lux using the Hamiltonian of Eq. 1.3. We take into account the nearest-neighbor in-plane hopping (γ_0) and two out-of plane hopping terms for two atoms sitting directly on top of each other

(γ_1) and two atoms belonging to different sublattices (γ_3) sitting out-of-phase. The layer-asymmetric potential U is caused by the perpendicular electric field which arises from the intercalated Cs. The latter hence dopes BLG, opens the band gap, and increases the value of γ_1 [16]. We first set the parameters that are independent of U, namely $\gamma_0 = 3$ eV and $\gamma_3 = 0.1$ eV [14]. The relation between U and chemical potential is taken from Ref. [145]. We rigidly shift the chemical potential to $E - E_\mathrm{D} = 0.9$ eV and align the bottom of CB1 with the peak seen in STS spectra at $E = -0.7$ eV in Fig. 5.3 (d) which we attribute to the VHSs of CB1 [139]. This leads to $U = 0.4$ eV in accordance with Ref. [145]. We set $\gamma_1 = 0.55$ eV to align CB2 to $E \approx -0.3$ eV where we find a shoulder in our spectra. The energy of the VHS peak and shoulder are marked with dashed lines in Fig. 5.3 (d). The resulting band structure in the KΓ direction is shown in Fig. 5.3 (d) in the form $E(2k)$ to allow a direct comparison with QPI.
The JDOS expression is obtained with the following equation:

$$J(\boldsymbol{k},E) = \int_{1.BZ} \frac{d^2\boldsymbol{q}}{S_{BZ}} \mathrm{Im\ Tr}\left[G^0(\boldsymbol{q},E)\right] \mathrm{Im\ Tr}\left[G^0(\boldsymbol{q}+\boldsymbol{k},E)\right], \tag{5.1}$$

with the volume of the 1. BZ, $S_{BZ} = \frac{8\pi^2}{\sqrt{3}a^2}$, and the free Green's function $G^0(\boldsymbol{k},E)$ in the sublattice basis:

$$G^0(\boldsymbol{k},E) = \left(E - H(\boldsymbol{k})\right)^{-1}. \tag{5.2}$$

Note that the JDOS approximation is independent of the scattering potential, and thus of the corresponding T-matrix that will appear below. The QPI pattern in k-space of the JDOS expression is shown in the background of Fig. 5.3 (d) (left panel). We find indeed four features arising from the principal scattering vectors. Note that the two interband scattering vectors are additionally split due to the different slopes in KΓ and KM direction, producing two features in QPI, respectively. This splitting is averaged out in our experiment due to our resolution and analysis procedure and therefore omitted in the following discussion. Comparing experiment and theory, we conclude that one of the features observed in QPI is $q_{22,\uparrow\downarrow}$ (red arrow), since it lies on top of the corresponding JDOS feature. We exclude that the short interband scattering wave vector $q_{12,\uparrow\uparrow}$ contributes to this feature as it shows no dispersion in JDOS, in contrast to our experimental observation. Though the dispersion of $q_{12,\uparrow\uparrow}$ is comparable to the feature at small wave vectors, it is not located at the same position in k-space. Since this experimental feature is close to our resolution limit we conclude that it is an experimental artifact, not a scattering vector of BLG. The second experimental feature is caused by $q_{12,\uparrow\downarrow}$ (green arrow), which is expected between $q_{11,\uparrow\downarrow}$ and $q_{22,\uparrow\downarrow}$. The weak feature that is barely visible in the experiment nicely

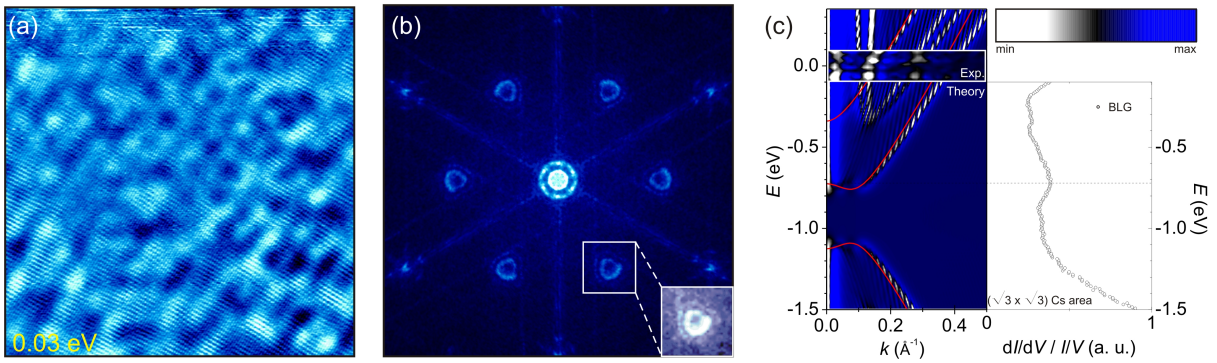


Figure 5.4: QPI in $\left(\sqrt{3}\times\sqrt{3}\right)$R30° Cs intercalated BLG: (a) STS map of BLG recorded at $E = 0.03$ eV (image size 30×30 nm^2). (b) FT of the STS image, revealing 2 pronounced features at Γ and K. The inset reveals an additional, very weak feature at K when increasing the contrast. (c) Energy resolved experimental and theoretical $\mathrm{d}^2i/\mathrm{d}k^2$ intensity for BLG on $\left(\sqrt{3}\times\sqrt{3}\right)$R30° Cs, superimposed with the band structure of BLG in the KΓ direction. A corresponding STS spectrum measured on BLG on $\left(\sqrt{3}\times\sqrt{3}\right)$R30° Cs is shown on the right. The singularity at the bottom of the lowest conduction band shows up as a peak in the STS spectrum. They are linked with a dashed line.

fits to $q_{11,\uparrow\downarrow}$ (black arrow). In summary, $q_{11,\uparrow\downarrow}$ and $q_{12,\uparrow\uparrow}$ are strongly suppressed in our measurements.

At Cs coverages higher than (2×2) we find a $\left(\sqrt{3}\times\sqrt{3}\right)$ R30° Cs superstructure, together with the reappearance of the MLG/Ir(111) moiré in STM images. We speculate that the difference in visibility is related to the periodicity which is with respect to Ir(111). The STS map in Fig. 5.4 (a) shows the LDOS in real space for BLG intercalated by a $\left(\sqrt{3}\times\sqrt{3}\right)$R30° Cs layer. We find a standing wave pattern arising from QPI. The corresponding FT in Fig. 5.4 (b) has six outer spots located at Γ'. They belong to the reciprocal lattice of BLG. In addition, one can observe two pronounced rings at the Γ point and two features at K, which stem from QPI. An additional, very weak feature is barely visible at the K point when increasing the contrast, see inset in Fig. 5.4 (b).

We again measure STS maps in a small energy range to analyze the dispersive behavior of the QPI features. As explained in detail for BLG on the (2×2) Cs area, we radially average the QPI intensity in our FT maps and take their second derivative. The result is shown in Fig. 5.4 (c), in which white (blue) corresponds to a high (low) intensity in the FT image. We find two dispersing features together with the experimental artifact at small k-values. One can now compare this dispersion to the band structure of BLG and its expected QPI dispersion using the JDOS approach. The chemical potential is slightly

increased such that $E - E_{\mathrm{D}} = 0.925$ eV to account for the increased doping due to the denser Cs layer underneath. All the other parameters are the same as for BLG on the (2×2) Cs structure. The shift is justified by comparing the van Hove singularity of BLG with the location of the peak found in the STS spectra, see Fig. 5.4 (c). The resulting band structure is shown in Fig. 5.4 (c), again in the form $E = (2k)$ for a direct comparison with QPI. The second derivative of the JDOS intensity is plotted in the background, in analogy to the experimental analysis. Comparing experiment and theory, one can attribute the feature with smaller diameter in k space to $q_{22,\uparrow\downarrow}$ since their dispersions match. The larger feature is attributed to $q_{12,\uparrow\downarrow}$ since it produces a dispersive feature which lies between CB1 and CB2. No pronounced feature is found at the location of $q_{11,\uparrow\downarrow}$ and $q_{12,\uparrow\uparrow}$, as found for BLG/(2×2)Cs/Ir(111).

5.3 T-matrix simulations

The simulations presented in the following were performed by A. Rosch and J. Lux.
The strong contributions of $q_{11,\uparrow\downarrow}$ and $q_{12,\uparrow\uparrow}$ found in the JDOS calculation are not in line with the experiment, i.e. the JDOS formalism can not explain our observation on a quantitative level. In order to understand the different weights of the scattering processes in QPI, we first restrict ourselves to the principal scattering wave vectors $q_{11,\uparrow\downarrow}$, $q_{22,\uparrow\downarrow}$, $q_{12,\uparrow\uparrow}$ and $q_{12,\uparrow\downarrow}$. This enables us to use a Fermi's Golden Rule expression:

$$|\rho(\boldsymbol{k},E)| \sim \left| \sum_{j=1}^{4} \mathrm{e}^{-i\boldsymbol{r}_j \cdot \boldsymbol{k}} \left(\sum_{s,s'=1}^{4} \sum_{\overline{\boldsymbol{q}}} \langle j|s,\overline{\boldsymbol{q}}\rangle \langle s,\overline{\boldsymbol{q}}|T(E)|s',\overline{\boldsymbol{q}}+\boldsymbol{k}\rangle \langle s',\overline{\boldsymbol{q}}+\boldsymbol{k}|j\rangle - \mathrm{h.c.} \right) \right|, \quad (5.3)$$

where the $\overline{\boldsymbol{q}}$ are chosen such that $H(\overline{\boldsymbol{q}})\,|s,\overline{\boldsymbol{q}}\rangle = E\,|s,\overline{\boldsymbol{q}}\rangle$ and $H(\overline{\boldsymbol{q}}+\boldsymbol{k})\,|s',\overline{\boldsymbol{q}}+\boldsymbol{k}\rangle = E\,|s',\overline{\boldsymbol{q}}+\boldsymbol{k}\rangle$, so they are eigenstates of the free Hamiltonian at the probing energy. The T-matrix is given by:

$$T(E) = \left(1 - V \int_{1.BZ} \frac{d^2\boldsymbol{k}}{S_{BZ}} G^0(\boldsymbol{k},E)\right)^{-1} V. \quad (5.4)$$

Note that the T-matrix is momentum-independent for a local potential. Since the quantitative behavior of the approximation in Eq. (5.3) depends on the details of the potential, the result is averaged over 100 different potentials with independent on-site energies on all four sites between -1 and 1 eV. We restrict ourselves to $k_{\mathrm{y}} = 0$ and consider only the backscattering processes sketched in Fig. 5.1 and Fig. 5.2 (h). There are 6 pairs of eigenstates, each connected by a vector $\boldsymbol{q} = (q_{\mathrm{x}},0)$. The two pairs contributing to inter-

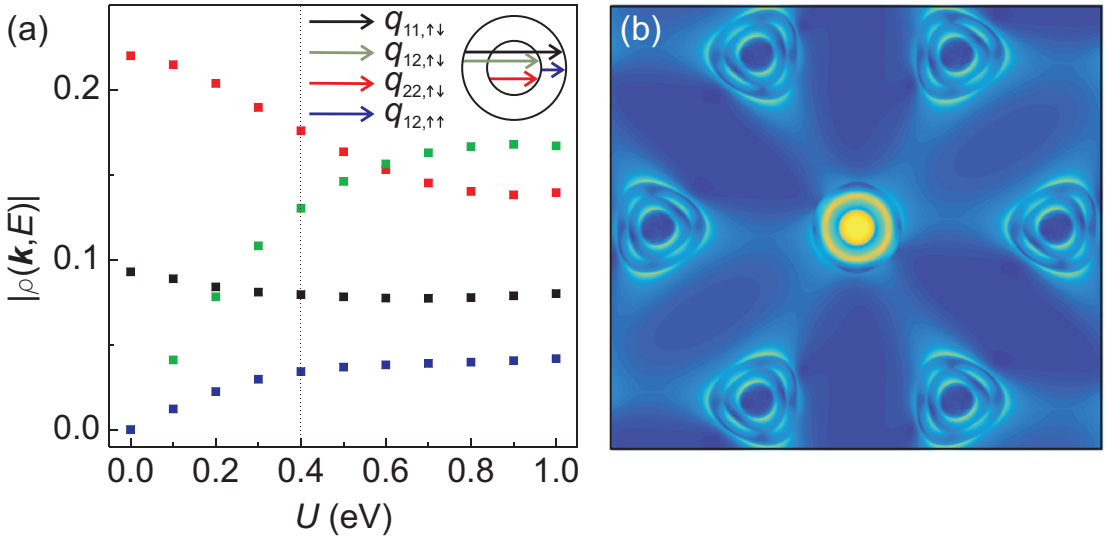


Figure 5.5: T-matrix simulations of BLG near the chemical potential: (a) The Fermi Golden Rule like expression $|\rho(\boldsymbol{k},E)|$ for $k_\mathrm{y} = 0$ around the Γ point. At $U = 0$ interband scattering is suppressed. With increasing U the interband scattering increases and for $U > 0.2$ eV the interband scattering rate exceeds the large intraband rate. (b) Calculated QPI pattern for an on-site potential of 1 eV on sublattice $A1$ and $E - E_\mathrm{D} = (0.9 + i\,0.04)$ eV. Three rings are present, which are best visible at the K point since the inner ring at the Γ point is hidden by the large contribution from $k = 0$ which is normalized to 1.

band scattering are almost, up to warping effects, at the same q_x so their contributions are added up.

The main advantage of this Fermi's Golden Rule expression is that it is not as time consuming as a full T-matrix simulation, which covers the entire k-space (instead of only the principal scattering vectors). Hence, not only the impact of a certain potential scatterer can be averaged out, but one is also able to investigate the dependence of the QPI intensities as a function of model parameters. One parameter that drastically changes the weight of certain principal scattering vectors is the potential U. As shown in Fig. 5.5 (a), in the symmetric case ($U = 0$), interband scattering is totally suppressed for $k_\mathrm{y} = 0$ due to the $A1 \leftrightarrow B2$, $B1 \leftrightarrow A2$, $k_\mathrm{y} \leftrightarrow -k_\mathrm{y}$ symmetry [146]. At finite U this symmetry is broken, and interband scattering is generically present at $k_\mathrm{y} = 0$. For $U = 0.4$ eV (as found in the experiment) we find the strongest contributions from $q_{22,\uparrow\downarrow}$ and $q_{12,\uparrow\downarrow}$, in agreement with our measurements. The smallest contribution arises from $q_{12,\uparrow\uparrow}$, again in line with the experiment. In conclusion, when $U \neq 0$ no symmetry seems to suppress one of the principal scattering wave vectors.

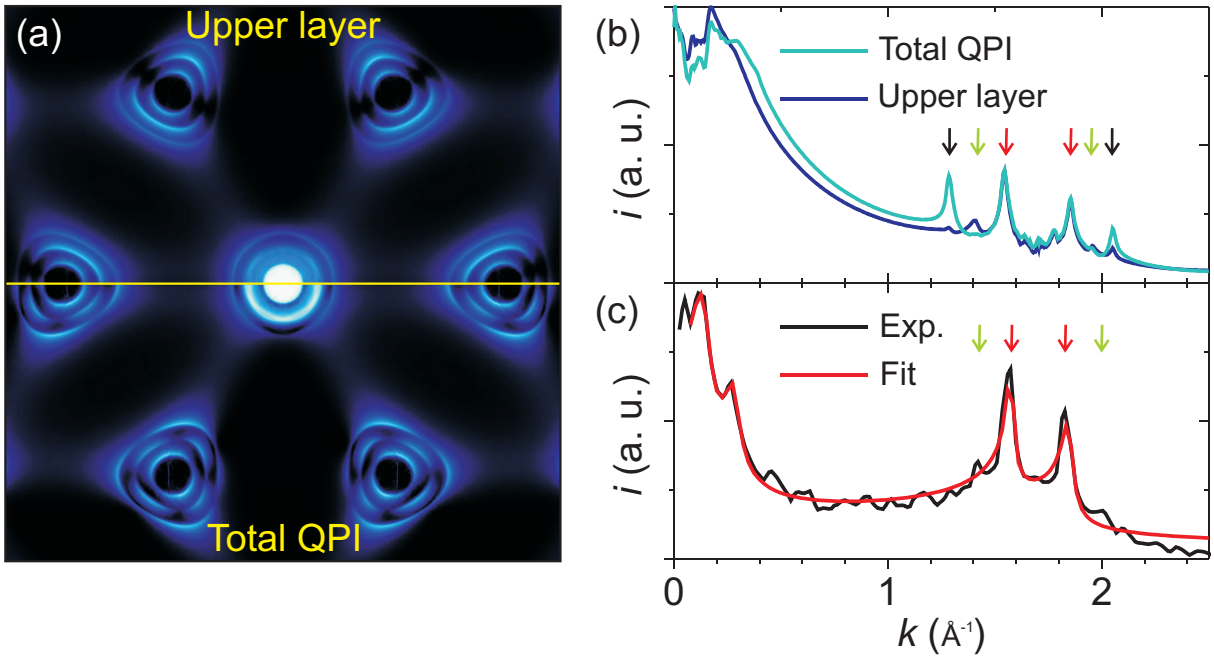


Figure 5.6: QPI intensity in the upper layer of BLG: (a) The top pattern is the calculated QPI pattern present in the upper layer, while the bottom pattern is the total QPI intensity. (b) Line scan along ΓK for the total QPI intensity, as well as the intensity present in the upper layer only. Both are normalized to 1 and obtained by averaging over 2000 different local impurities. At the K point, the inner feature (red arrow) is clearly favored, while the outer feature is strongly suppressed (black arrow). (c) Experimental line scan along ΓK ($E = 0.03$ eV), together with a 4-component fit using Eq. (B.14).

To visualize the suppression of $q_{12,\uparrow\uparrow}$ in QPI, we performed a full calculation using the T-matrix formalism. We calculate QPI intensities $|\rho(\boldsymbol{k},E)|$ with an impurity localized in a single unit cell. The detailed expression for ρ is given by:

$$\rho(\boldsymbol{k},E) = -\frac{\mathrm{e}^{i\boldsymbol{r}_0\cdot\boldsymbol{k}}}{2\pi i}\sum_{j=1}^{4}\mathrm{e}^{-i\boldsymbol{r}_j\cdot\boldsymbol{k}}\int_{1.BZ}\frac{d^2\boldsymbol{q}}{S_{BZ}} \left(\left[G^0(\boldsymbol{q},E)T(E)G^0(\boldsymbol{q}+\boldsymbol{k},E)\right]_{jj} - \left[G^0(\boldsymbol{q}+\boldsymbol{k},E)T(E)G^0(\boldsymbol{q},E)\right]^*_{jj}\right), \tag{5.5}$$

where $\boldsymbol{r}_j$ denotes the position of the $j-$th atom within the unit cell. We use $\boldsymbol{r}_1 = (\frac{a}{2},\frac{a}{2\sqrt{3}})$, $\boldsymbol{r}_2 = \boldsymbol{r}_3 = (0,0)$ and $\boldsymbol{r}_4 = (\frac{a}{2},-\frac{a}{2\sqrt{3}})$ for Bernal-stacked BLG. The major difficulty is the choice of the local potential, which has in principle 10 degrees of freedom: 4 on-site potentials, 2 intralayer hopping terms and 4 interlayer hopping terms. The QPI pattern calculated from the T-matrix quantitatively depends on the potential. The result shown in Fig. 5.5 (b) displays the QPI intensity of BLG for the simple case of an on-site potential at

sublattice $A1$ with the imaginary part (corresponding to the inverse quasiparticle lifetime) set to 0.04 eV. In contrast to the four rings found using the JDOS formalism, we find only three rings, which are best visible at K since the inner ring at Γ is hidden by the large contribution from $k = 0$. In line with experiment, but in stark contrast to the simpler JDOS-approach, we find a suppression of $q_{12,\uparrow\uparrow}$. However, the large wave vector $q_{11,\uparrow\downarrow}$, which is weak in the experiment, is still very pronounced in this T-matrix calculation.

The effect of layer polarization becomes evident when comparing the total QPI intensity with the intensity present in the upper layer, see Fig. 5.6 (a). The top part shows the QPI intensity present in the upper layer, while the bottom part show the total QPI intensity. We find that the intensity of $q_{11,\uparrow\downarrow}$ persists, while $q_{12,\uparrow\downarrow}$ and especially $q_{22,\uparrow\downarrow}$ are reduced. Though this effect is small in Fig. 5.6 (a) due to the specific choice of the scattering potential, it is clearly visible in the line scan along ΓK shown in Fig. 5.6 (b), which represents the QPI intensities averaged over 2000 different potentials using Gaussian distribution with a width of 2 eV both for onsite potentials and intralayer and interlayer hopping rates. Only the QPI intensity present in the upper layer is in good agreement with the experimental line scan shown in Fig. 5.6 (c).

5.4 Discussion

Though there is no fundamental symmetry that hinders electronic states to scatter in BLG, two principal scattering vectors ($q_{12,\uparrow\uparrow}$ and $q_{11,\uparrow\downarrow}$) that appear in the JDOS approximation are missing or weakened in the experiment. One of the two ($q_{12,\uparrow\uparrow}$) is also generally suppressed in T-matrix simulations. The obvious difference between $q_{12,\uparrow\uparrow}$ and the other three principal scattering vectors is that it connects two states with parallel velocities, while $q_{11,\uparrow\downarrow}$, $q_{11,\uparrow\downarrow}$ and $q_{11,\uparrow\downarrow}$ connect states with antiparallel velocities. Previously, intensities of scattering processes have been linked to the directions of the velocities of the states involved [92]. However, in Ref. [92] it was concluded that the latter case is favorable, whereas our experimental and theoretical results show the opposite effect.

To shed light onto this issue, A. Rosch developed an analytic model to predict the scattering intensity of parallel and antiparallel principal scattering vectors, which is derived in Appendix B. The important outcome of his calculation is that the singular contribution to the LDOS of two electron-like states with parallel velocities, such as $q_{12,\uparrow\uparrow}$ in BLG, is zero. In the case of antiparallel velocities, one finds a divergence in the intensity near to the principal scattering vector, which leads to a peak in the QPI map at the corresponding wave vector. The red line in Fig. 5.6 (c) represents a fit of the four main contributions us-

ing this analytical n-band model, Eq. (B.14) in App. B. Hence, the suppression of $q_{12,\uparrow\uparrow}$ in the experiment and in T-matrix calculations is due to the slopes of the bands involved in the scattering process. Note that this is a general result that should be of direct relevance for any QPI study of complex materials with multiple bands.
Our experimental setup, which measures an exponentially decaying tunneling current between sample and tip, is almost exclusively sensitive to the top layer of BLG. This becomes important when the states of the bands are preferentially located in one layer only as in the case of doped BLG. This means that the standing waves produced by $q_{11,\uparrow\downarrow}$ are present in BLG, but mainly localized in the lower layer and therefore strongly suppressed in the LDOS measured with STS.

5.5 Conclusions

In conclusion, we present a way to visualize the localization of states in BLG using QPI. We are able to measure QPI in strongly doped BLG and observe a suppression of $q_{11,\uparrow\downarrow}$ and $q_{12,\uparrow\uparrow}$ which is attributed to layer polarization and parallel velocities, respectively. The latter can be applied to any n-band material and should be of great relevance to any QPI study involving more than one band. While our study is the first that visualizes layer polarization with QPI, future STM studies on vdWs heterostructures with broken inversion symmetry as bilayers of transition metal dichalcogenides may use this technique to investigate the layer polarization. A smoking gun experiment which would underline our claims would be BLG doped with an electronegative element, which would reverse the localization of the states and hence switch the intensity of the intraband scattering vectors.

CHAPTER 6

Charge puddles in the bulk and on the surface of a compensated topological insulator

This chapter contains contributions from T. Knispel, W. Jolie, N. Borgwardt, J. Lux, Z. Wang, Y. Ando, A. Rosch, C. Busse, T. Michely, and M. Grüninger. M. Grüninger and T. Michely proposed the experiments, motivated by a recent publication on bulk charge puddles in $BiSbTeSe_2$ [18]. Z. Wang prepared the samples under the supervision of Y. Ando. T. Knispel mounted the sample for STM measurements under the supervision of W. Jolie and T. Michely. T. Knispel and W. Jolie collected the data. T. Knispel and W. Jolie analyzed the data. H. Legg provided the T-matrix calculations, under the supervision of A. Rosch. The results were discussed with T. Knispel, W. Jolie, H. Legg, N. Borgwardt, J. Lux, Z. Wang, Y. Ando, A. Rosch, C. Busse, T. Michely, and M. Grüninger. The results of this chapter can be found in Ref. [147]. Sections 6.2 and 6.4 can be found in Ref. [119].

6.1 Motivation

Topological insulators (TIs), a material class with electronic wave functions that span a Hilbert space with non-trivial topology [36], opened up a new aspect to the field of condensed matter physics. Various materials with non-trivial topology were discovered nowadays [36]. The most peculiar properties of three-dimensional (3D) TIs are induced at their surface, which represents a junction between a non-trivial and trivial TI; Dirac fermions, which are topologically protected through time-reversal symmetry, emerge at

the interface [20, 148, 149]. The spin-momentum locking of the surface states leads to spin-polarized currents that are needed for spintronic applications [7].

The main requirement to make practical use of the surface states of a 3D TI is to shift the chemical potential within the bulk band gap, leading to a suppression of the unwanted bulk conductivity [150]. Experimentally, this is achieved with compensation between donor-type and acceptor-type defects. A prominent example is the compensated 3D TI $Bi_{2-x}Sb_xTe_{3-y}Se_y$, which shows an excellent insulating behavior in the bulk for certain combinations of x and y [83], making it possible to achieve surface-dominated transport [151]. Compensation, however, also leads to random potential fluctuations that locally affect electronic states, giving rise to charge puddles in the bulk of the TI as recently reported by Borgwardt et al. [18] for $BiSbTeSe_2$: they found an increase in the optical conductivity at low temperatures that they attribute to the formation of conducting charge puddles that are not visible in DC measurements due to their localized nature.

Potential fluctuations due to charged impurities lead to a local band bending at the surface of TIs, which is directly accessible with STM and STS by measuring the corresponding shifts in the density of states. These *surface charge puddles* were reported for graphene monolayer [152–156], bilayer [157] and for the surface states of the 3D TIs $Bi_{2-x}Mn_xTe_3$, $Bi_{2-x}Ca_xTe_3$, $Bi_{2-x}Mn_xSe_3$ [158], Sb_2Te_3 [159] and $Bi_{1.5}Sb_{0.5}Te_{1.7}Se_{1.3}$ [160, 161]. The potential fluctuations reported so far, however, are much smaller than the fluctuations observed in the bulk of $BiSbTeSe_2$. In addition, there exists no study on the temperature-dependence of surface charge puddles, though bulk charge puddles in $BiSbTeSe_2$ surprisingly disappear at temperatures above 50 K [18]. The question, whether the material or the location of the puddle (bulk versus surface) mainly determines the different properties of surface and bulk charge puddles, remains experimentally unanswered so far. The importance to link these two phenomena is evident when envisioning devices that need control of the position of the chemical potential.

Theoretical progress has been made to understand the formation of charge puddles in the bulk and at the surface of 3D TIs. Skinner et al. [97, 99, 100] used numerical simulations to estimate the size of fluctuations in the random Coulomb potential of charge impurities. They found that the electronic states in the bulk poorly screen the fluctuations until bulk charge puddles are created. These charge carriers lead to a finite DOS at the chemical potential that hinders the fluctuations to increase further. The situation is different at the surface, where an additional screening channel is present due to the surface state. The latter is expected to reduce the potential fluctuations.

This chapter is devoted to the surface charge puddles of $BiSbTeSe_2$. Their lateral size, fluctuations and temperature dependence are measured with STM and STS. The results are compared with the properties of the bulk charge puddles of $BiSbTeSe_2$. The role of charge impurities to quasiparticle interference pattern is quantitatively discussed. The aim of the present work is to get a general, unifying physical picture of bulk and surface charge puddles that will be of great relevance for all compensated TIs.

6.2 Observation of surface charge puddles

Large-scale STM topographs of the cleaved $BiSbTeSe_2$ sample display flat terraces larger than 500 nm that are separated by steps of 10 Å height, or multiples thereof, consistent with a cleavage along the vdW gap between the quintuple layers of $BiSbTeSe_2$ (compare also [160]). The atomic-resolution STM topograph of Fig. 6.1 (a) shows the hexagonal lattice of the surface atoms together with variations in the apparent atom heights. Through the height profile along the blue line in the topograph of Fig. 6.1 (a), these height variations are quantified to be on the order of 50 pm. The variations are interpreted to result from the random arrangement of the chemical species in the mixed topmost Te/Se layer and in the mixed subsurface Bi/Sb layer. The chemical inhomogeneity is the origin of the apparent variation of the local electronic structure on the atomic scale. Similar observations were reported for the sister compound $Bi_{1.5}Sb_{0.5}Te_{1.7}Se_{1.3}$ [160, 161]. The cleaved surface is free of point defects (e.g. vacancies) and adsorbates.

Fig. 6.1 (b) displays a typical STS spectrum which shows the $\mathrm{d}I/\mathrm{d}V$ signal against the energy $E = eV$. It is rotated by 90°, so that it can directly be compared to the schematic band structure as derived from angle resolved photoemission spectroscopy [84, 160], which is sketched in Fig. 6.1 (b). We find a dip that is attributed to the Dirac energy E_D of the surface state, which is the energy at which the two surface state cones touch. The Dirac point is located close to the Fermi energy in accordance with ARPES measurements [84]. The top of the valence band is located at about -140 meV and the bottom of the conduction band at about 140 meV. Both are characterized by a slight change in slope of the $\mathrm{d}I/\mathrm{d}V$ signal. This implies a band gap of about 280 meV, which is comparable to 262 meV extracted by Borgwardt et al. [18] through optical spectroscopy. Note that a precise determination of the bulk band gap by STS is difficult here because of the small contribution of the bulk states compared to the large contribution of the surface states to the STS signal, as also found by Okada et al. [162]. In the energy range within the

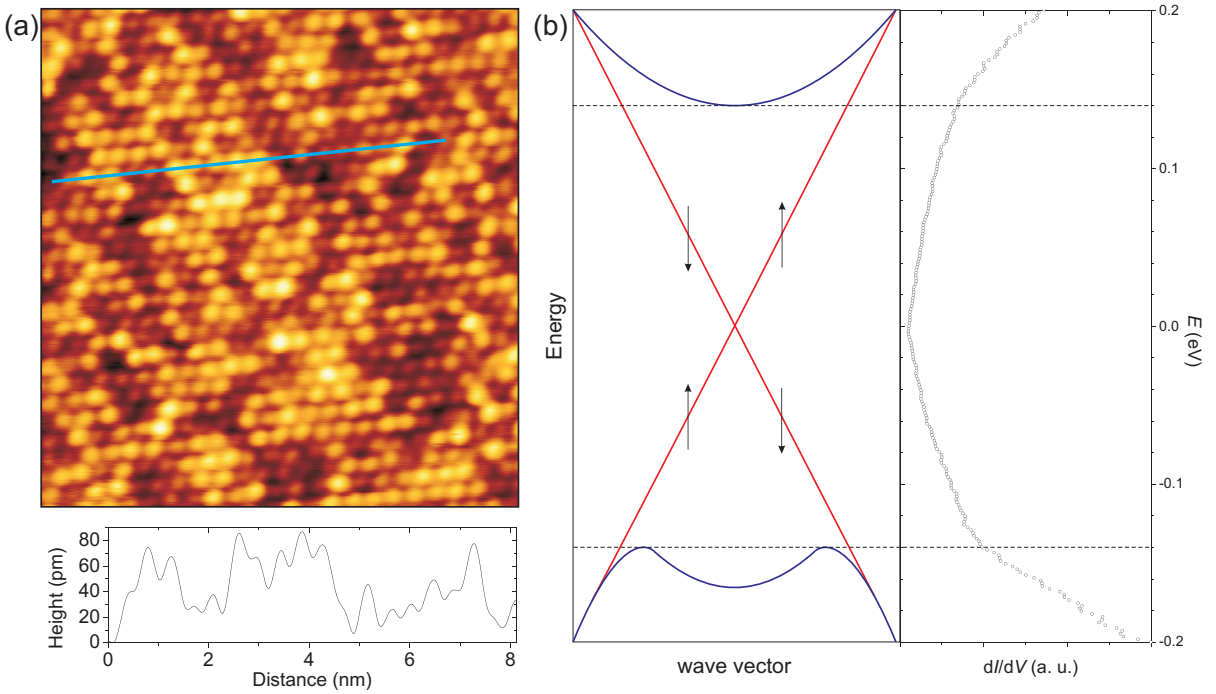


Figure 6.1: (a) Atomically resolved STM topograph of cleaved $BiSbTeSe_2$ ($V = -0.3$ V, $I = 0.05$ nA, image size 10×10 nm^2). The height profile along the blue line is plotted under the STM image. (b) Sketch of the band structure in the bulk (blue) and at the surface (red) of $BiSbTeSe_2$. The arrows visualize the spin of the two branches. A characteristic STS spectrum at 5.5 K is rotated and aligned to the band dispersion for direct comparison. The main spectral features (bulk valence band maximum and bulk conduction band minimum) are marked with dashed lines and linked to the corresponding band structure.

bulk band gap the spectrum results exclusively from the surface state. Its hallmark is the linear dependence of the LDOS on energy.

Local potential fluctuations due to ionized donors and acceptors lead to local shifts of the chemical potential and thus of the filling of the Dirac cone. Figure 6.2 (a) represents these fluctuations through a sequence of 50 STS spectra taken along a line of 80 nm length. The $\mathrm{d}I/\mathrm{d}V$ signal as a function of position and energy is visualized by a color scale ranging from blue to red. The minimum in the $\mathrm{d}I/\mathrm{d}V$ signal again corresponds to the Dirac point which smoothly shifts in energy with the lateral coordinate, whereby the characteristic length scale as given by the distance between minimum and maximum energy is of the order of $r_s = 40 - 50$ nm.

Figure 6.2 (b) displays the corresponding $\mathrm{d}I/\mathrm{d}V$ map taken near the Dirac energy at 5.5 K. The change in $\mathrm{d}I/\mathrm{d}V$ signal corresponds to the energy shift of the surface band structure in line with the formation of surface puddles as shown in Fig. 6.2 (a). Again a

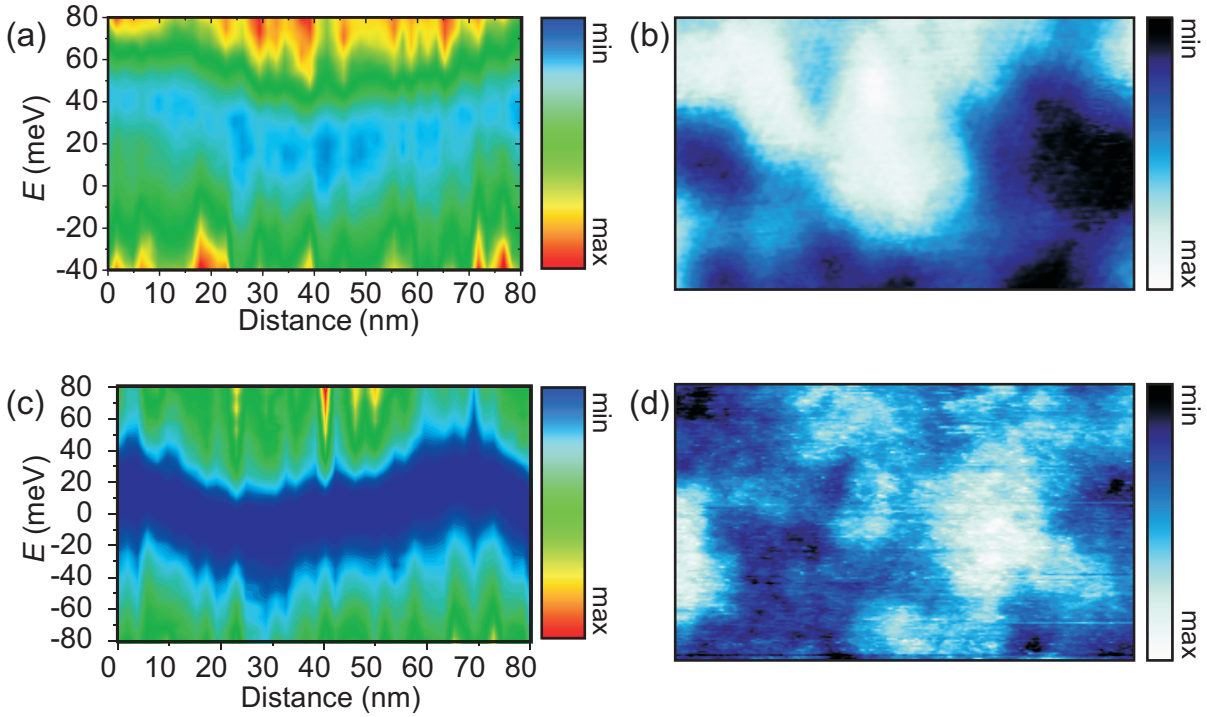


Figure 6.2: Probing surface charge puddles of $BiSbTeSe_2$: (a) 50 STS spectra over an energy range from -40 meV below the Fermi level to 80 meV above measured at 5 K. Each spectrum is plotted as a vertical stripe with the color scale indicating the dI/dV intensity from blue (low intensity) to red (high intensity). The spectra are taken equidistant along a straight line of 80 nm. The shift of the Dirac point (lowest dI/dV intensity) is of the order of 20 meV. (b) STS map recorded at 5.5 K ($V = 0.05$ V, $I = 0.07$ nA, image size 100×60 nm^2). Fluctuations in the dI/dV intensity visualize the fluctuations in the Dirac point position. (c) 50 STS spectra over an energy range from -80 meV below the Fermi level to 80 meV above measured at 77 K. (d) STS map recorded at 77 K ($V = 0.08$ V, $I = 0.05$ nA, image size 100×60 nm^2).

smooth shift in the LDOS is visible, showing the same characteristic length scale of about $r_s = 40 - 50$ nm from minimum to maximum.

We also performed STM and STS measurements at 77 K to investigate the temperature dependence of the puddles, which is significant in the bulk [18]. Fig. 6.2 (c)-(d) displays a dI/dV line scan as well as a dI/dV map taken at 77 K. It is more noisy but hardly distinguishable from the ones taken at 5.5 K. At first sight, this is remarkable since bulk puddles evaporate on a temperature scale of $40 - 60$ K, as discussed above.

Point spectra are measured along lines of 80 nm to 100 nm length at 5 (7) different sample locations resulting in a total of 185 (200) spectra at 5.5 K (77 K), to quantitatively characterize the potential fluctuations. The results are shown in Fig. 6.3 (a) and (b) for 5.5 K and 77 K, respectively. The energy of the dip found in each STS spectrum signi-

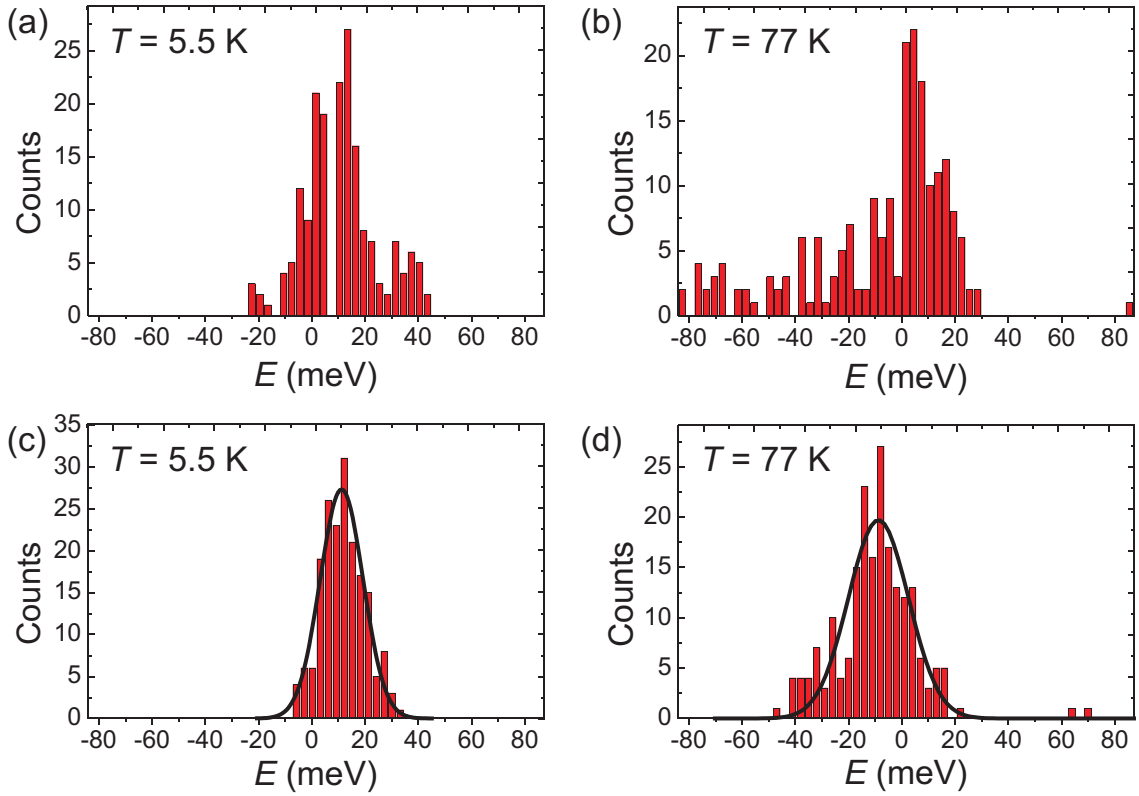


Figure 6.3: Temperature-dependence of the surface charge puddles in $BiSbTeSe_2$: (a) Distribution of the Dirac point position at 5.5 K. (b) Same distribution at 77 K. (c) Corrected distribution of the Dirac point position at 5.5 K, see text for details. (d) Corrected distribution at 77 K. Gaussian fits to distributions are shown as black lines. The bins in (a)-(d) have a width of 3 meV.

fying the local Dirac point position $E_D = e\phi$ is extracted and collected in bins of 3 meV, where ϕ denotes the local electric potential. The potential fluctuations can be characterized quantitatively through the standard deviation $\Gamma = e\sqrt{\frac{1}{N} \cdot \sum_i (\phi_i - \langle\phi\rangle)^2}$. At 5.5 K the average doping level of the sample is $\langle E_D\rangle = e\langle\phi\rangle = 11$ meV and the magnitude of the potential fluctuations is $\Gamma = 14$ meV. At 77 K we find $\langle E_D\rangle = -8$ meV and $\Gamma = 28$ meV. This representation of the data can be considered to be an upper bound for the potential fluctuations, as it assumes the absence of any tip-related effects on the data.

However, due to unavoidable occasional changes in the microscopic tip structure, e.g. by pick up of sample atoms, the tip density of states may change slightly between different locations at which the lines of spectra were taken. This may have an effect on the average measured doping level. To account for such possible parasitic effects related to the density of states of the tip, we subtracted the average Dirac energy of a line of spectra prior to their insertion into the histograms shown in Figs. 6.3-(c) and (d) and centered these histograms

at the respective global average. Applying this procedure, the standard deviation of the distribution measures a lower bound of the potential fluctuations. The magnitude of the potential fluctuations then is $\Gamma = 8\,\text{meV}$ at 5.5 K and $\Gamma = 15\,\text{meV}$ at 77 K. Here the distributions can be reasonably well fitted by Gaussians, which are shown in Figs. 6.3(c) and (d) as black lines.

Globally, it is fair to state that the samples of $BiSbTeSe_2$ are close to perfect compensation with the average doping level close to zero, in agreement with optical measurements [119]. Though our estimates of $\Gamma = 8 - 14\,\text{meV}$ at 5.5 K do not allow to precisely specify the magnitude of the potential fluctuations, we may safely conclude that Γ is small, about an order of magnitude smaller than the bulk band gap. Despite our limited statistics and possible sources of systematic errors, we further conclude that Γ is of similar magnitude at 5.5 K and 77 K. While the fluctuations of the bulk potential decrease with increasing temperature due to thermally activated carriers, we find no evidence for a decrease of the fluctuations Γ measured at the surface from 5.5 K to 77 K. With some reservation, our data rather suggest a slight increase.

6.3 Quasiparticle interference of $BiSbTeSe_2$

Random impurities near the surface of $BiSbTeSe_2$ not only lead to surface charge puddles, but also act as scattering centers for QPI as reported for graphene [153]. Both surface charge puddles and QPI can be measured simultaneously with STS maps, see Fig. 6.4 (a)-(c). The three STS maps were measured at the same location but at different energies, which are indicated in the figure. In Fig. 6.4 (a), one can clearly recognize two wavy patterns; one with a long wavelength of the order of 50 nm that is attributed to the surface charge puddles, another with a much shorter wavelength of the order of 10 nm that stems from QPI. The assignment is confirmed by the fact that only the short wavelength shows a dispersive behavior when increasing the bias voltage, while the long wavelength shows no energy-dependence [compare Fig. 6.4 (a) and Fig. 6.4 (b)], leading to the conclusion that it represents fluctuations in the LDOS due to the surface charge puddle rather than a scattering channel in QPI.

It is convenient to analyze the FT of the QPI pattern seen in STS maps. This is done in Fig. 6.4 (d)-(f) for the STS maps in Fig. 6.4 (a)-(c). The corresponding energy is again included in all FT patterns. The FTs show a pronounced disk centered at $k = 0$ in the energy range between $E = 0.125$ eV and $E = 0.225$ eV. In addition, there is an increase in the intensity close to $k = 0$. Note that this maximum near $k = 0$ may arise from the finite

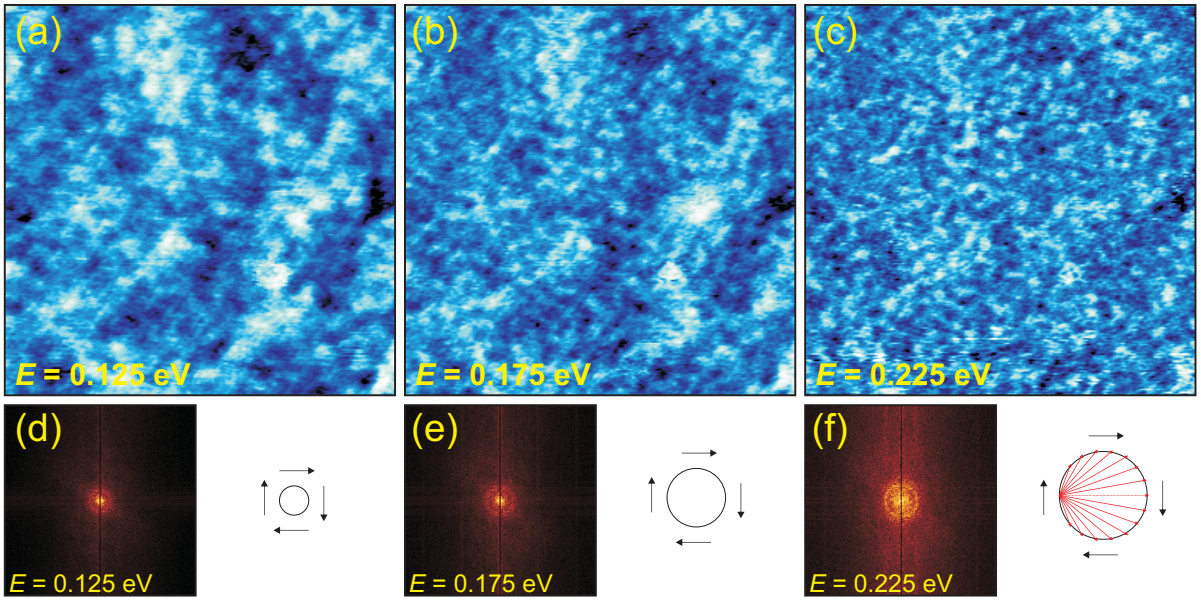


Figure 6.4: QPI on the surface of $BiSbTeSe_2$: (a)-(c) STS maps measured at different energies as indicated in the figure ($I = 0.08$ nA, image size 100×100 nm^2). Surface charge puddles together with standing waves arising from QPI are visible at low energies, while the latter dominate at higher energies. (d)-(f) FT of the STS maps, showing a disc around $k = 0$. The circular CEC responsible for QPI is sketched next to the FTs. The black arrows visualize the spin, while the red arrows in (f) show possible scattering vectors for a certain wave vector. The dashed red arrow shows scattering between states with opposite spin, which is strongly suppressed.

size of the image, similar to one of the principal scattering vectors in BLG, see Chap. 5.2. This artifact is, however, unlikely to appear here since the size of the STS maps is much larger than for BLG, leading to a better resolution at small wave vectors. The size of the disk increases with increasing energy.

The FT pattern is strongly related to the CEC of the band structure of $BiSbTeSe_2$ as reported in Ref. [160]. It is sketched in Fig. 6.4 (d)-(f) for the corresponding energies. We find that near to the Dirac energy, the CEC consists of a circle located at the Γ point. Drawing all possible scattering vectors as sketched with red arrows in the CEC at $E = 0.225$ eV [Fig. 6.4 (f)] reveals that backscattering represents the most intense wave vector as found for free electron-like surface states [101, 103], since it connects two states with antiparallel velocities that leads to strong nesting. However, this process is suppressed in $BiSbTeSe_2$ since two states with opposite momentum also have opposite spin due to spin-momentum locking [163, 164]. This is visualized with black arrows representing the spin and a dashed red arrow corresponding to the suppressed backscattering wave

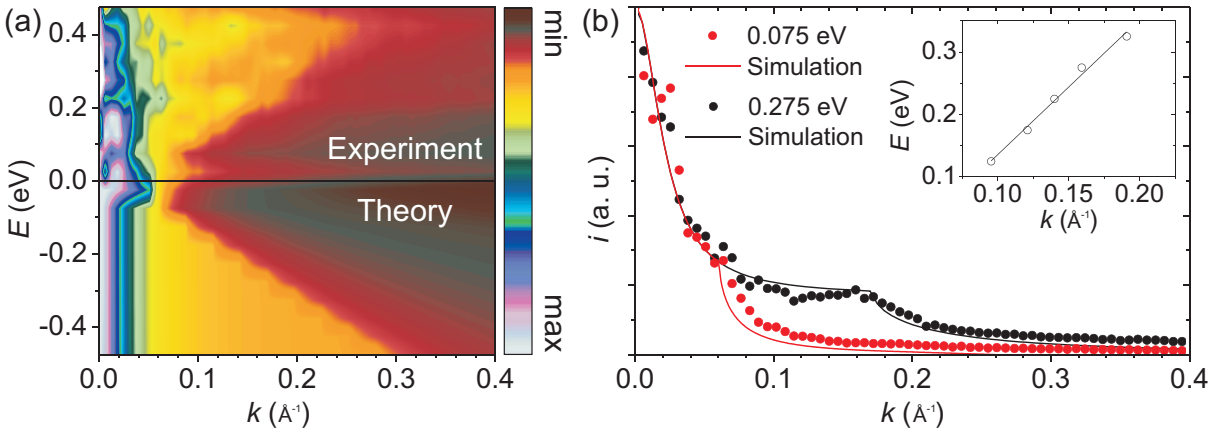


Figure 6.5: Dispersion of $BiSbTeSe_2$ obtained with QPI: (a) Dispersion of the QPI signal obtained experimentally with averaged isotropic line scans (above the chemical potential) and theoretically by fitting the experimental data (below the chemical potential). Note that both show the electron-like dispersion, though the theoretical result is mirrored for a direct comparison. (b) Individual line scans measured at $E = 0.075$ eV and $E = 0.275$ eV showing the step-like decrease in intensity, together with a narrow peak at $k = 0$. The line represent the fit of the T-matrix simulation including both Coulomb and delta potentials. The inset shows the experimentally extracted dispersion relation that is fitted with a linear function.

vector. Hence the wave vectors with the best nesting condition are suppressed due to the mismatch of their spins, leading to the disc (instead of a ring) found in experiment.

Mapping QPI at various energies enables us to extract the dispersion relation of $BiSbTeSe_2$. STS maps are measured from $E = 0.025$ eV to $E = 0.475$ eV to cover a large energy range of the electron-like cone of the surface state. We obtain radially averaged line scans measured in the corresponding FTs for each energy. They are shown in Fig. 6.5 (a), from $E = 0.025$ eV to $E = 0.475$ eV. The color scale is chosen such that it enhances the visibility of the dispersing feature, which is masked by the feature near $k = 0$ that will be addressed in the following. The dispersing wave vector increases nearly linearly with increasing energy, in accordance with electron-like Dirac fermions expected for the surface state of $BiSbTeSe_2$ [84]. Weak additional features with small wave vectors appear above 0.2 eV and are attributed to the valence band of the $BiSbTeSe_2$ bulk.

We compare the line scans to T-matrix calculations, which were performed by H. Legg. We restrict ourselves to the contribution of the surface state to the QPI intensity. We assume a Dirac Hamiltonian with a linear dispersion and neglect hexagonal warping effects [163, 164]. Starting with the simplest scenario, namely a delta potential within the Born approximation, one finds that the QPI intensity at the energy $\omega = E - E_D$ is given by [165]:

$$\rho_0(\mathbf{q},\omega) = -\frac{U_0}{4\pi^3}\mathrm{Im}\left\{T(\omega)\int \mathrm{d}\mathbf{k}\frac{\omega^2 + v_\mathrm{F}^2k^2 - v_\mathrm{F}^2\mathbf{k}\cdot\mathbf{q}}{\left(\omega^2 + v_\mathrm{F}^2k^2\right)\left(\omega^2 - v_\mathrm{F}^2\left(\mathbf{k}-\mathbf{q}\right)^2\right)}\right\}. \tag{6.1}$$

At the energy ω_i this leads to an isotropic disc with a abrupt edge at the radius $q = 2k_\mathrm{i}$, which exclusively depends on the magnitude of the wave vector of states at the probed energy with dispersion $\omega_\mathrm{i}(k_\mathrm{i})$. Note that for a two-dimensional electron gas with equal CEC, one gets a ring with radius $2k_\mathrm{i}$, not a disk. The difference is again attributed to the spin-momentum locking in the case of the TI surface states that suppresses backscattering, which would be favored otherwise due to the better nesting condition.

Since $BiSbTeSe_2$ is a compensated semiconductor one may suggest that charged impurities at the surface also contribute to QPI. This scenario can be simulated by using a screened Coulomb potential of the form $U(\mathbf{q}) = \frac{U_\mathrm{C}}{q^2+k_0^2}$ instead of a delta potential, with k_0 being the Thomas-Fermi screening wave vector. In the Born approximation, this leads to the following QPI intensity [165]:

$$\rho_\mathrm{C}(\mathbf{q},\omega) = -\frac{1}{4\pi^3}\frac{U_\mathrm{C}}{q^2+k_0^2}\mathrm{Im}\left\{T(\omega)\int \mathrm{d}\mathbf{k}\frac{\omega^2 + v_\mathrm{F}^2k^2 - v_\mathrm{F}^2\mathbf{k}\cdot\mathbf{q}}{\left(\omega^2 + v_\mathrm{F}^2k^2\right)\left(\omega^2 - v_\mathrm{F}^2\left(\mathbf{k}-\mathbf{q}\right)^2\right)}\right\}. \tag{6.2}$$

We find that the difference between the two potentials is only given by the prefactor. We first note that in both cases the dispersing behavior is only coming from the dispersion relation of the surface state, meaning that the position of the edge is still given by $2k_\mathrm{i}$. Nevertheless, $U(\mathbf{q})$ can dramatically change the overall shape of the QPI intensity, depending on the size of k_0. For $k_0 >> 2k_\mathrm{i}$, the prefactor is approximately $\frac{U_0}{k_0^2}$, leading to a constant increase or decrease of the overall intensity depending on the two factors. When k_0 is of the order of $2k_\mathrm{i}$, we find that additional structure enters into the QPI intensity; in addition to the step at $2k_\mathrm{i}$ we find a strong increase for small wave vectors. Finally, for $k_0 << 2k_\mathrm{i}$, the feature at small wave vectors completely suppresses the kink at $2k_\mathrm{i}$, so that no dispersion is found in QPI.

In general, one expects that both types of impurity are present on the sample. This can be modeled by fitting the experimental line scans using both scattering potentials simultaneously. The result has the following form [165]:

$$\rho(\mathbf{q},\omega) = n_0\cdot\rho_0(\mathbf{q},\omega) + n_\mathrm{C}\cdot\rho_\mathrm{C}(\mathbf{q},\omega). \tag{6.3}$$

A fit to the experimental line scans is shown in Fig. 6.5 (a). It is mirrored with respect to the experimental data to enable a direct comparison. At low energies close to E_D ($E <$ 0.75 eV) we find a Fermi velocity of $v_\mathrm{F} = (3.7 \pm 0.3) \times 10^5$ m/s, while for higher energies a larger $v_\mathrm{F} = (5.0 \pm 0.3) \times 10^5$ m/s is found. Both values are in good agreement with the

dispersion of $Bi_{1.5}Sb_{0.5}Te_{1.7}Se_{1.3}$ ($v_F = 3.5 \times 10^5$ m/s near E_D and $v_F = 4.9 \times 10^5$ m/s at higher energies) obtained using time-resolved ARPES [160]. The Dirac energy is set to $E_D = 0$ at low energies and to $E_D = -0.035$ eV at high energies. The screening length $r_s = 9.1$ nm used for the fit is slightly smaller than the screening length estimated from the size of surface charge puddles in STM images.

More insights on the contributions of the two scattering potentials is found when analyzing the fractions $\frac{n_0}{U_0}$ and $\frac{n_C}{U_C}$ which give the ratio of scattering events due to one of the types of impurities. From the fit, one obtains that 17% of the scattering events are caused by delta potentials, while 83% stem from scattering of a Coulomb potential.

The role of the two contributions is best visible when analyzing individual line scans, see Fig. 6.5 (b). We find that $\rho_C(\mathbf{q},\omega)$ is responsible for the maximum at low wave vectors, while $\rho_0(\mathbf{q},\omega)$ is constant up to $2k_F$. At $E = 0.075$ eV, we find that the kink is located on the tail of the feature caused by the Coulomb impurity. Hence both types of impurity contribute to this dispersive signal. At $E = 0.075$ eV, we find that the contribution of Coulomb impurities is strongly suppressed at $2k_F$. In conclusion, only delta potential impurities contribute to the dispersing feature at these high energies.

Another way to obtain the dispersion of the surface state is to directly extract the k-value of the kink in the experimental data. In the energy range between $E = 0.125 - 0.325$ eV, one expects a linear dispersion as found for $Bi_{1.5}Sb_{0.5}Te_{1.7}Se_{1.3}$. The inset in Fig. 6.5 (b) shows the resulting dispersion relation that is fitted with a linear function, resulting in a Dirac energy of $E_D = -0.08 \pm 0.02$ eV and a Fermi velocity of $v_F = 6.6 \pm 0.4 \times 10^5$ m/s, which is slightly higher than the velocity $v_F = 5.0 \pm 0.3 \times 10^5$ m/s found using the T-matrix simulation and $v_F = 4.9 \times 10^5$ m/s found for $Bi_{1.5}Sb_{0.5}Te_{1.7}Se_{1.3}$ [160]. Interestingly, a reduction in the Fermi velocity of $\approx 75\%$ has also been found when comparing the dispersion obtain with TR-ARPES and QPI in $Bi_{1.5}Sb_{0.5}Te_{1.7}Se_{1.3}$ [160]. This reduction is, however, not found when fitting the entire range using the T-matrix simulation.

6.4 Discussion

Why are the fluctuations at the surface so much smaller than the fluctuations in the bulk? To answer this question, one needs to recall which physical process prevents the fluctuations to grow even far above the size of the band gap. The mechanism is screening, which effectively only takes place when charge carriers are located at the chemical potential. There are two ways to create charge carriers in the bulk of $BiSbTeSe_2$, namely by band bending due to the potential fluctuations or by increasing the temperature, leading to

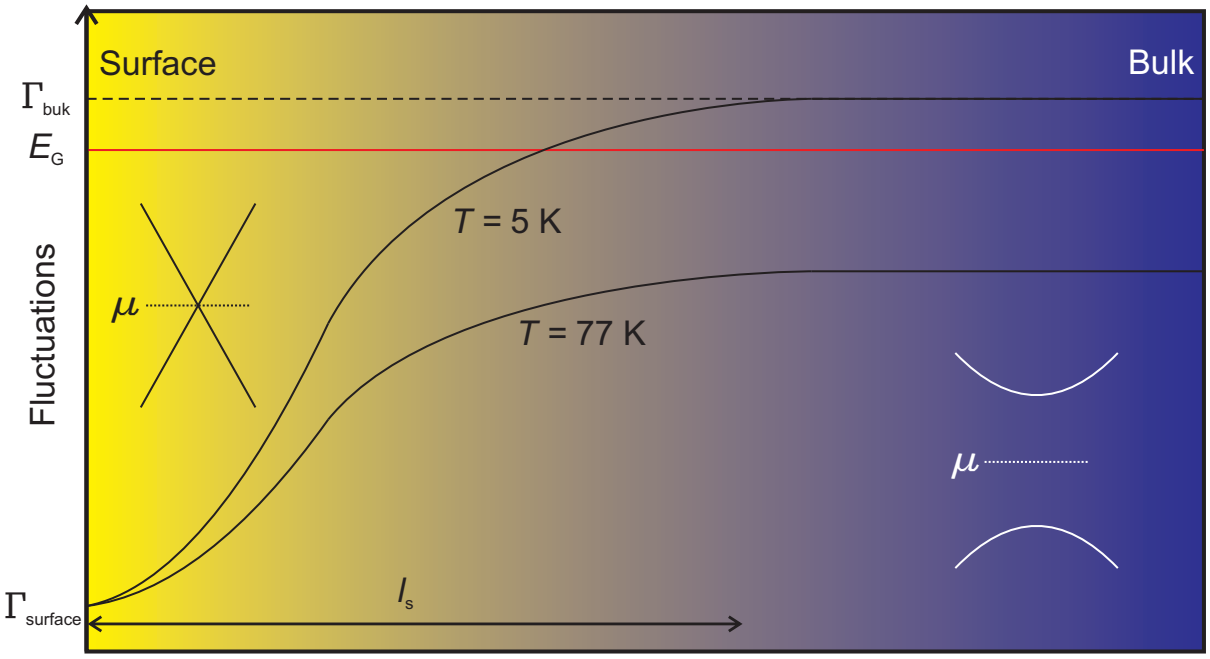


Figure 6.6: Potential fluctuations in compensated insulators at $T = 5$ K and $T = 77$ K: at 5 K, bulk charge puddles only start to screen the potential fluctuations when the bands are bend up or down to the chemical potential. Hence the fluctuation are of the order of the band gap. In contrast, surface charge puddles instantaneously screen the potential fluctuations due to the gapless band structure at the surface, drastically reducing the potential fluctuations. At 77 K, thermally activated charge carriers suppress the fluctuations in the bulk, so that no bulk charge puddles are formed, though surface charge puddles are barely affected due to the efficient screening of the surface state. Bulk and surface charge puddles are separated by a characteristic length scale l_s which, depending on its size compared to the screening length r_s of surface charge puddles, may indicate a possible interplay between the two.

thermally excited charge carriers [18]. As soon as charge carriers are present and screen the charges of the ionized acceptor and donors, the potential fluctuations will be automatically reduced, hence the screening and in consequence the formation of puddles is a highly non-linear process [18]. At low temperatures, screening can only start when the conduction or valence band reach the chemical potential, leading to potential fluctuations of $\Gamma_{\text{bulk}} \geqslant E_G/2$. In contrast, efficient screening channels are present at the surface already when small fluctuations are present due to the surface state which closes the band gap of the semiconducting bulk. Hence, screening can much faster prevent the fluctuations to increase further, leading to $\Gamma_{\text{surface}} << E_G/2$. The different energies of the fluctuations at the surface and in the bulk of a compensated TI are schematically shown in Fig. 6.6, which connects both Γ_{surface} and Γ_{bulk} within a length scale l_s. Below, we will argue that

in our system the assumption that $r_s \ll l_s$ is not valid, leading to an additional interplay between bulk and surface puddles.

We can quantitatively compare the potential fluctuations obtained at the surface of $BiSbTeSe_2$ with the theoretical expectations obtained using a self-consistent theory based on Thomas-Fermi screening by Dirac-like surface carriers, as done by Skinner and Shklovskii [99, 100]. They calculated the amplitude of potential fluctuations $\Gamma = e\langle(\phi - \langle\phi\rangle)^2\rangle^{1/2}$ at the TI surface as well as the characteristic size r_s of surface puddles caused by Coulomb disorder in the bulk for perfect compensation, $N_{\mathrm{def}} = N_D = N_A$ with N_D (N_A) defined as the donor (acceptor) density. For nominally perfectly compensated TIs in which the Dirac point lies at the chemical potential, $E_D = 0$, they find

$$r_s = (4\,\alpha_{\mathrm{eff}}^4 N_{\mathrm{def}})^{-1/3}, \tag{6.4}$$

with the *effective* fine structure constant

$$\alpha_{\mathrm{eff}} = \frac{e^2}{4\pi\varepsilon_0\varepsilon_{\mathrm{eff}}\hbar v_F} = \alpha\,\frac{c}{\varepsilon_{\mathrm{eff}} v_F}\,, \tag{6.5}$$

where $\alpha = 1/137$ denotes the fine structure constant, c the speed of light, and v_F the Fermi velocity. The effective dielectric constant at the surface is given by $\varepsilon_{\mathrm{eff}} = (\varepsilon + 1)/2$, where $\varepsilon \approx 200$ [18] denotes the bulk dielectric constant. In $Bi_{2-x}Sb_xTe_{3-y}Se_y$, the dispersion of the topological surface state is not perfectly linear, giving rise to a variation of v_F in the range of $3 - 5 \cdot 10^5\,\mathrm{m/s}$ [84, 160, 161]. Altogether, we find $\alpha_{\mathrm{eff}} = (8 \pm 2)\,\alpha \approx 0.04 - 0.07$, significantly smaller than the value of 0.24 estimated by Skinner and Shklovskii for Bi_2Se_3 [99]. With the optically determined defect density $N_{\mathrm{def}} = 1 - 4 \cdot 10^{20}\,\mathrm{cm}^{-3}$ of the same sample [119], we find $r_s \approx 30 - 90\,\mathrm{nm}$, in very good agreement with our STS result of $40 - 50\,\mathrm{nm}$.

Furthermore, Skinner and Shklovskii [99] find

$$\Gamma = 4\frac{E_C}{\alpha_{\mathrm{eff}}^{2/3}} \propto \left(\frac{v_F^2 N_{\mathrm{def}}}{\varepsilon}\right)^{1/3}, \tag{6.6}$$

again for nominally perfectly compensated samples, $E_D = 0$. With the experimental result of $E_C/k_B = 40 - 60\,\mathrm{K}$ derived from optical data of the same sample [119], this yields a theoretical prediction of $\Gamma = 80 - 170\,\mathrm{meV}$, much larger than the value of $8 - 14\,\mathrm{meV}$ observed in STS at 5.5 K.

This inconsistency between theory and experiment can also be derived using only the STS data, without reference to optical results. Theory predicts [99]

$$r_s\,\Gamma = \frac{4^{2/3}\,E_C}{\alpha_{\mathrm{eff}}^2 N_{\mathrm{def}}^{1/3}} = 4^{2/3}\pi\varepsilon_0(\hbar/e)^2 \cdot \varepsilon v_F^2, \tag{6.7}$$

which depends only on ε and v_F. The resulting prediction of $r_s\,\Gamma = 3 - 9\,\mathrm{eV\ nm}$ is an order of magnitude larger than the experimental STS result of $0.3 - 0.7\,\mathrm{eV\ nm}$ at 5.5 K. Equations (6.4) and (6.6) were derived for nominally perfectly compensated samples but are expected to apply as long as the chemical potential μ is smaller or at least not much larger than the potential fluctuations Γ. For doped compounds with $|\mu| \gg 2E_C/\alpha_{\mathrm{eff}}^{2/3}$ [cf. Eq. (6.6)], Skinner and Shklovskii find [99]

$$r_s = \frac{\hbar v_F}{\alpha_{\mathrm{eff}}\,|\mu|} \quad \text{and} \quad \Gamma^2 = \frac{16\pi\,E_C^3}{\alpha_{\mathrm{eff}}^2|\mu|}\,. \tag{6.8}$$

This limit of large μ is not applicable in $BiSbTeSe_2$, as demonstrated by our STS results. In fact, Eq. (6.8) predicts an even larger value of Γ than Eq. (6.6) for the experimentally determined parameters.

The calculations of Skinner et al. [97, 99] neglect the screening contribution of bulk puddles by assuming that all donors and acceptors are ionized. In other words, they assume that the formation of surface puddles is *not* affected by bulk puddles. This is valid for $r_s \ll l_s$, where l_s denotes the characteristic thickness of the near-surface layer in which bulk puddles are suppressed. For $r_s \ll l_s$, the Coulomb disorder near the surface is screened by surface carriers with potential fluctuations Γ (much) smaller than $\Delta/2$, preventing strong band bending and the formation of bulk puddles. The size R of bulk puddles – not to be confused with the thickness l_s of the near-surface layer – was estimated by Shklovskii and coworkers by a simple scaling argument [97]. It states that random fluctuations of the density of ionized defects in a volume R^3 give rise to an uncompensated charge $\propto(N_{\mathrm{def}}R^3)^{1/2}$ and thus to a Coulomb potential $\propto\sqrt{R}$. Bulk puddles are formed if these potential fluctuations are as large as $\Delta/2$, which leads to the estimate [97]

$$R = \frac{(\Delta/E_C)^2}{8\pi\,N_{\mathrm{def}}^{1/3}}\,. \tag{6.9}$$

Using $\Delta = 0.25\,\mathrm{eV}$, $E_C = 40 - 60\,\mathrm{K}$, and $N_{\mathrm{def}} = 1 - 4\cdot 10^{20}\,\mathrm{cm}^{-3}$ [119], we find $R \approx 100 - 500\,\mathrm{nm}$. However, recent numerical results combined with a refined scaling argument by Bömerich *et al.* [166] predict much smaller values with $R\propto(\Delta/E_C)^{1.1}$ for $\Delta/E_C \leqslant 40$ and

$$R\propto\frac{(\Delta/E_C)^2}{\ln(\Delta/E_C)} \tag{6.10}$$

for $\Delta/E_C \to \infty$. The same behavior but with a smaller prefactor is found for l_s [166]. Under the assumption that the surface carriers screen like a perfect metal, i.e., large $|\mu|$, Bömerich et al. predict $l_s \approx (7 - 12)/N_{\mathrm{def}}^{1/3}$ in the relevant range $\Delta/E_C = 50 - 75$. This corresponds to a thickness of the near-surface layer $l_s = 9 - 25\,\mathrm{nm}$ which is even *smaller*

than the measured characteristic size of surface puddles, $r_s = 40 - 50\,\mathrm{nm}$. The assumption of perfectly metallic surfaces with a high chemical potential rather overestimates the value of l_s in $BiSbTeSe_2$. This result thus clearly suggests that the assumption $r_s \ll l_s$ is not valid anymore. Therefore, screening by bulk puddles may contribute to the surface properties, effectively reducing the amplitude of potential fluctuations on the surface. Altogether, these results indicate that surface puddles are not fully independent from bulk puddles and that a full quantitative description of the experimental data requires to consider a self-consistent description of both, surface and bulk properties.

Another major difference between surface and bulk puddles in $BiSbTeSe_2$ is that the latter disappear at temperatures above 50-60 K [18, 119], while surface charge puddles are observed at temperatures up to 77 K, without any sign of a reduction in the fluctuations or puddle size. The reason is again hidden in the mechanism that prevents puddle formation at high temperatures, namely thermally activated charge carriers. The corresponding screening channel reduces the fluctuations at high temperatures, preventing the valence and conduction band to reach the chemical potential. Hence, no puddles are formed in the bulk. The situation at the surface is very different, because of the gapless surface state, leading to surface puddle formation even for very small fluctuations, also at 77 K. Naively, the fact that no significant difference in the size of the fluctuations at 5 K and 77 K seems to suggest that surface puddles are independent of bulk carriers. However, the suppression of bulk puddles is due to the thermal activation of carriers in the bulk. Accordingly, the screening capability of the bulk is smoothly enhanced with increasing temperature. In other words, screening in the bulk at low temperatures is due to bulk puddles, but this role is taken over by activated carriers with increasing temperature. Therefore, it is very well possible that the temperature scale for the suppression of bulk puddles has little relevance to surface puddles. The potential fluctuations at 5 K and 77 K are sketched in Fig. 6.6. To sum up, potential fluctuations are still present on the surface and in the bulk of $BiSbTeSe_2$ at high temperatures, though the latter are too small to create bulk charge puddles due to the large band gap and the screening of thermally activated charge carriers.

QPI in $BiSbTeSe_2$ near the Dirac energy is dominated by a linearly dispersing, disc-like feature that is analyzed to obtain the dispersion relation of the surface state. T-matrix calculations within the Born approximation indeed confirm that the radius of the disc is linked to the wave vector of the states at the corresponding energy. The extracted Fermi velocities [$v_\mathrm{F} = (3.7 \pm 0.3 \times 10^5$ m/s near E_D and $v_\mathrm{F} = (5.0 \pm 0.3) \times 10^5$ m/s at higher energies] are in excellent agreement with the Fermi velocity of the related compound

$Bi_{1.5}Sb_{0.5}Te_{1.7}Se_{1.3}$ ($v_F = 3.5 \times 10^5$ m/s near E_D and $v_F = 4.9 \times 10^5$ m/s at higher energies) [160], while a larger Fermi velocity [$v_F = (6.6 \pm 0.4) \times 10^5$ m/s at higher energies] is found when extracting the kinks directly from the experimental data in a small energy range and fitting them with one linear function only. Note that an reduction of the wave vector in QPI (resulting in a higher Fermi velocity) has also been observed in $Bi_{1.5}Sb_{0.5}Te_{1.7}Se_{1.3}$ and attributed to spin-momentum locking, which may lead to a suppression of backscattering due to the opposite spins involved in the scattering process [160]. We can rule out that the spins of the Dirac fermions cause a reduction of the QPI wave vector since it is not found in the T-matrix calculations, which explicitly take into account the spin of the states. Our calculations show that the consequence of the spin is that the QPI intensity forms a disc in k-space instead of a ring due to the interplay of nesting which favors backscattering and spin-momentum locking which suppresses backscattering. These two contributions tend to cancel each other, leading to the flat disc in the case of a delta potential. Instead, we argue that it is non-trivial to assign the weak kink (in contrast to a peak) in STS experiments, which is strongly suppressed away from the Dirac energy in the case of charged impurities. A fit using T-matrix calculations seems to be mandatory for these systems.

Using T-matrix simulations, we are not only able to extract the dispersion of the surface state, but can also disentangle the contributions of Coulomb and delta potential scatterers. Both are present in $BiSbTeSe_2$, and the contribution of Coulomb impurities leads to a suppression of the QPI intensity around $2k_i$, which might be the reason why this scattering channel is often not visible in experiment. The screening length $r_s = 9.1$ nm used for the fit is smaller than the length scale $r_s = 40 - 50$ nm obtain from STM images. This discrepancy might be due to different definitions of r_s. Indeed, using the first zeros of an autocorrelation function of the actual STS image, one obtains $r_s = (14 \pm 4)$ nm, in very good agreement with the simulation. Note that this leads to even stronger deviations from the theory developed by Skinner et al. [99].

6.5 Conclusions

STM and STS measurements on the compensated TI $BiSbTeSe_2$ revealed fluctuations on the surface that are attributed to surface charge puddles. Their lateral size and energy variation are much smaller than the bulk charge puddles of the same material due to the surface state that effectively screens the impurities and due to a possible interplay between surface and bulk charge puddles, leading to an additional reduction of the fluctuations.

These findings connect the large bulk charge puddles with strong temperature dependence and the small surface charge puddles with almost no temperature dependence and are of general importance for any compensated semiconductor with conducting surface states. In addition, experimental and theoretical QPI maps show that spin-momentum locking leads to a disc-like intensity in k-space, which can be analyzed to obtain various fundamental parameters of the system such as its dispersion and scattering potentials.

CHAPTER 7

Electronic properties of quasi-freestanding epitaxial molybdenum disulfide

This chapter contains contributions from C. Murray, W. Jolie, T. Michely, J. Hall and C. Busse. W. Jolie proposed the experiments, motivated by the recent advances in the growth of MoS_2 on graphene on Ir(111), MoS_2/MLG/Ir(111) (see Ref. [118]). C. Murray and W. Jolie prepared the samples using the recipe of Ref. [118]. C. Murray and W. Jolie collected and analyzed the data. The results were discussed with C. Murray, W. Jolie, J. Hall, T. Michely and C. Busse, and can be found partly in Ref. [118].

7.1 Motivation

Molybdenum disulfide (MoS_2) belongs to the TMDC family, a material class composed of transition metal (like Mo or W) and dichalcogene atoms (like S or Se) forming a layered crystal with weak vdW interaction between the layers, making it possible to reduce the thickness of TMDCs down to the atomic limit of one monolayer (ML) with exfoliation methods. ML MoS_2 consists of one Mo layer sandwiched between two S layers. Within each layer, the atoms form a strongly bound honeycomb lattice. Freestanding MoS_2 is semiconducting and has a transition from an indirect to direct band gap when thinned down to ML thickness [21, 167], making it interesting for applications such as ultimately thin transistors [168], photodetectors and electroluminescent devices [169]. While the top down approach is often used to obtain ML MoS_2, a bottom-up synthesis of high quality

MoS_2 on an inert substrate in UHV is highly desired, in order to analyze its fundamental properties using in situ surface sensitive techniques, to ease a comparison with theoretical calculations and to make it scalable for industrial applications.

Recently, we found a facile method to grow MoS_2 on graphene on Ir(111) [118] using a two-step molecular beam epitaxy synthesis with elemental Mo and S (see Chap. 4.2), which results in high quality epitaxial MoS_2, with a controlled thickness depending on the amount of material used. The great advantage of this method is that MoS_2 is prepared in situ and can be measured with surface sensitive techniques without breaking the vacuum, leading to clean, well defined MoS_2 sheets. One can also expect a weak coupling to the substrate due to the graphene between MoS_2 and Ir(111). This is in contrast to epitaxial MoS_2 on Au(111) [170], which is known to affect the fundamental electronic properties of MoS_2, especially those coming from orbitals pointing out-of-plane [25, 171].

The band structure of MoS_2 has been extensively measured in the past using different techniques. Photoluminescence measurements reported the optical band gap [21, 167], which is much smaller than the electronic band gap due to excitons with binding energies of the order of 500-1000 meV [24, 66]. Han et al. [67] reported on the occupied states of the band structure of MoS_2 using ARPES, which is however insensitive to the unoccupied band structure. An experimental tool capable of probing both occupied and unoccupied states is STS, which has the additional advantage of a high spatial resolution to study the impact of defects on the band structure. Many groups have already measured the electronic band gap of MoS_2 with STS: the band gap ranges from $E_G = 2.01(8)$ eV for MoS_2/MLG/SiC [172], $E_G = 2.1$ eV for MoS_2/SiO_2/Si [173], $E_G = 2.2$ eV for MoS_2/MLG/Au foil [174], and from $E_G = 1.9$ eV [175], $E_G = 2.15(6)$ eV [176], $E_G = 2.15(10)$ eV [177], to $E_G = 2.40(5)$ eV [178] for MoS_2/graphite. The largest band gap of $E_G = 2.7$ eV is reported for freestanding MoS_2 patches surrounded by MoS_2/Au(111), which are decoupled from the substrate due to the formation of vacancy islands underneath the intact MoS_2 sheet [179]. The scatter in the literature is likely due to the different substrates and the fact that the direct band gap is located at the K point, leading to a strong suppression of these states in STS due to their high $k_{||}$. Many groups also investigated the role of edges [172, 176, 178], which are often however not clearly resolved in STM images due to a possible contamination at the reactive edges of MoS_2 flakes during transfer.

It is possible to get access to the k-space structure of the states in MoS_2 by combining constant current and constant height modes in STS spectra [116]. This method has been applied to many TMDCs [116, 180, 181], such as $MoSe_2$, WSe_2, WS_2 and MoS_2 in ML, BL form and heterostructures thereof. In constant height mode, the tip is stabilized at

a setpoint of current and voltage. The $\mathrm{d}I/\mathrm{d}V$ spectrum is then measured with open feedback loop, leaving the tip at the same spatial position during data acquisition. In constant current mode, the feedback loop is closed, enabling the tip to move closer to the surface when less states are available or to retract the tip when more states tunnel between tip and sample. While $\mathrm{d}I/\mathrm{d}V$ in constant height gives a measure for the DOS of the surface, it may miss states with high wave vectors parallel to the surface due to the increased damping into vacuum with higher $k_{||}$. This problem can be overcome using constant current mode, which records a peak in $\mathrm{d}I/\mathrm{d}V$ at the energy of every extremum in the band structure. These extrema are called critical point energies (CPE) [116] in the following. To get access to the $k_{||}$ of the CPE one can measure $\mathrm{d}I/\mathrm{d}z$ instead of $\mathrm{d}I/\mathrm{d}V$ in constant current mode. This signal is directly related to the decay constant via $\kappa = \mathrm{d}I/2\mathrm{d}z$ [182]. The combination of these three measurements makes it possible to probe the CPE and to track their location in k-space.

In this chapter we will give a detailed analysis of the band structure of epitaxial MoS_2 on graphene on Ir(111) using constant height and constant current STS. The results are compared with ab initio calculations of freestanding MoS_2 and with the related substrates Au(111) and graphite that are often reported in literature. We will also examine the role of defects such as mirror twin boundaries (MTB) and zigzag edges, which drastically change the shape and size of the band gap. The great advantage of epitaxial MoS_2 on graphene on Ir(111) compared to other substrates is visualized via intercalation of Eu between graphene and Ir(111), demonstrating that epitaxial MoS_2 on graphene on Ir(111) not only gives us the opportunity to measure the fundamental electronic properties of MoS_2, but also enables us to tailor those by doping graphene from the backside.

7.2 Probing the bands of quasi-freestanding molybdenum disulfide

A large STM image of MoS_2/MLG/Ir(111) is shown in Fig 7.1 (a). The entire Ir(111) surface is covered with graphene, which forms wrinkles upon cooling due to thermal stress [183]. The steps in the image are Ir(111) step edges (from top right to bottom left). We find large MoS_2 flakes on graphene on Ir(111), together with small bilayers of MoS_2. The dark lines in MoS_2 represent grain boundaries that are formed when two grains of different orientation meet [73, 184–186]. Their visibility is greatly enhanced when lowering or inverting the bias voltage, see Fig. 7.1 (b), in which they appear as bright lines.

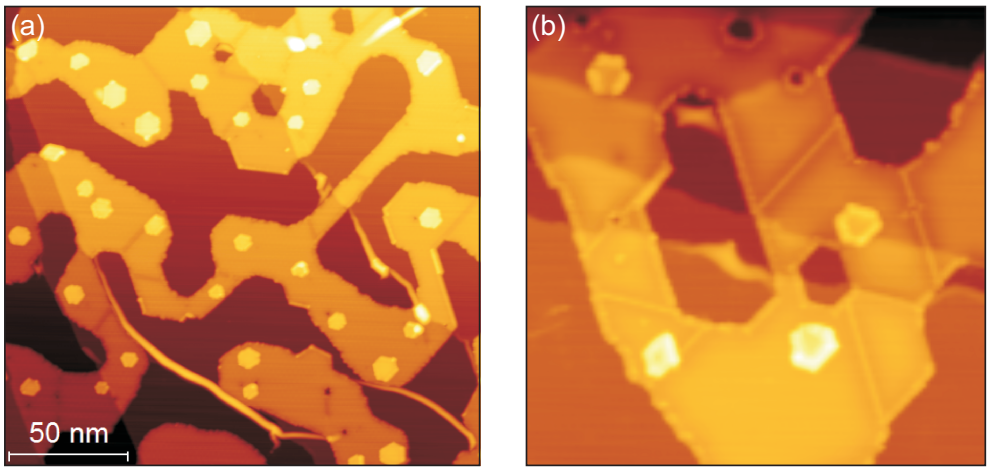


Figure 7.1: MoS_2/MLG/Ir(111): (a) STM image showing large MoS_2 flakes forming one-dimensional line defects upon grain merge ($U = 1.5$ V, $I = 0.01$ nA, image size 200×200 nm^2). Small bilayers are visible, together with Ir(111) step edges and graphene wrinkles. (b) STM image using a small bias voltage ($U = 0.9$ V, $I = 0.03$ nA, image size 75×75 nm^2). The line defects appear as bright lines.

Before focusing on MoS_2, one should note that the well investigated graphene on Ir(111) substrate can be used to check the low contribution of the tip density of states. A typical STS spectrum shows a shoulder at $E \approx -0.2$ eV, corresponding to the top of the hole-like, Rashba-split Ir(111) surface state located at the Γ point, which is known to persist under graphene [45, 46, 187, 188].

The LDOS of MoS_2 measured with STS in constant height mode is shown in Fig. 7.2 (a) in linear scale. Fig. 7.2 (b) shows the same spectrum in logarithmic scale. We find a peak at $E \approx -1.9$ eV and a monotonic increase starting at $E \approx 0.8$ eV. Between those we have a large energy range with vanishing signal that we attribute to the band gap of MoS_2. The signal in the gap is small but finite, which means it is possible to tunnel within the band gap of MoS_2. The spectrum is used to estimate the valence band maximum (VBM) and conduction band minimum (CBM) which are extracted using the start of the sharp rise of the signal on both sides of the spectrum. The VBM lies at $E = -1.750$ eV, the CBM at $E = 0.825$ eV, leading to a band gap of $E_G = 2.575$ eV. We find that MoS_2 is gated; the band gap is not symmetric with respect to the chemical potential, but shifted towards lower energies. This finding is consistent with the related system MoS_2/graphite, where all reported STS spectra show an gated band gap [175–178]. Note that tip-induced band bending [189, 190] is negligible here, presumably due to the conducting graphene under MoS_2 that pins the Fermi level [159, 191, 192].

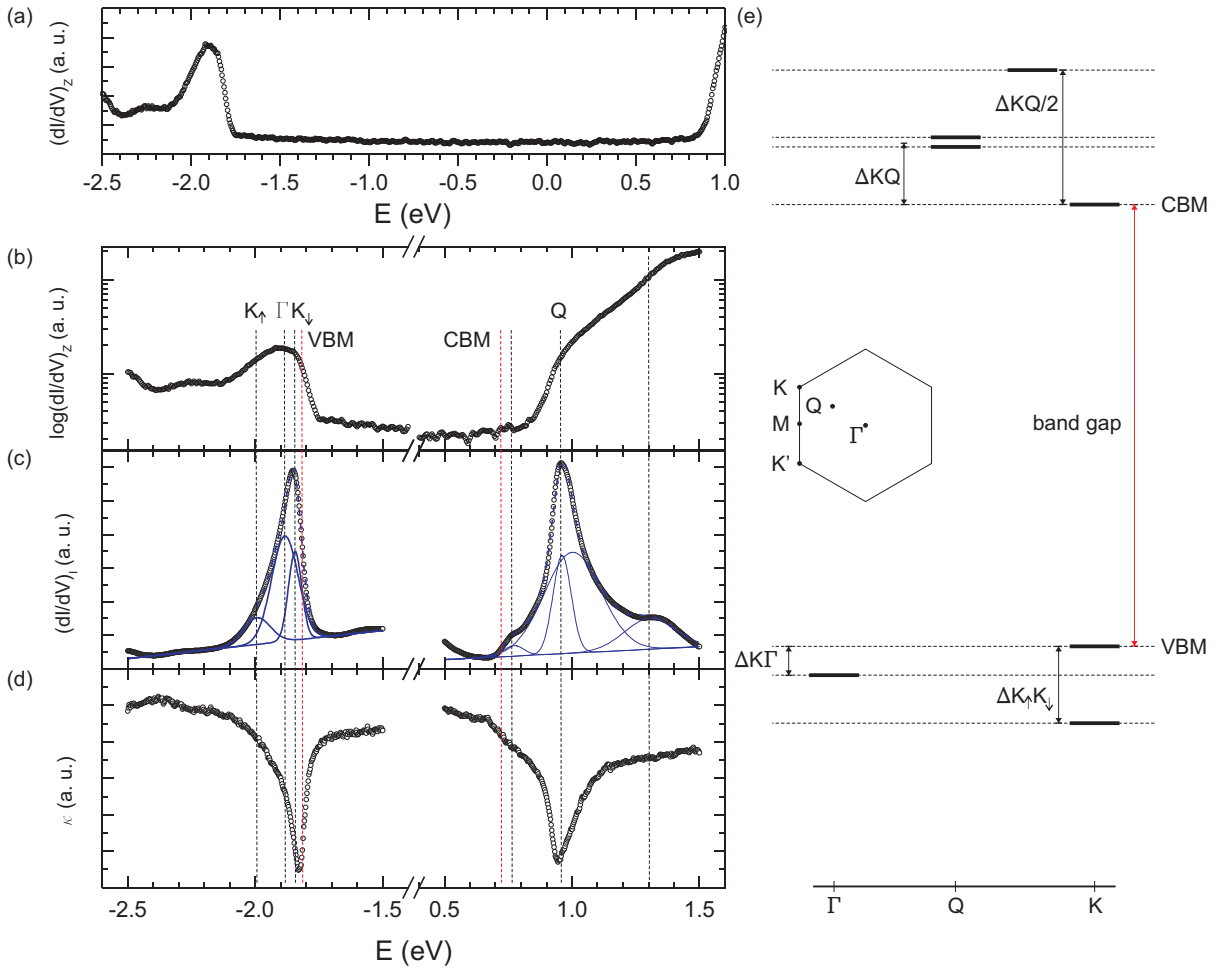


Figure 7.2: Electronic band gap and CPEs of MoS_2: (a) STS spectrum measured in constant height mode in linear scale revealing a band gap which is gated. (b) STS spectrum measured in constant height (log-scale). (c) STS spectra recorded in constant current mode. The peaks in constant current mode are fitted with Gaussian functions and plotted in the figure. The black dashed lines are at the peak positions of the Gaussian functions. The VBM and CBM are visualized with red dashed lines and obtained using the FWHM of the peaks nearest to the band gap. (d) STS spectra representing $\mathrm{d}I/\mathrm{d}z \propto \kappa$ recorded in constant current mode. (e) Sketch of the CPE of MoS_2 extracted from our measurements with the input of DFT calculations [66]. The 1. BZ of MoS_2 with the relevant high-symmetry points is sketched in the inset.

Using constant current STS in the energy ranges of the VBM and CBM enable us to distinguish the CPEs of MoS_2. In this mode, as soon as a new CPE starts to contribute to the tunneling current, the feedback loop retracts the tip to keep the current constant. This leads to a peak for every CPE in the STS spectrum [116]. In Fig. 7.2 (c) we use this technique to probe the various contributions to our spectrum and compare it with the STS spectrum measured in constant height mode shown in Fig.7.2 (b). The spectrum

measured in constant current mode reveals that three components form the broad peak in the occupied states. The Gaussian fits of the components are shown in Fig. 7.2 (c). We attribute them to the three CPE found in the band structure near the VBM that are located at Γ and K [66]. We also find a complex peak structure in the conduction band. Three features are clearly resolved. We add a broad fourth peak to improve the fit. We attribute the three narrow peaks to three CPE located near the CBM [66]. One striking difference between the two STS modes is that there is a small peak appearing at $E = 0.7$ eV in constant current mode that is not visible in constant height mode. We attribute this feature to the states located at K [66], which are strongly suppressed in constant height STS due to their large distance from the Γ point and, consequently, large $k_{||}$.

In addition, we measure the decay constant κ in order to distinguish the location of the states in k-space. In practice this is realized by recording $\mathrm{d}I/\mathrm{d}z \propto -\kappa$ in constant current mode, by applying a modulation voltage to the z-piezo instead of the bias voltage. The result is shown in Fig. 7.2 (d). We find a broad dip in the valence band that is attributed to states near to the Γ point with vanishing $k_{||}$. A strong increase in κ is found at higher negative energies that is attributed to states at K. The minimum of κ seems to correspond to the peak around $E = -1.85$ eV found in constant current mode. This however does not match with the maximum found in constant height that is attributed to Γ states. Since κ has additional contributions from the substrate, especially near the VBM where tunneling between tip and substrate becomes dominant in constant current mode, we link the peak found in constant height to the second peak found in constant current STS and attribute them to the CPE at Γ. The remaining two peaks are then attributed to the spin-split CPE at K.

In the conduction band we find different values for κ at three CPEs, which makes it possible to attribute the peaks to certain locations in k-space. According to DFT calculations [66], the CPE with the highest κ is located at the K point. Hence our peak starting at around $E = 0.725$ eV is attributed to the CPE at K. The smallest κ is found near Q, which is in our case around $E = 0.95$ eV. A reduced κ is found between K and Q, which in our spectrum could represents the peak around $E = 1.3$ eV. Note however that additional extrema appear around these energies between Γ and M, which makes our assignment rather tentative and it would have to be verified with other experimental techniques with k-resolution such as time-resolved ARPES (TR-ARPES).

Repeatedly performing the entire analysis at different locations on the sample enables us to give a good estimate for the location of the different bands, which are listed in Tab. 7.1,

	$\Delta K_\uparrow K_\downarrow$ (eV)	$\Delta\Gamma K$ (eV)	ΔKQ (eV)	$\Delta KQ/2$ (eV)
MoS_2/MLG/Ir(111)	0.16 ± 0.04	0.05 ± 0.01	0.15 ± 0.11	0.53 ± 0.06
MoS_2/graphite [116]			0.25	
MoS_2/Au(111) (ARPES [25])	0.145 ± 0.004	0.31		
MoS_2/Au(111) (STS [171])		0.36		
Freestanding MoS_2 (LDA [34])	0.148	0.05		
Freestanding MoS_2 (G_1W_0 [66])	0.146	0.15	0.19 (0.25)	0.47

Table 7.1: Positions of the CPE in the band structure of MoS_2 on different substrates. Our results for MoS_2/MLG/Ir(111) are compared with MoS_2/graphite, MoS_2 on Au(111) and theoretical calculations for freestanding MoS_2. The value in parenthesis stands for the second (spin-split) band.

together with the values of the related systems MoS_2 on Au(111), MoS_2 on graphite and freestanding MoS_2 calculated with DFT. Similar to Ref. [116], we use the peaks of the fits to compare the positions of the bands and the FWHM of the peaks to measure the top and bottom of the CBM and VBM to avoid an overestimation of the band gap E_G.

We first compare the valence band features with the theoretical calculations based on DFT. The separations $\Delta K_\uparrow K_\downarrow$ and $\Delta\Gamma K$ found in the experiment are in a very good agreement with the calculated band structure of Ref. [34], which uses the local-density approximation (LDA). In Ref. [66], which uses the *GW* approximation, the location of the CPE at Γ is slightly lower than both CPE at K. In contrast, MoS_2 on Au(111) shows only a good agreement for the spin-split $\Delta K_\uparrow K_\downarrow$ in the valence band, which is located in a projected bulk band gap of Au(111) [25]. The difference $\Delta\Gamma K$ is strongly increased due to the non-negligible interaction between MoS_2 and Au(111).

The features of the conduction band have corresponding CPE in the DFT calculation of Ref. [66]. The two spin-split bands near Q located around 0.19 eV and 0.25 eV above the CBM are very close to our feature located at 0.15 eV. Though no spin-splitting is visible in the experiment it may contribute to the larger error compared to the other CPEs. Zhang et al. [116] found a comparable splitting of $\Delta KQ = 0.25$ eV for MoS_2 on graphite. The energy difference $\Delta KQ/2$ is in quantitative agreement with the CPE found between K and Q, though additional CPEs may contribute to this signal. Note that three features are also observed on MoS_2/Au(111) in constant height STS [171], but at different energies ($\Delta E = 0.49 \pm 0.27$ eV and $\Delta E = 0.96 \pm 0.27$ eV with respect to the CBM) and are therefore not comparable to our results.

	VBM (eV)	CBM (eV)	E_G (eV)
Constant height mode (this work)	-1.750	0.825	2.575
Constant current mode (this work)	-1.83 ± 0.02	0.67 ± 0.06	2.50 ± 0.05
MoS_2/graphite [176–178]	$-(1.79 - 1.95)$	$0.26 - 0.45$	$1.90 - 2.45$
MoS_2/Au(111) (TR-ARPES [193])	-1.45	0.50	1.95 ± 0.05
MoS_2/Au(111) (STS [171])	-1.24 ± 0.06	0.50 ± 0.27	1.74 ± 0.27
Freestanding MoS_2 (G_1W_0 [66])			2.84

Table 7.2: Positions and size of the band gap of MoS_2/MLG/Ir(111) obtained in constant height and constant current mode. The results are compared with MoS_2 on graphite, MoS_2 on Au(111) and theoretical calculations for freestanding MoS_2.

The values for the VBM and CBM, together with the resulting band gap, are listed in Tab. 7.2. We find that the band gap is overestimated using constant height mode since the states located at K are missing in the conduction band. Note that the strong contribution of the states at Γ near the VBM lead to the opposite effect there, namely that the VBM is found at higher energies in constant height mode compared to constant current mode. The band gap obtained in constant current mode is more reliable since we see all CPEs in the spectrum, hence we take this value for comparison with other systems. The value of the band gap for MoS_2 on graphene on Ir(111) is more than 0.3 eV smaller than the calculated band gap for freestanding MoS_2, which is attributed to the small (but finite) contribution of the dielectric environment due to the substrate that is known to reduce the electronic band gap of TMDCs [24]. The size and shift of the band gap are very similar to the findings for MoS_2 on graphite, which leads us to conclude that graphene acts as an inert substrate and strongly suppresses the interaction between MoS_2 and Ir(111). The band gap of MoS_2 on Au(111) is much smaller than for free-standing MoS_2, as measured with TR-ARPES [193] and STS [171]. The reduction is again attributed to the interaction between MoS_2 and Au(111), leading to a strong band gap renormalization [171]. Note that an even smaller band gap of 1.39 eV is measured with ARPES in potassium doped MoS_2/Au(111) with ARPES [25], which is possibly an effect of the chemical gating that is used to shift the conduction band under the chemical potential.

7.3 Band bending near defects

We now investigate the electronic properties of our MoS_2 flakes near highly symmetric defects, starting with mirror twin boundaries (MTB). Fig. 7.3 (a) shows an STM image

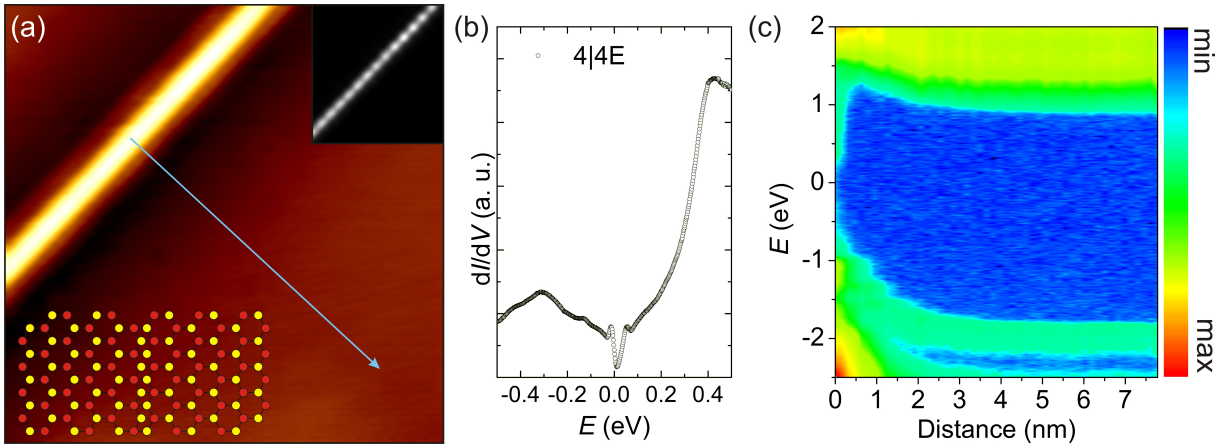


Figure 7.3: Constant height STS spectra near a 4|4E MTB in MoS_2: (a) STM image of a 4|4E MTB (U = 0.9 V, I = 0.2 nA, image size 10 × 10 nm^2). The structure of the line defect is sketched in the image. The inset in the top right shows the periodic modulation of the CDW measured in constant height. The arrow denotes the path of the tip during acquisition. (b) Averaged STS spectra measured along the MTB. We find a strongly reduced band gap. (c) Corresponding constant height STS line scan starting at the MTB and ending at defect-free MoS_2. The intensity is shown in log-scale. The bands are bending towards higher energies. New states appear in the vicinity of the MTB.

in which a bright line is visible. As is shown in detail in Chap. 8 this is likely caused by a 4|4E MTB. Its structure is sketched in the inset of Fig. 7.3 (a) and consists of two crystals (grains) with different orientations which form a line defect along the mirror plane between the two. STS spectra measured in constant height on the MTB show an extremely reduced band gap of 50 meV around the Fermi energy, see Fig. 7.3 (b). This gap is likely caused by a CDW transition, leading to a periodic beating in the density of states as shown in the upper right inset of Fig. 7.3 (a). The charge density wave will be topic of Chap. 8. Above the transition temperature of the CDW we expect a metallic edge state along this MTB, which would lead to a one-dimensional metal-semiconductor interface.

We can measure the evolution of the band gap from MoS_2 towards the MTB by recording STS spectra along the arrow shown in Fig. 7.3 (a), starting on the MTB and ending on MoS_2. The resulting STS spectra are shown in Fig. 7.3 (c). The blue region represents the band gap with vanishing density of states. We see a sharp increase in the band gap after less than 1 nm, underlying the true one-dimensionality of the states in the MTB. At a distance of 1 nm from the MTB we already find a band gap of more than 2 eV. It is still reduced compared to the band gap measure far away from the MTB. Going further away from the MTB, we can clearly see a bend bending towards lower energies in both

the conduction and valence band. This observation is very similar to the findings between ML and BL $MoSe_2$ [181]. The bend bending is continuous in the conduction band, while it seems to occur stepwise in the valence band. The abrupt changes in the occupied states could be attributed to additional interface states which were also observed at the zigzag boundary between ML and BL $MoSe_2$ [181]. The STS spectrum of defect-free MoS_2 is recovered at a distance of around 5 nm from the MTB.

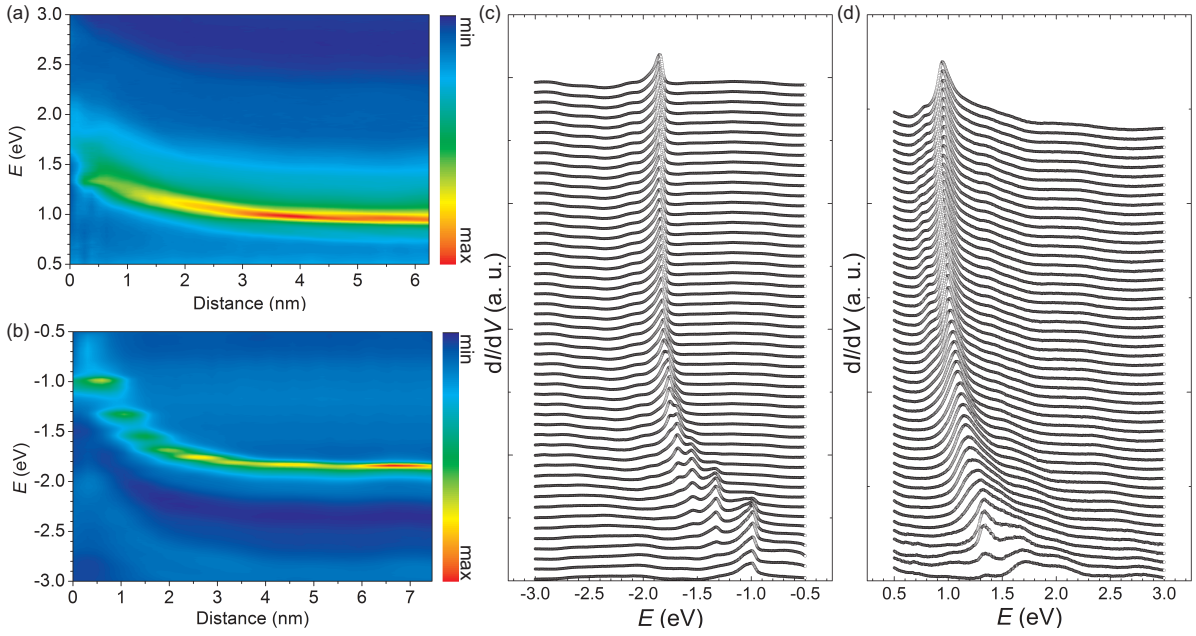


Figure 7.4: Constant current STS spectra measured near a 4|4E MTB in MoS_2: (a)-(b) STS scans of empty and occupied states measured at the same location as in Fig. 7.3. The intensity is shown in linear scale. We find a smooth band bending of the unoccupied states and a stepwise increase in energy of the occupied states. (c)-(d) Same set of STS spectra presented from top (defect-free MoS_2) to bottom (MTB) to highlight the band bending and appearance of additional states near the MTB.

We complement our constant height measurements with constant current STS spectra to track the evolution of the bulk bands towards the MTB. The result is shown in Fig. 7.4. The data is taken at the same location as in Fig. 7.3. The conduction band of MoS_2 is the dominant contribution in the spectra measured at positive energies, see Fig. 7.4 (a). We can track its location from the MTB towards MoS_2. The band bending occurs in a range from 0.5 nm to 5 nm. One finds a decrease of the valence band minimum from $E = 1.3$ eV (at the MTB) to $E = 0.7$ eV (far away from the MTB). Fig. 7.4 (b) shows the spectra measured at negative energies, starting again at the MTB. In agreement with our

constant height spectra we find a stepwise decrease in the local density of states instead of a smooth transition as found for the conduction band.

The different behavior observed between conduction and valence band is best visualized in Fig. 7.4 (c)-(d), which show the complete set of data measured from the MTB (bottom) towards MoS_2 (top) in constant current mode. The same set is (partially) displayed in Fig. 7.4 (a)-(b). Fig. 7.4 (c) shows the spectra measured at negative energies. We find that the spectra near to the MTB (bottom) are dominated by interface states between the MTB and MoS_2, which appear at fixed energies. Five energy steps are clearly resolved in Fig. 7.4 (c) and Fig. 7.4 (b) (two are located near to the original valence band of MoS_2). The interface states next to the MTB seem to be confined in a narrow area of less than 1 nm. Due to the similar spectral shape compared to bulk ML MoS_2, these interface states may still have a very similar structure to MoS_2, which would however lead to a stepwise bend bending, an observation that has not been reported so far to our knowledge. In contrast, the spectra recorded at positive energies which are displayed in Fig. 7.4 (d) show a smooth transition between MTB and MoS_2 that can be attributed to bend bending. In addition, we find that the peak shape of the unoccupied states changes when approaching the MTB, which may be due to the states of the MTB or variation in band bending depending on the CPEs. The latter could lead to a band gap transition from direct to indirect near the MTB, an interesting concept that could be modeled with DFT.

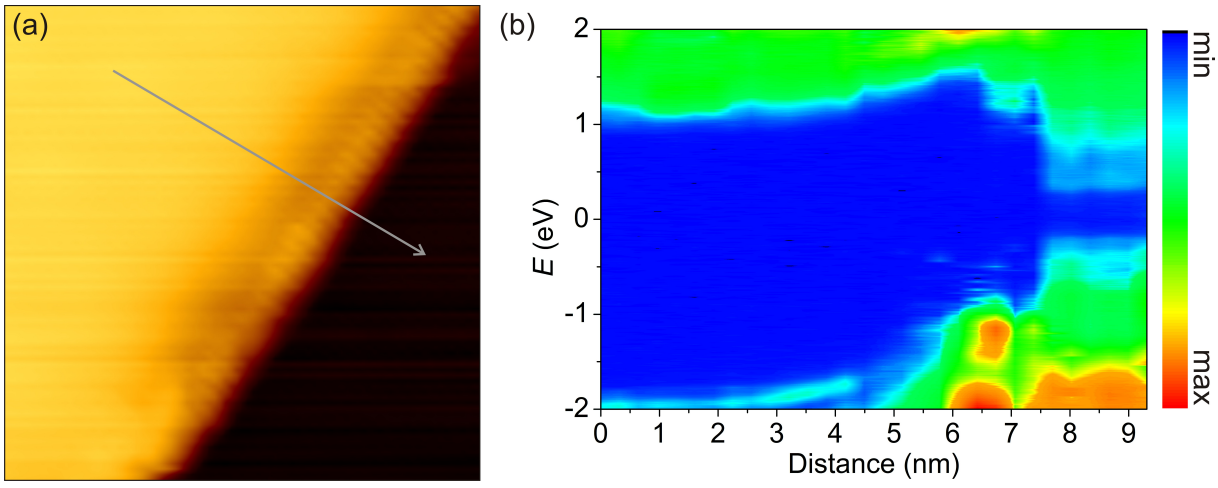


Figure 7.5: Constant height STS spectra along MoS_2 zigzag boundary: (a) STM image of a zigzag MoS_2 edge ($U = 1.5$ V, $I = 0.1$ nA, image size 10×10 nm^2). The periodicity at the edge corresponds to the lattice constant of MoS_2. The arrow denotes the position of the tip during acquisition. (b) STS spectra (log-scale) measured along the edge, starting on MoS_2 and ending on graphene on Ir(111).

We next analyze the changes in the density of states at zigzag edges of MoS_2. Since the flakes have hexagonal instead of triangular shapes, our sample shows no preference for either Mo or S edge termination on graphene on Ir(111), in contrast to MoS_2 on Au(111) where one edge termination is clearly preferred [194]. Fig. 7.5 (a) shows a zigzag edge at the rim of a MoS_2 flake. The periodic variation visible in the STM image corresponds to the lattice constant of MoS_2. The structure of the edge resembles other quasi-freestanding edges such as MoS_2 [170], graphene [195] or graphene-boron nitride zigzag interfaces [196]. Constant height STS spectra measured along the arrow sketched in the figure are shown in Fig. 7.4 (b). Similar to the behavior near MTBs, we find that band bending occurs in the valence and conduction band towards higher energies when approaching the termination of the flake. While additional states appear in the conduction band (between $1 - 1.5$ eV) that are localized at the edge of MoS_2, we are unable to disentangle the contributions from the bulk and edge in the valence band. In contrast to the MTB, we find a persisting band gap, which is reduced to 1.4 eV. The depletion length is around 5 nm, thus very similar to the depletion length at MTBs. Passing the edge of MoS_2 (at around 7 nm), the spectra show the typical shoulder at -0.2 eV arising from the Ir(111) surface state. The band bending is very similar to STS spectra measured at the edge of ML MoS_2 on graphite [176].

7.4 Manipulating the substrate interaction via doping

The fact that we are able to grow epitaxial MoS_2 on graphene on Ir(111) not only gives us the opportunity to measure the fundamental electronic properties of MoS_2, but also enables us to tailor those by manipulating graphene. One way to do this is via intercalation, which is known to change the chemical potential [128], work function [53], core level [197] and binding [198] of graphene.

We demonstrate the capability to manipulate the electronic properties of MoS_2 by intercalating Eu under graphene before MoS_2 growth. Eu is very stable under graphene [128], such that it does not desorb at the elevated temperatures used to grow MoS_2. STM images with and without Eu intercalation are shown in Fig. 7.6 (a)-(b), respectively. We see that Eu forms small islands next to MoS_2.

Constant height STS spectra measured on MoS_2 with and without Eu intercalation are compared in Fig. 7.6 (c)-(d) in linear and log-scale, respectively. Though we find a large band gap in both cases, changes in the $\mathrm{d}I/\mathrm{d}V$ signal are visible. The band gap shifts after Eu intercalation towards negative energies, which is attributed to the charge that

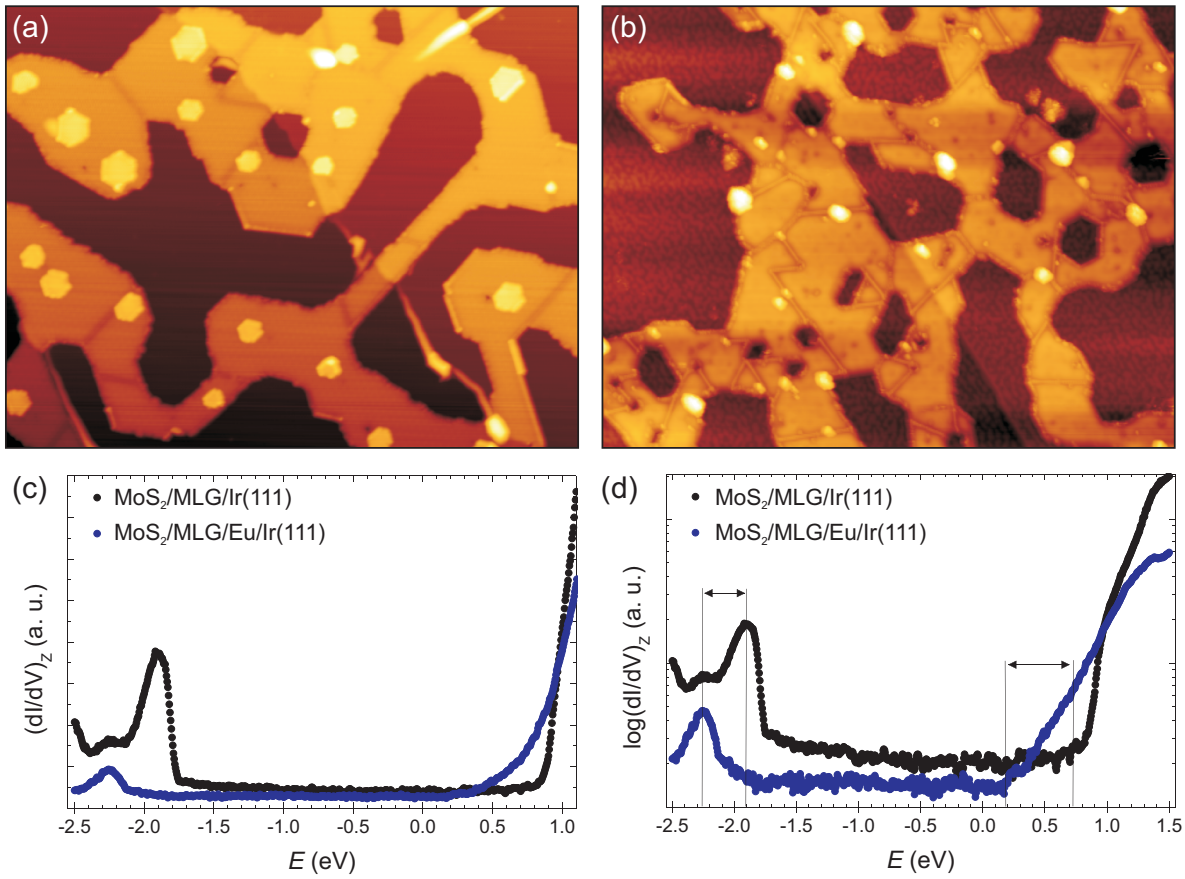


Figure 7.6: Tuning the substrate interaction: (a) STM image of MoS_2 on graphene on Ir(111) without Eu intercalation ($U = 1.5$ V, $I = 0.01$ nA, image size 135×175 nm^2). (b) STM image of MoS_2 with Eu intercalation ($U = 0.9$ V, $I = 0.02$ nA, image size 135×175 nm^2). (c) Constant height $\mathrm{d}I/\mathrm{d}V$-spectra of MoS_2 on neutral graphene (red) and strongly doped graphene (blue). (d) The log-scale analysis shows a shift and reduction of the band gap after Eu intercalation.

Eu transfers to its surrounding. In general this charge shifts the chemical potential up, thus gating the 2D material, as reported for graphene [54, 128], boron nitride [199], or MoS_2 on Au(111) [25]. In the case of Eu intercalated graphene, the chemical potential is shifted up by more than 1 eV [128], which is much more than the shift observed for Eu intercalated under MoS_2 on graphene, see Fig. 7.6 (b). The difference can be explained with the larger distance between MoS_2 and Eu and the screening from graphene between the two.

Another finding visible in Fig. 7.6 (b) is that the band gap reduces upon intercalation. By comparing the shifts of the VBM ($\Delta E = 0.35$ eV) and the CBM ($\Delta E = 0.55$ eV), one finds a strong reduction of 0.2 eV in the electronic band gap. A similar finding is reported for $MoSe_2$ [24], where the authors compared the band gap of $MoSe_2$ on bilayer graphene

with $MoSe_2$ on graphite. They found a difference of 0.22 eV in the band gap between the two substrates and attributed it to changes in the density of states of the substrate at the chemical potential. This argument can be verified with our system; graphene on Ir(111) is almost undoped. This leads to reduced screening due to the vanishing DOS at the Dirac energy near to the chemical potential [32]. Doping graphene with Eu however shifts the Dirac energy away from the chemical potential, leading to an enhancement of the DOS under MoS_2 and hence to a more efficient screening environment, which leads to a strong renormalization of the electronic band gap of MoS_2. This nicely demonstrates that manipulating the density of states of the substrate strongly affects the electronic properties of MoS_2.

7.5 Discussion

The band structure of epitaxial MoS_2/MLG/Ir(111) shows very good agreement with theoretical calculations of freestanding MoS_2, which points to a weak interaction between graphene and MoS_2 together with a negligible contribution from Ir(111). This is in stark contrast to MoS_2 on Au(111), where especially the valence band near to the Γ point shows strong deviations from freestanding MoS_2. The size of the band gap is comparable to the related system MoS_2 on graphite, confirming our statement that MoS_2 is decoupled from the metal underneath and mainly influenced by graphene. Our slightly larger value for the band gap can be attributed to the smaller density of states of graphene compared to graphite [24], together with the difficulties to obtain the band gap of MoS_2 using constant height STS only. The fact that our band gap is still considerably smaller than the theoretical band gap of 2.8 eV for freestanding MoS_2 reveals that there is still rather efficient screening from our substrate, which could be reduced for example by opening a band gap in graphene via intercalation.

MoS_2 on graphene on Ir(111) is gated, while graphene on Ir(111) is essentially undoped. This leads to the conclusion that charge redistribution is not responsible for the shift of the chemical potential of MoS_2. A similar gating is found for MoS_2 on graphite, which also represents a weakly interacting system without considerable charge transfer. We hence attribute the gating to the work function difference between graphene and MoS_2, which leads to band bending to adjust the chemical potential. While band bending at the interface between a semiconductor and a metal is well known for 3D materials, here the whole material volume is at the interface, leading to a *global* band bending. The work functions of graphene/Ir(111) (4.65 ± 0.10 eV [200]) and HOPG (4.80 eV [201]) are

comparable, so we expect a similar shift of the MoS_2 band gap. In the case of graphene on Ir(111), using the electron affinity of MoS_2 (3.92 eV [202]), one expects the CBM to be at CBM $= (4.65 - 3.92)$ eV $= 0.73$ eV, in very good agreement with our experimental value of 0.67 ± 0.06 eV. This supports our assignment that the different work functions are the main cause for the gating of MoS_2 on graphene on Ir(111). One should however bear in mind that the different shapes of conduction and valence band may also vary the position of the chemical potential.

While there is a global gating in MoS_2, we find additional band bending near one-dimensional defects such as MTB and zigzag edges. The bending in MoS_2 is towards higher energies for both line defects. At 4|4E MTBs, we find that the band bending occurs stepwise in the valence band, while a continuous band bending is observed in the conduction band. Additional interface states are strongly localized within the line defect. The edge states at zigzag edges of MoS_2 have comparable characteristic features to those observed at BL WSe_2 and $MoSe_2$ zigzag edges [181]. The new interface leads to a large depletion length of around 5 nm which is further evidence for the poor screening of the substrate, and is comparable to the depletion length of 10 nm (3-4 nm) found at the zigzag edges of BL WSe_2 ($MoSe_2$) on HOPG [181].

The possibility to tailor the electronic properties of MoS_2 via intercalation is demonstrated with Eu intercalation as a proof of principle experiment. We find that charge induced in graphene leads to band gap renormalization and charge redistribution, similar to the comparison of $MoSe_2$ on BL graphene and graphite [24]. However, our measurements have the big advantage that the chemical environment of MoS_2 is maintained, leaving no space for alternative explanations of these findings.

7.6 Conclusions

In conclusion, we are able to measure the electronic properties of epitaxial MoS_2 on graphene on Ir(111) using constant current and constant height STS. We find several CPEs near the VBM and CBM and attribute them to the corresponding bands known from density functional theory calculations. The good overall agreement let us conclude that graphene effectively decouples MoS_2 from Ir(111), making it *quasi-freestanding*. We demonstrate how one can control the electronic properties of MoS_2 with defects or by manipulating the backside of graphene via intercalation and envision that graphene on Ir(111) can become a model system to study the fundamental properties of MoS_2 and other epitaxial TMDCs.

CHAPTER 8

Charge density waves in mirror twin boundaries of molybdenum disulfide

This chapter contains contributions from W. Jolie, C. Murray, J. Hall, F. Portner, P. Weiß, N. Atodiresei, C. Busse, H.-P. Komsa, A. Krasheninnikov, A. Rosch, and T. Michely. W. Jolie proposed the experiment, motivated by the recent work of Barja et al. [27] and Ma et al. [28] on MTBs in $MoSe_2$. C. Murray and W. Jolie prepared the samples using the recipe of Ref. [118]. C. Murray and W. Jolie collected and analyzed the data. H.-P. Komsa and A. Krasheninnikov provided DFT calculations. All results were discussed with W. Jolie, C. Murray, J. Hall, F. Portner, P. Weiß, N. Atodiresei, C. Busse, H.-P. Komsa, A. Krasheninnikov, A. Rosch, and T. Michely.

8.1 Motivation

Electrons confined in one dimension are predicted to behave very differently from states in two or three dimensions, showing exotic physical phenomena such as spin-charge separation [203–205] and other Tomonaga-Luttinger liquid properties [206]. Line defects such as edges and grain boundaries in group-VI ML TMDCs are predicted to host one-dimensional metallic states embedded in an otherwise insulating surrounding [207–210], representing a model system for studies using surface sensitive methods. On top of the metallic behavior, these line defects are also predicted to exhibit magnetic properties, in contrast to their non-magnetic ML [211–213], that could explain experimental results in MoS_2 [214], and may host bound states such as Majorana fermions [215].

Different kinds of line defects can be found in TMDCs, which often host one-dimensional, metallic states. Bollinger et al. [170] found metallic edge states in MoS_2 flakes on Au(111), which can be used for catalytic reactions [216]. Edge states were shown to affect the band gap of TMDC MLs due to formation of a narrow-gap quantum wire as reported for MoS_2 on graphene on Au(111) [174] and MoS_2 on graphite [181]. A spatial modulation at edges of MoS_2 nanoribbons on Au(755) and Au(100) has also been reported [217, 218], which has been found to be stress-induced due to the MoS_2-Au interaction. The drawback of edges, however, is the lack of protection from passivation, which influences the electronic properties of edge states [211]. Hence it would be highly favorable to have one-dimensional states embedded in a line defect between two grains. These states would be protected by the surrounding TMDC ML. Such a situation is present at a mirror twin boundary (MTB) in TMDCs, in which the metallic states are confined between two grains rotated by 60° with respect to each other, leading to a mirror plane parallel to the line defect. It was shown recently for $MoSe_2$ [27, 28] that the metallic states within MTBs are electronically unstable, undergoing a Peierls transition which leads to a commensurate CDW at low temperatures. The CDW state is characterized by (i) a CDW gap opening in the LDOS at the Fermi energy, (ii) a periodic beating of the LDOS along the MTB and (iii) a phase-shift of π in real space between the highest occupied states and the lowest unoccupied states. All of these features were confirmed for the one-dimensional states in $MoSe_2$ MTBs, with a CDW gap of $2\Delta = (100 \pm 40)$ meV and a CDW periodicity of three times the lattice constant of $MoSe_2$ [27]. DFT confirmed the CDW scenario by intentionally introducing a small lattice distortion along the MTB, resulting in a near perfect match of the LDOS between theory and experiment [27].

While only one type of MTB (4|4P) is observed in $MoSe_2$ and $MoTe_2$ which form a dense network during growth [29, 30] due to their low formation energy [72], various TEM studies have identified additional MTBs in TMDCs [73, 185, 186, 219, 220], with some variation in the MTB structure depending on the type of TMDC and the physical origin of the MTB formation. A promising material is MoS_2, which hosts two different types of MTBs (4|4P and 4|4E) that originate from grain merging. There is, however, no report on the formation of CDWs in MoS_2 MTBs so far.

This chapter is devoted to the electronic properties of the states confined in MoS_2 MTBs on graphene on Ir(111). Two kinds of CDWs are observed and characterized at low temperatures ($T = 5$ K). STM and STS in constant current and constant height mode are used to identify the electronic fingerprints of these states with a focus on the CDW gap, phase behavior, inelastic excitations, confinement, role of defects and doping. The

experimental results are supported by DFT calculations for the two kinds of MTBs to link the MTB structure to its corresponding electronic properties. Finally, these insights are then used to control and even manipulate the CDWs, demonstrating the capability to choose the desired parameters of the MTB which change the one-dimensional system accordingly.

8.2 Identifying charge density waves

Our system is composed of the vdW heterostructure MoS_2/graphene/Ir(111). Details on the structure and growth of MoS_2 on graphene/Ir(111) can be found in Ref. [118] and in Chap. 4.2. The electronic properties of the semiconducting MoS_2/graphene/Ir(111) are subject of Chap. 7. A large scale constant current STM image of MoS_2/graphene/Ir(111) is shown in Fig. 8.1 (a). The Ir(111) substrate is completely covered with graphene. In addition to Ir(111) step edges and small graphene wrinkles one can identify large MoS_2 patches with small bilayer islands on top. Grain boundaries emerge upon MoS_2 growth when two MoS_2 grains with different orientations meet. The most common misalignment is close to 60° due to the epitaxial growth of MoS_2 on graphene on Ir(111), with only small scatter around the $R0°$ orientation observed in the corresponding LEED pattern. As shown in Appendix C, both grains have parallel dense-packed rows, leading to the conclusion that these line defects are MTBs. We find that small angle grain boundaries with angle up to 8° still form MTBs, though their characteristic length decreases with increased misalignment as expected for small angle grain boundaries [185]. Note that we also observe various grain boundaries that are not formed between two mirrored grains rotated by 60°, but those will not be discussed in this chapter. MTBs appear high in constant current STM images when the bias voltage is set close to or within the band gap of MoS_2, a first hint for the different electronic nature of the states confined along these one-dimensional line defects.

We can make use of the poor conductivity of MoS_2 ML within its band gap to measure the signal coming solely from the grain boundaries using constant height STM. Fig. 8.1 (b) shows a constant height image measured over two MoS_2 islands with a grain boundary in between. It was taken at a bias voltage higher than the start of the CBM of MoS_2, so that the dominant contribution to the tunneling current stems from the states of MoS_2. The superstructure arises from the graphene on Ir(111) moiré. Note that the graphene/Ir(111) which surrounds the two MoS_2 islands is not visible in constant height mode due to the increased distance between surface and tip. Fig. 8.1 (c) shows a constant

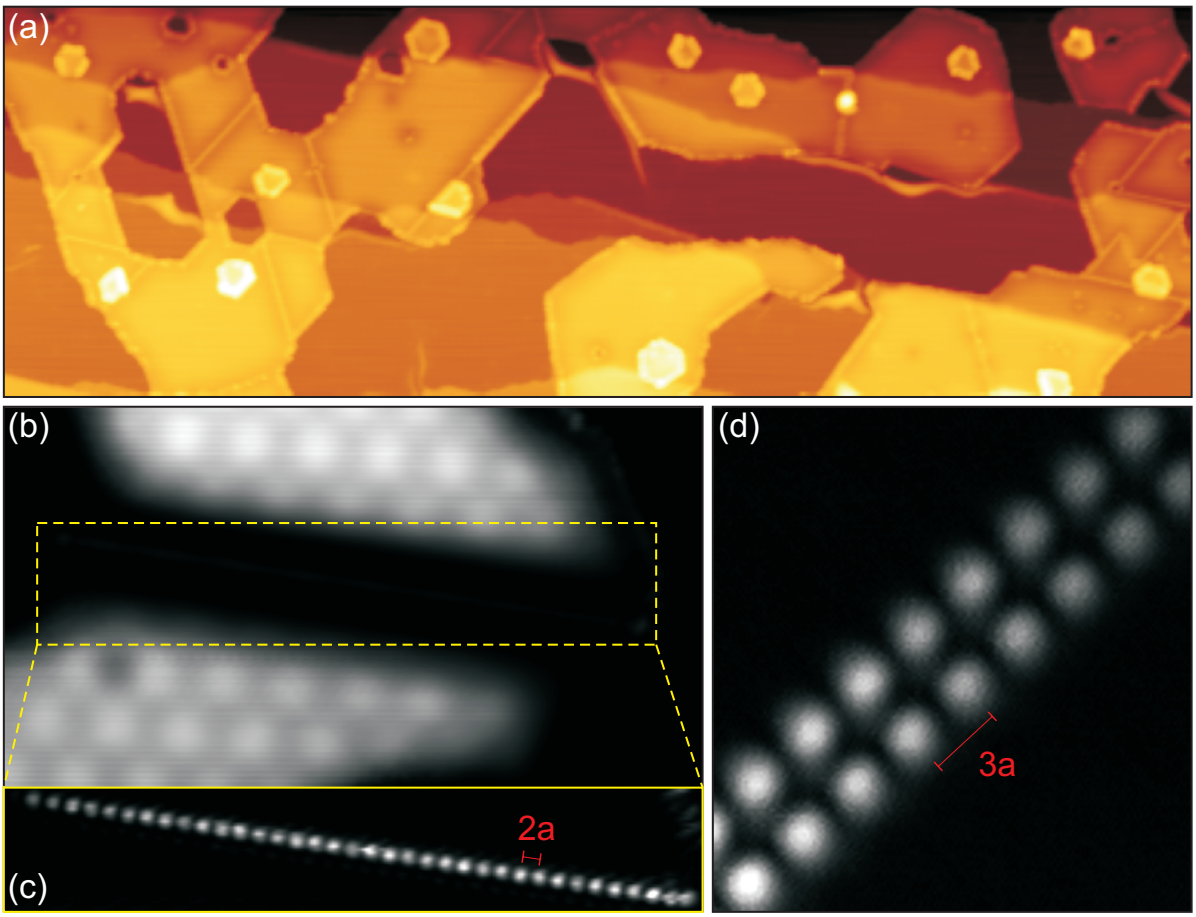


Figure 8.1: CDWs in MoS_2 grain boundaries: (a) Constant current STM image of MoS_2/graphene/Ir(111) (U = 0.9 V, I = 0.03 nA, image size 241 × 78.6 nm^2). We find large MoS_2 ML islands with a small fraction of MoS_2 bilayer. Line defects are observed as bright lines between grains of different orientations. (b) Constant height STM image of two MoS_2 grains measured at high bias voltage (U = 1.25 V, image size 26.3 × 19 nm^2). The tunneling current is dominated by MoS_2 bulk states with a periodic modulation from the graphene/Ir(111) moiré. (c) Constant height STM image measured at low bias voltage (U = 0.1 V, image size 23 × 4 nm^2). The tunneling current stems from the metallic states along the grain boundary, showing a beating with period twice the lattice constant of MoS_2. (d) Constant height STM image of a MTB showing a beating with period three times the lattice constant of MoS_2 (U = 0.006 V, image size 6.2 × 6.5 nm^2).

height image of the same grain boundary when applying a low bias voltage. Now the current is dominated by the states within the MTB while tunneling of MoS_2 bulk states is suppressed at these small voltages due to its semiconducting nature, leading to the conclusion that the band gap has to be drastically reduced at the MTB. A more striking finding is that the constant height image reveals a periodic beating along the MTB with a

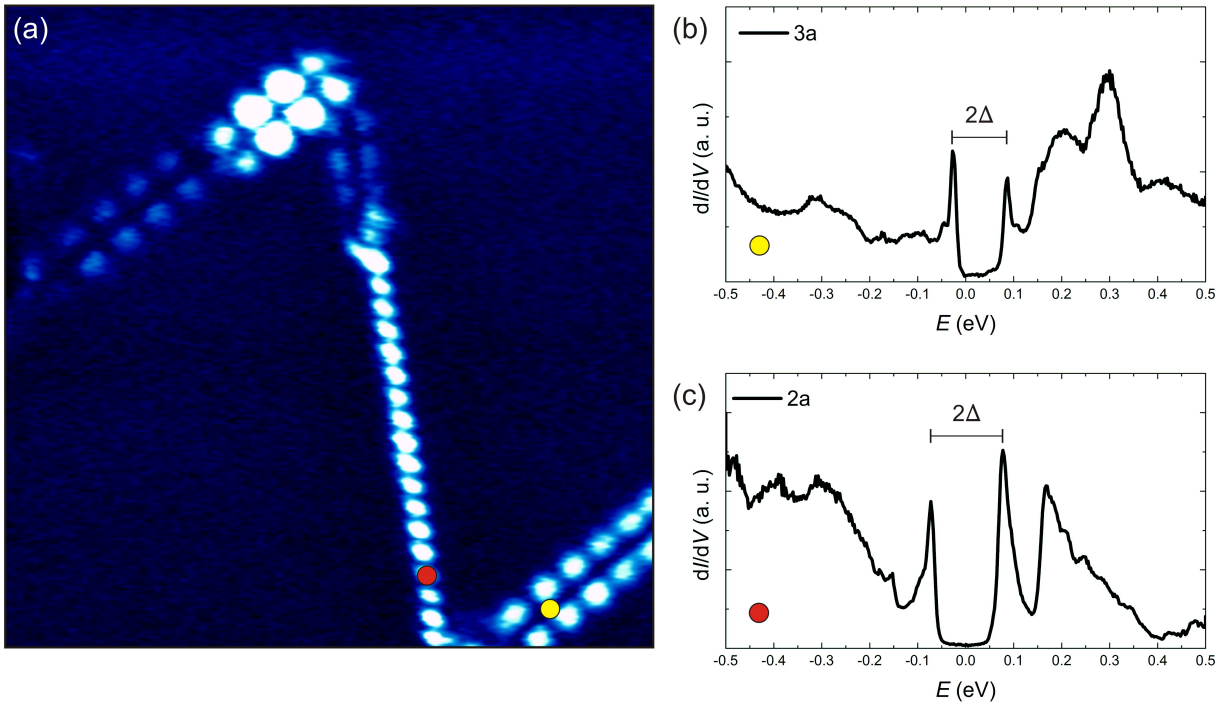


Figure 8.2: MTBs in MoS_2: (a) STS map measured on MTBs featuring both kind of CDWs ($U = 0.1$ V, image size 17×17 nm^2). (b) STS spectrum taken on one of the $3a$ CDWs showing a CDW gap 2Δ at the Fermi energy ($U_{\mathrm{stab}} = 0.5$ V, $I_{\mathrm{stab}} = 0.1$ nA). The yellow dot indicates the position of data acquisition. (c) STS spectrum taken on the $2a$ CDW ($U_{\mathrm{stab}} = 0.5$ V, $I_{\mathrm{stab}} = 0.1$ nA). It also shows a CDW gap 2Δ. The red dot indicates the position of data acquisition.

period of $2a$ (with $a \approx 0.315$ nm being the in-plane lattice constant of MoS_2). Though this is the most common periodicity that we find in MTB on MoS_2, we also observe a double-line structure along some of the MTBs with a periodic beating of $3a$, see Fig. 8.1 (d). We define the two electronic structures along MTBs as $2a$ and $3a$ CDWs, which will be justified below. The $3a$ CDW resembles the CDW found in $MoSe_2$ MTBs [27], while the $2a$ CDW has not been reported to the best of our knowledge.

STS can give more insights into the electronic structure of the states embedded in MoS_2 MTBs. Fig. 8.2 (a) shows an STS map of a complex MTB forming kinks with a characteristic angle close to 120°. Both kinds of CDWs ($2a$ and $3a$) are formed along this grain boundary. An STS spectrum measured on one of the $3a$ CDWs is shown in Fig. 8.2 (b). The yellow dot in Fig. 8.2 (a) indicates the position of the tip during data acquisition. The first stricking finding is that the DOS is finite within the bulk band gap of ML MoS2, which range from $E = -1.83$ eV to $E = 0.67$ eV, see Chap. 7. These states can be found on the MTB only. In addition, the STS spectrum reveals a pronounced gap denoted 2Δ at

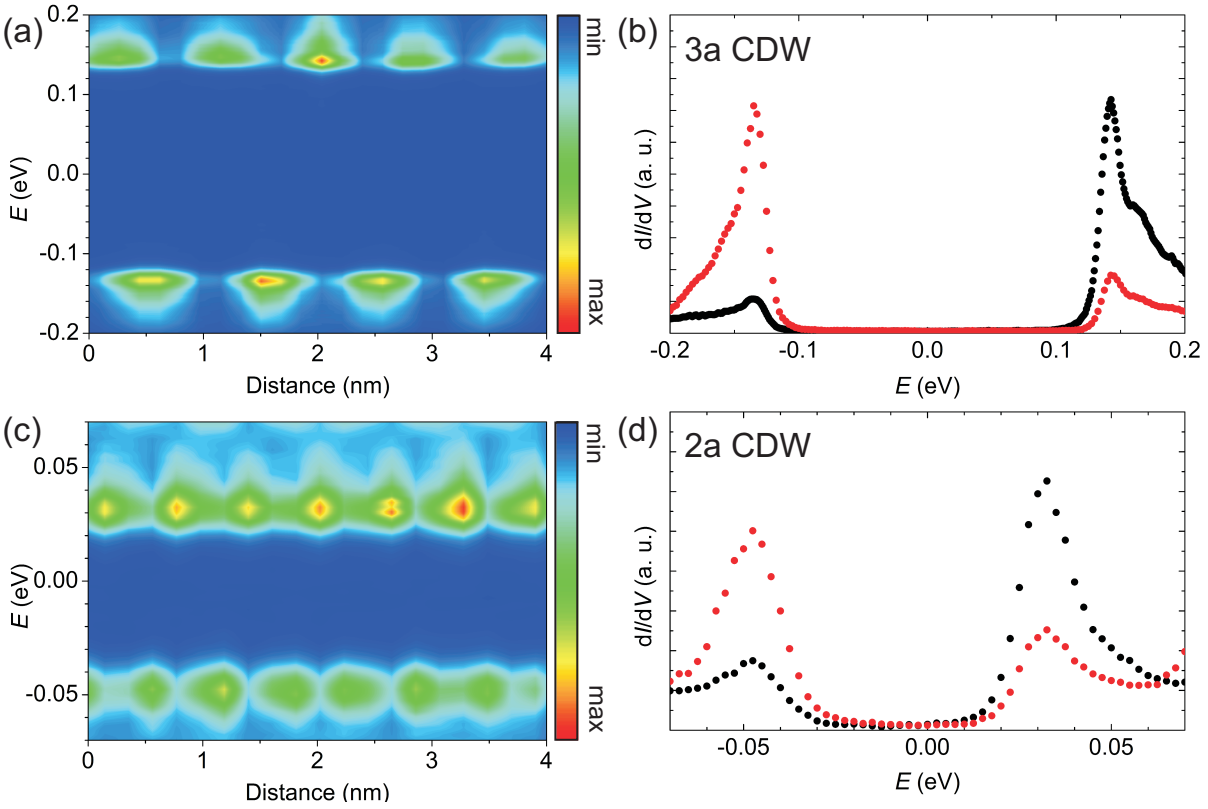


Figure 8.3: Localization of the CDW states in MoS_2: (a) A set of STS spectra measured along a $3a$ CDW (U_{stab} = 0.5 V, I_{stab} = 0.1 nA). The y-axis represents the energy E, the x-axis distance, and the colors the $\mathrm{d}I/\mathrm{d}V$-intensity. The two peaks separated by the gap are out-of-phase. (b) STS spectra taken on a $3a$ CDW at the (real space) locations of the state above (black) and below (red) the Fermi energy, respectively. (c) A set of STS spectra measured along a $2a$ CDW (U_{stab} = 0.5 V, I_{stab} = 0.1 nA). (d) STS spectra taken on a $2a$ CDW at the (real space) locations of the state above (black) and below (red) the Fermi energy, respectively.

the Fermi energy that is separated by two sharp peaks with additional satellite peaks. Two pronounced features are found in the unoccupied states. The spectrum is very similar to STS spectra measured on $3a$ CDWs in $MoSe_2$ MTBs [27]. Fig. 8.2 (c) shows a spectrum taken on a $2a$ CDW at the location marked with a red dot in Fig. 8.2 (a). The main features in the LDOS are again two peaks that are separated by a pronounced gap located at the Fermi energy. Note that the gaps found on the $2a$ and $3a$ CDW in MoS_2 are an order of magnitude smaller than the band gap of ML MoS_2, see Chap. 7. The large band gap of MoS_2 confines these one-dimensional states along the MTB, similar to the confinement of surface states at metal surfaces due to their location in the projected bulk band gap [110].

STS spectra measured along MTBs can track the real space location of the features found in the STS spectra on the atomic scale. A set taken along a MTB featuring a $3a$ CDW is shown in Fig. 8.3 (a). The colors indicate the $\mathrm{d}I/\mathrm{d}V$-intensity as a function of position and energy, respectively. The two peaks located above and below the Fermi energy are strongly localized along the MTB, with a peak-to-peak distance of around $3a$. These findings explain the $3a$ modulation visible in STM images. Furthermore, it reveals that these two peaks are not located at the same position in real space; They are localized out-of-phase with respect to each other. This is best visible when comparing two spectra measured at out-of-phase positions, see Fig. 8.3 (b). The black spectrum is taken at the position of the unoccupied state, which is where the occupied state is suppressed the most. The situation is reversed at the location of the occupied state, which is the red spectrum in Fig. 8.3 (b), emphasizing the high degree of localization. Similar findings are found when measuring STS spectra on $2a$ CDWs. In Fig. 8.3 (c) we find a period of $2a$ in the LDOS at the energies corresponding to peaks near the gap, hence they are responsible for the periodic beating in $2a$ CDWs. Their out-of-phase localization in space is shown in Fig. 8.3 (d), which shows two spectra of the set that are separated by a. In summary, the beating pattern observed in STM images along MTBs in MoS_2 is induced by the first occupied and unoccupied states along the MTB, which form an out-of-phase beating pattern with respect to each other far away from the edges of the MTB.
All these findings (periodic beating in real space, gap in the LDOS with out-of-phase states at the gap energies) can be explained with the formation of CDWs in MoS_2 MTBs: a Peierls-like distortion of the lattice opens a CDW gap 2Δ at the Fermi energy, leading to a reduced Brillouin zone that gives rise to standing waves with the corresponding periodicity. The states above and below the Fermi energy have the same wave vector k_F but different energies, resulting in the out-of-phase behavior in real space. This effect is analog to the phase behavior of the wave functions at the Brillouin zone boundaries, leading to an energy gain or cost depending on their location with respect to the ion cores [221].

8.3 Density functional theory calculations of mirror twin boundaries in molybdenum disulfide

DFT is a powerful method to obtain the structural and electronic properties of materials. In the case of MTBs in MoS_2, a computational model with a ribbon-like geometry is used, see Fig. 8.4 (a)-(b). Two MTBs are expected to form upon grain merge in MoS_2 [72], so

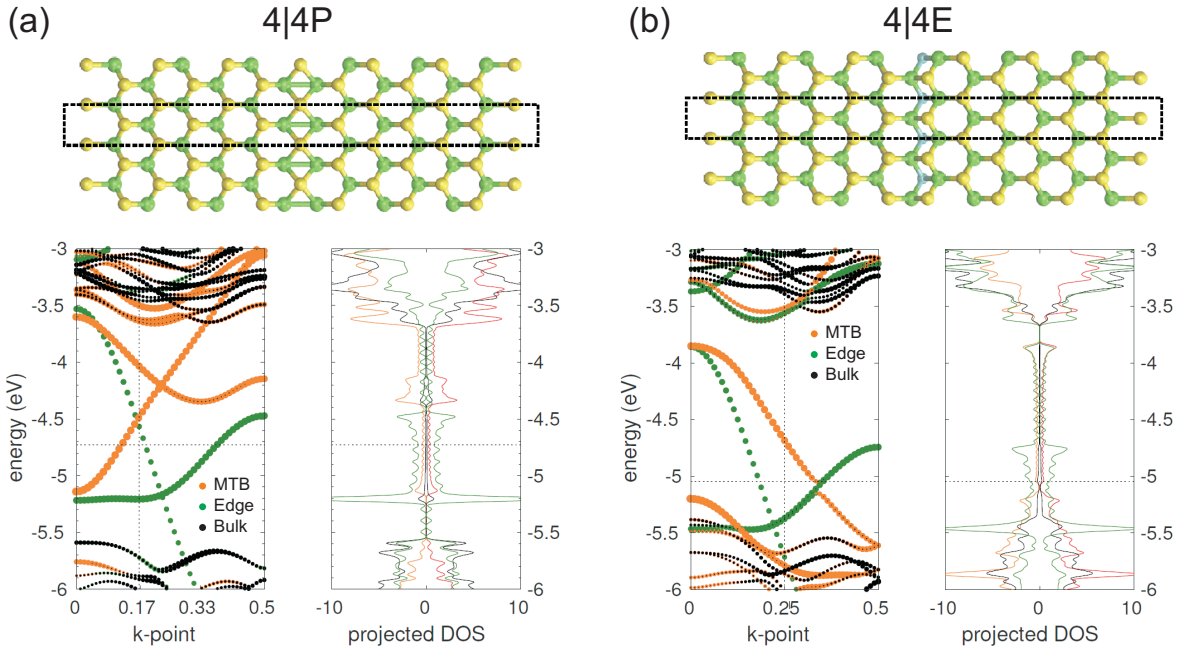


Figure 8.4: DFT calculations of MTBs in MoS_2 [222]: (a) Atomic structures for the whole ribbon model exposing two edges and a 4|4P MTB. Metal atom (green), chalcogen atom in top layer (yellow) or bottom layer (cyan) are shown in the model. The box (dashed line, black) shows the supercell used in calculation (except that there is more vacuum). The corresponding band structure and DOS for 4|4P has states colored orange, green, and black that are predominantly localized at the MTB, ribbon edge, or ribbon interior regions, respectively. The horizontal dashed line denotes the position of Fermi-level from the calculation, which is very close to $k_F = \pi/3a$ (vertical dashed line). The orange band of the states within the MTB that crosses the chemical potential is electron-like. (b) Atomic structures for the whole ribbon model exposing two edges and a 4|4E MTB. The corresponding band structure and DOS for 4|4E has a hole-like band crossing the chemical potential, which is expected to satisfy $k_F = \pi/2a$ (vertical dashed line). The horizontal dashed line denotes the position of Fermi-level from the calculation, which is not at the position found in the experiment.

we will focus our discussion on them. The energetics of the edges and MTBs were already given in Ref. [72]. All calculations were performed by H.P. Komsa [222].

We first focus on the 4|4P MTB. The grain boundary consists of four-membered rings that are connected by a point. The corresponding band structure is shown in Fig. 8.4 (a). The black dots correspond to the bulk, which shows a large band gap as expected for MoS_2. The green dots are states which are mainly localized at the two edges of the MoS_2 ribbon. The states mainly localized within the MTB are colored orange, so we restrict our discussion to them in the following. We find that a highly dispersive band

crosses the chemical potential, leading to the conclusion that the MTB is metallic. The band is electron-like, in close resemblance to the band of $MoSe_2$ observed in ARPES [28]. It hybridizes with a second band at higher energies. The chemical potential of the calculation, which is set by the vacuum level, is very close the expected chemical potential with $k_F = \pi/3a$. It should be noted, however, that the chemical potential in the system will be partly determined by the edges. Therefore, we set in the following the chemical to the observed nesting vector, which reduces the 1. BZ by a factor of three. The bands localized at the MTB are within the band gap of the bulk, leading the finite DOS near the chemical potential shown in Fig. 8.4 (a).

The 4|4E MTB is shown in Fig. 8.4 (b). It consists of four-membered rings connected by an edge. Its band structure is shown at the bottom of Fig. 8.4 (b). The orange band, which again is mainly localized within the MTB, is markedly different from the bands of the 4|4P MTB. We find a hole-like band that crosses the chemical potential, which is not at the expected Fermi wave vector $k_F = \pi/2a$. Again, this may be related to the edges of the model. The band localized at the MTB is again within the band gap of the bulk, leading to the finite DOS near the chemical potential shown in Fig. 8.4 (b). The results for both 4|4P and 4|4E are very similar to the electronic structure calculations for $MoSe_2$, though only one of the two MTBs appears in experiments during growth [72].

8.4 Phonon excitations

This section is devoted to the satellite peaks that are often observed near to the pronounced peaks of the CDW gap. Fig. 8.5 (a) shows a high resolution STS spectrum averaged over the entire length of a $3a$ CDW. One can clearly identify shoulders next to the two main peaks. The fact that they appear symmetric in both occupied and unoccupied states points to inelastic excitations as their likely origin. Typically, inelastic tunneling spectroscopy experiments exhibit shoulders in STS spectra due to the additional tunneling channel opening at $eV = E_i$, with E_i defined as the energy of the inelastic excitation. However, since our LDOS is strongly gaped around the Fermi energy due to the CDW, we see inelastic features appearing as peaks in STS spectra, similar to IETS of superconductor-superconductor and superconductor-metal junctions [223].

The fit shown in Fig. 8.5 (a) is used to extract the energy difference between main peak and the inelastic shoulders. Using Lorentz functions has proven to yield a better fit compared to Gaussian functions, so it is always used in the following. The peaks are characterized by the peak energy and width of the fit. The main (CDW) peaks have an average width

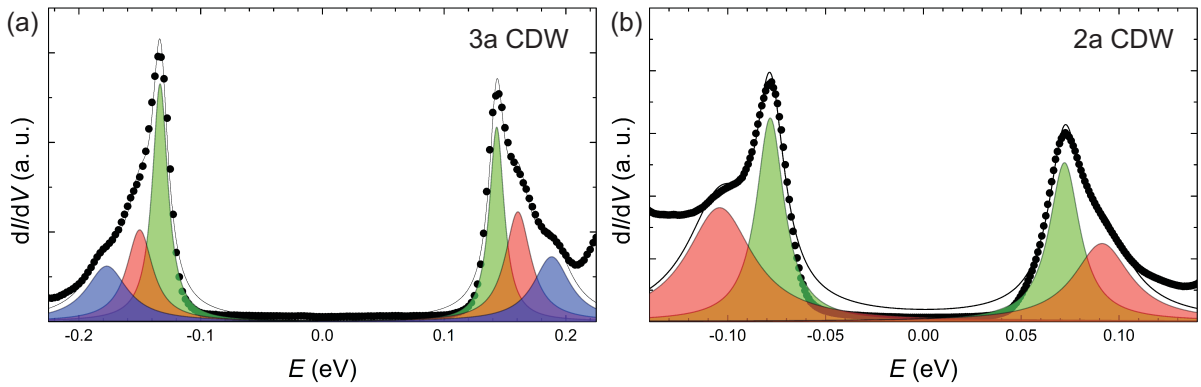


Figure 8.5: Excitations in MoS_2 mirror twin boundaries: (a) STS spectrum averaged along a $3a$ CDW ($U_{\mathrm{stab}} = 0.5$ V, $I_{\mathrm{stab}} = 0.1$ nA). The peaks are fit with three Lorentz functions each. The green component is related to the CDW gap, while the red and blue peaks stem from excitations. They are symmetric with respect to the CDW peaks. The peak energy difference between the excitations and the CDW peak (E_1 and E_2) and the peak width are extracted from the fit functions. (b) STS spectrum averaged along a $2a$ CDW ($U_{\mathrm{stab}} = 0.5$ V, $I_{\mathrm{stab}} = 0.1$ nA). Only one excitation appears in the spectrum.

of (16 ± 1) meV which is close to our resolution limit $\Delta E \approx 10$ meV [122]. The first inelastic peaks are slightly broader. The second peak has roughly twice the width of the first excitation. The increase in width is likely to stem from a decreased lifetime of the states. Energy differences and widths of the features are equal (within the error of the fits) in the occupied and unoccupied states, again supporting that they originate from inelastic tunneling. Note that the strongest deviation between the STS spectrum and the fit is within the CDW gap, which is due to the divergent nature of the DOS towards the gap that is in principle not properly described by a Lorentz peak, see Eq. 2.5.

STS spectra measured on $2a$ CDWs also exhibit shoulders near the main peaks around the Fermi energy. Fig. 8.5 (b) shows an averaged STS spectrum taken along a $2a$ CDW. Only one shoulder is visible in the occupied and unoccupied states, in contrast to STS spectra measured on $3a$ CDWs in which two shoulders are found in many spectra. The fit yields again a narrow width of 17 ± 1 meV for the main CDW peaks, while the first excitation has an increased width slightly larger than the width of the first excitation found in the $3a$ CDW. Following the trend of the excitations in the $3a$ CDW which shows an increase of the width away from the Fermi level, it is likely that the second excitation (if present) is not visible in STS spectra due its short lifetime or, equivalently, its large width.

Fitting the excitations of many MTBs hosting $2a$ and $3a$ CDWs gives an averaged value of the energy (which is defined as the energy difference between main peak and excitation)

and width of the features. They are listed in Tab. 8.1. We find that the first excitation (E_1) has the same energy for the $2a$ and $3a$ CDW within the error margin. Their widths also agree with each other, though one may recognize a trend towards larger widths for the $2a$ CDW. The similarities point to a lattice vibration of bulk MoS_2 as the cause for the excitation, not to lattice vibration confined within the MTB. Indeed, DFT calculations of the phonon dispersion find a peak in the phonon DOS around 21 meV [224], in very good agreement with E_1. The second excitation (E_2), which is only found in the $3a$ CDW, has an increased width compared to the first excitations. In line with the assignment of E_1, there are also pronounced peaks in the phonon DOS of ML MoS_2 around 50 meV [224]. These findings lead to the conclusion that the inelastic features arise from phonon modes of bulk MoS_2. The bulk nature of the excitation also explains the finding that the energy E_1 does not differ between the $2a$ and $3a$ CDW in MoS_2.

	E_1 (meV)	width (meV)	E_2 (meV)	width (meV)
$3a$ CDW	20 ± 3	28 ± 3	49 ± 3	60 ± 27
$2a$ CDW	22 ± 2	34 ± 4		
$3a$ CDW in $MoSe_2$ [27]	14.2 ± 0.8			

Table 8.1: Energy and width of the excitations in MoS_2 MTB. The values are extracted from a fit using Lorentz functions. The energy of the excitation found in $MoSe_2$ is listed as a comparison.

Barja et al. [27] also found inelastic satellite peaks next to the CDW peaks in $MoSe_2$ and attributed them to lattice vibrations. They extract an energy of $E_1 = (14.2 \pm 0.8)$ meV. This value is slightly lower than the value found in MoS_2. Since the two materials are composed of different elements one would expect their lattice vibrations to differ in energy. Indeed, DFT calculations of the phonon dispersion of ML $MoSe_2$ show that there is a shift of the phonon modes towards lower energies compared to MoS_2, with a flat phonon mode at around 15 meV that leads to a high DOS [225], confirming the assignment that the peaks are induced by bulk phonons of the TMDC. The difference between MoS_2 and $MoSe_2$ can be understood using the classical phonon dispersion relation of an atomic chain, which has a divergence in the DOS [221]:

$$D(\omega) = \frac{2L}{\pi a} \cdot \frac{1}{\sqrt{\omega_{\max}^2 - \omega^2}}. \tag{8.1}$$

The divergence takes place at the energy $\omega_{\max} = \sqrt{2K/M}$ which represents the top of the acoustic phonon branch and depends on the spring constant K and mass M of the atoms within the chain. In the case of MoS_2 and $MoSe_2$, the substituted elements are S and Se.

Since $M_S < M_{Se}$, we expect $\omega_{max} \propto \sqrt{1/M}$ to be higher in MoS_2 compared to $MoSe_2$, in line with the experimental observation.

8.5 Phase pinning and quantum confinement

Defects are known to introduce strong perturbations in one-dimensional systems, since a detour in an additional dimension cannot be taken to overcome the potential barrier. Prominent 0-dimensional defects in our system are the ends of MoS_2 MTBs. Their influence on the electronic properties of the CDW will be the topic of this section.

Fig. 8.6 (a) shows the STS signal measured along the entire length of a $2a$ CDW. We find again a vanishing signal around the Fermi energy that is attributed to the CDW gap 2Δ, together with a beating pattern above and below the gap. However, when looking closer to the pattern, one finds that the phase difference between the occupied and unoccupied state changes along the MTB; both states are in-phase at the start and end of the MTB, while out-of-phase in the middle of it. This is not in line with the CDW picture of an infinitely long chain, in which the phases of the wave functions near to the CDW gap are out-of-phase, as explained in Section 8.2. Furthermore, one can observe additional beating patterns appearing at certain discrete energies away from the gap. The energy difference between these states is around 50 meV in this case. All beating patterns are found to be in-phase at the start and end of the MTB.

The origin of the phase variation and additional peaks in the set of STS spectra along the MTB is likely related to quantum confinement. Assuming that the states within the MTB are trapped in a potential well of length L and that the potential at the boundary is strong, we can expect that the phase of the CDW will be pinned at the two ends of the MTB [226, 227], leading to in-phase behavior there. To get a quantitative picture of the role of confinement we can apply the non-interacting particle-in-a-box model to our one-dimensional states. The requirement that the wave functions vanish at the boundaries leads to quantization, which discretises the hole-like band to a set of wave functions Ψ_n. These fulfill the boundary condition $L = n\lambda_n/2 = n\pi/k_n$ with the integer n and the discrete values for wavelength λ_n and wave vector $k_n = 2\pi/\lambda_n$ of a state Ψ_n. Plotting $|\Psi_n|^2$ along the box as a function of energy using this model leads to the pattern sketched in Fig. 8.6 (b). The yellow boxes represent the maxima of $|\Psi_n|^2$, while the blue boxes are minima. Note that the number of maxima is equal to n. We see that λ_n is getting longer at higher energies, in accordance with the reduced k_n of the hole-like band. All neighboring states have $\Delta n = \pm 1$, which naturally leads to the out-of-phase behavior of

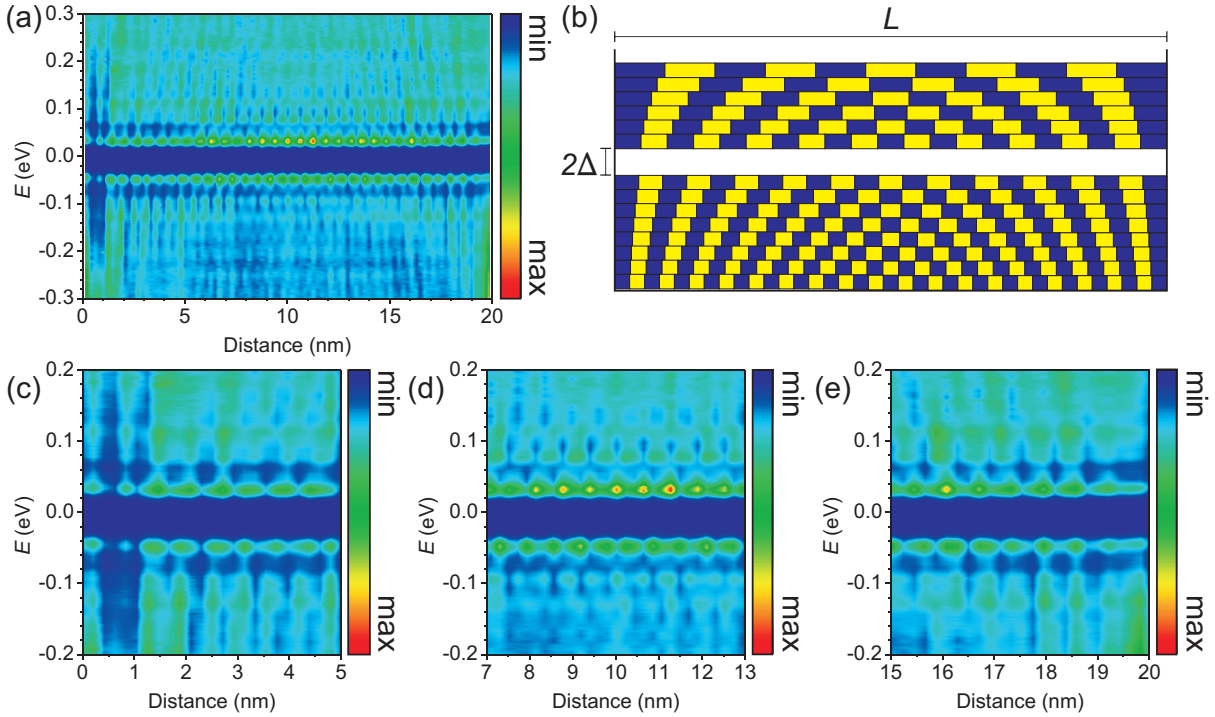


Figure 8.6: Phase behavior of the $2a$ CDW in MoS_2: (a) STS signal as a function of energy and position ($U_{\mathrm{stab}} = 0.5$ V, $I_{\mathrm{stab}} = 0.1$ nA). The reduced signal at the Fermi energy is due to the CDW gap 2Δ. The phase between the two peaks near to the gap starts and ends in-phase, while there are out-of-phase in the middle of the MTB. (b) Sketch of states in a hole-like band confined in a potential well of length L. The resulting standing wave in the LDOS is visualized with maxima (yellow) and minima (blue) along the length of the well. Their wavelength changes according to their band structure with the boundary condition that the wave vanishes at the edges of the well. (c) Zoom into the left side of the MTB, where states start in-phase. There is a tendency for the states to move to the right when increasing the energy, as found in the sketch. (d) Zoom into the middle of the MTB, where all neighboring states are out-of-phase. (e) Zoom into the right side of the MTB, where states are in-phase again. There is a tendency for the states to move to the left when increasing the energy. The same holds for the model.

neighboring states in the middle of the box, while being in-phase at the rim due to the boundary conditions.

To further underline that quantum confinement leads to the pattern shown in Fig. 8.6 (a), we can compare enlarged segments of the same set of STS spectra showing the $\mathrm{d}I/\mathrm{d}V$ signal at the start, middle and end of the MTB. They are shown in Fig. 8.6 (c)-(e). At the start [Fig. 8.6 (c)], one can recognize that the states at higher energies tend to move to the right, while they tend to move to the left at the end of the MTB [Fig. 8.6 (e)]. This behavior is also visible in the sketch in Fig. 8.6 (b) and is related to the longer wavelength

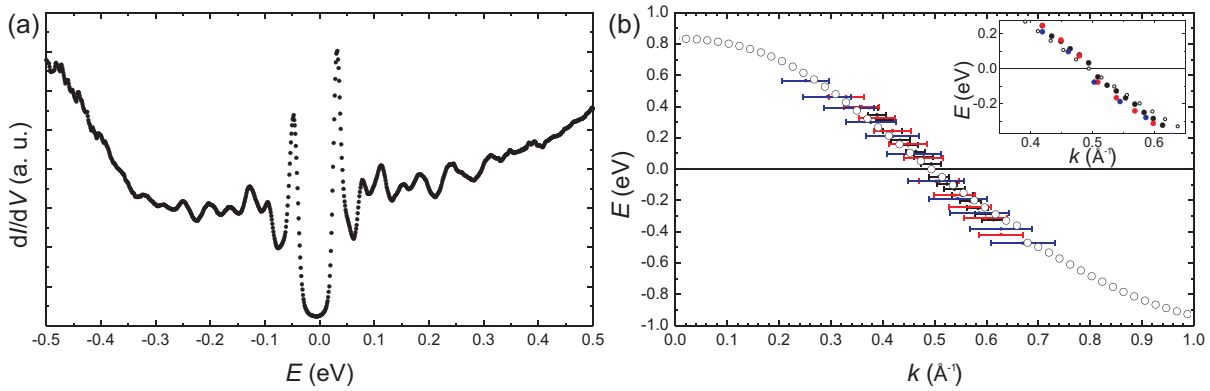


Figure 8.7: Confined states in $2a$ CDWs in MoS_2 MTBs: (a) STS spectrum averaged over the entire length (L = 21 nm) of a $2a$ CDW (U_{stab} = 0.5 V, I_{stab} = 0.1 nA). Additional peaks appear next to the CDW gap. (b) Dispersion of the confined states. The colors indicate states of different CDWs with varying length (black: 21 nm; red: 10.5 nm; blue: 7.5 nm). The open circles are taken from the DFT calculation. The inset shows the misalignment between the states above and below the Fermi energy due to the CDW gap.

of the standing wave pattern at higher energies. One can again clearly see that all states are in-phase at the edges while there is an out-of-phase behavior between all neighboring states in the middle of the wire. The same holds for the model, as discussed above.

Knowing the number of maxima along a MTB of a certain length enables us to extract its wave vector using $k_{\mathrm{n}} = n\pi/L$. By simply counting the maxima and reading their corresponding energies one is able to analyze the dispersion $E(k_{\mathrm{n}})$ of the confined states along the MTB. The maxima are best visible near the Fermi energy, but quickly become barely visible at higher and lower energies, though an enhanced intensity is still clearly visible in the STS spectrum at the corresponding energy. Therefore, we also extract the peaks found in averaged spectra along the MTB and use the relation $\Delta n = -1$ between energetically higher neighboring states and $\Delta n = +1$ between energetically lower neighboring states. As an example, the STS spectrum averaged over the set shown in Fig. 8.6 (a) is displayed in Fig. 8.7 (a). Many peaks are visible next to the CDW gap that are caused from the confined states. Fig. 8.7 (b) shows the resulting dispersion analyzed for three $2a$ CDWs. The error bars take into account the uncertainty in extracting the length ($\Delta L = \pm 0.5$ nm) and the possibility to miss one state ($\Delta n = \pm 1$). Note that the spacing $k_{\mathrm{n+1}} - k_{\mathrm{n}}$ between two consecutive wave vectors in the dispersion relation stays constant for all states in a single MTB, while it changes between states of different MTBs due to their different lengths L. The dispersion is hole-like in all three MTBs, in very good agreement with our DFT calculations of the 4|4E MTB in MoS_2, which is plotted in Fig. 8.7 (b) with

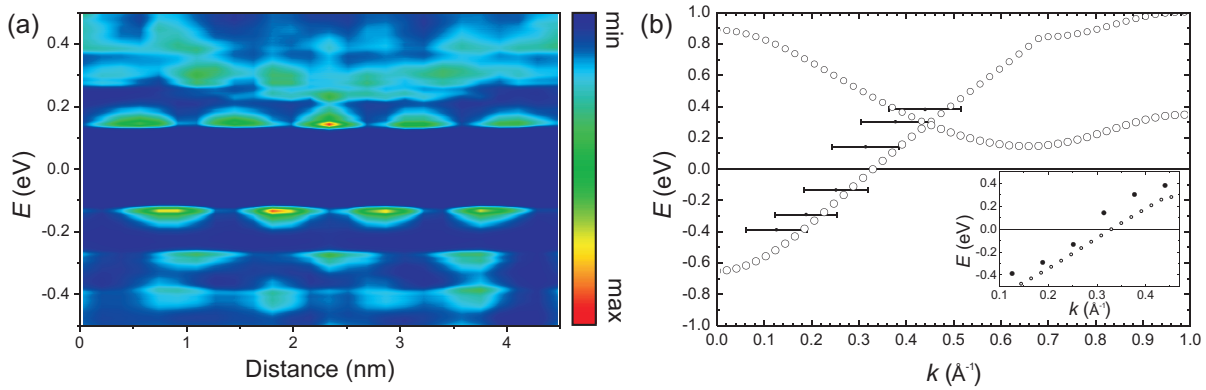


Figure 8.8: Confined states in $3a$ CDW in MoS_2: (a) Set of STS spectra along a $3a$ CDW ($U_{\mathrm{stab}} = 0.5$ V, $I_{\mathrm{stab}} = 0.1$ nA). We count $n = 2$ to $n = 7$ maxima in the LDOS. (b) Dispersion of the confined states. The open circles are taken from the DFT calculation. The inset shows the misalignment between the states above and below the Fermi energy due to the CDW gap.

open circles. Note that the bands are rigidly shifted in energy such that the states at the chemical potential have a wave vector of $k_{\mathrm{F}} = \pi/2a$ as found experimentally, and that the small discontinuity in the DFT calculation around $k = 0.67$ Å^{-1} arises from hybridization with an edge state of MoS_2, see Fig. 8.4. The latter is not expected to contribute to our experiments due to the large size of the MoS_2 flakes. The inset of Fig. 8.7 (b) shows a zoom of the same dispersion (without error bars), in which a clear discontinuity appears at the Fermi energy that is attributed to the CDW gap that opens between these states. This gap is not included in the DFT calculation, leading to a slight deviation between experiment and theory, especially near to the chemical potential.

The concept of confinement also holds for the states that form the $3a$ CDW. Fig. 8.8 (a) shows a set of STS spectra along a $3a$ wire. Starting at high energies, we find that the number of maxima decreases when the energy is decreased, in contrast to the $2a$ CDW where the number maxima increases. This finding is directly related to the hole-like versus electron-like band of the two MTBs. We can identify the states from $n = 2$ to $n = 7$ in the selected energy range by counting the maxima in the STS signal along the MTB. Note that the additional modulation of the $n = 2$ state at approximately $E = -0.4$ eV is likely to be a set point effect due to the stabilization of the tip at small positive bias voltage [115]. Another tentative explanation of the increase in n there could be spin-charge separation, leading to two bands with different dispersions. Though this effect has been observed in $MoSe_2$ using ARPES [28], the lack of additional maxima corresponding to the second band point to the set point effect to be the origin in this case. However, more MTBs have to be analyzed to give a concrete answer to this issue. In addition, we find that the states

at positive energies are not as clearly separated as the states at negative energies. The resulting dispersion relation in shown in Fig. 8.8 (b). It is electron-like, as predicted by our DFT calculations for the 4|4P MTB in MoS_2 and similar to the band structure of the 4|4P MTBs in $MoSe_2$ that also host a $3a$ CDW [27, 28]. The DFT calculation is included in Fig. 8.8 (b) and shows an excellent agreement, when the bands are rigidly shifted in energy such that the states at the chemical potential have a wave vector of $k = \pi/3a$. The second band in the unoccupied states might cause the decreased visibility of the states at positive energies. The inset of Fig. 8.8 (b) shows again a zoom of the same dispersion (neglecting the error margin), in which again a discontinuity appears at the Fermi energy due to the CDW gap which opens between these states.

8.6 Controlling and manipulating charge density waves

Now that we have determined the characteristic electronic properties of the CDWs in MoS_2 MTBs we can use this knowledge to control and manipulate them. Starting with confinement effects, we may alter the CDW properties by changing the length L of a MTB, which can be done simply by introducing a defect in a MTB. The result would be two MTBs that are separated by the defect. In general, one-dimensional systems are cursed to be extremely susceptible to small perturbations; a one-dimensional metallic chain may become insulating by the removal of a single atom.

Quasi-zero-dimensional defects are observed in MTBs in MoS_2. Fig. 8.9 (a) shows an STM image of a MTB containing a defect. Though one can clearly observe a discontinuity in the MTB, it is not possible to identify the exact atomic configuration of this particular defect. The STS spectra measured along the dashed line sketched in Fig. 8.9 (a) are shown in Fig. 8.9 (b). The CDW gap measured on each side of the defect is very different, though all STS spectra are recorded on the same MTB. Larger STM images reveal that the lower part of the MTB is much longer than the upper part, leading to very different quantization due to confinement, which strongly affects the size of the gap. This proof of concept shows how easily one can alter the fundamental properties of these CDWs by introducing atomic-scale defects. Note that not all defects may lead to strong confinement; step edges of the underlying Ir are found to not influence the CDW, leaving its electronic properties intact.

The tunability of the CDW gap is twofold; we can change the size of the CDW gap and the position of the gap with respect to the chemical potential. Fig. 8.10 (a)-(b) displays the L-dependence of the VB and CB for the $2a$ and $3a$ CDW, respectively. VB and CB

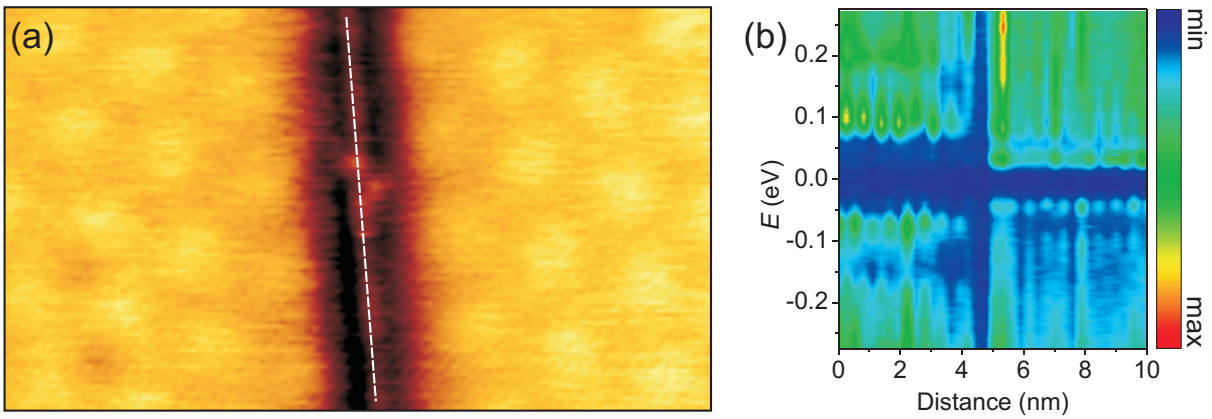


Figure 8.9: Impact of defects in MoS_2 MTBs: (a) STM image of a MTB with defect (U = 1.5 V, I = 0.005 nA, image size 17.5 × 10 nm^2). (b) STS spectra measured along the MTB (U_{stab} = 1.25 V, I_{stab} = 0.3 nA). The dashed line in the STM image shows the path of the tip when measuring STS spectra (starting at the top of the image).

are the peak energies near to the chemical potential. Confinement not only increases the size of the CDW gap when the MTB length gets shorter, but also shifts the middle of the gap away from the chemical potential. This can be explained with the location of the discrete k_{n} near to the chemical potential, that are usually not symmetric with respect to the Fermi energy.

Fig. 8.10 (c)-(d) shows the CDW gap as a function of MTB length L. The CDW varies from 70 meV to 175 meV in $2a$ CDWs, which is a factor of 2.5. For $3a$ CDW the gap varies even more, from 70 meV to 275 meV, which is a factor of almost 4. While it remains unclear how short the MTBs can be while still hosting a CDW (which would have the highest possible CDW gap), the longest MTB (with the shortest CDW gap) can be estimated by fitting the CDW gap with the following function:

$$E\,(L) = A/L + E_{\mathrm{fund}}. \tag{8.2}$$

This is physically justified with the linearity of the dispersion around the Fermi energy, leading to a energy difference $\Delta E_{\mathrm{n,n+1}} \propto \Delta k_{\mathrm{n,n+1}} \propto 1/L$. The fit is shown in Fig. 8.10 (c)-(d) for the two CDWs. Interestingly, the fit converges to a finite energy when $L \to \infty$. This is in contrast to quantum confinement only, and stems from the CDW phase that maintains the CDW gap in MTBs of infinite lengths. According to the fit, this fundamental CDW gap is found to be $E_{\mathrm{fund}} = (56 \pm 20)$ meV for $2a$ CDWs and $E_{\mathrm{fund}} = (80 \pm 40)$ meV for $3a$ CDWs.

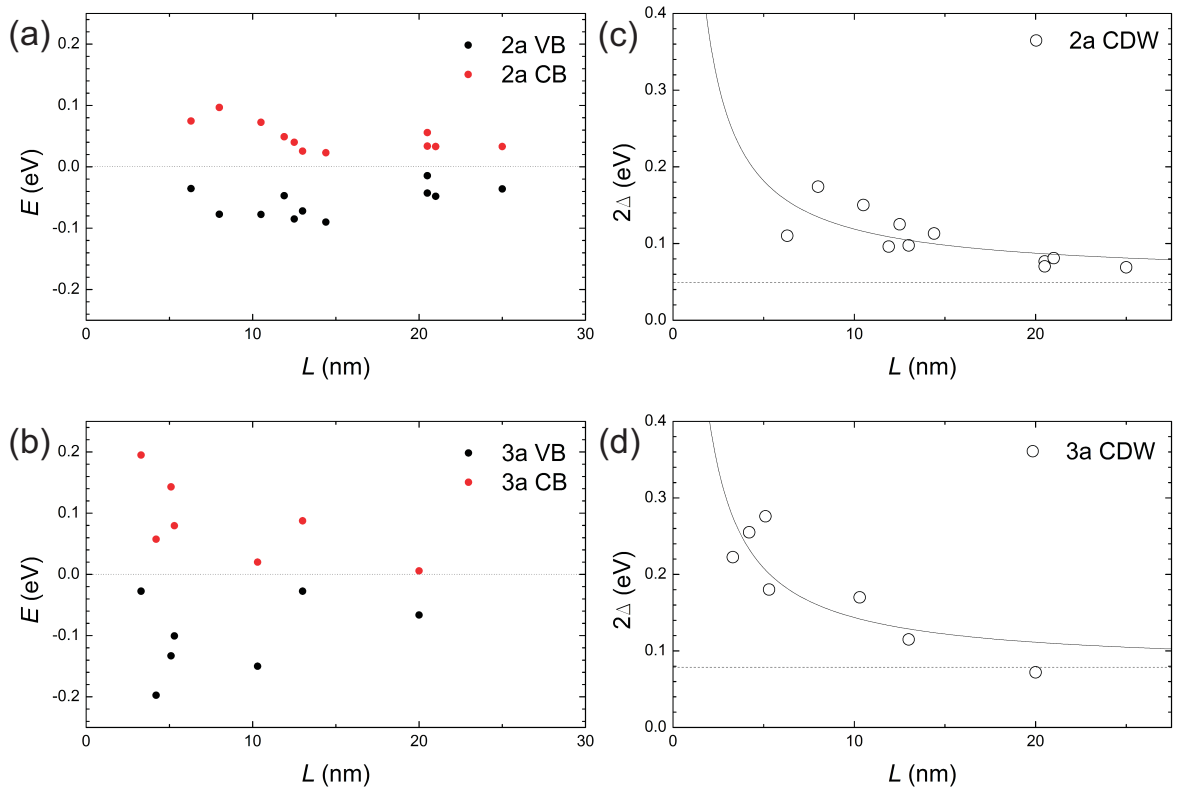


Figure 8.10: Tuning the gap of CDWs in MoS_2 MTBs: (a) L-dependence of the position of the VB and CB of the $2a$ CDW, defined as the peak energies around the chemical potential. The dashed line visualizes the chemical potential. The shifts of the CDW gap towards higher or lower energies is likely caused by confinement. (b) Same plot for the $3a$ CDW. (c) L-dependence of the $2a$ CDW gap. The line represents a fit that accounts for the L-dependence due to quantum confinement. The fit does not converge to zero due to the fundamental CDW gap E_{fund} of the CDW, which is indicated by the dashed line. (d) Same plot for the $3a$ CDW gap. The dashed line again indicates the fundamental CDW gap extracted from the fit.

In the following, we propose a way to manipulate CDWs in MoS_2 MTBs, namely via chemical gating. While graphene on Ir(111) is almost undoped [52], it is possible to use the backside of graphene to inject charge into it via intercalation between graphene and Ir(111). Fig. 8.11 (a) shows a large STM image of MoS_2/graphene/Ir(111) without chemical gating, where we find $2a$ and $3a$ CDWs. One example of a $2a$ CDW is shown in Fig. 8.11 (b). As shown with DFT and STS, the periodicity of this CDW is connected with its Fermi surface. In one-dimensional systems the Fermi surface is just a single point in k-space, which leads to the perfect nesting condition $E(k_{\mathrm{F}}) = E(-k_{\mathrm{F}})$ for the entire Fermi surface. The nesting scenario for a $2a$ CDW is sketched in Fig. 8.11 (c) at

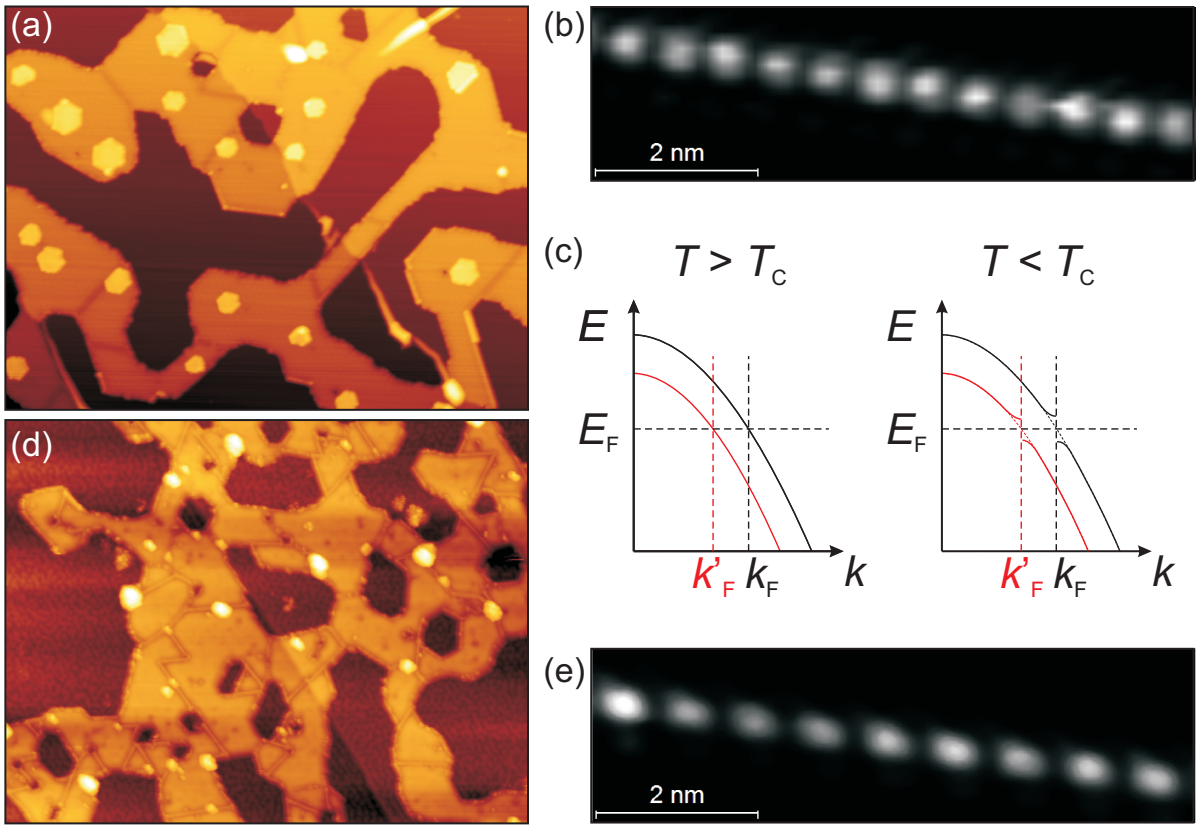


Figure 8.11: Gating MTBs in MoS_2: (a) STM image of MoS_2/MLG/Ir(111) ($U = 1.5$ V, $I = 0.01$ nA, image size 135×175 nm^2). (b) Constant height STM image of a $2a$ MTB ($U = 0.1$ V). (c) Sketch of the CDW gap opening mechanism below the CDW transition temperature T_C. The black band corresponds to MoS_2/MLG/Ir(111), the red band to MoS_2/MLG/Eu/Ir(111). The nesting vector gets smaller due to the shift of the band with respect to the Fermi energy. (d) STM image of MoS_2/graphene/Eu/Ir(111) ($U = 0.9$ V, $I = 0.02$ nA, image size 135×175 nm^2). (e) Constant height STM image of a (formally known as) $2a$ MTB ($U = 0.4$ V). Its periodicity has increased.

temperatures above and below the CDW phase transition temperature T_C. Above T_C, we have a hole-like band crossing the Fermi energy at a certain Fermi wave vector k_F. The states in the MTB are hence metallic at these temperatures. Upon cooling below T_C, the phase transition takes place, resulting in a gap opening *at the Fermi energy*. This will be important to understand the impact of chemical gating in the following.

Fig. 8.11 (d) shows a large STM image of MoS_2/graphene/Eu/Ir(111). Eu is known to give charge to graphene, shifting the band structure of graphene up with respect to the Fermi energy [128]. A similar gating effect of the semiconducting band gap of MoS_2 is discussed in Chap. 7. Fig. 8.11 (e) shows a constant height image taken on a MTB, revealing a beating pattern which is attributed to a CDW. The structure of the beating

pattern resembles the $2a$ CDW of the system without chemical gating. However, the periodicity of the CDW increased compared to the $2a$ CDW, from $2a$ to roughly $2.5a$. Hence doping MoS_2 MTB with Eu induces a phase transition, driving the system in an incommensurate CDW state.

The increase of the periodicity is again related to the Fermi surface of the one-dimensional states within the MTB. The band structure of chemically gated MoS_2 MTBs is sketched in red in Fig. 8.11 (c). The intercalated Eu, which is known to n-dope graphene, induces a shift of the bands in the MTB towards lower energies. This leads to a different Fermi surface with a reduced k_F. Accordingly, when the temperature is below T_C (which might have a gating-dependence), the CDW gap opens at a smaller wave vector since it is pinned to the Fermi energy and not to a certain wave vector. A smaller Fermi wave vector results in a smaller nesting vector, and thus to the larger periodicity of the CDW beating pattern observed experimentally. Hence, the potential of chemical gating is that it enables one to drive the one-dimensional state into the desired phase by injecting the right amount of charge into graphene via intercalation.

8.7 Discussion and outlook

CDWs in MoS_2 MTBs are well decoupled, truly one-dimensional states embedded in an insulating matrix. All basic CDW properties (periodic beating in real space, CDW gap, out-of-phase behavior of the first occupied and unoccupied states) are observed and can be tailored with only a few ingredients such as defects or doping. These experimental results clearly demonstrate that MTBs in MoS_2 on graphene on Ir(111) are a perfect model system to study the electronic properties of one-dimensional states with surface sensitive techniques such as STM.

The MTBs under investigation (4|4P and 4|4E) exhibit very different electronic states, the most obvious being the different CDW periodicities ($3a$ versus $2a$). DFT can link the electronic properties to the structure of the MTBs. The band structure of the states within a 4|4P MTB are electron-like, while a hole-like band is found for the states within the 4|4E structure. Both bands are confirmed with STS by observing a dispersing standing wave pattern arising from the states confined in finite MTBs. Additional predictions from DFT, such as the phonon dispersion, can explain the excitations found in STS. Their phononic origin could be shown on a qualitative level using the mass dependence of the phonon dispersion, and quantitatively by analyzing the phonon dispersion obtained with DFT for MoS_2 and $MoSe_2$. An analysis including the MTB geometry could give even

more insights, especially since it may shed light onto the contribution of electron-phonon coupling to the CDW formation.

Though the CDWs in MoS_2 MTB can be treated as decoupled from another and the substrate, they are still influenced by their length, leading to confinement effects that quantize the one-dimensional states and influence the phase of the CDW pattern. Even the longest MTB analyzed in this chapter showed a linear change in the phase between the first occupied and unoccupied states as expected from a one-dimensional, non-interacting electron gas confined in a potential well. Note that this is not the ground state of an infinite CDW, which favors out-of-phase behavior between these states. One could expect that longer MTBs show a transition between complete out-of-phase behavior and a distortion towards in-phase at the edges, separating the bulk and edge effects.

The confinement effects found in MoS_2 may explain recent results reported for $MoSe_2$ MTBs. The CDW band gap found in this material has a size of $2\Delta = (100 \pm 40)$ meV [27]. The transition temperatures of the (commensurate and incommensurate) CDW have been determined to be $T_1 = 205$ and $T_2 \approx 230$ K [28, 228], respectively. For comparison, in MoS_2 the beating pattern is still visible at room temperature, leading to a transition temperature $T_C > 300$ K. Its (fundamental) CDW gap is $E_{\text{fund}} = 56 \pm 20$ meV for $2a$ CDWs and $E_{\text{fund}} = 80 \pm 40$ meV for $3a$ CDWs, which is rather small compared to the CDW gap of $MoSe_2$. Generally one would expect that a higher transition temperature is related to a larger CDW gap. This is not the case here. The discrepancy may be related to confinement effects that were neglected when extracting the CDW gap 2Δ in $MoSe_2$, though many defects are present in the MTB network in this material that in principle confine one-dimensional states just like the ends and defects in MoS_2 MTBs. If confinement is present in $MoSe_2$, it will lead to a smaller fundamental CDW gap, in line with the smaller transition temperature compared to MoS_2. In addition, confinement may also explain the strong scatter in the CDW gap, that is not in line with the sharp transitions found in transport measurements. Note that the scatter in the fundamental gap in MoS_2 is due to the small set of CDW band gaps used for the fit and the difficulty to disentangle the CDW and confinement contributions. Therefore one may rather use the CDW gap of the longest MTB to estimate a higher bound to the fundamental CDW gap, which for both $2a$ and $3a$ CDW is $2\Delta = 70$ meV.

The actual transition temperature of the CDWs in MoS_2 is still unknown. It would be interesting to measure the transition temperature of the CDWs in MoS_2 in the future and find its relation to the CDW gap, which can be used to estimate the role of electron-

phonon coupling in the CDW formation [88]. As an estimate, we can use Eq. 2.4 to compute the transition temperature:

$$T_{\mathrm{C}} = \frac{2\Delta}{3.52 k_{\mathrm{B}}} \approx 230 \text{ K}. \tag{8.3}$$

The expected transition temperature is lower than room temperature. This is a puzzling result, since the periodic beating pattern of the CDWs is still visible at $T = 300$ K, far above the expected transition temperature. While weak electron-phonon coupling leads to the BCS formula, one expects a higher T_{C} than in Eq. 8.3 for strong electron-phonon coupling. The opposite is true here. While confinement effects alone may lead to a beating pattern along the MTBs, a calculation of our one-dimensional states including many-body interactions is mandatory to fully understand the physical properties of MTBs in MoS_2 [229].

Analyzing the confined states in MoS_2 MTBs not only enables one to accurately compute the dispersion of the one-dimensional states, but may also reveal exotic phenomena of one-dimensional systems, such as spin-charge separation which has been observed in $MoSe_2$ [28]. The electronic properties of the one-dimensional states are found to be strongly influenced by the MTB edges. An interesting question is whether a single atom is sufficient to control the properties of the states within a MTB, or whether the two resulting MTBs are still coupled to each other. Different approaches are feasible, such as atomic manipulation [230] or metal decoration [228, 231].

The fact that CDWs can be manipulated by gating makes it possible to potentially analyze their phase diagram upon doping. It should be noted that the resulting phase diagram would represent the true dependence on doping only, without the need to change the material itself. This is in contrast to conventional phase diagrams of three-dimensional materials, where doping is achieved by atomic substitution, inducing defects in the material which may influence the phase diagram as well. A phase transition has already been observed with the intercalation of Eu, from a commensurate to incommensurate CDW. It is not unlikely that the CDW can be completely suppressed at a certain doping level. For example, it has been shown that no CDW gap opens in $MoSe_2$ when the lattice distortion has a period of $2a$ [27]. Suppressing the CDW order would make it possible to study the metallic state of the Tomonaga-Luttinger liquid [206]. Even more exotic properties could emerge at a possible (quantum) critical point located at a certain doping level between the two [9, 232].

8.8 Conclusions

In conclusion, we analyzed the electronic properties of one-dimensional states embedded in MoS_2 MTBs. These states undergo a phase transition at low temperatures, forming CDWs along the MTB. To kinds of CDWs are found and linked to their corresponding structure. Both CDWs are characterized using STS and DFT, with an overall good agreement between the two. Inelastic features are found in STS spectra and linked to vibrational excitations. The finite length of the MTB leads to quantum confinement, which is used to analyze the dispersion of the states. This effect in turn enabled us to manipulate the fundamental properties of the CDWs. As a proof of principle, Eu intercalation showed that gating from below leads to a change in the beating pattern, and may be used to drive these one-dimensional states into other exotic phases.

CHAPTER 9

Charge density wave order in vanadium diselenide

This chapter contains contributions from T. Knispel, W. Jolie, N. Ehlen, K. Nikonov, A. Grüneis, C. Busse and T. Michely. T. Michely and A. Grüneis proposed the experiments. K. Nikonov prepared the samples under the supervision of A. Grüneis. N. Ehlen provided the TB simulation and ARPES data, under the supervision of A. Grüneis. T. Knispel mounted the sample for STM measurements under the supervision of W. Jolie and T. Michely. T. Knispel and W. Jolie collected the data. T. Knispel and W. Jolie analyzed the data, that were mainly discussed with T. Michely, but also with N. Ehlen, K. Nikonov, A. Grüneis and C. Busse. The main results of this chapter can be found in Ref. [147].

9.1 Motivation

Layered materials such as TMDCs tend to be electronically unstable due to their quasi-2D structure [3], which in combination with many-body interactions can lead to exotic phase transitions such as superconductivity [233], charge density waves (CDW) [88], or orbital order [234] at low temperatures. The origin of the phase transition in many TMDCs is still unclear because several factors - such as the near-perfect nesting condition due to the reduced dimensionality and strong electron-phonon coupling - are present in many of them. The various contributions lead to an interplay that is theoretically still not well understood [88]. Prominent examples are TaS_2 [234], $TaSe_2$, $TiSe_2$ [235] and $NbSe_2$ [236].

The TMDC compound 1T-VSe_2 has not been extensively investigated so far, though it has promising intrinsic photocatalytic properties [237] and has been shown to improve the performance of solar cells [238]. It is metallic with a strong in-plane dispersion and a weak out-of-plane dispersion due to the different intra- and interlayer coupling strengths [239]. It undergoes two CDW phase transitions at $T \approx 110$ K and $T \approx 80$ K, forming a commensurate (4×4) CDW in-plane with an incommensurate out-of-plane component ($q_c = 0.314c^*$ for 110 K > T > 80 K [79–81] and $q_c = 0.307c^*$ for $T < 80$ K [79, 81]). Note that a commensurate out-of-plane component ($q_c = c^*/3$) has been reported in Ref. [82]. The in-plane commensurability of the CDW has been confirmed with STM, though it remains unclear whether the CDW has a 6-fold symmetry or forms domains with an enhancement of the CDW pattern along a certain preferred direction [240–242]. No information on the out-of-plane component is obtained with STM since this technique is only sensitive to the surface of VSe_2. Yang et al. [243] found that the first CDW transition temperature decreases to 81.8 K when reducing the thickness down to 11.6 nm, while Xu et al. [244] found an increase of the CDW transition temperature to 135 K in even thinner samples. Both findings were confirmed by Pasztor et al. [94], who systematically investigated the thickness dependence of the CDW amplitude down to one monolayer.

In general a CDW phase is characterized by a CDW gap 2Δ that opens at the Fermi level in the DOS, a quantity that is directly accessible using STS. There is however strong scatter in literature concerning the size of the gap measured with STS: Wang et al. [245] reported a gap of $2\Delta = 80$ meV at $T = 4.2$ K, while Ekvall et al. [246] found a gap of $2\Delta = 160$ meV at $T = 60$ K. Another technique, which is sensitive to the occupied DOS and hence able to observe the formation of the gap upon CDW formation, is ARPES. Terashima et al. [247] reported a partial gap opening (often referred to as pseudogap) on the electron-like Fermi surface (FS) centered at the M(L) point. Upon cooling the sample across the transition temperature, they were able to find a reduction of the DOS in certain directions in k-space, which they attributed to the CDW formation. Their results point to a CDW gap $2\Delta = 160 - 200$ meV [247]. Sato et al. [248] showed that the pseudogap opens only at certain wave vectors perpendicular to the layers, due to the dispersive behavior out-of-plane and found a shift in the peak intensity away from the Fermi energy of $20 - 30$ meV. Strocov et al. [239] confirmed the 3-dimensional nesting vector with high-resolution ARPES measurements, but did not claim to see any gap opening. They experimentally analyzed the imaginary part of the electron susceptibility $\mathrm{Im}\chi_{\mathbf{q}}$ and found a peak near the CDW wave vector. It should be noted however that the real part of the

susceptibility Re$\chi_{\mathbf{q}}$ [defined as $\chi_0(q)$ in Eq. 2.2] causes the electronic instability due to nesting [31, 93], a quantity that is not directly available with ARPES.
In this chapter we perform STM and STS measurements to obtain information on the structural and electronic properties of VSe_2. The data is collected at $T = 5$ K, far below the two CDW phase transition temperatures. The symmetry of the in-plane (4×4) PLD is clarified, and a comprehensive analysis, supported by ARPES data and TB simulations, uncover the different contributions observed in STS spectra. The focus, however, lies on the CDW gap and the origin of the strong scatter in the values reported so far. The role of defects is discussed.

9.2 Structural and electronic properties of vanadium diselenide

Atomically resolved STM images of the surface of VSe_2 are shown in Fig. 9.1 (a) and (b). The surface atoms appear bright or dark, depending on the tip and tunneling conditions. While the STM contrast in Fig. 9.1 (b) is the most common one, it is not trivial to assign V or Se to the atomic positions: on the one hand the DOS near the Fermi level is governed by V d-states [242], but the surface consists of Se atoms which are therefore closer to the tip [240, 242]. In both STM images, a pronounced (4×4) periodic structure with respect to the atomic lattice is visible and attributed to the CDW of VSe_2. The commensurability is verified in areas free of defects by counting the atoms along the crystallographic directions and then dividing by the number of CDW periods. With this method one can minimize the systematic errors of the STM which are of the order of 5%. The resulting periodicity is $(4.00 \pm 0.07) \times a$ with a defined as the in-plane lattice constant of VSe_2, i.e. the structure is commensurate within the error margin. Note that STM is not able to measure the out-of-plane periodicity of the CDW.
The CDW period is also visible in the FT of STM images that give direct access to the reciprocal space. An example is shown in Fig. 9.1 (c), which represents the FT of Fig. 9.1 (a). We find six outer spots that are attributed to the reciprocal lattice vectors of the VSe_2 surface. One of the them is sketched in Fig. 9.1 (c), labeled $\mathbf{a}^*$. The six inner spots stem from the (4×4) periodicity of the CDW, which corresponds to $\mathbf{a}^*/4$ in reciprocal space. One is also sketched in Fig. 9.1 (c), labeled $\mathbf{q}_{\mathrm{CDW}}$. A ball model of the CDW structures is displayed in Fig.9.1 (d), in which the yellow balls represent the surface atoms of VSe_2 and the blue balls visualize the (4×4) structure of the CDW. The unit cells of VSe_2 and of the CDW are indicated.

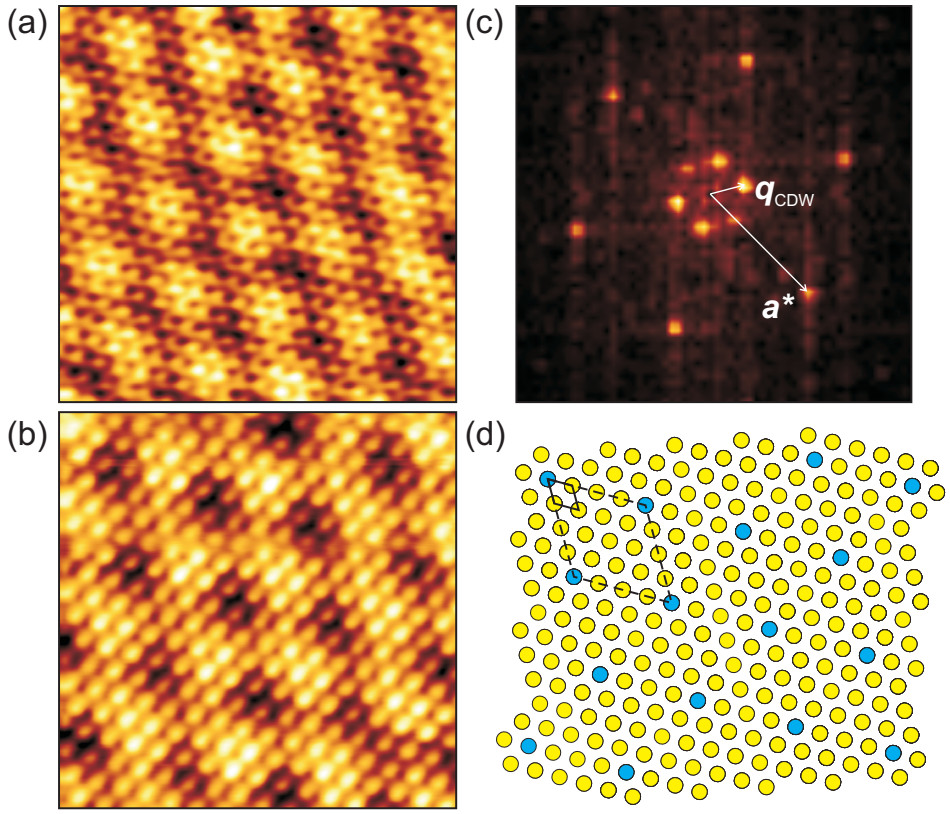


Figure 9.1: In-plane structure of VSe_2: (a) STM image of VSe_2 ($U = -0.75$ V, $I = 0.2$ nA, image size 6.2×6.2 nm^2). (b) STM image recorded with a different tip showing a different atomic contrast ($U = -0.2$ V, $I = 0.5$ nA, image size 5.3×5.3 nm^2). (c) FT of the STM image shown in (a). The large arrow represents a reciprocal lattice vector of VSe_2, while the small arrow represents a reciprocal lattice vector of the CDW. (d) Ball model of the (4×4) structure, in which the yellow balls are atoms and the blue balls the superstructure. The primitive unit cell of the lattice and superstructure are displayed with a continuous and dashed rhomboid, respectively.

Coleman et al. [240, 241] reported a pronounced unidirectional enhancement of the CDW pattern, while Kim et al. [242] found a 6-fold rotational symmetry. The STM images in Fig. 9.1 (a)-(b) point to a commensurate, periodic structure with 6-fold rotational symmetry. We observed that scanning the same area with different tips sometimes lead to both unidirectional CDW and 6-fold rotational CDW depending on the condition of the tip. This leads to the conclusion that the symmetry breaking reported by Coleman et al. [240] is likely to result from a anisotropic tip rather than from the CDW itself.

An STS spectrum which measures the LDOS present at the surface of VSe_2, is shown in Fig. 9.2. The (raw) $\mathrm{d}I/\mathrm{d}V$ signal obtained with lock-in amplifier is displayed in Fig. 9.2 (a). Several features are present that can be highlighted by dividing the $\mathrm{d}I/\mathrm{d}V$ sig-

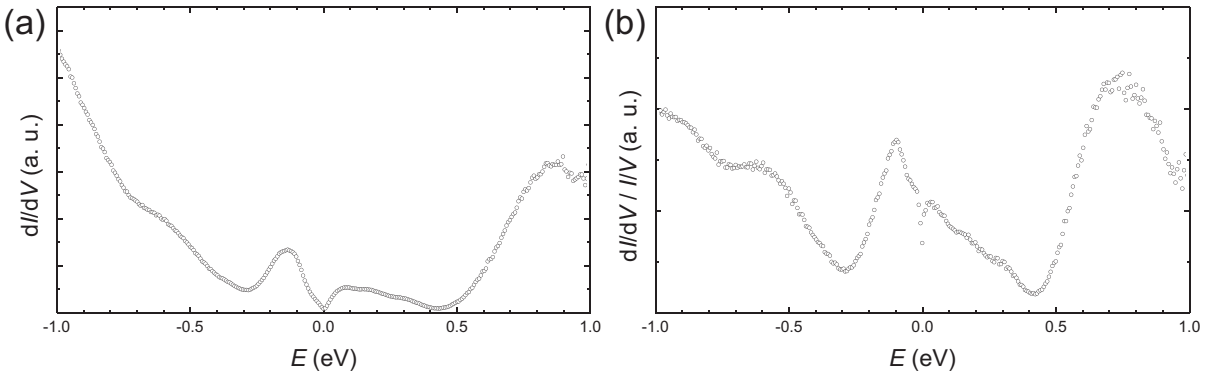


Figure 9.2: LDOS of VSe_2: (a) STS spectrum of VSe_2 ($U_{\mathrm{stab}} = -1$ V, $I_{\mathrm{stab}} = 1$ nA). (b) Normalized STS spectrum. We find peaks around -0.1 eV and 0.75 eV, dips around the Fermi level and 0.45 eV, and shoulders at -0.8 eV, -0.5 eV.

nal by I/V, which gives a better measure for the LDOS [114]. This is done in Fig. 9.2 (b) using the data of Fig. 9.2 (a). Both show a peak around $E = -0.1$ eV that is attributed to the d-states of V near to the Γ point [249], in line with the STS spectra reported by Ref. [246] and [94]. In addition we find dips around $E = -0.3$ eV, $E = 0.4$ eV and around the Fermi level, together with a pronounced shoulder around $E = -0.5$ eV and a broad peak around $E = 0.75$ eV. The overall shape of the spectrum is in accordance with Ref. [94] aside from the dip at the Fermi level. In the following we will discuss all these features and link them to their corresponding bands found in TB calculations of VSe_2, if present.

The band structure of VSe_2 obtained from samples of the same batch [62] is shown in Fig. 9.3 (a). The blue colored plots in the background represent spectra measured with ARPES, while the dots colored from black to red are the corresponding theoretical fit using a nearest neighbor TB model [62]. Note that additional $E_{\mathrm{i}}\,(k_{\mathrm{i}})$ maxima extracted from ARPES data were used for the fit, though they are not included in Fig. 9.3 (a). The color of the bands depends on their orbital character, which ranges from fully p-type (black) to fully d-type (red). The band which crosses the Fermi level is attributed to the d-band of V mentioned above, while additional bands coming from the p-orbitals of Se are located at slightly lower energies. The occupied band structure is in overall agreement with literature [239]. While there is a good agreement between ARPES and the TB simulation in the occupied states, a lack of constrains to the fit parameters of the TB Hamiltonian for the unoccupied band structure may lead to strong deviations there, as will be discussed below.

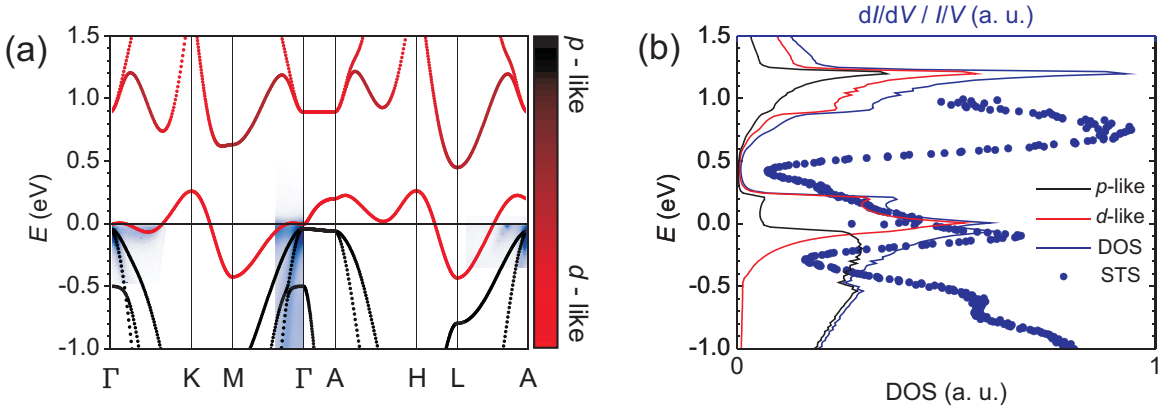


Figure 9.3: TB calculation of the bands and DOS of VSe_2: (a) band structure of VSe_2 in high symmetry directions. The color indicates whether the band has d orbital character (red) or p orbital character (black). ARPES scans used for the fit are shown in the background. (b) Corresponding DOS of VSe_2. The blue curve represents the total DOS, while the red (black) curve shows the contribution from d-states (p-states). The blue dots are from the STS spectrum. TB and ARPES data taken from Ref. [62].

The TB Hamiltonian can be used to compute the DOS of VSe_2, which is shown in Fig. 9.3 (b). The blue curve represents the total DOS, which is divided into the DOS arising from p-orbitals (black) and d-orbitals (red), respectively. We can now compare the simulated DOS with the STS spectrum that is plotted with blue dots in Fig. 9.3 (b). The peak seen in the STS spectrum at $E = -0.1$ eV is at the location where we find a peak in the TB simulated DOS. The main contribution to this peak stems from the d-states of V near the Fermi energy. The dip at $E = -0.4$ eV in the occupied states of the STS spectrum is located at the crossover between d-states and p-states, though it is much more pronounced in the STS spectrum. The shoulder at $E = -0.5$ eV is likely to be related to the additional contribution from the hole-like band at the Γ point that has a maximum at the corresponding energy.

While there is an overall good agreement in the occupied states, the situation is different at energies above the chemical potential. The peak measured with STS at $E = 0.75$ eV is likely to stem from the unoccupied bands, though their contribution to the simulated DOS forms a peak at much higher energies, around $E \approx 1$ eV. The dip at $E = 0.4$ eV between the peaks in the unoccupied states and near to the Fermi energy would then represent the minimum between the different d-bands that is also visible in the simulation, though much larger in size due to the high energies of the unoccupied d-bands. DFT calculations indeed show that the unoccupied bands tend to be lower in energy [239], in good agreement with our and reported STS spectra [94]. The difference in energy is attributed to fact that only

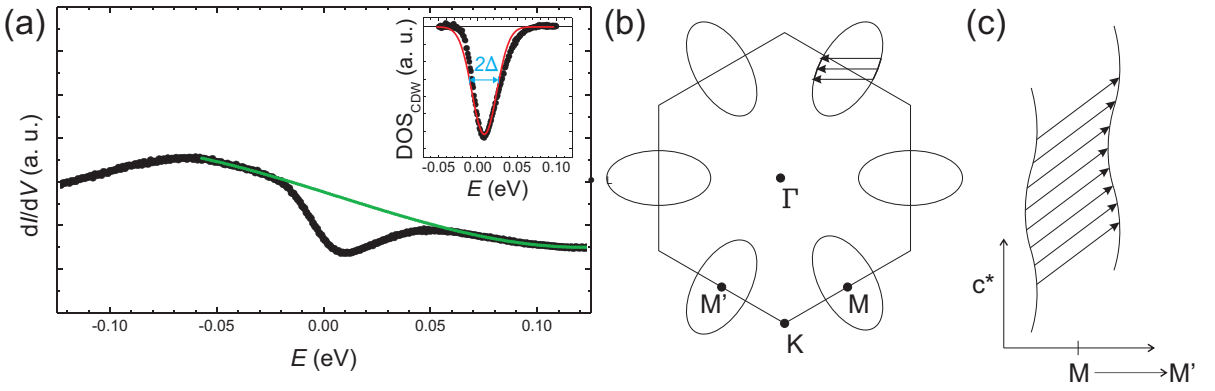


Figure 9.4: CDW gap in STS spectra: (a) High-resolution STS spectrum of VSe_2 (U_{stab} = 0.2 V, I_{stab} = 3.2 nA). We find again the features mentioned above, with a pronounced gap around the Fermi level. The green line represent a third order polynomial fit to the data in the vicinity of the Fermi energy, but neglecting the gap. The inset shows the difference between the STS spectrum and the polynomial fit, DOS_{CDW}, which is then fitted with a Gaussian to extract the CDW gap 2Δ from its FWHM. (b) 1. BZ of VSe_2 in the $k_x k_y$-plane at a fixed k_z. The arrows are the nesting vectors, which connect parts of the electron pockets along the MM' direction. (c) Out-of plane dispersion of the electron pocket. Perfect nesting occurs only when the wave vectors have a certain out-of-plane component.

the occupied bands can be properly fitted to ARPES data, while no information on the unoccupied states is known from this experimental technique. Note that the knowledge of the shape of the unoccupied states measured with STS has been incorporated in the fit, though the lack of knowledge on the location of the bands responsible for the high DOS still leads to a poor agreement. It is also important to note that it is not trivial to shift the unoccupied bands down in energy since they are interconnected with the occupied bands through hybridization effects.

Though the main features of the STS spectra can be attributed to the states of VSe_2, one is not reproduced by the TB calculation, namely the pronounced dip found at the Fermi level. It is hence attributed to the CDW gap 2Δ that opens in the CDW phase. Fig.9.4 (a) shows a high resolution STS spectrum measured around the Fermi level. The feature is rather continuous instead of abrupt, making it difficult to extract 2Δ. In addition, the peak arising from the *d*-states tends to mask the dip and leads to a pronounced asymmetry. Therefore, the spectrum is fitted in a small energy range around the Fermi level (omitting the gap) with a third-order polynomial function to deconvolute the gap from the peak arising from the *d*-states at the Γ point, which do not contribute to the CDW formation. The green line shows the polynomial fit to the spectrum in Fig. 9.4 (a). This can be seen

as the DOS at high temperatures, where no CDW and consequently no gap is present. The difference between these two curves (defined as DOS_{CDW}) is calculated and shown in the inset. By assuming that DOS_{CDW} is only related to the CDW gap opening 2Δ, it simply shows the suppression in the DOS due to the CDW phase transition. This feature can be fitted with a Gaussian to extract its FWHM, which then gives a measure of the CDW gap. The red curve in the inset of Fig. 9.4 (a) represents the Gaussian fit, with its FWHM indicated by a blue line. Using this procedure for 16 different normalized spectra leads to an average CDW gap $2\Delta = 26 \pm 6$ meV. The CDW gap is often slightly shifted away from the chemical potential, which may be due to the second phase transition since it changes the CDW nesting wave vector responsible for the gap opening.

The opening of the CDW gap at the chemical potential can be visualized with the nesting scenario, as explained in detail in Ref. [239]. In the following we will briefly mention the relation between Fermi surface and CDW formation. Fig. 9.4 (b) shows a sketch of the Fermi surface in the a^*b^*-plane at a fixed c^*. There are six electron pockets located around the M points. The arrows along the in-plane reciprocal lattice vectors of VSe_2 [which is the MM'-direction in the Fig. 9.4 (b)] represent the nesting wave vectors. These wave vectors connect segments of the CEC that are parallel and have opposite velocities and hence represent a highly favored wave vector for nesting [31]. On top of this, we find a wave vector connecting parallel segments of the CEC in the MM'-c^* plane, see Fig.9.4 (c). This leads to an ideal nesting situation along this direction, leading to a CDW with the corresponding periodicity in real space. Note that the DOS at the Fermi energy is reduced due to nesting but still finite, since not all states contribute to CDW formation. This is in agreement with the partial gap opening or pseudogap found in STS spectra. The fact that no abrupt decrease is found in the STS spectrum can be attributed to the three-dimensional nesting of the Fermi surface, leading to a small suppression near to the actual nesting wave vector as reported by ARPES measurements [247].

9.3 The role of defects

The influence of defects is of great importance in VSe_2 due to the difficulty to produce perfect stochiometric samples [250]. Non-stochiometric compositions of $V_{1+x}Se_2$ with $x = 0.01 - 0.28$ have been reported [251], in which the excess V is located in the vdW gap between two Se layers as interstitials [251]. The formation of Se or V vacancies is also reported in literature; while V vacancies are produced with ion bombardment [250, 252], atomically resolved STM images suggest that Se vacancies are imaged as missing

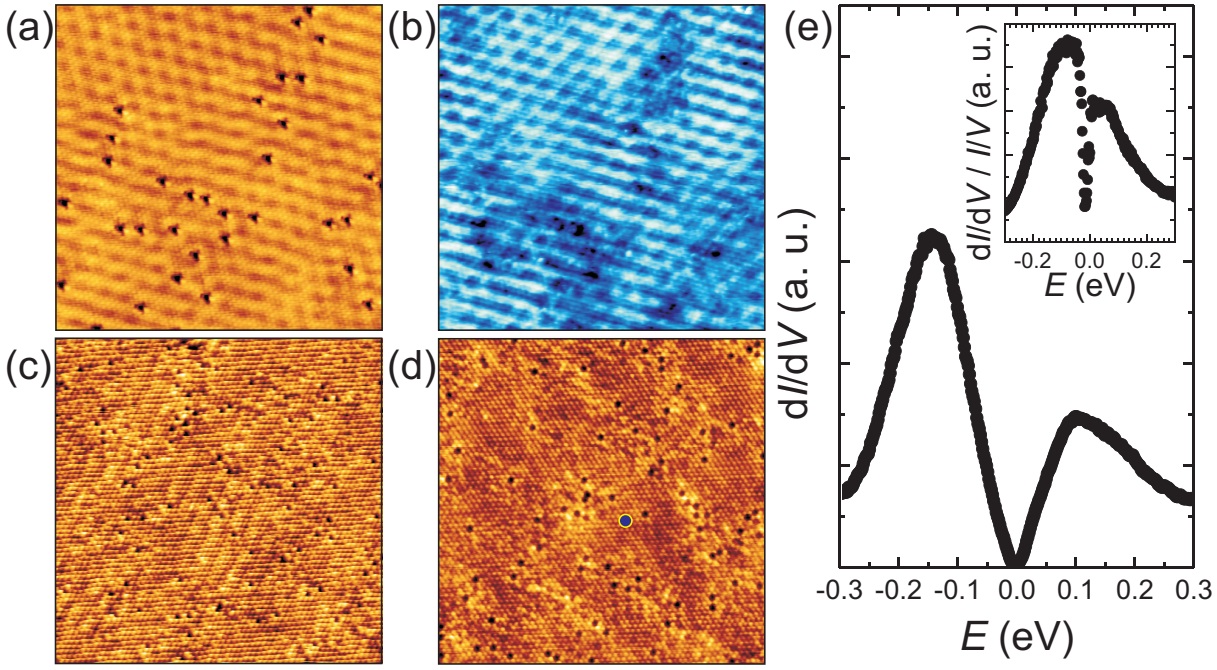


Figure 9.5: Defects in VSe_2: (a) STM image containing both vacancies and the CDW ($U = -0.3$ V, $I = 0.21$ nA, image size 20×20 nm^2). (b) Corresponding STS map recorded at $E = -0.05$ eV. (c) STM image containing a large defect density . The CDW is only barely visible ($U = 0.383$ V, $I = 0.11$ nA, image size 20×20 nm^2). (d) STM image in which no CDW periodicity is visible ($U = 0.355$ V, $I = 0.1$ nA, image size 20×20 nm^2). (e) STS spectra measure at the position marked by a blue dot in (d), showing a pronounced CDW gap though the CDW amplitude is strongly attenuated ($U_{\mathrm{stab}} = 0.5$ V, $I_{\mathrm{stab}} = 0.2$ nA).

atoms on the VSe_2 surface [241, 242], though the atomic resolution might stem from the V atoms underneath due to their high DOS near the chemical potential [242].

Impurities can be modeled as potential scatterers that tend to pin the CDW phase [226]. One can define two different regimes; the *strong pinning regime* with strong impurity potential or a dilute impurity concentration and *the weak pinning regime* that applies when the impurity potential is weak or the impurity concentration is dense [226]. In both cases the CDW periodicity is perturbed near defects, where it can minimize the impurity energy by matching its phase to the impurity location, in cost of elastic energy due to the resulting distortion. CDW pinning is reported to play an important role for the CDWs properties in $NbSe_2$ [253] and doped $NbSe_3$ [254], as well as in the formation of the CDW phase at the ultrathin Sn/Ge(111)-α interface [255].

The effects of defects in VSe_2 is investigated by analyzing different batches of VSe_2 with varying defect concentrations. The defects are likely point defects such as Se vacancies or V interstitials, but could also stem from the transport agent used for sample preparations.

Fig. 9.5 (a) shows an STM image with a moderate concentration of defects. The upper left part of the image, which is essentially defect-free, shows a pronounced, symmetric (4×4) periodicity due to the CDW formation. This periodicity is strongly perturbed near to defects, resulting in a distorted wave pattern. This perturbation is also visible in STS maps taken at the same location, see Fig. 9.5 (b). The energy is chosen to be near to the CDW gap since this is the energy where one expects the standing wave pattern to be most pronounced due to the selected (nesting) wave vector. The CDW periodicity is best visible in the defect-free region, while it is attenuated near the defect bunches such as in the right and lower part of the image. These observations clearly show that defects strongly influence the appearance of the CDW in VSe_2 when imaged with STM. The attenuation in the LDOS points to weak pinning instead of strong pinning, which is also plausible due to the high concentration of defects in the image.

It is possible to suppress the CDW amplitude on the surface of VSe_2 even further by increasing the defect concentration as shown in Fig. 9.5 (c) and (d). While the CDW is still visible in real space and in the FT of Fig. 9.5 (c) it is almost completely suppressed in Fig. 9.5 (d) and not visible in its FT. The defects induce an incoherent pattern on the surface due to the pinning of the CDW phase at the defects [226]. Interestingly, the CDW gap in the DOS is unaffected by the disappearance of the CDW, see Fig. 9.5 (e). The spectrum is taken at the blue dot in Fig. 9.5 (d) and shows a pronounced gap in both $\mathrm{d}I/\mathrm{d}V$ and $\mathrm{d}I/\mathrm{d}V/I/V$ that is in agreement (within error margin) with CDW gaps taken at locations free of defects. This leads to the conclusion that though defects act as local potential scatterers that affect the phase coherence of the CDW, they barely influence the amplitude of the CDW and its corresponding phase transition. These findings agree with reported ion bombardment experiments on VSe_2 [250], which found that the phase transition only reduces from 110 K to around 80 K when introducing a fraction of displaced metal atoms as large as 10^{-2} [252].

9.4 Discussion

The electronic properties of VSe_2 that are accessible with STS spectra are two-fold. First, one is able to resolve the non-monotonic energy-dependence of the VSe_2 DOS. The strong deviation between STS and the TB model in the unoccupied DOS reveals the need to probe both occupied and unoccupied states to get a complete and reliable picture of the band structure and resulting DOS of VSe_2. The flat band at the Γ point near to the Fermi level is the most pronounced feature in STS spectra due to its vanishing $k_{||}$.

In addition, we find a pronounced suppression in the DOS around the Fermi level that is attributed to the CDW formation at low temperatures. This gap is located very near to the peak that arises due to the flat VSe_2 band. The latter can easily be mistaken as the CDW gap, an issue which is likely the main reason for the strong scattering of the CDW gap 2Δ reported in STS experiments [245, 246]. Only with the knowledge of the DOS of VSe_2, one may be able to extract the CDW gap by subtracting the contribution of the undistorted VSe_2 DOS. Another important aspect of the CDW gap is that it lacks a sharp edge in STS spectra, presumably due to the small fraction of the Fermi surface involved in the CDW gap opening. This makes a quantitative analysis difficult. Our way of analyzing the size of the CDW gap may be viewed as a lower bound for 2Δ.
The extracted CDW gap 2Δ can be used to estimate the electron-phonon coupling strength in VSe_2. Using Eq. 2.4, the transition temperature T_C of VSe_2 is given by:

$$T_C = \frac{2\Delta}{3.52 k_B} = 80 \pm 20 \text{ K}. \tag{9.1}$$

This represents the expected transition temperature in the case of weak electron-phonon coupling. Note that large electron-phonon coupling leads to a overestimation of T_C [88]. As a reminder, the actual transition temperatures of VSe_2 are 110 K (incommensurate) and 80 K (commensurate). These values are very near to the expected transition temperature using the above formula, leading to the conclusion that the CDW formed in VSe_2 is induced by a weak electron-phonon coupling and governed by the states near to the Fermi energy only. Note that the tendency to even lower transition temperatures than the actual T_C may be related to the way we extracted the CDW gap, as mentioned above. This is in contrast to other CDWs in TMDC with strong electron-phonon coupling such as TaS_2, which has a larger CDW gap compared to its actual transition temperature and also shows a perturbed band structure in a wide energy range in the CDW phase, together with a strong lattice distortion of 7% [88]. The weak electron-phonon coupling in VSe_2 is also in line with ARPES measurements which show only small changes, if any, in the band structure when crossing T_C, together with the lack of replica bands expected when the electron-phonon coupling would be strong [239, 247, 248].
Assuming that the electron-phonon coupling is weak, Pasztor et al. [94] proposed that the CDW modulation amplitude, which is proportional to the CDW gap in the mean field approximation [87], can be used as an order parameter to obtain the transition temperature and CDW gap of VSe_2. They were able to obtain the thickness-dependent transition temperature of VSe_2 using this analysis, a strong evidence that this method is indeed reliable. However, our results show that defects strongly affect the CDW modulation in

STM images, though the CDW gap is still present, without any measurable size reduction. This leads to the conclusion that the amplitude measured in STM is not a reliable quantity to measure the CDW amplitude as soon as defects are present on the surface of VSe_2. Nevertheless, the good agreement between experiment and theoretical model in the data of Pasztor et al. [94] shows that, at least on very clean surfaces, the amplitude may be a good quantity to extract the CDW gap.

9.5 Conclusions

The DOS of VSe_2 is analyzed with STS. It is mainly attributed to the various bands of the TMDC. The knowledge of the expected DOS using ARPES and TB is mandatory to extract the CDW gap from STS spectra. The theoretical transition temperature that is obtained with the CDW gap is in line with its actual transition temperature, leading to the conclusion that the CDW in VSe_2 is induced by weak electron-phonon coupling. The CDW is shown to persevere at high defect densities, though the CDW modulation amplitude is strongly suppressed, presumably due to weak pinning.

PART IV

Summary

The electronic properties of the layered materials BLG, $BiSbTeSe_2$, ML MoS_2, and VSe_2 were investigated in this thesis. In general, the most important message is that gaining knowledge of the interactions involved in the system often leads to a high level of control of it, which is ultimately used to manipulate the fundamental electronic properties of layered materials. Current and possible future realizations of these goals are summarized in the following.

The electronic properties of strongly n-doped BLG were investigated by mapping QPI patterns on the top layer. These patterns revealed that two principal scattering wave vectors produce a strong QPI signal, while two additional principal scattering wave vectors are absent or weak. The latter finding is attributed to layer polarization and antiparallel velocities of the states involved in the scattering process. The general result that antiparallel velocities are much more favored compared to parallel velocities may drastically simplify the identification of scattering vectors found in future QPI studies, especially when several bands are present in the CEC of the material under investigation. With the second finding that layer polarization manifests itself in our experiments, it is now possible to monitor with QPI the degree of localization that results from p- or n-doping from the backside of any layer-polarized bilayer. While Cs intercalation has been demonstrated for BLG in this thesis, one could intercalate in future studies other elements between BLG and Ir(111), which should lead to drastic changes in the QPI intensities according to our claims. A promising example would be O intercalation, which has been shown to significantly p-dope graphene [256] and should therefore - with respect to the Cs case - reverse the intensities of the scattering vectors which are sensitive to the layer polarization. An enhanced level of complexity may even be realized by Ge intercalation, which, depending on its concentration, leads simultaneously to p and n doping of graphene ribbons on SiC [40]. The resulting system could be used to study the role of layer polarization in the transmission probability through pn-junctions with QPI, by analyzing the contribution of each scattering channel to the standing waves measured at the junction.

Future devices designed to utilize the surface state of TIs need a high level of control regarding the position of the chemical potential, to be able to induce spin-polarized currents of Dirac electrons and holes while maintaining an insulating bulk. Significant efforts have been made to obtain bulk-insulating, compensated TIs. However, large fluctuations of the order of the band gap were found to result in bulk charge puddles, representing a major loss of control regarding the position of the chemical potential. Yet our study shows that these large potential fluctuations in the bulk are strongly suppressed on the surface, which is attributed to the surface state and a possible interplay of bulk and surface charge

puddles. Hence, though compensated TIs do host charge puddles that locally affect the position of the Dirac cone with respect to the chemical potential, these effects are found to be of the order of 10 meV at the surface, so that a high level of control is maintained in these materials. The small fluctuations are additionally demonstrated with QPI, which finds a well-defined, linear, electron-like band and in general shows very good agreement with theoretical calculations based on the T-matrix theory. The standing wave pattern is composed of two contributions, which arise from delta potentials and screened Coulomb potentials. The ratio of these, as well as the screening radius of the surface state, is extracted from a fit to the experimental data. These insights may lead to otherwise hidden information in future QPI studies, which generally tend to underestimate the role of the scattering potential.

Quasi-freestanding 2D materials such as MoS_2 on MLG/Ir(111) are found to be very responsive to defects and charge. After characterizing the band gap of MoS_2 in detail, several types of line defects were investigated to understand their influence on the electronic properties of MoS_2. The impact of charge is demonstrated with Eu intercalation between MLG and Ir(111), leading to a shift and reduction of the band gap of MoS_2. Future studies of MoS_2/MLG/Ir(111) using other defects or different doping levels may lead to a complete, atomic-scale picture of the electronic properties of quasi-freestanding MoS_2 in dependence on defect type and concentration, as well as charge depletion and accumulation, which is mandatory to achieve full control of these peculiar 2D materials in possible optoelectronic devices.

One-dimensional states are fundamentally interesting due to their unique electronic characteristics, which often lead to interesting phase transitions. The MTBs found in MoS_2 on MLG/Ir(111) feature such one-dimensional states with a wealth of fascinating properties. Two types of MTBs are observed, which can be attributed to be of 4|4E and 4|4P structure, respectively. We find a CDW gap in the density of states, which is related to the periodic beating found in real space. Additional peaks appear due to the finite size of the MTBs and the corresponding confinement of the states. Excitation found in STS spectra can be linked to lattice vibrations present in monolayer MoS_2. An interesting future task will be to investigate line defects in other TMDCs such as WS_2, which may also feature different MTB structures such as the 55|8 MTB - composed of two 5-membered rings connected to an 8-membered ring - which hosts strongly localized, spin-polarized states [72]. It should also be noted that the understanding of the present one-dimensional states in MoS_2 is far from being complete. Nevertheless, the strong length-dependence of the CDW gap, as well as the changes in the beating pattern upon doping, indicate several

routes towards the control and manipulation of these one-dimensional states, which might permit deliberate tailoring on the atomic scale, ultimately by removing or adding a single atom. Its full phase diagram as a function of doping represents a hot topic which should be addressed experimentally and theoretically in the future.

Knowledge of the fundamental electronic properties of metallic TMDCs with complex band structures is essential to investigating subtle effects in the DOS caused by the corresponding phase transitions. In the case of VSe_2, strong features in the DOS near the chemical potential mask the CDW gap, leading to a strong scatter of the gap size in literature. The identification of these features with the help of ARPES and TB calculations makes it possible to subtract these contributions and thereupon extract the CDW gap. As a result, we could identify VSe_2 as a CDW material of the weak-coupling type. Perturbations in the form of defects strongly suppress the CDW amplitude in real space due to weak pinning, while the gap remains unchanged in the DOS. In the future, it could become possible to reduce the defect density such that the effect of single, well-separated atoms may be studied. This could be achieved by deliberately depositing single atoms on the clean VSe_2 surface at low temperatures. These scattering centers may cause strong pinning, leading to a possible increase of the CDW amplitude, which in turn can also have a global influence on the CDW phase, as found in related systems [253, 255].

PART V

Appendix

APPENDIX A

Varying the hopping parameters of bilayer graphene

The influence of the various in-plane (γ_0) and out-of-plane (γ_1, γ_3, γ_4) hopping parameters can be visualized best by comparing the resulting band structure when varying one of the hopping parameters. In Fig. A.1 (a) γ_0 is increased from 0.2 eV to 0.4 eV. We clearly see that the slope of the bands are strongly influenced by this hopping parameter, as in MLG. The CBM and VBM are not affected. Fig. A.1 (b) shows the changes in the band structure when increasing γ_1 from 0.1 eV to 0.5 eV. The major changes are at the K point, where a gap opens between the second valence and conduction band. This gap increases with increasing γ_1.

While γ_0 and γ_1 cause severe changes in the band structure of BLG, the hopping parameters γ_3 and γ_4 are found to cause only minor perturbations on the energy scale that is accessible in our experiments, see Fig. A.1 (c)-(d).

The changes in the band structure when increasing the potential U are shown in Fig. A.2. For $U = 0$, the valence band minimum and conduction band maximum touch each at the K point. Hence, when both layers are equivalent, BLG is a zero-band gap semiconductor. When increasing U, we find that a gap opens at the K point. For $U \geqslant 0.15$ in Fig. A.2, one can clearly recognize the two maxima at the valence band maximum, forming a Mexican hat structure. A very similar shape is found at the conduction band minimum.

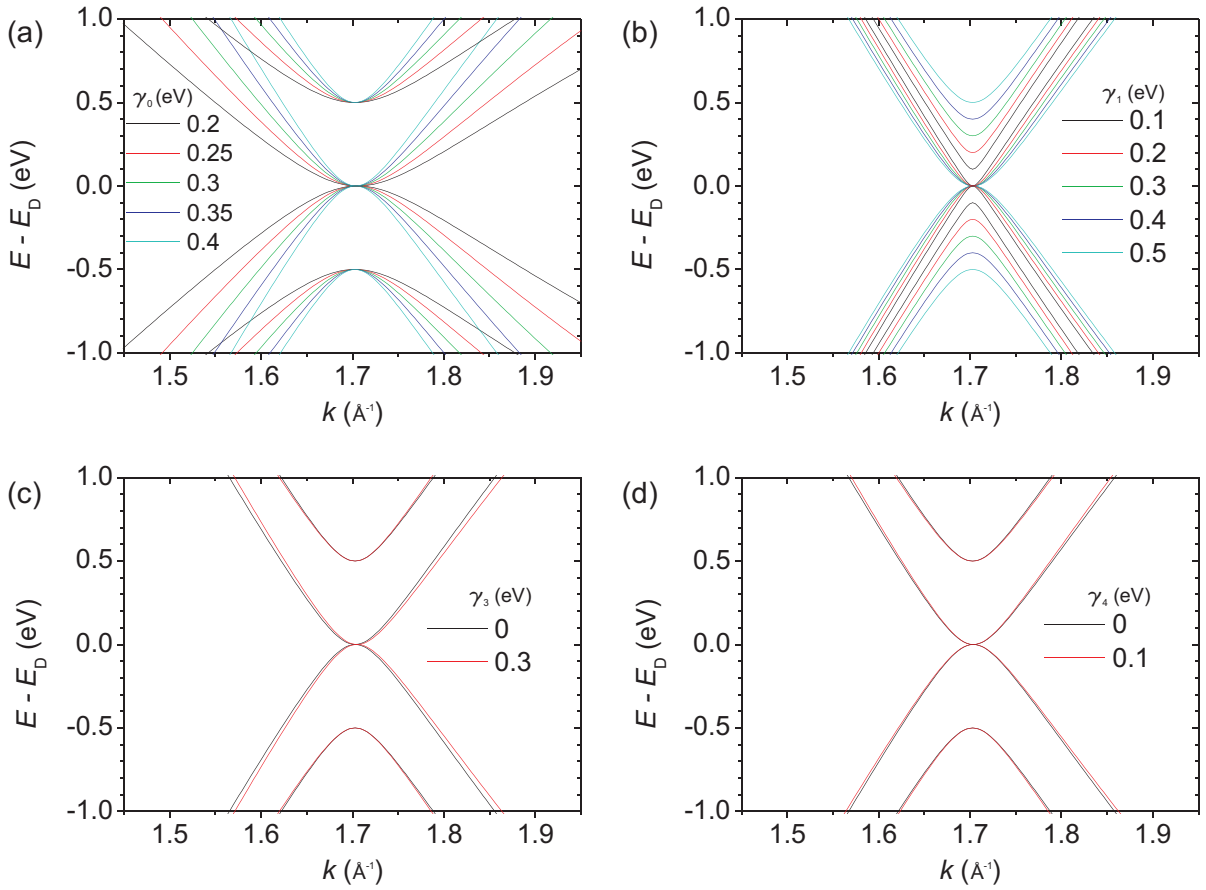


Figure A.1: Band structure of BLG with various hopping parameters: (a) Dependence on γ_0 ($\gamma_1 = 0.5$, $\gamma_3 = 0.1$, $\gamma_4 = 0$, $U = 0$). (b) Dependence on γ_1 ($\gamma_0 = 4$, $\gamma_3 = 0{,}1$, $\gamma_4 = 0$, $U = 0$). (c) Dependence on γ_3 ($\gamma_0 = 4$, $\gamma_1 = 0{,}5$, $\gamma_4 = 0$, $U = 0$). (d) Dependence on γ_4 ($\gamma_0 = 4$, $\gamma_1 = 0.5$, $\gamma_3 = 0.1$, $U = 0$).

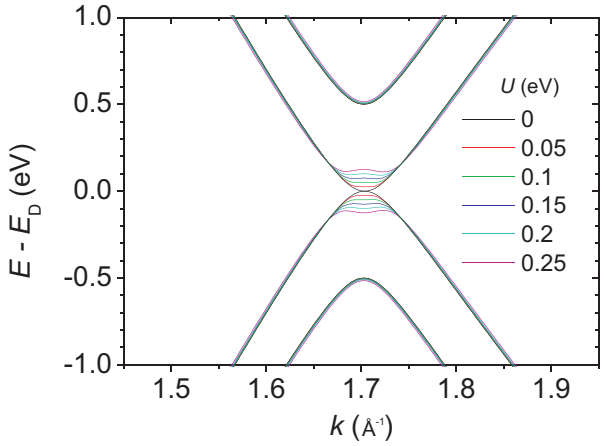


Figure A.2: Band structure of BLG with different potentials U ($\gamma_0 = 4$, $\gamma_1 = 0.5$, $\gamma_3 = 0.1$, $\gamma_4 = 0$).

APPENDIX B

Parallel versus antiparallel velocities in QPI - n-band model

In the following, A. Rosch investigated the role of parallel / antiparallel velocities on QPI for an n-band material in general.

First, it is useful to diagonalize the unperturbed Green's function using $G^0(\boldsymbol{k},E) = \sum_n |n,\boldsymbol{k}\rangle g_n^0(\boldsymbol{k},E)\langle n,\boldsymbol{k}|$ where $g_n^0(\boldsymbol{k},E) = \frac{1}{E-E_n(\boldsymbol{k})}$ describes the Green's function of the nth band. Using this notation one can rewrite $\rho(\boldsymbol{k},E)$ in the useful form

$$\rho(\boldsymbol{k},E) = -\frac{\mathrm{e}^{i\boldsymbol{r}_0\cdot\boldsymbol{k}}}{2\pi i}\sum_{nm}\int_{1.BZ}\frac{d^2\boldsymbol{q}}{S_{BZ}} g_n^0(\boldsymbol{q},E)g_m^0(\boldsymbol{q}+\boldsymbol{k},E)T^{nm}_{\boldsymbol{q},\boldsymbol{q}+\boldsymbol{k}}(E) - \left(g_n^0(\boldsymbol{q},E)g_m^0(\boldsymbol{q}+\boldsymbol{k},E)\right)^* (T^\dagger)^{nm}_{\boldsymbol{q},\boldsymbol{q}+\boldsymbol{k}}(E), \tag{B.1}$$

$$T^{nm}_{\boldsymbol{q},\boldsymbol{q}+\boldsymbol{k}}(E) = \sum_{j=1}^{4}\gamma_j\,\mathrm{e}^{-i\boldsymbol{r}_j\cdot\boldsymbol{k}}\langle j|n,\boldsymbol{q}\rangle\langle n,\boldsymbol{q}|T(E)|m,\boldsymbol{q}+\boldsymbol{k}\rangle\langle m,\boldsymbol{q}+\boldsymbol{k}|j\rangle, \tag{B.2}$$

$$(T^\dagger)^{nm}_{\boldsymbol{q},\boldsymbol{q}+\boldsymbol{k}}(E) = \sum_{j=1}^{4}\gamma_j\,\mathrm{e}^{-i\boldsymbol{r}_j\cdot\boldsymbol{k}}\langle j|n,\boldsymbol{q}\rangle\langle n,\boldsymbol{q}|T(E)^\dagger|m,\boldsymbol{q}+\boldsymbol{k}\rangle\langle m,\boldsymbol{q}+\boldsymbol{k}|j\rangle, \tag{B.3}$$

where $T^{nm}_{\boldsymbol{k},\boldsymbol{k}'}$ is the T-matrix for scattering from band m and momentum $\boldsymbol{k}'$ to band n and momentum $\boldsymbol{k}$ projected onto the states measured by the STM.

For local impurities the momentum dependence of the T-matrix is expected to be rather smooth and sharp peaks in the Fourier transformed QPI arise from the momentum dependence of

$$\Lambda_{nm}(\boldsymbol{k},E) = \int_{1.BZ}\frac{d^2\boldsymbol{q}}{S_{BZ}} g_n^0(\boldsymbol{q},E)g_m^0(\boldsymbol{q}+\boldsymbol{k},E) \tag{B.4}$$

with

$$g_n^0(\boldsymbol{q},E) = \frac{1}{E - E_{\mathbf{q}}^n + i\Gamma_{\boldsymbol{q}}^n} \tag{B.5}$$

where $E_{\boldsymbol{q}}^n$ is the dispersion of band n and we use Γ^n to mimic the effects of other impurities and inelastic scattering. In the limit of small Γ^n, peaks in $\Lambda_{nm}(\boldsymbol{k},E)$ arise along lines in reciprocal space, $\boldsymbol{k} \approx \boldsymbol{k}_\theta^p$ where $\boldsymbol{k}_\theta^p$ are the principle scattering vectors parametrized by θ. These vectors connect points, $\boldsymbol{q}_\theta$ and $\boldsymbol{q}_\theta + \boldsymbol{k}_\theta^p$ on the energy surface characterized by parallel or antiparallel Fermi velocities. For momenta $\boldsymbol{q}$ close to $\boldsymbol{q}_\theta$, we can use the Taylor expansion

$$\begin{aligned} E_{\boldsymbol{q}}^n &\approx E + v_1^\theta \hbar q_\parallel + \frac{\hbar^2}{2m_1^\theta} q_\perp^2 \\ E_{\boldsymbol{q}+\boldsymbol{k}}^m &\approx E + v_2^\theta \hbar (q_\parallel - \delta k) + \frac{\hbar^2}{2m_2^\theta} q_\perp^2 \end{aligned} \tag{B.6}$$

where $q_\parallel$ ($q_\perp$) is the distance from $\boldsymbol{q}_\theta$ measured parallel (perpendicular) to the Fermi velocities, respectively, $\boldsymbol{q} = \boldsymbol{q}_\theta + q_\parallel \hat{\boldsymbol{v}} + q_\perp(\hat{\boldsymbol{z}} \times \hat{\boldsymbol{v}})$, $\hat{\boldsymbol{v}} = \boldsymbol{v}_1^\theta / |v_1^\theta|$. v_1^θ and v_2^θ are the Fermi velocities at $\boldsymbol{q}_\theta$ and $\boldsymbol{q}_\theta + \boldsymbol{k}_\theta^p$, respectively. m_1^θ and m_2^θ are the corresponding masses which parametrize the local curvature of the Fermi surface. $\delta k = -\hat{v}(\boldsymbol{k} - \boldsymbol{k}_\theta^p)$ is the distance of the momentum $\boldsymbol{k}$ from the line of principle scattering vectors. For the chosen coordinate system we have $v_1^\theta > 0$ while v_2^θ can be either positive (parallel) or negative (antiparallel). A positive δk describes for particle-like (hole like) Fermi surface that $\boldsymbol{k}$ is too long (too short) to connect the two Fermi surfaces.

As we will show below, Λ_{nm} diverges in the limit $\Gamma_i, \delta k \to 0$. This singular contribution $\Lambda_{nm}^{\text{sing}}$ can be calculated in a straightforward way by a contour integration using the Taylor expansion (B.6).

$$\Lambda_{nm}^{\text{sing}}(\theta,\delta k) = \int \frac{dq_\perp dq_\parallel}{S_{BZ}} \frac{1}{-v_1^\theta \hbar q_\parallel - \frac{\hbar^2 q_\perp^2}{2m_1^\theta} + i\Gamma_1^\theta} \frac{1}{-v_2^\theta \hbar (q_\parallel - \delta k) - \frac{\hbar^2 q_\perp^2}{2m_2^\theta} + i\Gamma_2^\theta} \tag{B.7}$$

We first perform the integration over $q_\parallel$. If both velocities have the same sign, both poles of the integrand of Eq. (B.4) are located in the same half-plane and the integral vanishes exactly,

$$\Lambda_{nm}^{\text{sing}} = 0 \qquad \text{for parallel velocities} \tag{B.8}$$

Note that this is only the singular contribution, a regular contribution which is finite for $\Gamma^n \to 0$ and $\delta k \to 0$ will remain.

For antiparallel velocities, however, the integrals above do not vanish and we obtain after integrating out $q_\perp$

$$\begin{aligned}\Lambda^{\mathrm{sing}}_{nm}(\theta,\delta k) =& \frac{(2\pi)^2}{S_{BZ}}\left(\frac{m_1^\theta m_2^\theta}{2\hbar^5(m_1^\theta|v_1^\theta| + m_2^\theta|v_2^\theta|)|v_1^\theta v_2^\theta|}\right)^{1/2} \\ &\times \left(\frac{1}{|\delta k|}\right)^{1/2} g\left[\frac{\hbar v_1^\theta v_2^\theta\,\delta k}{v_2^\theta\Gamma_1^\theta - v_1^\theta\Gamma_2^\theta}\right] \qquad \text{(B.9)} \\ g(x) =& -\sqrt{|x|}\frac{1}{\sqrt{i-x}} \qquad \text{(B.10)} \\ \approx& -\Theta[-x] + i\Theta[x] \quad \text{for } |x| \gg 1\end{aligned}$$

where $\Theta(x>0)=1$ and $\Theta(x<0)=0$ are used to describe the asymptotics for small Γ_i^θ. To compute the singular part of the Fourier transformed QPI from a single impurity at a vector $\boldsymbol{k}$, one has first to identify the closest principle scattering vector $\boldsymbol{k}_\theta^p$ connecting bands n and m at points with antiparallel velocities. Then the closest distance δk to the line of principle scattering vectors can be determined. The singular part $\rho^{\mathrm{sing}}(\boldsymbol{k},E)$ of $\rho(\boldsymbol{k},E)$ is obtained from a complex linear combination of $\Lambda^{\mathrm{sing}}_{nm}$ and its complex conjugate

$$\begin{aligned}\rho^{\mathrm{sing}}(\boldsymbol{k},E) &= z_1^\theta\,\Lambda^{\mathrm{sing}}_{nm}(\theta,\delta k) + z_2^\theta\,(\Lambda^{\mathrm{sing}}_{nm}(\theta,\delta k))^* \qquad \text{(B.11)} \\ z_1^\theta &= -\frac{\mathrm{e}^{i\boldsymbol{r}_0\cdot\boldsymbol{k}}}{2\pi i}T^{nm}_{\boldsymbol{q}_\theta,\boldsymbol{q}_\theta+\boldsymbol{k}_\theta^p}(E) \\ z_2^\theta &= \frac{\mathrm{e}^{i\boldsymbol{r}_0\cdot\boldsymbol{k}}}{2\pi i}(T^\dagger)^{nm}_{\boldsymbol{q}_\theta,\boldsymbol{q}_\theta+\boldsymbol{k}_\theta^p}(E)\end{aligned}$$

In most cases the T-matrix is not known and $z_1^\theta, z_2^\theta \in \mathbb{C}$ should be viewed as (independent) complex fitting parameters. If several principle scattering vectors from a several pairs of bands n_i and m_i in distance δk_i are close by, one has to add the contributions from all i. Besides the singular contribution, there is in general also a smooth background, $\rho(\boldsymbol{k},E) = \rho^{\mathrm{sing}}(\boldsymbol{k},E) + \rho^{\mathrm{bg}}(\boldsymbol{k},E)$, which may be peaked around high-symmetry points in the BZ or around points connecting the middle of the bands. In a given sample many impurities located at positions $\boldsymbol{r}_0^i$ are present and one has to add their contributions $\rho_i(\boldsymbol{k},E)$. Assuming that rapidly oscillating contributions $\sim e^{i\boldsymbol{k}(\boldsymbol{r}_0^i-\boldsymbol{r}_0^j)}$ are filtered out during the experimental analysis, one effectively finds $|\rho(\boldsymbol{k},E)|^2 \approx \sum_i |\rho_i(\boldsymbol{k},E)|^2$. We have checked that to fit the singular contribution of the sum, it is sufficient to use the formula for a single impurity with adjusted parameters z_1^θ and z_2^θ. After absorbing also the prefactor of Eq. (B.11) into the fitting parameters, a fitting formula for a line scan

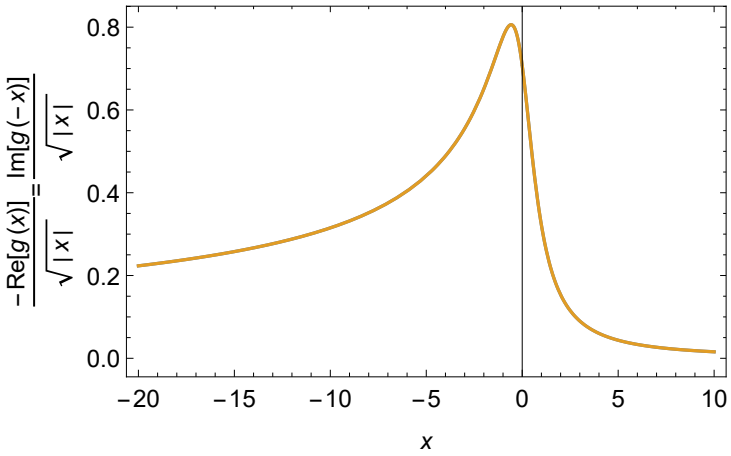


Figure B.1: The function $g(x)$ determines the shape of the peak with $\mathrm{Re}\, g(x) = -\mathrm{Im}\, g(-x)$. For positive masses, the real part of Λ_{nm} is proportional to the real part of $g(x)/\sqrt{x}$ which shows a $1/\sqrt{-x}$ behavior for negative $x \propto \delta k$, while it drops proportional to $1/x^{3/2}$ for positive x. The peak is located at $x = -1/\sqrt{3} \approx -0.58$. The k dependence of the Fourier transformed QPI is determined from a linear combination of real and imaginary part of Λ_{nm}. While one expects generically an asymmetric peak, the sign of the asymmetry therefore depends on the structure of the T matrix.

crossing several principle scattering vectors (with antiparallel velocities only) at position k_i^p is obtained,

$$\rho^{\mathrm{sing}}(k,E) \approx \sum_i c_i \frac{g\left(\frac{k-k_i^p}{\kappa_i}\right)}{\sqrt{|k-k_i^p|}} + \tilde{c}_i e^{i\phi_i} \frac{g^*\left(\frac{k-k_i^p}{\kappa_i}\right)}{\sqrt{|k-k_i^p|}} \tag{B.12}$$

$$\tag{B.13}$$

where four real fitting parameters c_i,$\tilde{c}_i$,ϕ_i,κ_i are used to fit the amplitude, shape and width for each peak.

Peaks in the QPI arise because Λ_{sing} increases proportional to $1/\sqrt{|\delta k|}$ upon approaching the lines of principle scattering vectors giving rise to the characteristic ring in Fourier transformed QPI. The $1/\sqrt{\delta k}$ divergence is directly related to a slow decay of the corresponding correlations in real space [257] and has been obtained analytically for 2d Dirac or Weyl fermion by Guo and Franz [258] and for a single parabolic band by Capriotti, Scalapino and Sedgewick [259]. Our formula generalizes those results to multi-band situation, including the case of parallel velocities where all singular contributions vanish.

The formula (B.9) shows under what conditions the prefactor of the $1/\sqrt{\delta k}$ singularity gets large: this occurs when both velocities become slow $v_i^\theta \to 0$, when both masses become large (nesting of parallel Fermi surfaces), or when $m_1^\theta |v_1^\theta| + m_2^\theta |v_2^\theta| \approx 0$. To understand

the significance of the latter condition, we observe that according to Eq. (B.6) the shape of the Fermi surface is approximately given by $q_\parallel \approx -\frac{\hbar^2}{2v_i^\theta m_i^\theta} q_\perp^2$. The prefactor therefore diverges when there is a nesting of a particle-like and a hole-like Fermi surface. Due to the conditions that the Fermi velocities should be opposite to each other, a nesting of two particle like Fermi surfaces is only possible when both Fermi surfaces are flat, $m_i^\theta \to \infty$. While our formulas correctly describe the behavior in the proximity of such points, they are not valid exactly at such nesting points, where one has to use higher orders in the Taylor expansion (B.6).

The function $g(x)$ describes the asymmetric line shape arising from the real and imaginary parts of $\Lambda_{nm}^{\mathrm{sing}}$. When δk gets smaller than the inverse mean-free path of the electrons, the divergence is cut off. The properties of $g(x)$ are discussed in Fig. B.1. Note that our calculation has not included vertex corrections which arise when one computes the disorder-average of $|\rho(\boldsymbol{k},E)|^2$. These vertex corrections describe how the presence of other impurities affect the interference pattern. These effects can modify the line-shape in the regime $|x| \lesssim 1$. In contrast, if the main effect of broadening arises from electron-electron or electron-phonon interactions, the predicted line shape should be exact in the low-disorder limit. The highly asymmetric properties of $g(x)$ for $|x| \gg 1$, see Eq. (B.10), are, however, unaffected by both types of corrections as they vanish in the limit of a large mean free path.

Experimentally, the FT of the QPI pattern is proportional to $|\rho(k,E)|$. Using the definition of $g(x)$, an experimental line scan with n features can be fitted by the following function:

$$|\rho^{\mathrm{sing}}(k,E)| \approx \sum_i \sqrt{\frac{1}{\kappa_i}\left[\frac{c_i^2+\tilde{c}_i^2}{\sqrt{1+\left(\frac{k-k_i^p}{\kappa_i}\right)^2}} - \frac{2c_i\tilde{c}_i}{1+\left(\frac{k-k_i^p}{\kappa_i}\right)^2}\left(\sin\phi_i + \frac{k-k_i^p}{\kappa_i}\cos\phi_i\right)\right]}. \tag{B.14}$$

As a proof of principle, a fit of this formula to an experimental line scan is shown in Fig. 5.6 (c). Here, only the four most pronounced peaks were included in the fit and the artifact at low k was excluded. It is evident that the formula is able to reproduce the experimental data. At the present time, however, it is not clear whether this fit is unique and what is the physical meaning of the fit parameters. In addition, the fit could be further improved by the incorporation of additional peaks and the subtraction of a suitable, smooth background.

Further work is necessary to examine the full power of our fitting function, ideally with improved experimental resolution or in a simpler system.

APPENDIX C

Identifying mirror twin boundaries in molybdenum disulfide

Atomically resolved STM images of MTBs in MoS_2/graphene/Ir(111) are shown in Fig. C.1. In Fig. C.1 (a), one finds two grains separated by a line defects, which has a periodic modulation with a period of $2a$. An inspection of the orientation of both grains leads to the conclusion, that both have the same orientation. This is visualized with white lines in

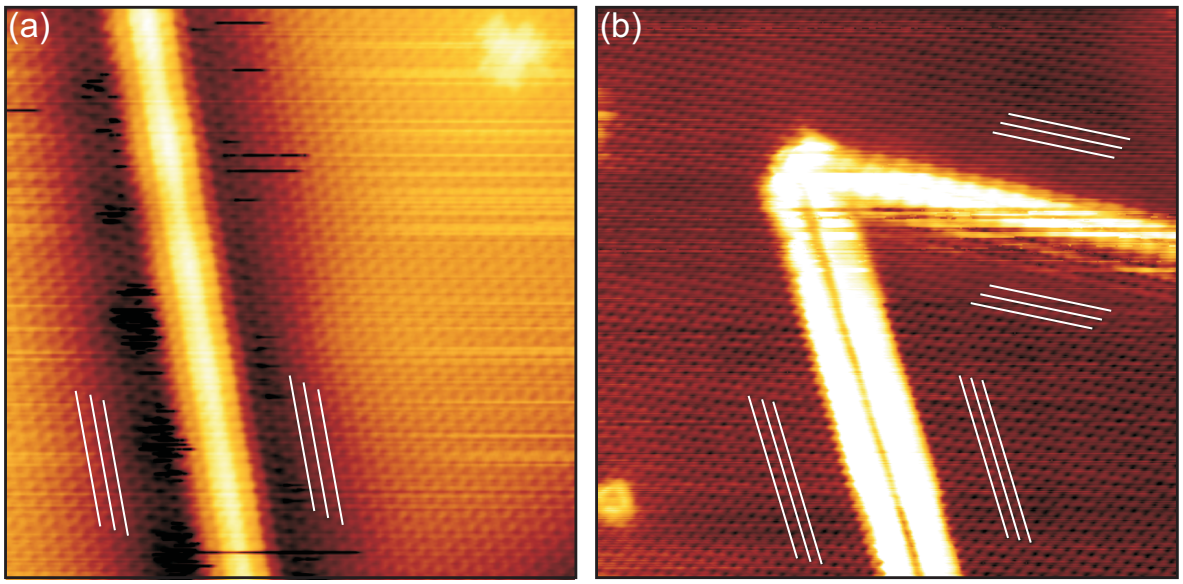


Figure C.1: MTBs in MoS_2: (a) Constant current STM image of a 4|4E MTB in MoS_2/graphene/Ir(111) (U = 0.9 V, I = 0.5 nA, image size (12 × 12) nm^2). The white lines show that both grains are perfectly alined. (b) Constant current STM image of a grain boundary forming both a 4|4E and a 4|4P MTB (U = 0.4 V, I = 1 nA, image size (15 × 15) nm^2).

Fig. C.1 (a). Hence this grain boundary must be a MTB. With its electronic signature, which is described in Chap. 8, the MTB can be attributed to a 4|4E MTB.
Another atomically resolved STM image is shown in Fig. C.1 (b). It show one line defect with a periodic beating of $2a$, together with another grain boundary which displays double tracks instead of a single track. This feature, together with a periodic beating of $3a$, clearly distinguishes both boundaries. When identifying the orientation of the atomic rows, however, one finds that both grains have the same orientation. Hence both grain boundaries must be MTBs. The MTB with double tracks is attributed to a 4|4P MTB, as described in Chap. 8.

APPENDIX D

Deutsche Kurzzusammenfassung *(German Abstract)*

Diese Arbeit beschäftigt sich mit den elektronischen Eigenschaften von geschichteten Materialien, mit Fokus auf die zugrunde liegenden Wechselwirkungen. Experimentell wird ein Rastertunnelmikroskop benutzt, um die Zustandsdichte an der Oberfläche dieser Materialien zu messen. Die zu untersuchenden Materialien sind Bilagen-Graphen, topologische Isolatoren und Übergangsmetalldichalkogenide. Die Ergebnisse werden verglichen mit theoretischen Rechnungen basierend auf Dichtefunktionaltheorie und Tight-Binding, die von Kooperationspartnern bereitgestellt wurden.

Das Streuverhalten von Bilagen-Graphen wurde untersucht. Dieses Material besitzt eine lagenpolarisierte Bandstruktur, was bedeutet, dass die elektronischen Zustände eher in einer von beiden Lagen zu finden sind. Die Lagenpolarisierung führt dazu, dass einige Streukanäle stark unterdrückt sind. Unsere Streuexperimente liefern also einen indirekten Nachweis dieses Phänomens. Ein weiterer Streuvektor ist stark unterdrückt, da er Zustände mit parallelen Geschwindigkeiten verbindet. Letzteres ist ein generelles Resultat, welches Anwendung im Falle von komplexen Systemen mit mehreren Bändern findet.

Ein weiteres Thema dieser Arbeit befasst sich mit Potentialfluktuationen in kompensierten topologischen Isolatoren. Diese Fluktuationen, die vor kurzem optisch nachgewiesen wurden, entstehen durch geladene Störatome und sind von der Größenordnung der Bandlücke des Materials. Sie stellen eine große Herausforderung dar, wenn man den spinaufgelösten Oberflächenzustand ohne störenden Beitrag der Elektronen im Kristall erforschen möchte. Unsere Untersuchungen der Fluktuationen auf der Oberfläche des topologischen Isolators $BiSbTeSe_2$ haben ergeben, dass diese viel kleiner sind als die Flukuationen im Kristall. Es stellte sich heraus, dass der Oberflächenzustand selbst die Fluktuationen dämpft, indem er die Ladungen mit Hilfe von Screening verdeckt. Die Kopplung zwischen den Fluktua-

tionen im Innern und an der Oberfläche des Kristalls scheint einen zusätzlichen Beitrag zu leisten, der die Fluktuationen noch weiter dämpft. So wird der Effekt an der Oberfläche um eine Größenordnung reduziert. Außerdem ist die Streuung der Dirac-Elektronen in sehr guter Übereinstimmung mit theoretischen Rechnungen, welche weitere physikalische Parameter des Systems, wie das Verhältnis zwischen geladenen und ungeladenen Potentialen, sowie die Screening-Länge der Dirac-Elektronen, liefern.
Die elektronischen Eigenschaften von MoS_2 auf Graphen/Ir(111) wurden genau untersucht. Die Zustände nahe der Bandlücke wurden genau bestimmt und verglichen mit ab initio-Rechnungen. MoS_2 besitzt eine große Spin-Aufspaltung in einigen der Bänder durch die starke Spin-Bahn-Kopplung in diesem Material. Es ist möglich, die Bandlücke lokal stark zu beeinflussen, was wir anhand verschiedener Beispiele, wie Defekten und Dotierung, zeigen.
Ein Kapitel dieser Arbeit befasst sich mit der Beobachtung, dass elektronische Zustände in spiegelsymmetrischen Zwillingsgrenzen in MoS_2 bei tiefen Temperaturen zu einer Ladungsdichtewelle zu kondensieren scheinen. Da MoS_2 einen Halbleiter ist, stellen unsere Ladungsdichtewellen ein traumhaftes System für Grundlagenfoschung an eindimensionalen Zuständen dar. Wir können die elektronischen Eigenschaften der Ladungsdichtewelle messen und manipulieren, indem wir zum Beispiel Defekte einbauen, die Länge der Zwillingsgrenze variieren, oder die Unterlage dotieren.
In der Literatur werden die Eigenschaften der dreidimensionalen Ladungsdichtewelle in VSe_2 diskutiert, wobei starke Variationen zu finden sind: Die experimentell bestimmte Bandlücke, die bei Temperaturen unter dem Phasenübergang in dem Material entsteht, schwankt zwischen 0 und 160 meV. Außerdem ist der Mechanismus, der für den Phasenübergang verantwortlich gemacht wird, nicht gut verstanden. Unsere Messungen zeigen, dass die Signale, die zum Teil in der Literatur für die Bandlücke gehalten wurden, durch Van-Hove-Singularitäten in der Bandstruktur entstehen und unabhängig von der Ladungsdichtewelle sind. Erst unter Berücksichtigung dieser Signale kann die Bandlücke von VSe_2, welche in Einklang mit der Theorie schwacher Elektron-Phonon-Kopplung steht, analysiert werden.

APPENDIX E

Liste der Teilpublikationen
(List of Publications)

Teile dieser Arbeit wurden bereits veröffentlicht in den folgenden Fachzeitschriften:
Parts of the results presented in this thesis can be found in the following publications:

[130] Daniela Dombrowski, **Wouter Jolie**, Marin Petrović, Sven Runte, Fabian Craes, Jürgen Klinkhammer, Marko Kralj, Predrag Lazić, Eran Sela and Carsten Busse
Energy-Dependent Chirality Effects in Quasifree-Standing Graphene
Physical Review Letter **118**, 116401 (2017)

[119] Timo Knispel, **Wouter Jolie**, Nick Borgwardt, Jonathan Lux, Zhiwei Wang, Yoichi Ando, Achim Rosch, Thomas Michely, Markus Grüninger
Charge puddles in the bulk and on the surface of the topological insulator $BiSbTeSe_2$ studied by scanning tunneling microscopy and optical spectroscopy
Submitted to Phys. Rev. B

[118] Joshua Hall, Borna Piélic, Clifford Murray, **Wouter Jolie**, Tobias Wekking, Carten Busse, Marko Kralj, and Thomas Michely
Molecular beam epitaxy of quasi-freestanding transition metal disulfide monolayers on van der Waals substrates: A growth study
Submitted to 2D Mater.

[129] **Wouter Jolie**, Jonathan Lux, Mathias Pörtner, Daniela Dombrowski, Charlotte Herbig, Timo Knispel, Sabina Simon, Thomas Michely, Achim Rosch, Carsten Busse
Visualizing layer polarization in bilayer graphene with quasiparticle interference
Submitted to Phys. Rev. Lett.

[260] **Wouter Jolie**, Clifford Murray, Fabian Portner, Joshua Hall, Nicolae Atodiresei, Arkadi Krasheninnikov, Carsten Busse, Achim Rosch, Hannu-Pekka Komsa, Thomas Michely
One-dimensional charge density waves in MoS_2 grain boundaries
In preparation

Weitere Publikationen:
Further publications:

[45] **Wouter Jolie**, Fabian Craes, Marin Petrović, Nicolae Atodiresei, Vasile Caciuc, Stefan Blügel, Marko Kralj, Thomas Michely, Carsten Busse
Confinement of Dirac electrons in graphene quantum dots
Physical Review B **89**, 155435 (2014)

[261] Charlotte Herbig, E. Harriet Åhlgren, **Wouter Jolie**, Carsten Busse, Jani Kotakoski, Arkady V. Krasheninnikov, Thomas Michely
Interfacial Carbon Nanoplatelet Formation by Ion Irradiation of Graphene on Iridium(111)
ACS Nano **8**, 12208–12218 (2014)

[46] **Wouter Jolie**, Fabian Craes, Carsten Busse
Graphene on weakly interacting metals: Dirac states vs. surface states
Physical Review B **91**, 115419 (2015)

[262] Charlotte Herbig, E. Harriet Åhlgren, Ulrike A. Schröder, Antonio J. Martinez-Galera, Mohammad A. Arman, **Wouter Jolie**, Carsten Busse, Jani Kotakoski, Jan Knudsen, Arkady V. Krasheninnikov, Thomas Michely
Comment on Interfacial Carbon Nanoplatelet Formation by Ion Irradiation of Graphene on Iridium(111)
ACS Nano **9**, 4664-4665 (2015)

[263] Antonio J. Martinez-Galera, Ulrike A. Schröder, Felix Huttmann, **Wouter Jolie**, Fabian Craes, Carsten Busse, Vasile Caciuc, Nicolae Atodiresei, Stefan Blügel and Thomas Michely
Oxygen orders differently under graphene: new superstructures on Ir(111)
Nanoscale **8**, 1932 (2016)

[264] Iva Srut Rakić, Marko Kralj, **Wouter Jolie**, Predrag Lazić, Wenhao Sun, José Avila, Maria-Carmen Asensio, Fabian Craes, Vesna Miksić Trontl, Carsten Busse,

Petar Pervan
Step-induced faceting and related electronic effects for graphene on Ir(332)
Carbon **110**, 267-277 (2016)

[265] Ferdinand H. Farwick zum Hagen, Domenik M. Zimmermann, Caio C. Silva, Christoph Schlueter, Nicolae Atodiresei, **Wouter Jolie**, Antonio J. Martinez-Galera, Daniela Dombrowski, Ulrike A. Schröder, Moritz Will, Predrag Lazić, Vasile Caciuc, Stefan Blügel, Tien-Lin Lee, Thomas Michely, Carsten Busse
Structure and Growth of Hexagonal Boron Nitride on Ir(111)
ACS Nano **10**, 11012-11026 (2016)

Konferenzbeiträge als präsentierender Autor:
Conference contributions:

- DFG Schwerpunktprogramm 1459 *Graphene*, contributed poster entitled *Confinement of Dirac electrons on graphene quantum dots*, Chemnitz (2014)
- The European Workshop on Epitaxial Graphene and 2D Materials, contributed talk entitled *Confinement of Dirac electrons on graphene quantum dots*, Primosten (2014)
- Quantum Matter and Materials Retreat, contributed talk entitled *Quasiparticle scattering in graphene*, Bad Breisig (2014)
- DPG Frühjahrstagung der Sektion Kondensierte Materie, contributed talk entitled *Graphene on weakly interacting metals*, Berlin (2014)
- Bonn-Cologne Graduate School of Physics and Astronomy Poster Session, contributed poster entitled *Confinement on graphene quantum dots*, Cologne (2015)
- Frontiers in Scanning Probe Microscopy, contributed poster entitled *Confinement on graphene quantum dots*, Bad Honnef (2015)
- The European Workshop on Epitaxial Graphene and 2D Materials, contributed poster entitled *Confinement on graphene quantum dots*, Bergisch Gladbach (2016)
- Bonn-Cologne Graduate School of Physics and Astronomy Poster Session, contributed poster entitled *Doping bilayer graphene from below*, Bonn (2016)
- Young Academics *Graphen und 2D-Materialien* Poster Session, contributed poster entitled *Doping bilayer graphene from below*, Siegen (2016)
- 7. NRW Nano-Konferenz, contributed poster entitled *Doping bilayer graphene from below*, Münster (2016)
- DPG Frühjahrstagung der Sektion Kondensierte Materie, contributed poster entitled *Quasiparticle interferences in highly doped bilayer graphene*, Dresden (2017)

Preise und Auszeichnungen:
Awards and Honors:

- 2D Materials Focus Topic Student Travel Grant, AVS-64th International Symposium and Exhibition, Tampa, 2017
- Poster Prize of the Young Academics *Graphen und 2D-Materialien* Poster Session, Siegen 2016
- Member of the Honors Branch of the Bonn Cologne Graduate School of Physics and Astronomy (scholarship)

APPENDIX F

Bibliography

[1] J. Bardeen, L. N. Cooper, and J. R. Schrieffer: "Theory of Superconductivity". Phys. Rev. **108** 1175–1204 (1957).

[2] C. de la Cruz et al.: "Magnetic order close to superconductivity in the iron-based layered $LaO_{1-x}F_xFeAs$ systems". Nature **453** 899–902 (2008).

[3] R. E. Peierls: Quantum Theory of Solids. Oxford: Clarendon (1955).

[4] S. Mühlbauer et al.: "Skyrmion Lattice in a Chiral Magnet". Science **323** 915–919 (2009).

[5] M. Z. Hasan and C. L. Kane: "Colloquium : Topological insulators". Rev. Mod. Phys. **82** 3045–3067 (2010).

[6] S. A. Wolf: "Spintronics: A Spin-Based Electronics Vision for the Future". Science **294** 1488–1495 (2001).

[7] D. Pesin and A. H. MacDonald: "Spintronics and pseudospintronics in graphene and topological insulators". Nat. Mater. **11** 409–416 (2012).

[8] A. K. Nayak et al.: "Magnetic antiskyrmions above room temperature in tetragonal Heusler materials". Nature **548** 561–566 (2017).

[9] S. Sachdev: "Quantum Criticality: Competing Ground States in Low Dimensions". Science **288** 475–480 (2000).

[10] E. Dagotto: "Correlated electrons in high-temperature superconductors". Rev. Mod. Phys. **66** 763–840 (1994).

[11] J. Wilson, F. Di Salvo, and S. Mahajan: "Charge-density waves and superlattices in the metallic layered transition metal dichalcogenides". Adv. Phys. **24** 117–201 (1975).

[12] K. S. Novoselov et al.: "Two-dimensional gas of massless Dirac fermions in graphene". Nature **438** 197–200 (2005).

[13] K. S. Novoselov et al.: "Two-dimensional atomic crystals". Proc. Natl. Acad. Sci. **102** 10451–10453 (2005).

[14] E. McCann and M. Koshino: "The electronic properties of bilayer graphene". Reports Prog. Phys. **76** 056503 (2013).

[15] E. V. Castro et al.: "Biased Bilayer Graphene: Semiconductor with a Gap Tunable by the Electric Field Effect". Phys. Rev. Lett. **99** 216802 (2007).

[16] T. Ohta et al.: "Controlling the electronic structure of bilayer graphene". Science **313** 951–954 (2006).

[17] F. Schwierz: "Graphene transistors". Nat. Nanotechnol. **5** 487–496 (2010).

[18] N. Borgwardt et al.: "Self-organized charge puddles in a three-dimensional topological material". Phys. Rev. B **93** 245149 (2016).

[19] L. Fu, C. L. Kane, and E. J. Mele: "Topological Insulators in Three Dimensions". Phys. Rev. Lett. **98** 106803 (2007).

[20] H. Zhang et al.: "Topological insulators in Bi_2Se_3, Bi_2Te_3 and Sb_2Te_3 with a single Dirac cone on the surface". Nat. Phys. **5** 438–442 (2009).

[21] K. F. Mak et al.: "Atomically Thin MoS_2: A New Direct-Gap Semiconductor". Phys. Rev. Lett. **105** 136805 (2010).

[22] G.-H. Lee et al.: "Flexible and Transparent MoS_2 Field-Effect Transistors on Hexagonal Boron Nitride-Graphene Heterostructures". ACS Nano **7** 7931–7936 (2013).

[23] D. Jariwala et al.: "Emerging Device Applications for Semiconducting Two-Dimensional Transition Metal Dichalcogenides". ACS Nano **8** 1102–1120 (2014).

[24] M. M. Ugeda et al.: "Giant bandgap renormalization and excitonic effects in a monolayer transition metal dichalcogenide semiconductor". Nat. Mater. **13** 1091–1095 (2014).

[25] J. A. Miwa et al.: "Electronic Structure of Epitaxial Single-Layer MoS_2". Phys. Rev. Lett. **114** 046802 (2015).

[26] D. Pierucci et al.: "Band alignment and minigaps in monolayer MoS2-graphene van der Waals heterostructures". Nano Lett. **16** 4054–4061 (2016).

[27] S. Barja et al.: "Charge density wave order in 1D mirror twin boundaries of single-layer MoSe2". Nat. Phys. **12** 751–756 (2016).

[28] Y. Ma et al.: "Angle resolved photoemission spectroscopy reveals spin charge separation in metallic $MoSe_2$ grain boundary". Nat. Commun. **8** 14231 (2017).

[29] H. Liu et al.: "Dense Network of One-Dimensional Midgap Metallic Modes in Monolayer $MoSe_2$ and Their Spatial Undulations". Phys. Rev. Lett. **113** 066105 (2014).

[30] H. C. Diaz et al.: "High density of (pseudo) periodic twin-grain boundaries in molecular beam epitaxy-grown van der Waals heterostructure: $MoTe_2/MoS_2$". Appl. Phys. Lett. **108** 191606 (2016).

[31] M. D. Johannes and I. I. Mazin: "Fermi surface nesting and the origin of charge density waves in metals". Phys. Rev. B **77** 165135 (2008).

[32] A. H. Castro Neto et al.: "The electronic properties of graphene". Rev. Mod. Phys. **81** 109–162 (2009).

[33] A. Rozhkov et al.: "Electronic properties of graphene-based bilayer systems". Phys. Rep. **648** 1–104 (2016).

[34] Z. Y. Zhu, Y. C. Cheng, and U. Schwingenschlögl: "Giant spin-orbit-induced spin splitting in two-dimensional transition-metal dichalcogenide semiconductors". Phys. Rev. B **84** 153402 (2011).

[35] D. Xiao et al.: "Coupled Spin and Valley Physics in Monolayers of MoS_2 and Other Group-VI Dichalcogenides". Phys. Rev. Lett. **108** 196802 (2012).

[36] Y. Ando: "Topological Insulator Materials". J. Phys. Soc. Japan **82** 102001 (2013).

[37] K. S. Novoselov: "Electric Field Effect in Atomically Thin Carbon Films". Science **306** 666–669 (2004).

[38] A. K. Geim and K. S. Novoselov: "The rise of graphene". Nat. Mater. **6** 183–191 (2007).

[39] L. A. Ponomarenko et al.: "Chaotic Dirac billiard in graphene quantum dots." Science **320** 356–358 (2008).

[40] J. Baringhaus et al.: "Ballistic bipolar junctions in chemically gated graphene ribbons". Sci. Rep. **5** 9955 (2015).

[41] S Reich et al.: "Tight-binding description of graphene". Phys. Rev. B **66** 035412 (2002).

[42] G. Li, A. Luican, and E. Y. Andrei: "Scanning tunneling spectroscopy of graphene on graphite." Phys. Rev. Lett. **102** 176804 (2009).

[43] N. Levy et al.: "Strain-Induced Pseudo-Magnetic Fields Greater Than 300 Tesla in Graphene Nanobubbles". Science **329** 544–547 (2010).

[44] W. Yan et al.: "Strain and curvature induced evolution of electronic band structures in twisted graphene bilayer." Nat. Commun. **4** 2159 (2013).

[45] W. Jolie et al.: "Confinement of Dirac electrons in graphene quantum dots". Phys. Rev. B **89** 155435 (2014).

[46] W. Jolie, F. Craes, and C. Busse: "Graphene on weakly interacting metals: Dirac states versus surface states". Phys. Rev. B **91** 115419 (2015).

[47] M. F. Crommie, C. P. Lutz, and D. M. Eigler: "Confinement of electrons to quantum corrals on a metal surface." Science **262** 218–220 (1993).

[48] C. Tao et al.: "Spatially resolving edge states of chiral graphene nanoribbons". Nat. Phys. **7** 616–620 (2011).

[49] M. M. Ugeda et al.: "Missing Atom as a Source of Carbon Magnetism". Phys. Rev. Lett. **104** 096804 (2010).

[50] H. Gonzalez-Herrero et al.: "Atomic-scale control of graphene magnetism by using hydrogen atoms". Science **352** 437–441 (2016).

[51] A. Varykhalov et al.: "Electronic and Magnetic Properties of Quasifreestanding Graphene on Ni". Phys. Rev. Lett. **101** 157601 (2008).

[52] I. Pletikosić et al.: "Dirac Cones and Minigaps for Graphene on Ir(111)". Phys. Rev. Lett. **102** 056808 (2009).

[53] F. Craes et al.: "Mapping Image Potential States on Graphene Quantum Dots". Phys. Rev. Lett. **111** 056804 (2013).

[54] M. Petrović et al.: "The mechanism of caesium intercalation of graphene". Nat. Commun. **4** 2772 (2013).

[55] E. Gränäs et al.: "Oxygen intercalation under graphene on Ir(111): energetics, kinetics, and the role of graphene edges." ACS Nano **6** 9951–9963 (2012).

[56] U. A. Schröder et al.: "Core level shifts of intercalated graphene". 2D Mater. **4** 015013 (2016).

[57] I. Brihuega et al.: "Unraveling the Intrinsic and Robust Nature of van Hove Singularities in Twisted Bilayer Graphene by Scanning Tunneling Microscopy and Theoretical Analysis". Phys. Rev. Lett. **109** 196802 (2012).

[58] K. S. Kim et al.: "Coexisting massive and massless Dirac fermions in symmetry-broken bilayer graphene". Nat. Mater. **12** 887–892 (2013).

[59] J. Sánchez-Barriga et al.: "Effect of structural modulation and thickness of a graphene overlayer on the binding energy of the Rashba-type surface state of Ir(111)". New J. Phys. **15** (2013).

[60] S. Nie et al.: "Growth from Below: Graphene Bilayers on Ir(111)". ACS Nano **5** 2298–2306 (2011).

[61] M. Yankowitz et al.: "Emergence of superlattice Dirac points in graphene on hexagonal boron nitride". Nat. Phys. **8** 382–386 (2012).

[62] N. Ehlen: Private Communication.

[63] M. C. Lucking et al.: "Multivalency-Induced Band Gap Opening at MoS_2 Edges". Chem. Mater. **27** 3326–3331 (2015).

[64] J. Silva-Guillén, P. San-Jose, and R. Roldán: "Electronic Band Structure of Transition Metal Dichalcogenides from Ab Initio and Slater-Koster Tight-Binding Model". Appl. Sci. **6** 284 (2016).

[65] K. Yao et al.: "Optically Discriminating Carrier-Induced Quasiparticle Band Gap and Exciton Energy Renormalization in Monolayer MoS_2". Phys. Rev. Lett. **119** 087401 (2017).

[66] D. Y. Qiu, F. H. da Jornada, and S. G. Louie: "Optical Spectrum of MoS_2: Many-Body Effects and Diversity of Exciton States". Phys. Rev. Lett. **111** 216805 (2013).

[67] S. W. Han et al.: "Band-gap transition induced by interlayer van der Waals interaction in MoS_2". Phys. Rev. B **84** 045409 (2011).

[68] Y. Zhang et al.: "Direct observation of the transition from indirect to direct bandgap in atomically thin epitaxial $MoSe_2$". Nat. Nanotechnol. **9** 111–115 (2013).

[69] X. Zhang et al.: "Hidden spin polarization in inversion-symmetric bulk crystals". Nat. Phys. **10** 387–393 (2014).

[70] E. Razzoli et al.: "Selective Probing of Hidden Spin-Polarized States in Inversion-Symmetric Bulk MoS_2". Phys. Rev. Lett. **118** 086402 (2017).

[71] A. Pulkin and O. V. Yazyev: "Spin- and valley-polarized transport across line defects in monolayer MoS_2". Phys. Rev. B **93** 041419 (2016).

[72] H.-P. Komsa and A. V. Krasheninnikov: "Engineering the Electronic Properties of Two-Dimensional Transition Metal Dichalcogenides by Introducing Mirror Twin Boundaries". Adv. Electron. Mater. **3** 1600468 (2017).

[73] W. Zhou et al.: "Intrinsic structural defects in monolayer molybdenum disulfide". Nano Lett. **13** 2615–2622 (2013).

[74] J. Henk, A. Ernst, and P. Bruno: "Spin polarization of the L-gap surface states on Au(111)". Phys. Rev. B **68** 165416 (2003).

[75] L. El-Kareh et al.: "A combined experimental and theoretical study of Rashba-split surface states on the $(\sqrt{3} \times \sqrt{3})$ Pb/Ag(111)$R30°$ surface". New J. Phys. **16** 045017 (2014).

[76] K. Tsutsumi et al.: "Incommensurate Periodic Lattice Distortion Perpendicular to the Layer in 1T-VSe_2". J. Phys. Soc. Japan **49** 837–838 (1980).

[77] R. Friend et al.: "Pressure enhancement of charge density wave formation in VSe_2; The role of coulomb correlations". Solid State Commun. **27** 169–173 (1978).

[78] S. Sugai et al.: "Investigation of the charge density waves in 1T-VSe_2 by Raman scattering". Le J. Phys. Colloq. **42** 740–742 (1981).

[79] K. Tsutsumi: "X-ray-diffraction study of the periodic lattice distortion associated with a charge-density wave in 1T-VSe_2". Phys. Rev. B **26** 5756–5759 (1982).

[80] S. Sugai: "Lattice Vibrations in the Charge-Density- Wave States of Layered Transition Metal Dichalcogenides". Phys. Status Solidi **129** 13–39 (1985).

[81] D. J. Eaglesham, R. L. Withers, and D. M. Bird: "Charge-density-wave transitions in 1T-VSe_2". J. Phys. C Solid State Phys. **19** 359–367 (1986).

[82] J. Mahy, J. Van Landuyt, and S. Amelinckx: "Diffraction Evidence for Superstructures in Vanadium Diselenide". Phys. status solidi **74** K89–K91 (1982).

[83] Z. Ren et al.: "Optimizing $Bi_{2-x}Sb_xTe_{3-y}Se_y$ solid solutions to approach the intrisic topological insulator regime". Phys. Rev. B **84** 165311 (2011).

[84] T. Arakane et al.: "Tunable Dirac cone in the topological insulator $Bi_{2-x}Sb_xTe_{3-y}Se_y$". Nat. Commun. **3** 636 (2012).

[85] L. Fu and C. L. Kane: "Topological insulators with inversion symmetry". Phys. Rev. B **76** 045302 (2007).

[86] D. I. Khomskii: Basic Aspects of the Quantum Theory of Solids. Cambridge: Cambridge University Press (2012).

[87] G. Grüner: Density Waves in Solids. Boulder: Westview Press (2000).

[88] K. Rossnagel: "On the origin of charge-density waves in select layered transition-metal dichalcogenides." J. Phys. Condens. Matter **23** 213001 (2011).

[89] B. Skinner, T. Chen, and B. I. Shklovskii: "Effects of bulk charged impurities on the bulk and surface transport in three-dimensional topological insulators". J. Exp. Theor. Phys. **117** 579–592 (2013).

[90] J. J. Sakurai: Modern Quantum Mechanics. Ed. by S. F. Tuan. Revised Ed. Addison-Wesley Publishing Company, Inc. (1994).

[91] A. Altland: Advanced Quantum Mechanics - Lecture Notes. 2011.

[92] L. Simon et al.: "Fourier-transform scanning tunnelling spectroscopy: the possibility to obtain constant-energy maps and band dispersion using a local measurement". J. Phys. D. Appl. Phys. **44** 464010 (2011).

[93] S.-K. Chan and V. Heine: "Spin density wave and soft phonon mode from nesting Fermi surfaces". J. Phys. F Met. Phys. **3** 795–809 (1973).

[94] Á. Pásztor et al.: "Dimensional crossover of the charge density wave transition in thin exfoliated VSe_2". 2D Mater. **4** 041005 (2017).

[95] N. W. Ashcroft and N. D. Mermin: Solid State Physics. Saunders College Publishing (1976).

[96] B. I. Shklovskii and A. L. Efros: "Completely Compensated Crystalline Semiconductors as a Model of an Amorphous Semiconductor". Zhurnal Eksp. I Teor. Fiz. **62** 1156 (1972).

[97] B. Skinner, T. Chen, and B. I. Shklovskii: "Why Is the Bulk Resistivity of Topological Insulators So Small?" Phys. Rev. Lett. **109** 176801 (2012).

[98] T. Chen and B. I. Shklovskii: "Anomalously small resistivity and thermopower of strongly compensated semiconductors and topological insulators". Phys. Rev. B **87** 165119 (2013).

[99] B. Skinner, T. Chen, and B. I. Shklovskii: "Effects of bulk charged impurities on the bulk and surface transport in three-dimensional topological insulators". J. Exp. Theor. Phys. **117** 579–592 (2013).

[100] B. Skinner and B. I. Shklovskii: "Theory of the random potential and conductivity at the surface of a topological insulator". Phys. Rev. B **87** 075454 (2013).

[101] M. F. Crommie, C. P. Lutz, and D. M. Eigler: "Imaging standing waves in a two-dimensional electron gas". Nature **363** 524–527 (1993).

[102] Y. Hasegawa and P. Avouris: "Direct observation of standing wave formation at surface steps using scanning tunneling spectroscopy". Phys. Rev. Lett. **71** 1071–1074 (1993).

[103] L. Petersen et al.: "Direct imaging of the two-dimensional Fermi contour: Fourier-transform STM". Phys. Rev. B **57** R6858–R6861 (1998).

[104] M. Steinbrecher et al.: "Rashba-type spin splitting from interband scattering in quasiparticle interference maps". Phys. Rev. B **87** 245436 (2013).

[105] P. Leicht et al.: "Rashba splitting of graphene-covered Au(111) revealed by quasiparticle interference mapping". Phys. Rev. B **90** 241406 (2014).

[106] L. Szunyogh: http://newton.phy.bme.hu/~szunyogh/Elszerk/Kkr-slides.pdf.

[107] S. Chi et al.: "Sign inversion in the superconducting order parameter of LiFeAs inferred from Bogoliubov quasiparticle interference". Phys. Rev. B **89** 104522 (2014).

[108] F. Craes: "Scanning Tunneling Spectroscopy on Graphene Nanostructures". PhD thesis. Universität zu Köln (2014).

[109] B. Voigtländer: Scanning Probe Microscopy. Springer Berlin Heidelberg (2015).

[110] K. Oura et al.: Surface Science. Springer Berlin Heidelberg (2003).

[111] G. Binnig et al.: "Tunneling through a controllable vacuum gap". Appl. Phys. Lett. **40** 178–180 (1982).

[112] G Binnig and H Rohrer: "Scanning tunneling microscopy". Surf. Sci. **126** 236–244 (1983).

[113] G. Binnig et al.: "7 × 7 Reconstruction on Si(111) Resolved in Real Space". Phys. Rev. Lett. **50** 120–123 (1983).

[114] R. Feenstra, J. A. Stroscio, and A. Fein: "Tunneling spectroscopy of the Si(111)2×1 surface". Surf. Sci. **181** 295–306 (1987).

[115] A. J. Macdonald et al.: "Dispersing artifacts in FT-STS: a comparison of set point effects across acquisition modes". Nanotechnology **27** 414004 (2016).

[116] C. Zhang et al.: "Probing Critical Point Energies of Transition Metal Dichalcogenides: Surprising Indirect Gap of Single Layer WSe_2". Nano Lett. **15** 6494–6500 (2015).

[117] N. Hatter et al.: "Magnetic anisotropy in Shiba bound states across a quantum phase transition". Nat. Commun. **6** 8988 (2015).

[118] J. Hall et al.: "Molecular beam epitaxy of quasi-freestanding transition metal disulphide monolayers on van der Waals substrates: A growth study". Submitt. to 2D Mater. (2017).

[119] T. Knispel et al.: "Charge puddles in the bulk and on the surface of the topological insulator $BiSbTeSe_2$ studied by scanning tunneling microscopy and optical spectroscopy". Submitt. to Phys. Rev. B (2017).

[120] S Runte: "Atomic and Electronic Structure of Graphene and Graphene Intercalation Compounds". PhD thesis. Universität zu Köln (2013).

[121] J. Klinkhammer: "Electronic Structure and Magnetism of EuO Films on the Nanometer Scale". PhD thesis. Universität zu Köln (2013).

[122] M. Morgenstern: "Probing the local density of states of dilute electron systems in different dimensions". Surf. Rev. Lett. **10** 933–962 (2003).

[123] I. Horcas et al.: "WSXM: A software for scanning probe microscopy and a tool for nanotechnology". Rev. Sci. Instrum. **78** 013705 (2007).

[124] J. Coraux et al.: "Growth of graphene on Ir(111)". New J. Phys. **11** 023006 (2009).

[125] J. Coraux et al.: "Structural Coherency of Graphene on Ir(111)". Nano Lett. **8** 565–570 (2008).

[126] A. T. N'Diaye et al.: "Structure of epitaxial graphene on Ir(111)". New J. Phys. **10** 043033 (2008).

[127] C. Herbig et al.: "From Permeation to Cluster Arrays: Graphene on Ir(111) Exposed to Carbon Vapor". Nano Lett. **17** 3105–3112 (2017).

[128] S. Schumacher et al.: "Europium underneath graphene on Ir(111): Intercalation mechanism, magnetism, and band structure". Phys. Rev. B **90** 235437 (2014).

[129] W. Jolie et al.: "Visualizing layer polarization in bilayer graphene with quasiparticle interference". Submitt. to Phys. Rev. Lett. (2017).

[130] D. Dombrowski et al.: "Energy-Dependent Chirality Effects in Quasifree-Standing Graphene". Phys. Rev. Lett. **118** 116401 (2017).

[131] K. S. Novoselov et al.: "2D materials and van der Waals heterostructures." Science **353** 9439 (2016).

[132] A. K. Geim and I. V. Grigorieva: "Van der Waals heterostructures." Nature **499** 419–425 (2013).

[133] B. J. LeRoy and M. Yankowitz: "Emergent complex states in bilayer graphene". Science **345** 31–32 (2014).

[134] A. Kou et al.: "Electron-hole asymmetric integer and fractional quantum Hall effect in bilayer graphene". Science **345** 55–57 (2014).

[135] K. Lee et al.: "Chemical potential and quantum Hall ferromagnetism in bilayer graphene". Science **345** 58–61 (2014).

[136] P. Maher et al.: "Tunable fractional quantum Hall phases in bilayer graphene". Science **345** 61–64 (2014).

[137] Q. Tong et al.: "Topological mosaics in moiré superlattices of van der Waals heterobilayers". Nat. Phys. **13** 356–362 (2016).

[138] C. Pan et al.: "Layer Polarizability and Easy-Axis Quantum Hall Ferromagnetism in Bilayer Graphene". Nano Lett. **17** 3416–3420 (2017).

[139] K. S. Kim et al.: "Visualizing Atomic-Scale Negative Differential Resistance in Bilayer Graphene". Phys. Rev. Lett. **110** 036804 (2013).

[140] G. M. Rutter et al.: "Scattering and interference in epitaxial graphene." Science **317** 219–222 (2007).

[141] P. Mallet et al.: "Role of pseudospin in quasiparticle interferences in epitaxial graphene probed by high-resolution scanning tunneling microscopy". Phys. Rev. B **86** 045444 (2012).

[142] M. Yankowitz et al.: "Band structure mapping of bilayer graphene via quasiparticle scattering". APL Mater. **2** 092503 (2014).

[143] L. Simon et al.: "Symmetry of standing waves generated by a point defect in epitaxial graphene". Eur. Phys. J. B **69** 351–355 (2009).

[144] C. Bena: "Effect of a single localized impurity on the local density of States in monolayer and bilayer graphene." Phys. Rev. Lett. **100** 076601 (2008).

[145] K. Sugawara et al.: "Semiconductor-Metal Transition and Band-Gap Tuning in Quasi-Free-Standing Epitaxial Bilayer Graphene on SiC". J. Phys. Soc. Japan **80** 024705 (2011).

[146] B. Van Duppen and F. M. Peeters: "Four-band tunneling in bilayer graphene". Phys. Rev. B **87** 205427 (2013).

[147] T. Knispel: "STM and STS on in situ cleaved bulk crystals: Charge puddles and charge density waves". Master thesis. Universität zu Köln (2017).

[148] Y. Xia et al.: "Observation of a large-gap topological-insulator class with a single Dirac cone on the surface". Nat. Phys. **5** 398–402 (2009).

[149] D. Hsieh et al.: "Observation of Unconventional Quantum Spin Textures in Topological Insulators". Science **323** 919–922 (2009).

[150] C. H. Li et al.: "Electrical detection of charge-current-induced spin polarization due to spin-momentum locking in Bi_2Se_3". Nat. Nanotechnol. **9** 218–224 (2014).

[151] A. A. Taskin et al.: "Observation of Dirac Holes and Electrons in a Topological Insulator". Phys. Rev. Lett. **107** 016801 (2011).

[152] J. Martin et al.: "Observation of electron-hole puddles in graphene using a scanning single-electron transistor". Nat. Phys. **4** 144–148 (2008).

[153] Y. Zhang et al.: "Origin of spatial charge inhomogeneity in graphene". Nat. Phys. **5** 722–726 (2009).

[154] A. Deshpande et al.: "Spatially resolved spectroscopy of monolayer graphene on SiO_2". Phys. Rev. B **79** 205411 (2009).

[155] J. Xue et al.: "Scanning tunnelling microscopy and spectroscopy of ultra-flat graphene on hexagonal boron nitride". Nat. Mater. **10** 282–285 (2011).

[156] S. Samaddar et al.: "Charge Puddles in Graphene near the Dirac Point". Phys. Rev. Lett. **116** 126804 (2016).

[157] A. Deshpande et al.: "Spatial Mapping of the Dirac Point in Monolayer and Bilayer Graphene". IEEE Trans. Nanotechnol. **10** 88–91 (2011).

[158] H. Beidenkopf et al.: "Spatial fluctuations of helical Dirac fermions on the surface of topological insulators". Nat. Phys. **7** 939–943 (2011).

[159] C. Pauly et al.: "Spatially resolved Landau level spectroscopy of the topological Dirac cone of bulk-type $Sb_2Te_3(0001)$: Potential fluctuations and quasiparticle lifetime". Phys. Rev. B **92** 085140 (2015).

[160] S. Kim et al.: "Robust protection from backscattering in the topological insulator $Bi_{1.5}Sb_{0.5}Te_{1.7}Se_{1.3}$". Phys. Rev. Lett. **112** 136802 (2014).

[161] W. Ko et al.: "Local potential fluctuation of topological surface states in $Bi_{1.5}Sb_{0.5}Te_{1.7}Se_{1.3}$ observed by Landau level spectroscopy". Appl. Phys. Lett. **108** 083109 (2016).

[162] Y. Okada et al.: "Direct Observation of Broken Time-Reversal Symmetry on the Surface of a Magnetically Doped Topological Insulator". Phys. Rev. Lett. **106** 206805 (2011).

[163] L. Fu: "Hexagonal Warping Effects in the Surface States of the Topological Insulator Bi_2Te_3". Phys. Rev. Lett. **103** 266801 (2009).

[164] Z. Alpichshev et al.: "STM Imaging of Electronic Waves on the Surface of Bi_2Te_3: Topologically Protected Surface States and Hexagonal Warping Effects". Phys. Rev. Lett. **104** 016401 (2010).

[165] Henry Legg: Private Communication.

[166] T. Bömerich et al.: "Length scale of puddle formation in compensation-doped semiconductors and topological insulators". Phys. Rev. B **96** 075204 (2017).

[167] A. Splendiani et al.: "Emerging photoluminescence in monolayer MoS_2". Nano Lett. **10** 1271–1275 (2010).

[168] B. Radisavljevic et al.: "Single-layer MoS_2 transistors". Nat. Nanotechnol. **6** 147–150 (2011).

[169] Q. H. Wang et al.: "Electronics and optoelectronics of two-dimensional transition metal dichalcogenides". Nat. Nanotechnol. **7** 699–712 (2012).

[170] M. V. Bollinger et al.: "One-Dimensional Metallic Edge States in MoS_2". Phys. Rev. Lett. **87** 196803 (2001).

[171] A. Bruix et al.: "Single-layer MoS_2 on Au(111): Band gap renormalization and substrate interaction". Phys. Rev. B **93** 165422 (2016).

[172] X. Liu et al.: "Rotationally commensurate growth of MoS_2 on epitaxial graphene". ACS Nano **10** 1067–1075 (2016).

[173] X. Zhou et al.: "Periodic Modulation of the Doping Level in Striped MoS_2 Superstructures". ACS Nano **10** 3461–3468 (2016).

[174] J. Shi et al.: "Narrow-Gap Quantum Wires Arising from the Edges of Monolayer MoS_2 Synthesized on Graphene". Adv. Mater. Interfaces **3** 1600332 (2016).

[175] C.-I. Lu et al.: "Graphite edge controlled registration of monolayer MoS_2 crystal orientation". Appl. Phys. Lett. **106** 181904 (2015).

[176] C. Zhang et al.: "Direct Imaging of Band Profile in Single Layer MoS_2 on Graphite: Quasiparticle Energy Gap, Metallic Edge States, and Edge Band Bending". Nano Lett. **14** 2443–2447 (2014).

[177] M.-H. Chiu et al.: "Determination of band alignment in the single-layer MoS_2/WSe_2 heterojunction". Nat. Commun. **6** 7666 (2015).

[178] Y. L. Huang et al.: "Bandgap tunability at single-layer molybdenum disulphide grain boundaries." Nat. Commun. **6** 6298 (2015).

[179] N. Krane et al.: "Electronic Structure and Luminescence of Quasi-Freestanding MoS_2 Nanopatches on Au(111)". Nano Lett. **16** 5163–5168 (2016).

[180] C. Zhang et al.: "Interlayer couplings, Moiré patterns, and 2D electronic superlattices in MoS_2 /WSe_2 hetero-bilayers". Sci. Adv. **3** e1601459 (2017).

[181] C. Zhang et al.: "Visualizing band offsets and edge states in bilayer-monolayer transition metal dichalcogenides lateral heterojunction". Nat. Commun. **7** 10349 (2016).

[182] J. Kim et al.: "Quantum size effects on the work function of metallic thin film nanostructures". Proc. Natl. Acad. Sci. **107** 12761–12765 (2010).

[183] A. T. N'Diaye et al.: "In situ observation of stress relaxation in epitaxial graphene". New J. Phys. **11** 113056 (2009).

[184] A. M. van der Zande et al.: "Grains and grain boundaries in highly crystalline monolayer molybdenum disulphide." Nat. Mater. **12** 554–61 (2013).

[185] T. H. Ly et al.: "Misorientation-angle-dependent electrical transport across molybdenum disulfide grain boundaries". Nat. Commun. **7** 10426 (2016).

[186] J. Lin, S. T. Pantelides, and W. Zhou: "Vacancy-Induced Formation and Growth of Inversion Domains in Transition-Metal Dichalcogenide Monolayer". ACS Nano **9** 5189–5197 (2015).

[187] S. J. Altenburg et al.: "Local Gating of an Ir(111) Surface Resonance by Graphene Islands". Phys. Rev. Lett. **108** 206805 (2012).

[188] A. Varykhalov et al.: "Ir(111) Surface State with Giant Rashba Splitting Persists under Graphene in Air". Phys. Rev. Lett. **108** 66804 (2012).

[189] R. M. Feenstra: "Tunneling spectroscopy of the GaAs(110) surface". J. Vac. Sci. Technol. B Microelectron. Nanom. Struct. **5** 923 (1987).

[190] R. M. Feenstra et al.: "Influence of tip-induced band bending on tunnelling spectra of semiconductor surfaces". Nanotechnology **18** 044015 (2007).

[191] T. Yamauchi et al.: "Metal Adsorption Effect on Tunneling Spectra in Scanning Tunneling Spectroscopy of InAs Quantum Dots on GaAs(001)". Jpn. J. Appl. Phys. **42** 4495–4498 (2003).

[192] F. Herbert et al.: "Quantification of electronic band gap and surface states on FeS_2(100)". Surf. Sci. **618** 53–61 (2013).

[193] A. Grubišić Čabo et al.: "Observation of Ultrafast Free Carrier Dynamics in Single Layer MoS_2". Nano Lett. **15** 5883–5887 (2015).

[194] J. V. Lauritsen et al.: "Size-dependent structure of MoS_2 nanocrystals". Nat. Nanotechnol. **2** 53–58 (2007).

[195] X. Zhang et al.: "Experimentally Engineering the Edge Termination of Graphene Nanoribbons". ACS Nano **7** 198–202 (2013).

[196] R. Drost et al.: "Electronic States at the Graphene-Hexagonal Boron Nitride Zigzag Interface". Nano Lett. **14** 5128–5132 (2014).

[197] U. A. Schröder et al.: "Core level shifts of intercalated graphene". 2D Mater. **4** 015013 (2016).

[198] S. Schumacher et al.: "The Backside of Graphene: Manipulating Adsorption by Intercalation". Nano Lett. **13** 5013–5019 (2013).

[199] A. V. Fedorov et al.: "Efficient gating of epitaxial boron nitride monolayers by substrate functionalization". Phys. Rev. B **92** 125440 (2015).

[200] D. Niesner et al.: "Trapping surface electrons on graphene layers and islands". Phys. Rev. B **85** 081402 (2012).

[201] M. Shiraishi and M. Ata: "Work function of carbon nanotubes". Carbon N. Y. **39** 1913–1917 (2001).

[202] S. Y. Lee et al.: "Large Work Function Modulation of Monolayer MoS_2 by Ambient Gases". ACS Nano **10** 6100–6107 (2016).

[203] C. Kim et al.: "Separation of spin and charge excitations in one-dimensional $SrCuO_2$". Phys. Rev. B **56** 15589–15595 (1997).

[204] B. J. Kim et al.: "Distinct spinon and holon dispersions in photoemission spectral functions from one-dimensional SrCuO2". Nat. Phys. **2** 397–401 (2006).

[205] M. Hashisaka et al.: "Waveform measurement of charge- and spin-density wavepackets in a chiral Tomonaga-Luttinger liquid". Nat. Phys. **13** 559–562 (2017).

[206] C. Blumenstein et al.: "Atomically controlled quantum chains hosting a Tomonaga-Luttinger liquid". Nat. Phys. **7** 776–780 (2011).

[207] X. Zou, Y. Liu, and B. I. Yakobson: "Predicting Dislocations and Grain Boundaries in Two-Dimensional Metal-Disulfides from the First Principles". Nano Lett. **13** 253–258 (2013).

[208] D. Le and T. S. Rahman: "Joined edges in MoS_2: metallic and half-metallic wires". J. Phys. Condens. Matter **25** 312201 (2013).

[209] M. Gibertini and N. Marzari: "Emergence of One-Dimensional Wires of Free Carriers in Transition-Metal-Dichalcogenide Nanostructures". Nano Lett. **15** 6229–6238 (2015).

[210] M. Farmanbar, T. Amlaki, and G. Brocks: "Green's function approach to edge states in transition metal dichalcogenides". Phys. Rev. B **93** 205444 (2016).

[211] A. R. Botello-Méndez et al.: "Metallic and ferromagnetic edges in molybdenum disulfide nanoribbons". Nanotechnology **20** 325703 (2009).

[212] A. Vojvodic, B. Hinnemann, and J. K. Nørskov: "Magnetic edge states in MoS_2 characterized using density-functional theory". Phys. Rev. B **80** 125416 (2009).

[213] F. Khoeini, K. Shakouri, and F. M. Peeters: "Peculiar half-metallic state in zigzag nanoribbons of MoS_2 : Spin filtering". Phys. Rev. B **94** 125412 (2016).

[214] J. Zhang et al.: "Magnetic Molybdenum Disulfide Nanosheet Films". Nano Lett. **7** 2370–2376 (2007).

[215] R.-L. Chu et al.: "Spin-orbit-coupled quantum wires and Majorana fermions on zigzag edges of monolayer transition-metal dichalcogenides". Phys. Rev. B **89** 155317 (2014).

[216] J. V. Lauritsen et al.: "Chemistry of one-dimensional metallic edge states in MoS_2 nanoclusters". Nanotechnology **14** 385–389 (2003).

[217] H. Xu et al.: "Oscillating edge states in one-dimensional MoS_2 nanowires". Nat. Commun. **7** 12904 (2016).

[218] F. Cheng et al.: "Controlled Growth of 1D $MoSe_2$ Nanoribbons with Spatially Modulated Edge States". Nano Lett. **17** 1116–1120 (2017).

[219] A. N. Enyashin et al.: "Line Defects in Molybdenum Disulfide Layers". J. Phys. Chem. C **117** 10842–10848 (2013).

[220] S. Wang et al.: "Detailed Atomic Reconstruction of Extended Line Defects in Monolayer MoS_2". ACS Nano **10** 5419–5430 (2016).

[221] C Kittel: Introduction to Solid State Physics. 4th ed. New York: John Wiley & Sons, Inc. (1971).

[222] H.-P. Komsa: Private Communication.

[223] P. Berggren and J. Fransson: "Theory of spin inelastic tunneling spectroscopy for superconductor-superconductor and superconductor-metal junctions". Phys. Rev. B **91** 205438 (2015).

[224] A. Molina-Sánchez and L. Wirtz: "Phonons in single-layer and few-layer MoS_2 and WS_2". Phys. Rev. B **84** 155413 (2011).

[225] S. Horzum et al.: "Phonon softening and direct to indirect band gap crossover in strained single-layer $MoSe_2$". Phys. Rev. B **87** 125415 (2013).

[226] H. Fukuyama and P. A. Lee: "Dynamics of the charge-density wave. I. Impurity pinning in a single chain". Phys. Rev. B **17** 535–541 (1978).

[227] D. M. Oh and H. W. Yeom: "Atomistic view of impurities interacting with a quasi-one-dimensional charge density wave". Phys. Rev. B **93** 235448 (2016).

[228] Y. Ma et al.: "Metallic Twin Grain Boundaries Embedded in $MoSe_2$ Monolayers Grown by Molecular Beam Epitaxy". ACS Nano **11** 5130–5139 (2017).

[229] F. Anfuso and S. Eggert: "Luttinger liquid in a finite one-dimensional wire with box-like boundary conditions". Phys. Rev. B **68** 241301 (2003).

[230] B. E. Feldman et al.: "High-resolution studies of the Majorana atomic chain platform". Nat. Phys. **13** 286–291 (2016).

[231] A. T. N'Diaye et al.: "Two-Dimensional Ir Cluster Lattice on a Graphene Moiré on Ir(111)". Phys. Rev. Lett. **97** 215501 (2006).

[232] M. Vojta: "Quantum phase transitions". Reports Prog. Phys. **66** 2069–2110 (2003).

[233] X. Xi et al.: "Strongly enhanced charge-density-wave order in monolayer $NbSe_2$". Nat. Nanotechnol. **10** 765–769 (2015).

[234] T. Ritschel et al.: "Orbital textures and charge density waves in transition metal dichalcogenides". Nat. Phys. **11** 328–331 (2015).

[235] M Porer et al.: "Non-thermal separation of electronic and structural orders in a persisting charge density wave." Nat. Mater. **13** 857–61 (2014).

[236] X. Xi et al.: "Gate Tuning of Electronic Phase Transitions in Two-Dimensional $NbSe_2$". Phys. Rev. Lett. **117** 106801 (2016).

[237] S. He et al.: "Synthesis, Stability and Intrinsic Photocatalytic Properties of Vanadium Diselenide". J. Mater. Chem. A **5** 2163–2171 (2016).

[238] J. Gao et al.: "Preparation of vanadium diselenide thin films and their application in CdTe solar cells". Thin Solid Films **550** 638–642 (2014).

[239] V. N. Strocov et al.: "Three-Dimensional Electron Realm in VSe_2 by Soft-X-Ray Photoelectron Spectroscopy: Origin of Charge-Density Waves". Phys. Rev. Lett. **109** 086401 (2012).

[240] R. Coleman et al.: "Scanning tunnelling microscopy of charge-density waves in transition metal chalcogenides". Adv. Phys. **37** 559–644 (1988).

[241] B. Giambattista et al.: "Scanning tunneling microscopy of atoms and charge-density waves in $1T$-TaS_2, $1T$-$TaSe_2$, and $1T$-VSe_2". Phys. Rev. B **41** 10082–10103 (1990).

[242] J. J. Kim, C. Park, and H. Olin: "A study of charge-density-waves associated with the periodic lattice distortion in 1T-VSe_2 using a low temperature scanning tunneling microscope". J. Korean Phys. Soc. **31** 713–716 (1997).

[243] J. Yang et al.: "Thickness dependence of the charge-density-wave transition temperature in VSe_2". Appl. Phys. Lett. **105** 063109 (2014).

[244] K. Xu et al.: "Ultrathin Nanosheets of Vanadium Diselenide: A Metallic Two-Dimensional Material with Ferromagnetic Charge-Density-Wave Behavior". Angew. Chemie Int. Ed. **52** 10477–10481 (2013).

[245] C. Wang: "Spectroscopy of dichalcogenides and trichalcogenides using scanning tunneling microscopy". J. Vac. Sci. Technol. B Microelectron. Nanom. Struct. **9** 1048 (1991).

[246] I. Ekvall et al.: "Locally modified charge-density waves in Na intercalated VSe_2 studied by scanning tunneling microscopy and spectroscopy". Phys. Rev. B **59** 7751–7761 (1999).

[247] K. Terashima et al.: "Charge-density wave transition of $1T$-VSe_2 studied by angle-resolved photoemission spectroscopy". Phys. Rev. B **68** 155108 (2003).

[248] T. Sato et al.: "Three-Dimensional Fermi-Surface Nesting in 1T-VSe_2 Studied by Angle-Resolved Photoemission Spectroscopy". J. Phys. Soc. Japan **73** 3331–3334 (2004).

[249] H. E. Brauer et al.: "Electronic structure of pure and alkali-metal-intercalated VSe_2". Phys. Rev. B **58** 10031–10045 (1998).

[250] H. Mutka and P. Molinie: "Irradiation-induced defects in layered dichalcogenides: the case of VSe_2". J. Phys. C Solid State Phys. **15** 6305 (1982).

[251] K. Hayashi and M. Nakahira: "Stability and the equilibrium selenium vapor pressure of the VSe2 phase". J. Solid State Chem. **24** 153–161 (1978).

[252] H. Mutka et al.: "Effects of defects on charge density waves in layered dichalcogenides". Solid State Commun. **50** 161–164 (1984).

[253] C. J. Arguello et al.: "Visualizing the charge density wave transition in 2H-$NbSe_2$ in real space". Phys. Rev. B **89** 235115 (2014).

[254] J. McCarten et al.: "Charge-density-wave pinning and finite-size effects in $NbSe_3$". Phys. Rev. B **46** 4456–4482 (1992).

[255] H. H. Weitering: "Defect-Mediated Condensation of a Charge Density Wave". Science **285** 2107–2110 (1999).

[256] R. Larciprete et al.: "Oxygen switching of the epitaxial graphene-metal interaction." ACS Nano **6** 9551–9558 (2012).

[257] Q. Liu, X.-L. Qi, and S.-C. Zhang: "Stationary phase approximation approach to the quasiparticle interference on the surface of a strong topological insulator". Phys. Rev. B **85** 125314 (2012).

[258] H.-M. Guo and M. Franz: "Theory of quasiparticle interference on the surface of a strong topological insulator". Phys. Rev. B **81** 041102 (2010).

[259] L. Capriotti, D. J. Scalapino, and R. D. Sedgewick: "Wave-vector power spectrum of the local tunneling density of states: Ripples in a d-wave sea". Phys. Rev. B **68** 014508 (2003).

[260] W. Jolie et al.: "One-dimensional charge density waves in MoS_2 grain boundaries". In Prep. (2017).

[261] C. Herbig et al.: "Interfacial Carbon Nanoplatelet Formation by Ion Irradiation of Graphene on Iridium(111)". ACS Nano **8** 12208–12218 (2014).

[262] C. Herbig et al.: “Comment on "Interfacial Carbon Nanoplatelet Formation by Ion Irradiation of Graphene on Iridium(111)"”. ACS Nano **9** 4664–4665 (2015).

[263] A. J. Martínez-Galera et al.: “Oxygen orders differently under graphene: new superstructures on Ir(111)”. Nanoscale **8** 1932–1943 (2016).

[264] I. Šrut Rakić et al.: “Step-induced faceting and related electronic effects for graphene on Ir(332)”. Carbon N. Y. **110** 267–277 (2016).

[265] F. H. Farwick zum Hagen et al.: “Structure and Growth of Hexagonal Boron Nitride on Ir(111)”. ACS Nano **10** 11012–11026 (2016).

APPENDIX G

Danksagung *(Acknowledgments)*

Many people contributed to this work. To those I would finally like to express my gratitude.

- Prof. **Carsten Busse** to offer me the opportunity to do my PhD in his group. Though often more (Münster and Siegen) or less (red floor) separated during the whole PhD I felt constant support and interest in my work from him. I am really grateful for his confidence in my ideas and his countless advices.

- Prof. **Thomas Michely** to referee my work. Though being in Carsten's group, I felt very much like having two supervisors, and parts of this thesis have indeed been proposed by Thomas, who largely discussed the results with us.

- Prof. **Achim Rosch** to be the *Vorsitzender der Prüfungskommission* and for the various collaborations during my PhD thesis. Many discussions in your and Thomas' office have brought forward many of the topics covered in this thesis.

- Dr. **Christoph Grams** möchte ich danken für die Übernahme des Beisitzes.

- all people that worked with me at TSTM: Dr. **Fabian Craes**, Dr. **Sven Runte**, Dr. **Jürgen Klinkhammer** who introduced me to the system. Dr. **Charlotte Herbig** who investigated the electronic properties of blisters. **Daniela Dombrowski** who started her PhD less than a year after me at TSTM. It is so much nicer to have someone to discuss recent results or thinking about further steps. **Stefan Kraus** who built a noise detector, **Jiaqi Cai** who updated the drawings of our sample holders and with whom I worked a lot on boron nitride. **Mathias Pörtner** who learned many useful things about STS and the Createc software in Nijmegen. He also helped me to measure the standing wave and spectra of bilayer graphene day and

night and, together with **Thomas Pradella**, measured very appealing magnetic signals using spin-polarized STS. **Tobias Hartl** who made our Faraday cup and assisted me during the bilayer graphene sample preparation. **Timo Knispel** who mounted the bulk layered crystals on the Createc sample holder and measured many of the results presented in this thesis. Last but not least, a big thanks to **Clifford Murray** who worked with me on molybdenum disulfide and is now responsible for the lab. It has been an honor to work with you guys!

- Dr **Jonathan Lux**, **Henry Legg**, **Fabian Portner** and **Philipp Weiß** from the AG Rosch. Having you as collaborators sitting next door has proven to increase the productivity a lot, resulting in many results that are nicely backed up by theoretical simulations, increasing the impact of many topics.

- **Konstantin Nikonov** who prepared the VSe_2 crystals, **Niels Ehlen** who provided various TB simulations and ARPES results, as well as Prof. **Alexander Grüneis** for valuable discussions.

- Prof. **Yoichi Ando**, Prof **Markus Grüninger**, Dr. **Zhiwei Wang** and **Nick Borgwardt** who contributed to the work on $BiSbTeSe_2$.

- Dr. **Hannu-Pekka Komsa** who provided density functional theory calculations on MoS_2 mirror twin boundaries. I also need to thank Dr. **Arkady Krasheninnikov** and Dr. **Nicolae Atodiresei** who also contributed to this project.

- **Clifford Murray**, **Joshua Hall**, Dr. **Ulrike Schröder**, **Timo Knispel**, Dr. **Felix Huttmann**, **Nick Borgwardt** and **Kerstin Spyker** for a critical read through all these pages.

- **Norbert Henn** for his numerous technical advices.

- All past, current and future members of **AG Michely**, **AG Busse** and of the Institute of Physics II for the familiar atmosphere.

- The Bonn-Cologne Graduate School of Physics and Astronomy for the financial support during and after my PhD, especially Dr. **Petra Neubauer-Guenther**.

- My family, friends and girlfriend who showed me every day that physics cannot be the only content of a fulfilled life.

APPENDIX H

Offizielle Erklärung

Ich versichere, dass ich die von mir vorgelegte Dissertation selbstständig angefertigt, die benutzten Quellen und Hilfsmittel vollständig angegeben und die Stellen der Arbeit - einschließlich Tabellen, Karten und Abbildungen -, die anderen Werken im Wortlaut oder dem Sinn nach entnommen sind, in jedem Einzelfall als Entlehnung kenntlich gemacht habe; dass diese Dissertation noch keiner anderen Fakultät oder Universität zur Prüfung vorgelegen hat; dass sie - abgesehen von den angegebenen Teilpublikationen - noch nicht veröffentlicht worden ist, sowie, dass ich eine solche Veröffentlichung vor Abschluss des Promotionsverfahrens nicht vornehmen werde. Die Bestimmungen der Promotionsordnung sind mir bekannt. Die von mir vorgelegte Dissertation ist von Prof. Dr. Carsten Busse betreut worden.

Köln, den 16.10.2017

Wouter Jolie